Centre for Future Air-Space Transportation Technology
Department of Mechanical and Aerospace Engineering
Faculty of Engineering
University of Strathclyde

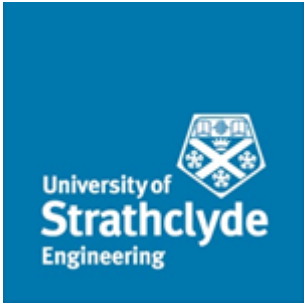

Multi-Disciplinary Modelling of Future Space-Access Vehicles

Romain Wuilbercq

Submitted in partial fulfillment of the requirements for the degree of

Doctor of Philosophy

2015

This thesis is the result of the author's original research. It has been composed by the author and has not been previously submitted for examination which has led to the award of a degree.

Romain Wuilbercq
Glasgow, Scotland, 18/03/2015

To my family.

Keep Ithaka always in your mind.
Arriving there is what you are destined for.
But do not hurry the journey at all.
Better if it lasts for years,
so you are old by the time you reach the island,
wealthy with all you have gained on the way,
not expecting Ithaka to make you rich.

– C. P. Cavafy

Acknowledgements

A number of people deserve a wholehearted thank you for their ability to stay on board my very own *Endeavour* ship throughout the entire course of my Ph.D, a vessel travelling sometimes across shallow water, at times through storms.

On the port side, I would like to thank my supervisor, Prof. Richard E Brown, for his advice, support and insight during my Ph.D. I would like to thank my colleagues from the Centre for Future Air-Space Transportation Technology (CFASTT) for their support, technical and moral, before and during the writing up of this dissertation. I would like to thank Alessandro Mogavero for his technical help and for giving me access to his HyPro computer program.

On the starboard side, I would like to thank my friends for their encouragement and support. More importantly, I would like to thank Paulina Christophoridou for both her patience during these long hours exclusively dedicated to writing up my thesis and for her overall ability to bear with me throughout this very long journey. Her continuous support has helped me in completing this dissertation.

Finally, *at port*, I would like to express my most profound love towards my family for always encouraging me and being there for me. They have been my greatest support throughout those years. I have also a thought for my Grandpa who has left us the year I started my Ph.D.

Abstract

Re-usable Single-Stage-To-Orbit (SSTO) vehicles represent a promising alternative to conventional expendable rocket launchers, since they will be capable of taking off from a conventional runway, delivering a payload to orbit and gliding back to their spaceport before preparing for re-launch. SSTOs are foreseen to reduce drastically the current costs of access to space and to increase the diversity of practical and economic space applications.

The design of aircraft-like launchers is hampered by a myriad of design challenges, however. The coupling between the behaviour of their various systems challenges conventional aircraft design practices and requires that a detailed cross-disciplinary and systemic modelling approach be applied early on in their evolution toward a workable prototype. This dissertation focuses on the development of efficient algorithms and modelling strategies for the purpose of the multidisciplinary design and optimization of the next generation of fully reusable aircraft-like launch systems. The approach followed is to represent the vehicle as an interconnected system which can then be discretized into a series of constituent components.

The resulting multidisciplinary design environment combines the use of a new reduced-order aerothermodynamic model, specifically conceived to provide a predictive accuracy suitable for preliminary design, with a series of tools that have been developed to model some of the critical components of SSTOs. This modelling environment can be used to predict the overall performance, mass and trajectory of the vehicle, to concurrently size the active and passive thermal shields, organize the internal configuration of the vehicle, and evaluate the performance of the propulsive device. A number of design applications and validations are provided to support the relevance of this approach to the modelling of the characteristics of the next generation of space-access vehicles.

Contents

List of Acronyms

ACS	Active Cooling System
APAS	Aerodynamic Preliminary Analysis System
ASTPE	Aero-Servo-Thermo-Propulso-Elastic
ATMU	Active Thermal Management Unit
CBAERO	Configuration-Based Aerodynamics
CFD	Computational Fluid Dynamics
CoM	Centre of Mass
DCS	Direct Cooling System
DSMC	Direct Simulation Monte Carlo
ECEF	Earth-Centered Earth-Fixed
ELV	Expendable Launch Vehicle
ERN	Equivalent Resistive Network
FEA	Finite Element Analysis
FET	Finite Element in Time
GTOM	Gross Take-Off Mass
HASA	Hypersonic Aerospace Sizing Analysis
HOTOL	Horizontal Take-Off and Landing
IDEA	Inflationary Differential Evolution Algorithm
IML	Inner Mould Line
JAXA	Japan Aerospace Exploration Agency
LATCH	Langley Approximate Three-Dimensional Convective Heating
LAURA	Langley Aero-thermodynamic Upwind Relaxation Algorithm
LaWGS	Langley Wireframe Geometry Standard
LCN	Lumped Capacitance Network
LEO	Low Earth Orbit
LSI	Local Surface Inclination
MDAO	Multi-disciplinary Design, Analysis and Optimization
MDO	Multi-disciplinary Design and Optimization
MOPED	Multi-Objective Parzen-based Estimation of Distribution
MSIS	Mass Spectrometer & Incoherent Scatter
MUSCL	Monotonic Upwind Scheme for Conservation Laws
NASA	National Aeronautics and Space Administration
NASP	National Aero-Space Plane
NIA	National Institute of Aerospace

NOLL	North-Oriented Local Level
NS-IE	Normal Shock Isentropic Expansion
OML	Outer Mould Line
OMS	Orbital Maneuvering System
OOP	Object-Oriented Programming
PDE	Partial Differential Equation
RAM	Re-entry Aerodynamics Module
RBCC	Rocket-Based Combined Cycle
RCC	Reinforced Carbon-Carbon
RCS	Reaction Control System
RLV	Re-usable Launch Vehicle
RSI	Re-usable Surface Insulation
SCCREAM	Simulated Combined-Cycle Rocket Engine Analysis Module
S/HAPB	Supersonic/Hypersonic Arbitrary Body Program
SSTO	Single-Stage-To-Orbit
STA	Space Trajectory Analysis
STL	Stereolithography
STS	Space Transportation System
TAEM	Terminal Area Energy Management
TCAT	Thermal Calculation Analysis Tool
TPS	Thermal Protection System
TRL	Technology Readiness Level
TSTO	Two-Stage-To-Orbit
UCDA	University of Colorado Vehicle Design and Analysis
VKF	Von Kármán Facility
WGS	World Geodetic System

A dedicated nomenclature can be found at the end of each individual chapter.

List of Figures

List of Tables

Chapter 1

Introduction

"How many things have been denied one day, only to become realities the next?"
– From the Earth to the Moon, Jules Verne.

In this introductory chapter, the research context and objectives of the thesis are defined. A background discussion about the future generation of fully re-usable space transportation systems is first given in Section 1.1. This background discussion is then used to define the rationale for the dissertation in Section 1.2. Section 1.3 subsequently introduces the research objectives, while Section 1.4 presents an outline of the thesis. Finally, Section 1.5 provides an overview of the conference papers where the present work has been published (or will soon be).

1.1 Background

Re-usable space transportation technology has always remained of broad and current interest only for a number of renowned experts who have always advocated the use of Re-usable Launch Vehicles (RLV) to achieve orders of magnitude reduction in the cost of access-to-space. Nonetheless, despite several decades of indifference, the aerospace field has recently seen a significant resurgence of interest in re-usable launchers – i.e. for example, the recent attempt of the privately-owned company SpaceX to soft land the re-usable first stage of their Falcon 9 rocket on a floating launch pad in January 2015. This recent enthusiasm for re-usable launchers has been motivated by the recent retirement of NASA's partially re-usable Space Transportation System (STS) in August 2011 (which was

the first of its kind), but is mainly driven by both the prohibitive cost of the current generation of Expendable Launch Vehicles (ELVs) as well as our increasing dependence on space-derived services – e.g. telecommunication, navigation, Earth observation, weather and so on. In fact, since the early days of space exploration in the 1960s, the number of satellites and services has increased beyond expectations. Nonetheless, the launch segment, that relies on the well proven but dated rocket technology, represents still today a major contribution to the overall cost of a space mission. A perpetual debate therefore remains and divides the aerospace community within two distinct groups: those in favor of continuing the development of ELVs (the single-use throwaway rocket technology) and those who see RLVs as the next stepping stone in the field. This debate is certainly complex. ELV advocates claim that the development of an RLV would require breakthroughs in a large number of critical technologies (e.g. propulsion system, material and thermal management system). Their main concern is however on the reliability rate that these systems may have to reach. Indeed, the current generation of ELVs has a reliability rate of the order of one failure in twenty launches, often achieved through decades of operations. The same reliability rate for reusable aerospace planes would not be able to redeem the much higher investment required to conceive and build these vehicles (1). In fact, a clear trade-off is required between non-recurring and recurring costs. RLVs may require an extensive (and most likely expensive) Research and Development (R&D) campaign – i.e. "*twenty-five billion dollars investment to achieve significant RLV progress is not out of the question.*" (2) – but will generate much lower recurring costs as these vehicles will be re-used and serve several missions before being replaced. A single space plane must indeed be capable of hundreds of flights. Instead, ELVs need to be fabricated every time a new mission is being planned, but the manufacturing and operational costs are much further reduced and rocket technology is well understood. Nonetheless, the main argument of RLV enthusiasts, beyond the principal economical aspect (i.e. reduction in launch costs), concerns the numerous possibilities offered once a reliable, flexible and low-cost transportation to space is conceived and routinely operated. For example, the success of many ambitious space projects, often referred to as *the final frontier*, is tightly coupled to the development of a new generation of fully re-usable launch vehicles capable of accessing space anytime: lunar colonization (i.e. lunar spacelines concept of Bentley (3)), asteroid mining, space manufacturing, space exploration and so on. Re-usability thus appears to be the only way for a flourishing future in space. In

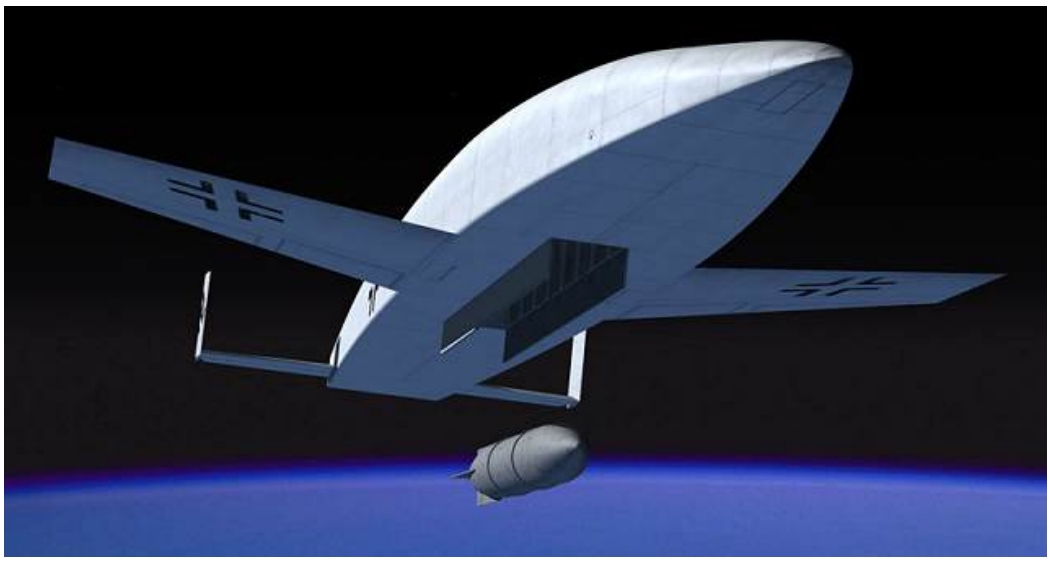

Figure 1.1: An illustration of the "*Silverbird*" concept - Artist impression of Sänger's sub-orbital bomber, developed in the late 1930s by Dr Eugen Sänger in collaboration with Irene Bredt, that first incorporated the principle of the lifting body for a long range hypersonic vehicle (original artwork by Josha Hildwine).

the present dissertation, the emphasis will therefore be on the robust and rapid preliminary modelling of the next generation of heavy-lift fully re-usable aircraft-like launch systems that may potentially be capable of reliably serving future space transportation needs to Low Earth Orbit (LEO) at only a fraction of the current costs of access-to-space.

1.1.1 Historical Facts

One of the very first attempts to develop a winged spacecraft was initiated in the late 1930s as a secret project under development in Nazi Germany, named the Antipodal Bomber - also known as the "*Silbervogel*" - and conceived by Austrian space pioneer Dr Eugen Sänger and his wife, mathematician, Irene Bredt (4). The vehicle's flattened bottom fuselage, shown in Fig. 1.1, was planned to be functionally similar to the body of the American Space Shuttle (i.e. lifting body configuration), but unlike the STS and its space-access purpose, the Sänger-Bredt military spaceplane was designed as a suborbital weapon. In fact, the aerospace vehicle was designed to only skip across the atmosphere (to increase its range) until it reached its antipodal target, dropped its bomb load, and then glided back to its landing runway in Nazi-allied Japan or Germany. As a conse-

quence of the various avant-gardist technologies conceived in the design process by Sänger and Bredt, such as the regeneratively-cooled liquid oxygen engine and the flat-bottomed fuselage (nicknamed the "*flat iron*"), the Silbervogel is often acknowledged to be a forerunner of the oncoming generation of launch systems such as liquid fuel-propelled rockets and, of course later, the Space Shuttle whose study was initiated in 1969 (while its programme officially started in 1972). Indeed, the Silbervogel concept suggested the use of wings to increase the range of a rocket-powered vehicle and, as such, was often described as one of the first real studies of a single-stage vehicle that could attain near orbital speed (5).

Nonetheless, despite Sänger's advanced military concept and the early designs of winged launchers proposed by space visionary Wernher von Braun (when he was brought to the United States of America with its rocket team after the second world war), interest in space planes faded after this aerospace plane era of the 1950s and 1960s. It was only decades after, towards the end of the space race between the United States of America and the Soviet Union, more precisely at the beginning of the 1980s that a renewed interest for aircraft-like fully re-usable spaceplanes was ignited. Indeed several hypersonic vehicle research programs were pushed worldwide by various national space agencies and companies who anticipated the future need for reliable, flexible and frequent access to Earth orbit. These programs included the British HOrizontal Take-Off and Landing (HOTOL), the French Shuttle-like Hermes (i.e. Ariane upper-stage), the West-German Two-Stage-To-Orbit (TSTO) Sänger vehicle (from the well-known company Messerschmitt-Bölkow-Blohm) and last but not least, the American National Aero Space Plane (NASP), designated the X-30, a joint effort between NASA and the US Air Force initiated during the Ronald Reagan administration (a flight demonstrator project which cost billions of dollars). In 1986, the American President Ronald Reagan predicted, in his State of the Union address, the development of "*a new Orient Express that could, by the end of the next decade, take off from Dulles Airport, accelerate up to 25 times the speed of sound, attaining low earth orbit or flying to Tokyo within two hours.*" Indeed, besides their full re-usability, both the HOTOL and X-30 aerospace planes were also meant to reduce quite significantly the cost of present day conventional rocket launch systems by taking advantage of both a horizontal take-off from a conventional airport runway - providing flexibility to the launch location (whereas rockets require an extensive and dedicated launch infrastructure) - and the use of an air-breathing engine in the lower atmosphere whose sole purpose was to reduce drastically the

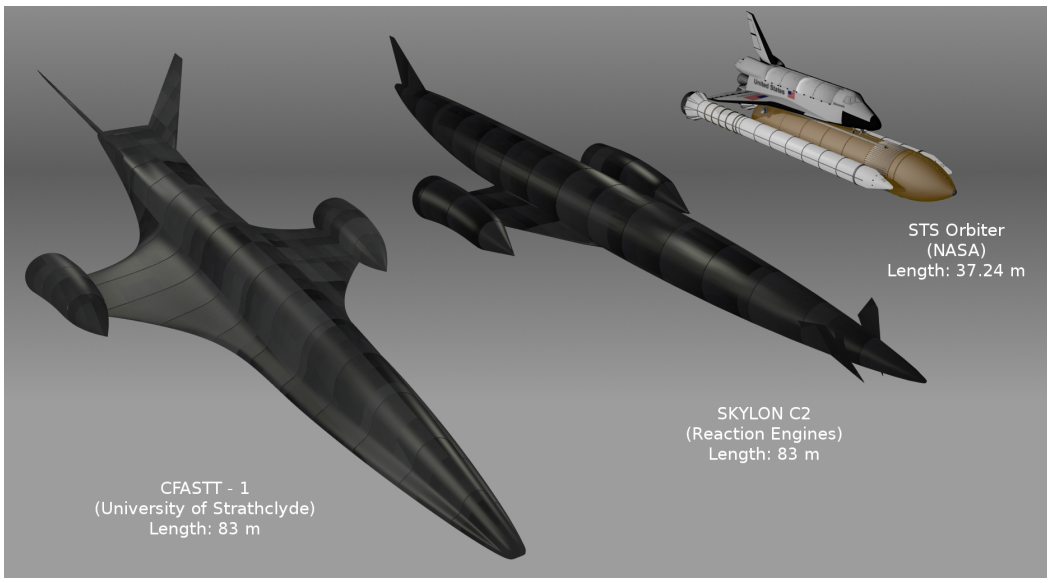

Figure 1.2: A comparison between future and past re-usable space-access concepts - The configuration of a historical partially re-usable craft (NASA's Space Shuttle, at right) compared to proposed fully re-usable SSTO vehicles (Reaction Engines Ltd.'s Skylon, middle, and University of Strathclyde's CFASTT1, at left).

amount of oxidizer required to be carried on-board of the vehicle by utilising atmospheric oxygen as the aircraft would have climbed through the denser regions of the atmosphere.

For various technical and economical reasons however, none of these Earth-launched Single-Stage-To-Orbit (SSTO) vehicles has ever been successfully constructed or operated. Nonetheless, a new range of re-usable hypersonic vehicles is currently being considered as a viable alternative to the expensive but more conventional expendable launch systems that are currently used to gain access to space. Indeed, a number of programmes to develop SSTO vehicles are active worldwide, with the promise of several exciting new developments in the very near future such as the Skylon SSTO vehicle developed by Reaction Engines Ltd. in Oxfordshire, UK, depicted in Fig. 1.2 (middle configuration).

1.1.2 Single-Stage-To-Orbit Vehicles

The principal hope for achieving SSTO capability with a practically-useful payload mass fraction is presumed to rely on the development of a hybrid propulsion technology that exploits, from low to intermediate altitudes, the very high specific

impulse that is achievable with air-breathing jet engines (6). Since the ratio of thrust-to-weight of all practically-conceivable hybrid propulsion systems (at least in air-breathing jet mode) is less than unity, this will necessitate almost universally a lifting configuration for the vehicle. Optimisation to include the low-speed, low altitude flight regime will almost inevitably result in a configuration that is at least partially aircraft-like, and thus a vehicle that is geometrically much more complex than the space vehicles that have been designed in the past (7). A Single-Stage-to-Orbit (SSTO) vehicle is therefore defined as a lifting configuration that can travel to and from Earth orbit without jettisoning stages or any of its constituting components once the fuel it contains has been fully expended. Additionally, these fully re-usable vehicles are also formally defined as launch systems that are capable of inserting a payload into orbit more than once. A comparison between a historical partially re-usable space transportation system and two fully re-usable SSTO concepts is shown in Fig. 1.2. SSTO configurations are thus foreseen to bridge the gap between atmospheric and space flight technologies – i.e. operating like an aircraft and attaining orbit like a conventional launcher.

An SSTO vehicle is thus an aircraft-like re-usable launcher capable of taking off horizontally from a spaceport runaway, of ascending into space using a complex combined-cycle engine (i.e. multiple propulsion systems gathered into a single thrust unit), of delivering up to 15 tons of payload into Low Earth Orbit (LEO) and of subsequently re-entering within the terrestrial atmosphere before landing horizontally at a dedicated spaceport. Therefore, SSTO vehicles will operate a challenging mission profile composed of a number of critical phases, *inter alia*, take-off, ascent-to-orbit, orbital delivery, re-entry, landing and ground-hold operations. During its ascent-to-orbit phase, the vehicle will first make use of a low-speed accelerator (e.g. an air-augmented rocket) to accelerate up to speeds at which a ramjet engine can be ignited (i.e. from about Mach 1.5-3). Indeed, a ramjet engine collects and compresses the air through a series of shocks at its intake and thus requires an initial forward motion prior to be used. At about Mach 5, the temperature and pressure associated with the flow deceleration from supersonic to subsonic speed within the combustion chamber is such that the dissociation of the combustion products may occur and alter the system efficiency. From about Mach 5, the vehicle might thus employ a scramjet engine (i.e. supersonic combustion ramjet) in order to take advantage of their higher specific impulse before the thrust unit finally switches to a pure rocket mode for

orbital insertion. The ascent trajectory of future SSTO vehicles will therefore be much longer than that of current ELVs and their acceleration to very high speeds (when operating in air-breathing mode) will take place in the denser regions of the atmosphere, i.e. inducing severe thermal loads. During its re-entry instead, the vehicle will most probably follow an unpowered gliding trajectory similar to that adopted by the American Space Shuttle. Indeed, after a de-orbit velocity impulse, the vehicle will descend from its entry point at about 120 km down to the Terminal Area Energy Management (TAEM) interface which corresponds to the transition between the vehicle's high angle of attack entry and an aerodynamically controlled supersonic flight.

After mission completion, the vehicle will have to be recovered intact, ready for its inspection and a very limited amount of servicing. SSTOs are indeed expected to adopt a very short-turnaround mode of operation which is closer to that of a civil airliner than that of current expendable launchers. Their design should, in theory, require very few if not no maintenance operations between subsequent flights – i.e. albeit perhaps some routine visual inspections as is common practice in civil aviation – in order to provide a cost-efficient, reliable and routine access to Low Earth Orbits (LEOs) and possibly beyond. For instance, one of the numerous lessons learnt from the Space Shuttle programme was how sensitive the economics of a re-usable vehicle may be to the robustness and maintainability of its thermal protection structure (i.e. to avoid additional operational costs). Indeed, re-usable SSTO vehicles cannot exploit ablative systems or other simple Thermal Protection System (TPS) technologies requiring extensive post-flight refurbishment without destroying the economics of the vehicle and its operational flexibility. This targeted short-turnaround mode of operation may therefore ensure that their cost of acquisition can be amortized over a number of missions. For example, the company Reaction Engines Ltd. seeks to reduce the cost per flight of the Skylon vehicle by amortizing the production cost over up to two hundred missions (8). Therefore, SSTO vehicles will have to repeat a challenging mission profile a large number of times without any major overhaul between subsequent payload delivery missions. This demanding mission requirement becomes a difficult challenge that must be overcome by a careful and synergistic design of the various subsystems of the vehicle (i.e. small design margins).

Therefore, the re-usability of these trans-atmospheric systems is fraught with a myriad of design complexities that require first to be addressed to guarantee that the economics of the whole re-usable concept becomes plausible. Indeed, the high

speed at which such hypersonic vehicles will travel will force them to face some severe technological challenges, not least in terms of their structures and thermal shield, as will be discussed in upcoming sections.

1.1.3 Challenges in Hypersonic Systems Design

In the aerospace jargon, the term hypersonic flow, first used by Caltech Professor Hsue-Shen Tsien in 1946 (5), is usually employed to describe a flow for which the free-stream Mach number is greater or equal to five. At multiple times the speed of sound (i.e. up to Mach 25 for an SSTO vehicle), the flow physics become extremely difficult to predict and lead to various complicated fluid phenomena that are peculiar to that speed range. Indeed, in addition to the well-known difficulties associated with compressible flows, such as the complexity in the determination and modelling of the transition from a laminar state to turbulence, hypersonic flows may also involve additional real-gas effects such as molecular dissociation (e.g. from 2000 K, oxygen molecules dissociate), equilibrium or non-equilibrium chemical reactions, and requires studies of the hypersonic flow behaviour in the transitional regime between the continuum and free-molecular ranges. In point of fact, the hypersonic flow regime covers the whole range from continuum flow in the denser part of the terrestrial atmosphere (i.e. for altitudes below 90-100 km for a typical SSTO vehicle) to free-molecular flow at very high altitudes when the vehicle operates in LEO. The detailed study of hypersonic flows thus requires sophisticated numerical methods that, in general, consume a considerable amount of computational resources, and remain unfortunately still impractical in preliminary design and optimization studies. For instance, it shall be remarked that the relatively simple geometry of most spacecraft that have been conceived and operated up to now - even those with a lifting configuration such as the Space Shuttle - was, in many cases, borne out of a well-justified skepticism regarding the ability of contemporary analysis techniques to characterise properly the aerodynamics of vehicles with any greater geometric complexity (7).

Therefore, the rapid and accurate characterization of the aero-thermodynamic environment that surrounds these complex vehicle configurations appears paramount, early on in the design process, when the feasibility of a concept is being assessed. Indeed, space flight history has shown that many hypersonic programmes have been cancelled due to unforeseen operational costs as a result of perhaps neglected uncertainties as well as a lack of detailed and collaborative analyses during the

preliminary design process. For instance, mis-prediction of the aerodynamic heating during re-entry is a particularly critical problem in the design of a re-usable SSTO vehicle given that any predictive uncertainty must be accommodated by over-design of the TPS, or, in the case where the heating of the vehicle is over-predicted to the point where indications are that the thermal load cannot be accommodated by a passive system, complex and expensive palliative measures, for example a switch to an active TPS (where for instance the surface of the vehicle is cooled by the recirculation of propellant), may be introduced unnecessarily. All of these measures embody the risk of adding to the overall structural mass and reduce the total amount of payload the vehicle can possibly be capable of carrying into LEO. Inaccuracies in design predictions (and margins) may therefore impinge on the whole economics of this new generation of space-access vehicles whose mission may be economically challenged by other strong contenders, such as partially re-usable conventional launchers (e.g. SpaceX's Falcon 9-R partially re-usable rocket) and Two-Stage-To-Orbit (TSTO) vehicles. Therefore, the accuracy of the aero-thermodynamic predictions during the preliminary design phase appears to be key to the economic success of these re-usable winged launchers.

Furthermore, the development of major aerospace research programmes such as that of an SSTO launch system requires the establishment of an important technological ground in order to lessen the risk of unforeseen design difficulties during the development programme (i.e. most likely associated with extra costs). This technological foundation needs to be supported by a careful quantitative and qualitative definition of the design interactions and couplings between major systems and disciplines (e.g. an SSTO vehicle might require its propulsion system to be fully integrated onto its airframe). In fact, in 1988, the British government withdrew additional funding for the HOTOL programme as the project suffered both from aerodynamic problems related to the heavy rear-mounted engines whose weights moved the Centre of Mass (CoM) of the vehicle far too rearwards (i.e. large discrepancy between the location of the centre of pressure and CoM) as well as from operational and economic disadvantages with regards to the conventional rocket systems of that time – i.e. indeed, these aforementioned trim problems eventually lead to a reduction of the useful payload mass fraction and, by consequence, lowered the prospective economic success of the HOTOL programme (9). A number of additional historical examples could motivate even further the importance of using cross-disciplinary and synergistic processes early

on in the design of the future generation of fully re-usable launch vehicles. For example, as reported in a review of NASA's integrated design environment provided by Robinson *et al.* (10), at the request of the United States Congress, the US National Institute of Aerospace (NIA) developed and released a document in 2005 titled "*Responding to the Call: Aviation Plan for American Leadership*" where it was mentioned within the section of the document dedicated to hypersonics that the first critical area identified in the field was Multi-disciplinary Design, Analysis and Optimization (MDAO).

1.2 Rationale for Dissertation

The present work describes an attempt to develop a set of fully integrated design tools and a modelling approach to aid in the preliminary design of the next generation of re-usable SSTO vehicles. In doing so, a rapid and accurate means of quantifying the complex aerothermodynamic environment to which future re-usable launch vehicles will be exposed is first required during the preliminary design phase. In the open literature, a number of technical details concerning the implementation of reduced-order aero-thermodynamic models, their mesh discretisation method as well as the reliability and accuracy of their estimates in terms of heat transfer rates often remain un-published (or, at most, are partially published). Furthermore, most of these engineering codes are either of restricted access or are dated and not versatile enough – i.e. for instance, they might employ a proprietary file format not always adapted to present-days multi-fidelity approaches. This instance justifies the development of a new *in-house* aerodynamic code, dubbed HyFlow, the development of which is well-justified by the necessity to provide a fully integrated, tailor-made and time-efficient computational tool for the quantification of the aero-thermodynamic environment of advanced, geometrically complex vehicle shapes for use in the context of design optimisation studies. The versatility of such a reduced-order model, given its implementation in the framework of Object-Oriented Programming (OOP), must provide the possibility to study and model a number of flow phenomena that, somewhat ironically given past flight experience, have traditionally been regarded as of secondary importance during the preliminary design phase such as the roughness-induced boundary layer transition from a laminar state to turbulence. Additionally, a detailed validation study must be performed to provide an

understanding of both the strengths and limitations of the aero-thermodynamic methodology adopted in the present thesis work.

Furthermore, the cross-disciplinary nature of the design process required for this new generation of fully re-usable space transportation systems, in order to concurrently optimise their performance and mission phases (i.e. ascent, entry and ground-hold operations), is also an extremely complex problem. In fact, the process used to design re-usable space-access vehicles is fraught with a multitude of design uncertainties as well as inter-dependences between its various constituting disciplines. This process thus often requires difficult trade-offs between competing objectives such as safety, performance, reliability, operability and cost to be made (11). A highly integrated Multi-disciplinary Design and Optimisation (MDO) approach is thus recognised to be paramount in order to optimise concurrently the performance of future space-access vehicles to a point where the overall re-usable SSTO paradigm may become technically and economically viable. For instance, the necessary requirement that the vehicle must be able to re-enter the Earth's atmosphere and be recovered intact ready for re-launch poses a series of particularly significant problems, not least in terms of the Thermal Protection System (TPS) that is required during descent to dissipate into the atmosphere the energy that is gained by the vehicle during its ascent to orbit. To reduce the overall mass of the craft to the extent that a worthwhile payload mass fraction is achieved, there is therefore a strong design demand to operate close to the boundaries of existing materials technology, or to employ a synergistic and holistic design approach in order to optimally and concurrently conceive hybrid (passive and active) thermal shields while dynamically controlling the ascent to orbit and subsequent atmospheric entry as a means to minimize the total heat load absorbed by the vehicle throughout its mission profile (e.g. coupling flight dynamics with various other engineering disciplines). Therefore, several MDO methods have been motivated by the cognizance that the development of such complex hypersonic systems could no longer be achieved by a sequential treatment of their various components. Indeed, the requirement for high performance and high cost-efficiency of future space-access vehicles will most likely not only be achieved by single large technological breakthroughs, but also, at least partially, by the use of more flexible, more versatile and more detailed MDO frameworks in all the vehicle definition and development phases (12). Moreover, the constant growth in computer power and capacities makes such integrated processes a practical option for design.

A robust, modular and versatile systemic approach, solely dedicated to the design of future re-usable space transportation systems and accounting for uncertainties in their constituting components, must therefore be derived and coupled to a reduced-order aero-thermodynamic approach in order to provide preliminary capabilities to mathematically model the behaviour of this future class of (complex) re-usable SSTO vehicles.

1.3 Research Objectives

The core element of the work presented in this thesis relates therefore to the development of efficient algorithms and modelling strategies for the purpose of the Multi-disciplinary Design and Optimization (MDO) of the future generation of re-usable winged launchers. Consequently, building upon the background discussion in Section 1.1 as well as the rationale for the dissertation given in Section 1.2, the following three main research objectives can be defined:

1. to devise a rapid aero-thermodynamic methodology that can be used efficiently to provide accurate estimates of the severe aero-thermodynamic environment over complex winged space-access configurations during both their ascent and subsequent entry trajectories where the emphasis must be on the *computational efficiency*, *robustness* and *accuracy* of its aero-thermodynamic predictions.

2. to develop a *modular*, *systemic*, *efficient* and *integrated* multi-disciplinary design environment in order to assist in the design of future fully Re-usable Launch Vehicles (RLVs) and improve the state of the art through a detailed modelling of critical system components where a re-usable spaceplane can be modelled with a sufficient level of detail to permit the evaluation of its overall performance. In doing so, various key models must be developed and integrated within a system environment including an atmosphere model, flight simulation model, thermal model, mass model and propulsion model.

3. to provide a methodology that accounts for design uncertainties in the inherent properties of the various system components. This robust strategy must be derived to identify potential problems that may require further investigations before the design of a fully re-usable space transportation system can be considered successful.

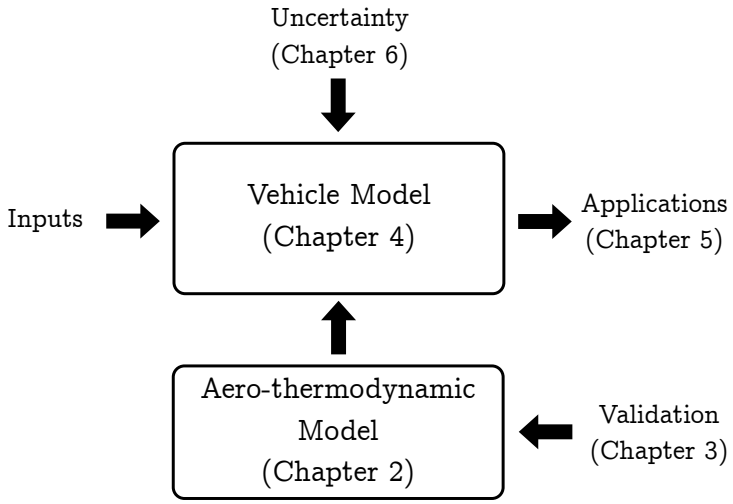

Figure 1.3: The organisation of the thesis - The diagram describes the affiliation between the various chapters of the thesis.

1.4 Synopsis

The work presented in the thesis can be divided into two main parts: the first part consists of Chapter 2 and Chapter 3 and is used to describe and validate a new modular reduced-order model specifically developed to rapidly quantify the complex aero-thermodynamic environment of the next generation of re-usable aerospace plane configurations. The second part spans Chapter 4 to Chapter 6 and concerns more specifically the multi-disciplinary modelling, design and optimisation of these un-conventional space transportation systems. The diagram in Fig. 1.3 summarizes the organisation of the work covered in the thesis.

Chapter 2 focuses on the rapid characterization of the complex aero-thermal environment that accompanies hypersonic flight. In this chapter, the properties of a newly developed aerodynamic model, dubbed HyFlow, which has been optimized for use in the context of the Multi-disciplinary Design and Optimization (MDO) of future re-usable space-access vehicles, are introduced.

Then, chapter 3 introduces a number of representative test cases to provide both a validation and an acknowledgment of the limitations of the reduced-order aero-thermodynamic model introduced in Chapter 2. The validation cases include a number of blunt and slender hypersonic bodies such as a ballistic shape (HB-2 geometry), a blunt-nosed conical body (Re-entry F flight experiment) and NASA's Space Shuttle Orbiter using a combination of numerical and empirical results.

Chapter 4 marks the start of the second part of the thesis and focuses on the development of a fully integrated multi-disciplinary analysis process for the design of space transportation vehicles. To this end, chapter 4 introduces a new MDO platform, written in the context of Object-Oriented Programming (OOP), which is solely dedicated to the design of future fully re-usable space-access vehicles. After an extended discussion about the numerous challenges related to the design of such complex hypersonic vehicles, various miscellaneous models, used to simulate the various subsystems of future re-usable launchers, are presented.

Thereafter, Chapter 5 illustrates the various models presented in the preceding chapters. The performance of a representative space transportation system configuration is then investigated at representative conditions along its mission trajectory.

Finally, Chapter 6 emphasizes on the importance of uncertainty quantification in hypersonic applications, and in particular during the preliminary design of future re-usable launch systems. The aim of this chapter is thus to introduce a robust methodology in order to account for elements of operational impact in the miscellaneous subsystem models described throughout the thesis, for instance in the atmosphere, thermal and aerodynamic models.

It shall also be remarked that each separate chapter finishes with some preliminary conclusions, which come together in the overall conclusions chapter at the end of the dissertation, whence a discussion on possible future extensions to the present work is also provided.

1.5 Publications

Some of the research presented in this dissertation has been or will be published as part of conference proceedings. The content of Chapter 2 and 5, that explores the effect of roughness-induced transition on the trajectory optimisation of space-access vehicles, is largely derived from a paper by Wuilbercq, Pescetelli, Minisci and Brown which was presented at the 19^{th} AIAA International Space Planes and Hypersonic Systems and Technologies Conference in Atlanta (USA) in June 2014 (13).

All the content of Chapter 4 and part of Chapter 5 formed the basis of a paper about the robust multi-disciplinary design of space-access vehicles by Wuilbercq,

Pescetelli, Mogavero, Minisci and Brown which has been presented at the 19^{th} AIAA International Space Planes and Hypersonic Systems and Technologies Conference in Atlanta (USA) in June 2014 (14).

A preliminary paper giving a summary of the potential problems related to the modelling of the aero-thermodynamics of re-usable space-access vehicle via reduced-order models was presented at the 18^{th} AIAA/3AF International Space Planes and Hypersonic Systems and Technologies Conference in Tours, France, in September 2012. Parts of this paper are dispersed throughout the present dissertation (7).

Then, a summary of the content of Chapter 2 and Chapter 3 was presented at the 8^{th} European Symposium on Aero-thermodynamics for Space Vehicles, held from the 2^{nd} to the 6^{th} of March 2015 in Lisbon, Portugal, in a paper by Wuilbercq and Brown titled: "*Rapid Aero-Thermodynamic Analysis for Hypersonic Air Vehicles*." (15)

Finally, a follow-up paper to the aforementioned multi-disciplinary design work first presented in June 2014 by Wuilbercq, Mogavero and Brown will partially reproduce some of the new contents of Chapters 4, 5 and 6, and, as a paper titled "*Robust Multi-disciplinary Modelling of Future Re-usable Aerospace Planes*," will be presented at the 20^{th} AIAA International Space Planes and Hypersonic Systems and Technologies Conference to be held in Glasgow, United Kingdom, in July 2015.

Chapter 2

Reduced-Order Aero-Thermodynamic Model

This chapter describes an engineering methodology that can be used in the context of the preliminary design of Re-usable Launch Vehicles (RLV) to rapidly quantify their aero-thermodynamics. Section 2.1 sheds light on some of the peculiarities of the hypersonic flight environment and then briefly introduces those existing reduced-order models. Section 2.2 describes the various flow regimes in which future Space Transportation Systems (STSs) will operate. In Section 2.3, the miscellaneous methods employed to compute the aerodynamics of hypersonic vehicles are introduced, whereas a method to account for viscous loads is presented in Section 2.4. Then, two different mechanisms for the boundary layer transition from a laminar state to turbulence are discussed in Section 2.5. Thereafter, a method to compute the aerodynamic forces is presented in Section 2.6 while a method to calculate the heat transfer rates acting on space-access vehicles is introduced in Section 2.7. Finally, some preliminary discussions and conclusions are given in Sections 2.8 and 2.9.

2.1 Introduction

The aero-thermodynamics of the ascent and subsequent re-entry into the terrestrial atmosphere of fully re-usable space-access vehicles is an extremely complex problem. Although the scope of hypersonic aero-thermodynamics may be appreciated with the help of the comprehensive overview provided by the books of

Anderson (16) and Bertin (17), a sketch of the intrinsic challenges of the field is given in the following introductory paragraphs.

Hypersonic Flight Regime

At hypersonic speeds (i.e. when the free-stream Mach number is greater than five), characteristic effects of the flow field pose a series of peculiar problems to the designers of re-usable aerospace vehicles. Amongst other effects, the detailed geometry of the strong shock waves produced by the vehicle travelling at hypersonic velocities, the interaction between the inviscid flow behind the shock waves and the viscous boundary layer near the wall of the vehicle, as well as the presence of real-gas effects such as the excitation of internal modes of energy storage within the gas molecules and chemical reactions with the surface of the vehicle (e.g. molecular recombination for catalytic walls), all can have a significant effect on the aerodynamic loading and heating experienced by space-access vehicles. In fact, at relatively high hypersonic speeds and when passing through the strong shock waves that always form ahead of hypersonic vehicles, air molecules start to vibrate (i.e. vibrational excitation of air molecules starts from 800 K) and molecular bonds might break apart through a process known as molecular dissociation (i.e. at 2000 K oxygen dissociates, at 6000 K nitrogen follows). As the flight velocity increases to even greater hypersonic speeds and local temperatures eventually reach 9000 K, ionization then occurs and electrons are thus released from the atoms to create positively and negatively charged ions. Although some of these effects only arise at very high hypersonic speeds and, as such, are not entirely relevant in the study of space transportation to Low Earth Orbits (LEOs), all cause the air to deviate from a perfect gas behaviour and most of them should, in general, be accounted for when analyzing the aero-thermodynamics of prospective Re-usable Launch Vehicles (RLVs). Therefore, much progress has been made towards developing computational methods that can incorporate all these complex effects and phenomena. Nevertheless, despite the advent of massively parallel computation, these numerical methods remain extremely time-intensive, often taking several days to produce aero-thermodynamic data for a single point within the operational envelope of the vehicle (a single point along the vehicle's trajectory). Therefore, despite the complexity of hypersonic flows, preliminary design, and particularly multi-disciplinary design optimisation, must still rely, to a large

extent, on the use of time-efficient reduced-order models to rapidly characterise the aero-thermodynamics of prospective re-usable space-access concepts.

Reduced-Order Aero-thermodynamic Models

Practical methods for preliminary design and optimisation are generally limited to those based on relatively simple engineering models for the behaviour of the flow around the vehicle, for instance, those based on a Newtonian flow assumption or the approximation of the vehicle as a composite of simple, non-interacting geometric components for which the flow can be calculated using simple shock theory – albeit perhaps with some empirical embellishment.

Indeed, a number of industry-standard methods for employing these techniques currently exist such as the United States Air Force (USAF) Missile Datcom (18). The accuracy of the software reduces however above Mach 6-7 (19). The Supersonic Hypersonic Arbitrary Body Program (S/HABP) (20), initially developed in the 1960s by Gentry from Douglas Aircraft, is likely to be the most well-known piece of software, as until the middle of the 1990s it was used extensively by many organisations and companies for the preliminary design and analysis of hypersonic vehicles – it was most notably used in the preliminary design of the American Space Shuttle (16). The software employs a proprietary file format called the NASA Langley Wireframe Geometry Standard (LaWGS) to generate the mesh of a vehicle (i.e. structured grid). More recently perhaps, the Configuration Based Aerodynamics (CBAERO) code of Kinney (21, 22), developed at NASA's Ames Research Centre, although of restricted-access to North-American companies and organisations, has been developed to provide a comprehensive and complete set of engineering-level methods that can be used very efficiently to quantify the aerothermodynamic environment of complex hypersonic vehicles throughout their operating flight envelope (i.e. from subsonic to hypersonic flight). As opposed to all aforementioned reduced-order codes, CBAERO employs an unstructured grid of triangular panels. A large number of reduced-order models, perhaps less renowned and of more restricted capabilities, developed in the context of Multi-disciplinary Design and Optimization (MDO), can also be identified in the open literature: an example of these is the Re-entry Aerodynamics Module (RAM) of Dirkx (23). This module was initially developed as part of an open-source software project called the Space Trajectory Analysis (STA). The software, which

embeds a collection of Local Surface Inclination (LSI) methods with a sophisticated method selection process, makes use of a structured grid as input. The inviscid solver has been modified recently in order to include the prediction of viscous loads (24). Finally, the computer code HYPAERO (25), developed at the University of Queensland, Australia, represents another example of an *in-house* reduced-order model developed to provide preliminary design capabilities for hypersonic transport aircraft. The code is based on the well-known principles of strip theory (and is therefore restricted to small angle of attack). The model has successfully been validated for Mach numbers in the range $M_\infty \in [5, 14]$ and altitudes up to 40 km.

The foremost advantage of these reduced-order models for preliminary design is of course the ease with which parametric variations in the properties of the system can rapidly be explored. Historically, this approach has been very successful notwithstanding notable exceptions such as in predicting the well-known Shuttle pitching moment anomaly (12). The concern, however, is that the inevitable increase in configurational complexity that will accompany the practical embodiment of future space transportation systems (see Section 1.1.2 of Chapter 1) will force designers to retreat from the conservatism with which these industry-standard models have been applied in the past (7).

The HyFlow Model

In the context of the work presented in the thesis, a new reduced-order model, dubbed HyFlow (which stands simply for "Hypersonic Flow"), has therefore been developed for predicting the aerodynamic and aero-thermal environments of general three-dimensional hypersonic vehicle configurations. HyFlow has been conceived to provide a predictive accuracy suitable for preliminary design. The code has a structure that takes advantage of the intrinsic modularity of the Object-Oriented Programming (OOP) formalism embodied within the Matlab environment. This modularity brings significant flexibility and versatility to the HyFlow code by allowing it to be configured to easily model miscellaneous flow phenomena (e.g. roughness-induced transition), and new modules can easily be added and connected to existing ones using the intrinsic property of inheritance embedded in the OOP software architecture. The reduction in terms of physical realism that accompanies this approach, especially when compared to modern numerical techniques such as Computational Fluid Dynamics (CFD) and Direct Simulation

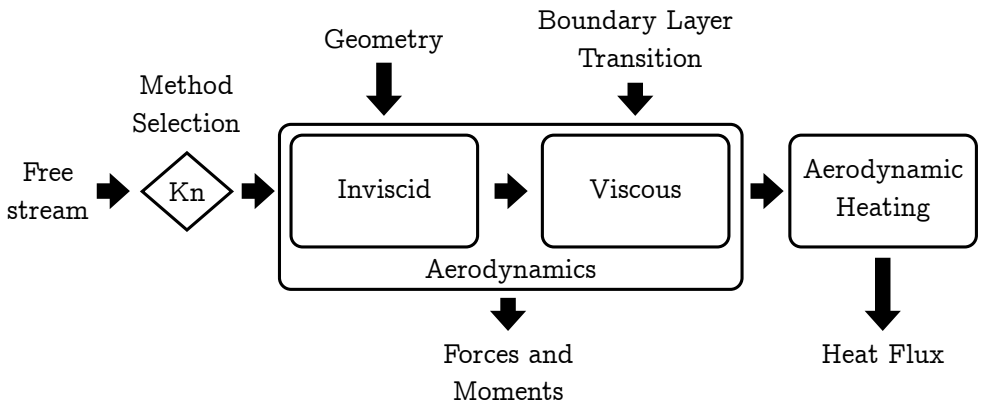

Figure 2.1: The underlying architecture of the HyFlow model - The diagram introduces the various models implemented within the HyFlow environment. Each of these models is described in a dedicated section within the present chapter.

Monte Carlo (DSMC), is offset almost entirely, in many practical applications, by the very low computational cost and parametric flexibility of the approach. Indeed, although designers can rely on these aforementioned more-sophisticated techniques during more detailed design analyses, the overarching aim of HyFlow is to provide an accurate and efficient engineering approach that is particularly crafted and optimised to aid in the preliminary design of future complex re-usable launch vehicle configurations. Indeed, HyFlow has been developed to support an integrated multi-disciplinary design environment, and to provide this with the overall aerodynamic forces and moments required for trajectory planning, as well as the detailed distribution of aero-thermal loads over the surface of the vehicle that is required for airframe design.

The diagram presented in Fig. 2.1 represents the high-level organization of the present reduced-order model and summarizes its various modules. The aerodynamic model within the HyFlow code uses a combination of well-established independent panel compression methods (and, albeit to a lesser extent, expansion methods) in order to predict the aerodynamics of vehicles travelling at hypersonic Mach numbers from free-molecular flow conditions at very high altitude down to the continuum flow regime when the vehicle operates in the lower regions of the terrestrial atmosphere. It shall however be remarked that a significant part of the trajectory followed by these space-access vehicles (either during their ascent or subsequent re-entry) occurs within the limits of the continuum flow regime. Furthermore, the demand for an increased level of accuracy requires HyFlow

Flight Regime	Kn Range
Free-Molecular	$Kn \geq 10$
Transitional	$0.01 < Kn < 10$
Continuum	$Kn \leq 0.01$

Table 2.1: The various flight regimes encountered by re-usable launch systems - The table introduces the division of fluid mechanics into various operating flight regimes according to the level of rarefaction associated with the value of the free-stream Knudsen number.

to account for both inviscid and viscous aerodynamics. In the current model, and notwithstanding the comments made in the introductory paragraphs to this chapter, all analyses are run under the assumption of thermally and calorically perfect gas to a first approximation. The present chapter describes therefore how all these engineering methods, which have traditionally been used in hypersonic preliminary design, are implemented within the HyFlow object-oriented framework for use in the Multi-Disciplinary Design and Optimisation (MDO) of hypersonic space planes (as will be demonstrated in the second part of the present thesis).

2.2 High-Speed Mixed-Density Flows

During a typical mission, a re-usable space transportation system will pass from the denser regions of the lower atmosphere, through the upper regions of the terrestrial atmosphere, to the near-vacuum conditions of space, then return again – the vehicle will thus be exposed to a wide range of gas densities (26). The aerodynamic regime to which the vehicle is exposed will thus change from continuum flow at lower altitudes to free-molecular flow at high altitudes, passing through a transitional flow regime in between. The regime in which the vehicle is operating depends on a non-dimensional parameter called the Knudsen number, denoted K_n^∞, which measures the relative importance of the particulate nature of the gas. The Knudsen number is formally defined as the ratio of the mean free path of the gas, denoted λ_∞, through which the vehicle is travelling to an appropriate measure of the dimensions of the vehicle (e.g. the nose radius or mean aerodynamic chord, depending on context). The molecular mean free path, which corresponds to the averaged distance travelled by a molecule between successive collisions, can

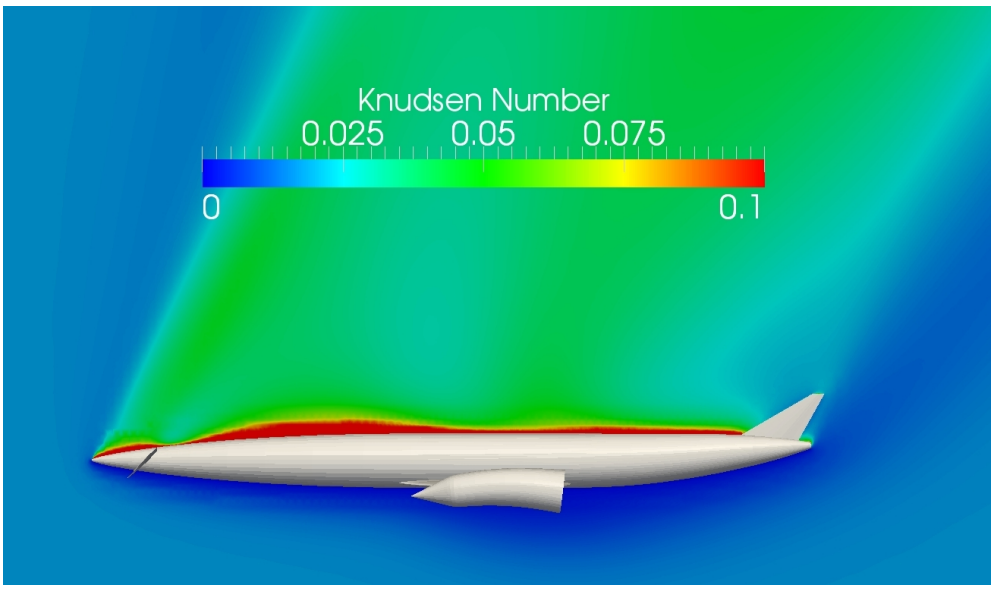

Figure 2.2: Distribution of local Knudsen number over a Skylon SSTO configuration - Direct Simulation Monte-Carlo (DSMC) results obtained using the *dsmcFoam* (27) solver showing the level of rarefaction in the flow field (through the estimated local Knudsen number) that surrounds a representative RLV configuration (Skylon from Reaction Engines Ltd) during its re-entry at 114 km-altitude at a speed of Mach 23 where the estimated free-stream Knudsen number, based on the length of the vehicle (81 m), is slightly greater than 0.01 (7).

be approximated as a function of the altitude at which the vehicle is travelling by

$$\lambda_\infty = \frac{k_B T_\infty}{\sqrt{2}\pi d_{air}^2 P_\infty} \tag{2.1}$$

where k_B is the Boltzmann constant ($= 1.380648813 \times 10^{-23}$ J/K), d_{air} is the effective diameter of the dry air particles ($= 4 \times 10^{-10}$ m), and T_∞ and P_∞ are the free-stream temperature and pressure, respectively. The various flow regimes encountered by an RLV during its mission, as a function of the free-stream Knudsen number, are summarized in Table 2.1. It is however crucial to remark that care needs to be taken with such a broad characterization of the nature of the flow as that pictured in Table 2.1, considering the possible presence of local non-continuum effects on parts of the vehicle surface when the external flow field is assumed entirely within the continuum regime, i.e. particularly in the neighbourhood of shock interactions and in regions with large surface curvature (7). Similarly, at hypersonic speeds, the strong shock that always forms ahead of the vehicle compresses the gas near the wall of the vehicle and therefore increases

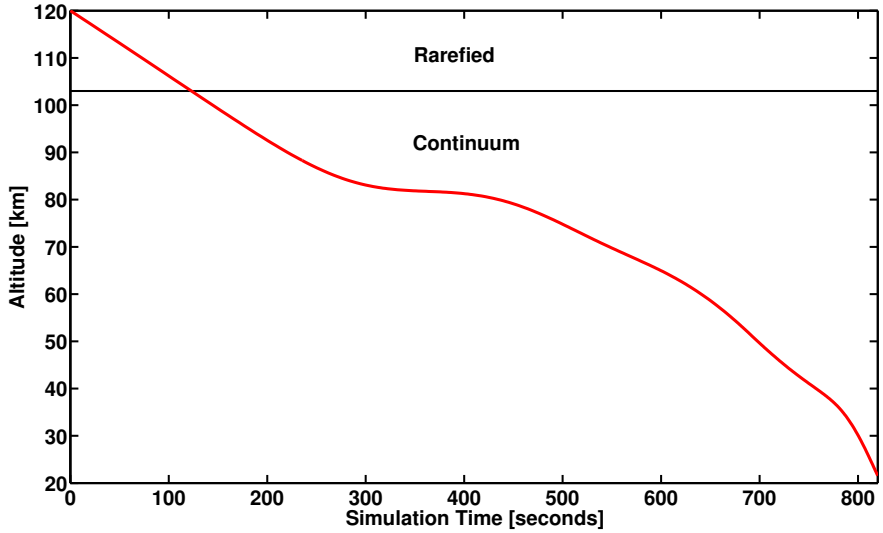

Figure 2.3: Boundary between the rarefied and continuum flow regimes along a typical re-entry trajectory - A typical re-entry trajectory is shown for a representative re-usable space-access vehicle. It can readily be seen that the vehicle will operate mostly within the continuum flow regime.

to a considerable extent the local density resulting in a mean free path behind the shock and in the stagnation regions which is significantly smaller than that in the free-stream (28). The results of a study performed by Wuilbercq *et al.* (7) and based on DSMC computations, which are partially reproduced in Fig. 2.2, emphasize the presence of a mixed-flow regime in the flow field that surrounds a representative aerospace plane upon its entry into the Earth's atmosphere at about 114 km altitude (where it operates at the boundary between continuum and transitional flows) (7).

Therefore, in order to circumvent these problems related to the presence of a mixed-flow regime, HyFlow can be set to automatically select the appropriate method for the computation of the aero-thermodynamic environment. The method is based on the estimation of the local Knudsen number, denoted K_n^l, which is computed in HyFlow as

$$K_n^l = \frac{M_{edge}}{Re^*} \sqrt{\frac{\gamma^* \pi}{2}} \propto \frac{1}{\rho^* x_i} \tag{2.2}$$

where the local properties M_{edge}, ρ^* and Re^* are, respectively, the Mach number at the edge of the boundary layer, the reference density within the boundary layer and the local Reynolds number (see Section 2.4), and γ^* is the effective ratio of

specific heats of the fluid. This measure of the local Knudsen number introduced in Eq. 2.2 uses the running length of a local surface streamline, here denoted by x_i, as the local characteristic length where the running length is evaluated under the assumption of continuum flow (see Section 2.4.1). This local criterion can thus be used in HyFlow to automatically discriminate continuum from non-continuum regions of the flow geometry while the vehicle operates at the boundary between the continuum and transitional flow regimes. This evaluation of the local Knudsen number can indeed be considered physically reasonable in the near-continuum regime since when considering only the macroscopic flow quantities (i.e. neglecting the flow structure), such as temperature and density, there is no significant difference between the predictions obtained using either a continuum or a molecular method (29). Nevertheless, although it has been mentioned that the ascent and subsequent re-entry trajectories of the vehicles considered in the present thesis will occur mostly in regions where the flow behaves as a continuum as illustrated in Fig. 2.3 (i.e. considering their relatively large dimensions as well as their entry point located slightly above the Kármán line, i.e. 100 km), local non-continuum effects may however still be encountered: e.g. in separation regions as a result of the high angle of attack of the vehicle during re-entry. This method represents a hybrid continuum/rarefied engineering approach.

2.3 Aerodynamic Model

The following sections introduce the miscellaneous methods embedded within the HyFlow environment that are used to quantify the inviscid aerodynamics of hypersonic vehicles. These inviscid analysis routines require only the configuration geometry, the surface element impact angle, here denoted by θ (or its equivalent local inclination angle $\phi = \frac{\pi}{2} - \theta$), and the free-stream conditions (M_∞, P_∞ and T_∞) as inputs and thus conveniently do not require any information about the flow field that surrounds the vehicle.

2.3.1 Geometry

HyFlow is a panel-based implementation which uses a stereolithography (STL) file format to describe the geometry of the vehicle being modelled. An STL file describes a tessellation of the vehicle surface through the connectivity matrix

and vertices of its constituent triangles, ordered according to the right-hand rule, in a three-dimensional Cartesian coordinate system. The use of a tessellation allows complex shapes, such as those of the configurations investigated within the present dissertation, to be discretized easily as opposed to the quadrilateral panels used in previous reduced-order codes such as S/HAPB. As such, the routines in HyFlow may be applied to any appropriate geometry no matter how complicated. Piecewise constant surface properties are then assumed across the area of each panel.

The accuracy of HyFlow's estimates increases as the number of triangular faces is increased. A moderately coarse mesh is usually employed however in order to maintain a relatively good computational efficiency, particularly when using the model in optimisation studies, but local mesh refinement can be applied judiciously in sensitive regions of the geometry, such as on highly curved surfaces and near stagnation features, to improve the overall accuracy of the predictions (7). In this work, the modelling of the vehicles as well as the various modifications of the mesh have been performed with the help of the open-source three-dimensional modelling software dubbed Blender ©. An example of a low resolution mesh read in HyFlow from an STL file is presented in Fig. 2.4.

2.3.2 Continuum Regime

In the continuum flow regime, which is characterized by very low Knudsen numbers ($K_n^\infty < 0.01$), the study performed by Wilmoth, Blanchard and Moss (30) suggests that the overall loads on the vehicle would only be very moderately affected by rarefaction effects. For the continuum regime, the HyFlow model uses a collection of Local Surface Inclination (LSI) methods to simulate the flows.

2.3.2.1 Newtonian Flow Theory

Assuming a Newtonian flow, the pressure exerted on the vehicle is solely due to the total loss of momentum of the fluid in the direction normal to the vehicle's surface, as depicted in Fig. 2.5. The local pressure coefficient $C_{p,i}$ at any point i on the body is then given by (16)

$$C_{p,i} = \begin{cases} C_{p,max} \cos^2 \theta_i & \text{if } \theta_i > \frac{\pi}{2} \\ 0 & \text{otherwise} \end{cases} \tag{2.3}$$

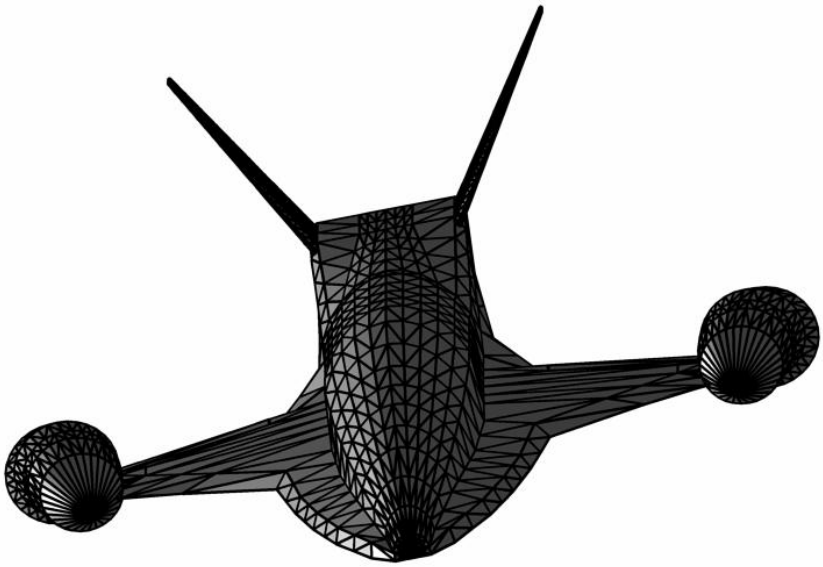

Figure 2.4: An example of a triangulation of the CFASTT-1 vehicle concept - An example of a low resolution un-structured mesh for the CFASTT-1 launch vehicle concept used as an input to the HyFlow code.

where θ_i represents the local deflection angle between the free-stream velocity vector $\vec{V}_\infty$ and the body outward unit normal vector of a given panel, denoted $\hat{n}_i$ (see Fig. 2.5). As suggested by the work of Lester Lees (31), the modified Newtonian theory used in the Hyflow model accounts for the total pressure loss across the normal shock that is invariably located in the flow upstream of the vehicle. It therefore uses the Rayleigh-Pitot tube formula to relate the stagnation pressure behind a normal shock wave $p_{0,2}$ to the free-stream pressure p_∞ as

$$\frac{p_{0,2}}{p_\infty} = \left(\frac{1-\gamma+2\gamma M_\infty^2}{\gamma+1}\right) \times \left(\frac{(\gamma+1)^2 M_\infty^2}{4\gamma M_\infty^2 - 2(\gamma-1)}\right)^{\gamma/(\gamma-1)} \tag{2.4}$$

where M_∞ is the free-stream Mach number, and γ is the ratio of specific heats. The maximum pressure coefficient in Eq. 2.3 is thus given by

$$C_{p,max} = \frac{2}{\gamma M_\infty^2} \times \left(\frac{p_{0,2}}{p_\infty} - 1\right) \tag{2.5}$$

Finally, it shall be remarked that for the classic Newtonian theory, the maximum pressure coefficient is set constant, i.e. $C_{p,max} = 2$.

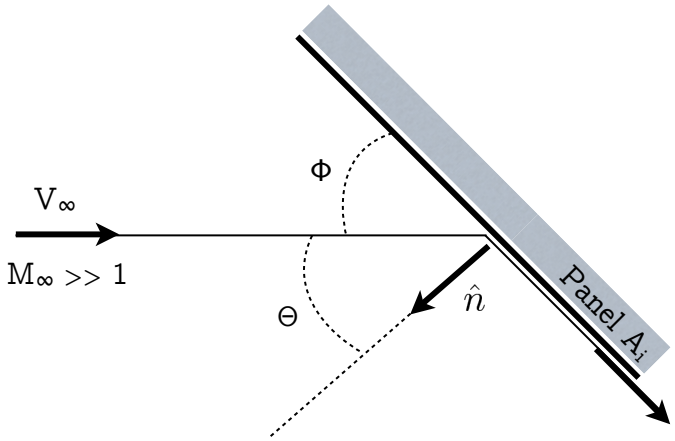

Figure 2.5: Newtonian flow theory - Schematic of the Newtonian theory model. This relatively simple description of the flow field, whose particles are assumed to move at the same rate following a rectilinear motion until they impact an obstacle, along which they continue by moving tangentially, was originally presented by Sir Isaac Newton to describe the behaviour of a flow travelling at subsonic speed (16).

2.3.2.2 Tangent-Wedge Method

In the Tangent-Wedge approach, also known as the hypersonic wedge method, the two-dimensional flow field is determined by constructing an equivalent wedge tangent to a given point P_i on the geometry and assuming that the flow properties at that point on the wedge, which is at an half-angle ϕ_i with respect to the free-stream flow, are similar to those at the same point on the original body (see Fig. 2.6). Therefore, instead of calculating the flow field around the vehicle itself, the oblique shock relations can simply be applied to the constructed wedge shape to evaluate the properties at the point in question, such as the local surface pressure coefficient, $C_{p,i}$, for a given surface inclination angle of ϕ_i, and a given free-stream Mach number of M_∞. Indeed, once the corresponding two-dimensional shock angle, denoted $\beta_{w,i}$, has been computed using the aforementioned oblique shock relations, the tangent wedge method makes use of Eq. 2.6 below to calculate the local pressure coefficient as

$$C_{p,i} = \frac{4(M_\infty^2 \sin {\beta_{w,i}}^2 - 1)}{(\gamma + 1)M_\infty^2} \tag{2.6}$$

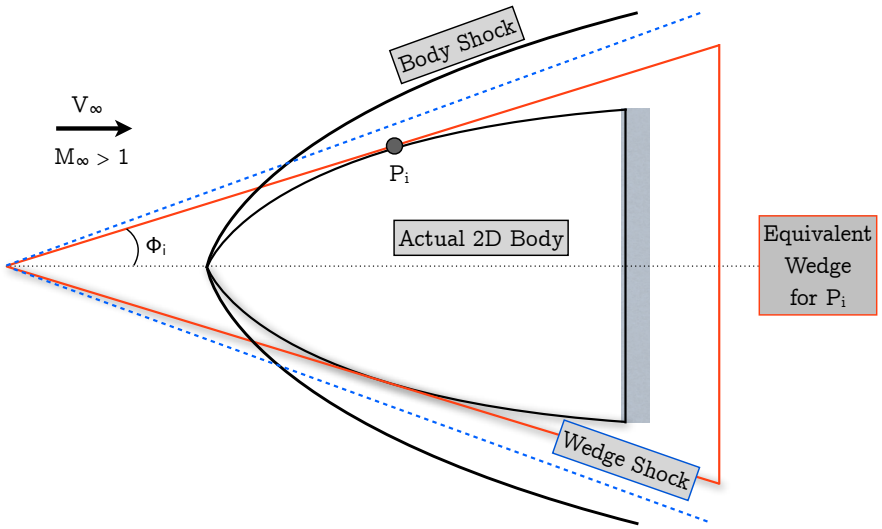

Figure 2.6: Tangent-wedge method

However, when the local inclination angle ϕ_i is greater than the maximum deflection angle for the given flow conditions, the resulting shock wave becomes detached, and the exact tangent-wedge method can no longer be applied. For those panels, the model locally applies the modified Newtonian theory (see Section 2.3.2.1) in order to provide a solution to the pressure coefficients.

2.3.2.3 Tangent-Cone Method

The Tangent-Cone approach follows a similar process to the one described in the previous section but instead is applied to axi-symmetric flows (see Fig. 2.7). In the tangent-cone method, the three-dimensional flow field is thus determined by constructing an equivalent cone tangent to a given point P_i on the geometry and assuming that the properties at that point on the cone, which is at an half-angle ϕ_i with respect to the free-stream flow, are similar to those at the same point on the vehicle. The conditions behind the shock are then determined either by solving iteratively the Taylor-Maccoll equations (32) or simply by using a lookup table procedure. Indeed, when time efficiency is required or when the local deflection angle ϕ_i is greater than the shock detachment angle for the given flow conditions, HyFlow uses an empirical Tangent-Cone method, initially derived by Edwards (33) for use in a study of supersonic planes, in which the surface pressure is given by

$$C_{p,i} = \frac{48 M_n^2 \sin^2 \phi_i}{23 M_n^2 - 5} \tag{2.7}$$

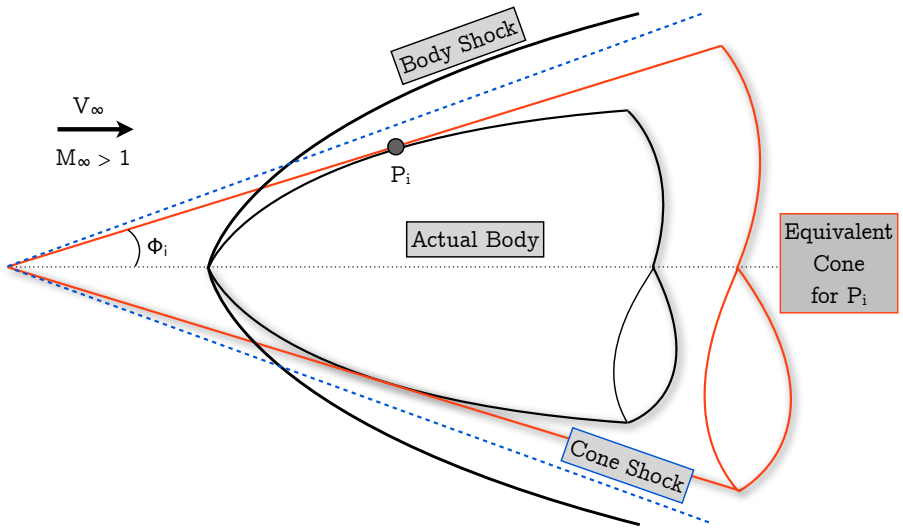

Figure 2.7: Tangent-cone method

where the local Mach number normal to the conical shock, denoted $M_{n,i}$, is empirically defined as

$$M_{n,i} = (0.87M_{\infty} - 0.544)\sin\phi_i + 0.53 \tag{2.8}$$

2.3.2.4 Method Selection Process

As clearly stated by Anderson (16), there is no set of rules to follow in order to determine which of the previously described LSI methods may return the most accurate estimates for a given application but instead, the selection process requires some rather "*intuitive logic*". For instance, since the modified Newtonian theory assumes a strong normal shock upstream of the vehicle, the method is often used for the analysis of blunt-nosed bodies or space-planes when operating at high angle of attack such as during their entry into the terrestrial atmosphere – i.e. since in that context, their aerodynamics resemble indeed quite closely those of a blunt body.

Furthermore, in addition to the nature of the flow field that surround the space-access configuration, Bertin suggests in his book (17) that the choice of the local surface inclination method that provides the best estimates of the wall pressure depends on a certain number of parameters. These parameters include the velocity at which the vehicle operates, the angle of attack and the configuration geometry. Therefore, in order to account for the nature of the local geometry, a

rapid surface primitives extraction technique, based on the region-growing algorithm described in the paper of Garcia (34), has been implemented in HyFlow to automatically discriminate planar from non-planar regions of the flow geometry in order to switch from Newtonian flow theory to a Tangent-Wedge or Tangent-Cone approximation where appropriate – i.e. when the free-stream Mach number and the angle of attack are such that $M_\infty \leq 6-7$ and $\alpha \leq 20$ degrees, for instance. Nevertheless, if a more detailed LSI method selection procedure is required, a technique in the vein of that described in the paper of Dirkx *et al.* (23) may be implemented in HyFlow.

2.3.3 Free-Molecular Regime

When the flow is sufficiently rarefied and the mean free path is everywhere greater than a given characteristic length of the vehicle ($K_n^\infty \geq 10$), such a flow is defined as a free-molecular flow. For free-molecular flows, the collision between an impinging free-stream particle and a molecule re-emitted after wall impact is unlikely. Therefore, collisions between oncoming gas molecules and the wall of the vehicle immersed in a free-molecular flow prevail. In other words, the oncoming flow is so dilute that collisions within the gas can be ignored. The equation, derived by Probstein and Hayes (28) on the basis of the kinetic theory of gases and used by the reduced-order model for computing the surface pressure under free-molecular conditions, denoted $C_{p,i_{fm}}$, is presented below as a function of the local inclination angle ϕ_i.

$$C_{p,i_{fm}} = \left(\frac{1}{\sigma_s^2}\right)\left(\left[\frac{2-f_n}{\sqrt{\pi}}K_s + \frac{f_n}{2}\sqrt{\frac{T_w}{T_\infty}}\right]\exp(-K_s^2) + \left[(2-f_n)(K_s^2+\frac{1}{2}) + \frac{f_n}{2}\sqrt{\pi}\sqrt{\frac{T_w}{T_\infty}}(K_s)\right][1+\mathrm{erf}(K_s)]\right) \quad (2.9)$$

where f_n is the normal momentum accommodation coefficient (i.e. it takes the value of zero for specular reflection or unity for completely diffuse reflection; see Fig. 2.8) and K_s is defined as

$$K_s = \sigma_s \sin\phi_i \quad (2.10)$$

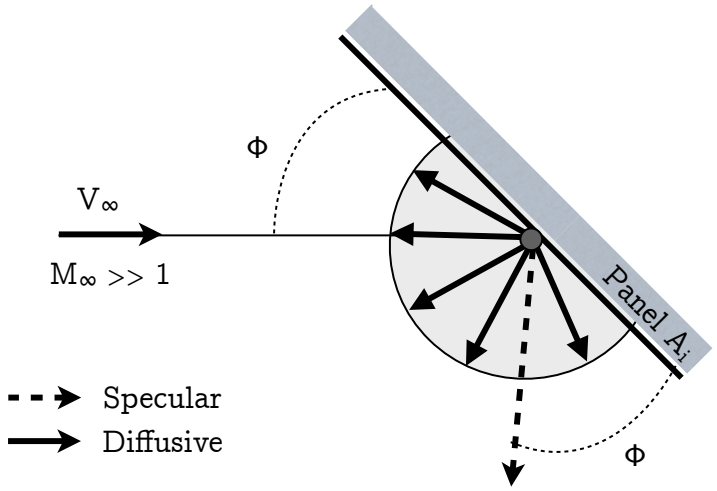

Figure 2.8: Free-molecular flow - Schematic of the free-molecular flow model. In this diagram, both the diffuse and specular reflection models are presented.

where the quantity σ_s represents the speed ratio and can be expressed in terms of the free-stream Mach number as

$$\sigma_s = \sqrt{\frac{\gamma}{2}} M_\infty \tag{2.11}$$

and $\mathrm{erf}(x)$ is the error function given by

$$\mathrm{erf}(x) = \frac{2}{\pi} \int_0^x \exp\left[-(x)^2\right] dx \tag{2.12}$$

In HyFlow, while a specular reflection model can be used to describe the gas-surface interaction (see again Fig. 2.8), it is however assumed, by default, that air molecules are diffusely reflected from the surface of the body upon impact. The angle ϕ' between the trajectory of the reflected particle and the local surface may thus differ from the original impact angle ϕ (see Fig. 2.8). The tangential and normal momentum coefficients have therefore been set to unity in the current formulation – i.e. molecules are assumed to be completely accommodated to the surface conditions.

2.3.4 Transitional Regime

When the estimated Knudsen number lies within the transitional regime, the flow cannot be considered as a continuum, nor can the particulate nature of the gas

be neglected. Several methods for accounting for this onset of non-continuum effects in reduced-order models for the aero-thermodynamics of re-usable launch vehicles have been proposed, the most interesting of which being those that rely on an algebraic bridging function to merge local surface properties from those encountered in the continuum regime to those that would be experienced were the vehicle be subjected to free-molecular flow – see the study of Wilmoth *et al.* (30). These methods have been applied very successfully to analyse the aero-thermodynamics of simple shapes (for example to re-entry blunt-body capsules). As a result, HyFlow makes use of these so-called bridging techniques to provide engineering aerodynamic predictions in the transitional flow regime. The functional relation embedded in our reduced-order model can be expressed in the general form

$$C_{trans} = C_{cont} + P_B(C_{fm} - C_{cont}) \tag{2.13}$$

where C_{trans} can either be a local or global coefficient, and $P_B = f(K_n)$ is a bridging function that defines the variation in the value of the coefficients between the free-molecular and continuum limits using an interpolation function based on the free-stream value of the Knudsen number. The level of complexity in existing bridging techniques varies appreciably and can be as simple as (35).

$$P_B = \frac{K_n}{1 + K_n} \tag{2.14}$$

However, the HyFlow model employs the bridging technique given in Eq. 2.15, defaulting to a simple sine-squared law, to interpolate between the pressure predictions obtained from its free-molecular and continuum-flow models.

$$P_B = \sin^n \chi \tag{2.15}$$

where χ is defined as

$$\chi = \pi \times (k_1 + k_2 \times \log_{10} K_n) \tag{2.16}$$

where n, k_1 and k_2 are constants that are derived from the continuum and free-molecular bounds of the Knudsen number range (e.g. $n = 2$, $k_1 = 3/8$ and $k_2 = 1/8$ based on the Shuttle Orbiter data (36)). However, despite its common

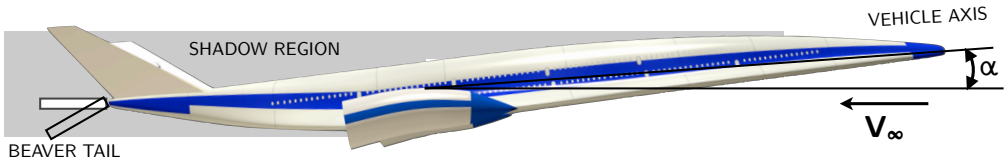

Figure 2.9: An illustration of the Shadowing of the Beaver Tail at Low Angle of Attack

use for hypersonic flows (most notably for capsule-like blunt body aerodynamics), the sine-squared function could not be applied entirely successfully to all the flight data obtained from the various American Space Shuttle missions (30). Indeed, the ability of the current bridging approach to handle more complex vehicle geometries remains to be tested. Therefore, a new bridging technique, adapted to the characterization of the transitional environment of future space-access vehicles, and based on DSMC computations, will be required to strengthen the aerodynamic estimates in this transitional regime.

2.3.5 Shadowing Effects

The aerodynamic model embedded in HyFlow accounts for the effect of one part of the vehicle blocking the flow onto another at angle of attack. At hypersonic speeds, parts of the vehicle can effectively shield others from exposure to the oncoming flow. Indeed, under the assumption that the flow obeys Newtonian theory, the air particles lose all their momentum normal to the surface at the point at which they first impact the vehicle. The flow thus cannot wrap around the vehicle or pass over obstacles in order to impact panels located further downstream in the shadowed region. For vehicles with geometries as complex as those that are expected to characterise future space-access systems (particularly those which might have protrusions such as wings, canards, flaps etc...), the effect of panel shielding may become important in determining the overall aerodynamic moment and force acting on the vehicle under hypersonic flow conditions (see Chapter 3). HyFlow can automatically identify any triangular faces that are blocked or partially shielded by other upstream portions of the body surface – for instance, those on a rear beaver-tail (i.e. body flap) that might, at least at low angle of attack, be reduced in effectiveness through being aerodynamically "shadowed" behind the frontal area of the fuselage, as illustrated in Fig. 2.9. The panels that are shielded from the flow in these shadowed regions are eliminated

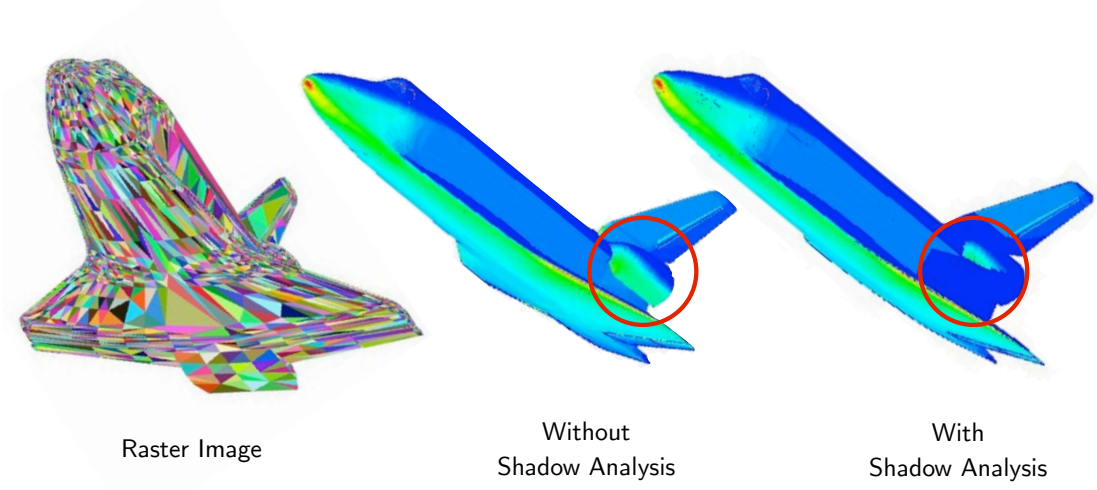

Figure 2.10: The effect of shadowing on the Space Shuttle Orbiter - The figure illustrates the effect of shadowing on the pressure distribution of the Space Shuttle Orbiter when operating at 40 degrees angle of attack and 20 degrees sideslip angle (for demonstration purposes). On the left-hand side, an example of a raster image utilized by the algorithm to detect windward panels is also depicted.

from the computation of the force and moment acting on the body. In addition, in HyFlow, all panels that compose the geometry of the vehicle are identified as being part of either the windward or leeward side of the body being modelled. For convex bodies, the screening between leeward and windward faces relies solely on the angle the local panel outward unit normals form with the unit vector oriented in the direction of the free-stream velocity vector (i.e. HyFlow simply analyses the orientation of the local unit normal vectors with respect to the free-stream flow). The criterion used to discriminate windward from leeward panels is

$$\frac{\vec{V}_\infty}{\|\vec{V}_\infty\|}.\hat{n}_i \begin{cases} < 0 & \text{windward side} \\ \geq 0 & \text{leeward side} \end{cases} \tag{2.17}$$

However, for concave bodies, some forward-facing panels, identified using this simple criterion (Eq. 2.17), may still be shadowed by upstream forward-facing surfaces. Therefore, a rapid and more accurate sorting algorithm – known as the back-face culling algorithm – has been derived and implemented in HyFlow.

Back-face Culling Algorithm

The algorithm, which is used to cull all triangles that face away from the viewer (who sees the vehicle in the direction of the oncoming flow), follows the steps below:

1. First, a unique colour is randomly assigned to each of the triangular panels that compose the geometry.

2. Thereafter, the tessellated geometry, correctly oriented in the direction of the oncoming flow, is converted into a raster image which corresponds to a data structure representing a grid of pixels (also known as points of colour).

3. Finally, the set of colour values in the raster graphics (color matrix) can be used to identify the corresponding panels in the tessellation.

These identified panels are then classified as windward panels while the remainder of the triangular faces are assumed to be located on the leeward side of the body (i.e. in the shadowed region). An example of such process is shown in Fig. 2.10 for the Space Shuttle Orbiter. The development of this algorithm was necessary to provide a fast method that would avoid the high computational complexity often involved in the use of ray-tracing algorithms to determine faces that are impacted (or visible) by the oncoming hypersonic flow (as it requires a large number of rays to be traced).

Leeward Side

The surface regions on the leeward side of the body are aerodynamically shadowed, and thus require a particular treatment. Indeed, the modified Newtonian theory of hypersonic flows (or any of the methods previously described) does not predict the local pressure in this particular region of the flow field where separation and strong vorticity may occur. In HyFlow, the surface pressure in the shadow region of the vehicle is, by default, simply assumed to be the free-stream static pressure (16), that is the pressure coefficient is set to zero on those shadowed portions of the body as asserted by Eq. 2.3 repeated here for convenience:

$$C_{p,i} = 0 \qquad \text{if } \theta_i \leq \frac{\pi}{2} \tag{2.18}$$

This method is simply used to define a flow expansion model in that shielded region of the flow field. Other methods, included in HyFlow (mainly to correct for base pressure) and commonly adopted in the literature, consist in setting the pressure coefficients in the shadow region as $C_{p,i} = -1/(\gamma M_\infty^2)$ – see for instance the RAM model of Dirkx (23) – or using the empirical base pressure method from

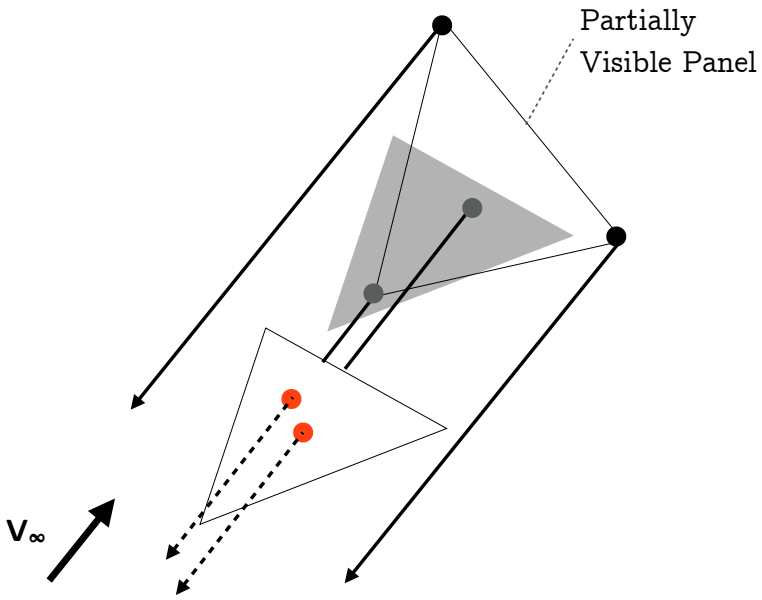

Figure 2.11: An illustration of the algorithm used to detect partially shielded panels - If a windward-facing panel is partially shadowed by another panel located upstream, the area of the panel in question, which is impacted by the oncoming hypersonic flow, can be estimated through the computation of a visibility ratio based on a fast ray-tracing algorithm implemented in HyFlow (limiting the number of rays to be traced). In the present illustration, half of the panel are considered shielded and thus $R_v = 0.5$.

the Aerodynamic Preliminary Analysis System (APAS) code of Dunn *et al.* (37) derived from, *inter alia*, Space Shuttle and X-15 data.

Nonetheless, it is worth noting that, in HyFlow, the surface streamlines in the shadow regions (described later in Section 2.4.1) are still computed in the same way as those over the windward side of the vehicle. However, if the change in geometry between a windward region and an adjacent leeward region is too steep (i.e. a situation which would, in reality, induce a sudden change in the direction of the local edge velocities), a separation region can be enforced – i.e. in this particular region, the surface streamlines are not computed. The method employed here to detect these specific regions is similar to that described in the report of Villa (24).

Figure 2.12: Distribution of the visibility ratio per panel over the Space Shuttle Orbiter - The figure depicts the visibility fraction over the tessellated representation of the Space Shuttle Orbiter as result of partial shielding – i.e. when the vehicle operates at 40 degrees angle of attack and 20 degrees sideslip angle.

Partially-Shielded Panels

All the local surface inclination methods embedded within the HyFlow code treat any windward triangular panel as a compression panel. Nonetheless, when two windward panels are only partially behind one another, this assumption needs to be revised as the fast sorting algorithm previously derived may classify a panel in its entirety as a windward panel while it may only be partially impacted by the oncoming hypersonic flow. This effect is particularly important when HyFlow is used in conjunction with a low resolution mesh (such as the one shown in Fig. 2.4), and thus a correction measure is required. Nonetheless, instead of calculating all combinations of panels as well as the occurrence and size of overlapping regions such as in the method of Dirkx (23) (high computational complexity), the size and extent of the area of a given windward panel which is impacted can more efficiently be assessed in HyFlow using a fast ray-casting algorithm (38) and by applying the following procedure (illustrated in Fig. 2.11) to each of the previously identified windward panels in the mesh:

1. Four rays are traced in the direction opposite to the oncoming hypersonic flow. The origins of these rays must be the three vertices of a given windward-facing triangle and its centroid.

2. The number of rays that intersect other upstream windward panels define the visibility fraction per panel denoted by $R_{v,i} \in [0, 0.25, 0.5, 1]$.

Then, once the visibility fraction per panel is approximated, the pressure exerted on the panel in question can be derived from a weighted estimation of the pressure estimates given by the selected windward region compression method, here denoted C_{p,i_w}, and those given by the shadow region expansion method (Eq. 2.18), here simply denoted C_{p,i_s}, as

$$C_{p,i} = R_{v,i} C_{p,i_w} + (1 - R_{v,i}) C_{p,i_s} \tag{2.19}$$

This particular treatment of the partially shielded panels allows a more accurate definition of the local aerodynamic load acting on each panel of the vehicle. Furthermore, it ensures the possibility of relying on these reduced-order models for the study of complex configurations even when a low resolution mesh is being used (see Fig. 2.12). The importance of the shadowing effect will be demonstrated in Chapter 3.

2.4 Viscous Model

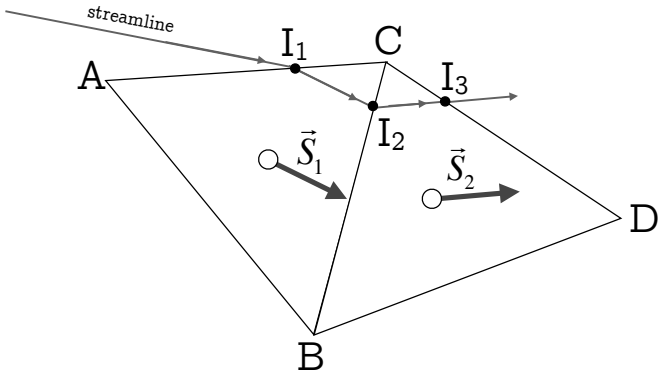

Figure 2.13: Illustration of the algorithm for surface streamlines - When a streamline enters within the physical domain delimited by triangle ABC at intersection point I_1, the next segment being traced follows the shear velocity vector of triangle ABC, denoted $\vec{S}_1$, until it intersects the edge BC of the triangular panel at point I_2. From point I_2, the path line follows the velocity vector of triangle BCD, denoted $\vec{S}_2$, up to the intersection point I_3 between the streamline and the edge CD etc.

As the Mach number is increased, the strong shock that is always found upstream of the vehicle moves closer to the body while the boundary layer grows rapidly in

thickness. At hypersonic Mach numbers, viscous interactions between the outer inviscid flow, the shock, and the boundary layer become significant and therefore cannot be neglected. For instance, the results of a study by Oppenheimer *et al.* (40) show that "*drag increments due to viscous effects are not minimal, pitching moment increments due to viscosity are small, and lift due to viscosity is negligible*," thus reinforcing the importance of accounting for viscous effects in order to accurately quantify the performance of prospective hypersonic configurations as those may have a substantial influence on the total force acting in the direction of travel on such vehicles. In fact, it has been shown that viscous stresses can contribute more than a quarter of the drag force acting on hypersonic configurations (16). In his book however, Bertin argues that the computation of the viscous flows is "*the most challenging aspect of analysing the flow over a complex shape [...] due to difficulties in developing simple, yet realistic models.*" (17) Nonetheless, as is the case with many other industry-standard codes (such as the S/HAPB and CBAERO codes mentioned earlier), HyFlow accounts for viscous effects by determining the trajectories of the streamlines across the surface of the vehicle, then integrating along the streamlines to find the local Reynolds number and hence the local skin friction coefficients (see Section 2.4.4).

2.4.1 Surface Streamlines

In HyFlow, the surface velocity field is based on a Newtonian impact assumption (i.e. the flow remains tangent to the surface after impact), and is applied to the entire surface of the vehicle. For each of the panels describing the geometry of the vehicle, the tangential velocity vector is therefore defined as the free-stream velocity vector minus its normal component at a given point P_i on the body and is given by (41)

$$\vec{S}_i = \left(\hat{n}_i \times \frac{\vec{V}_\infty}{\|\vec{V}_\infty\|} \right) \times \hat{n}_i = \frac{\vec{V}_\infty}{\|\vec{V}_\infty\|} - \left(\frac{\vec{V}_\infty}{\|\vec{V}_\infty\|} . \hat{n}_i \right) . \hat{n}_i \tag{2.20}$$

where $\hat{S}_i = \vec{S}_i / \|\vec{S}_i\|$ is the unit vector in the direction of the tangential velocity vector on the i-th panel. In other words, it is assumed that the flow changes instantaneously its direction from its free-stream orientation to a direction tangential to the surface of the vehicle upon impact. This assumption remains valid under the thin shock layer approximation which is often considered in hypersonic

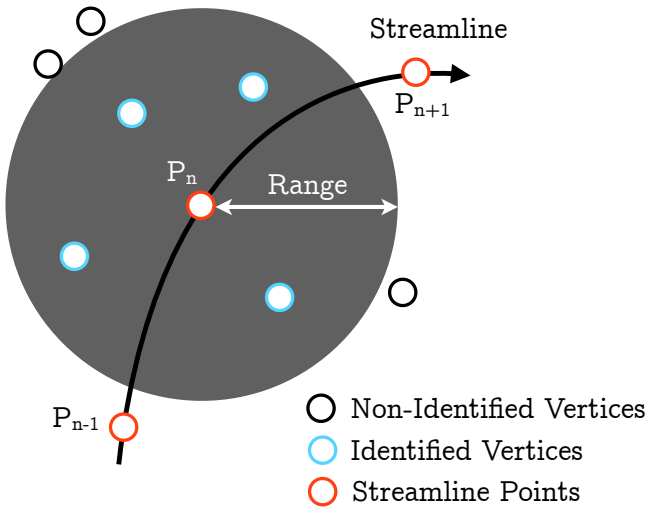

Figure 2.14: Illustration of a range search using a 3-dimensional k-d tree - A 3-dimensional k-d tree search object is used to identify all the vertices located in the direct vicinity of a streamline currently being traced (i.e. the distance range must be specified). Identified points (shown in blue) can then have the running length of their streamline approximated from the current streamline.

flows and forms the basis of the viscous model embedded in HyFlow. The simplified streamline distribution is then determined using a simple tracking routine that propagates backward the lines in piecewise-continuous fashion from panel to panel while ensuring that they always remain tangent to the flow on the surface of the vehicle as illustrated in Fig. 2.13. Since the location of the stagnation features within the flow is hardly ever apparent prior to tracing the streamlines, the velocity field is reversed with respect to Eq. 2.20 (and is therefore given by $\hat{V}_{stream,i} = -\hat{S}_i$) and the streamlines are propagated upstream, starting from the rear of the vehicle. This backward propagation also guarantees a full coverage of the geometry with surface streamlines.

Nonetheless, to limit the number of streamlines that need to be computed, and in the vein of the technique implemented within CBAERO (22), HyFlow employs a 3-dimensional k-d tree object to detect efficiently all vertices of the surface mesh that lie within a small region surrounding each streamline that has already been computed (see Fig. 2.14). The indices of those vertices so identified are then removed from the list of candidate starting points for subsequent streamlines, thus greatly reducing the computational expense of the model. It should however be noted that beforehand, great care is taken to sort all the vertices of

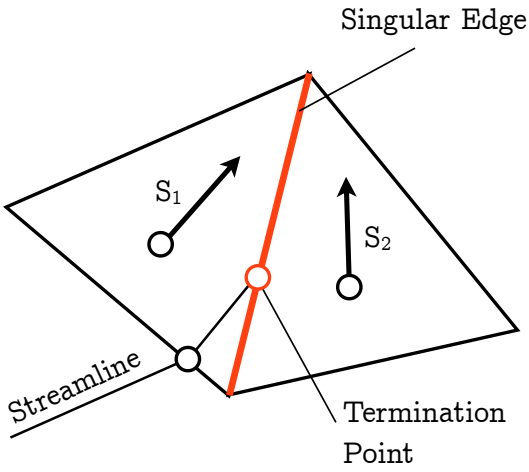

Figure 2.15: Singular edge problem - An edge is singular "*if the vector values associated with the panels lying on both sides have opposite normal components with respect to the edge.*" (42)

the tessellation in ascending order with respect to their longitudinal coordinates and the vertex located the furthest away from the tip of the vehicle is always used to trace the next streamline. This preliminary step is performed in order to maximize the number of vertices encountered in the neighbourhood of the streamline currently being propagated. The results of the streamlines computed via the aforementioned geometric algorithm are not always satisfying, however. Indeed, the streamlines may either not converge towards the stagnation features or stop propagating forward due to the presence of a singular edge, a phenomenon illustrated in Fig. 2.15. These problems, whose concomitant effect on the evaluation of the local Reynolds number is non-negligible, have therefore motivated the implementation of another streamline integration algorithm based on a predictor-corrector method (i.e. implicit second-order Runge-Kutta method), also known as the method of Heun (43), which is discussed below.

Numerical Integration of Surface Streamlines

In HyFlow, the velocity vector field is then numerically integrated in order to determine the surface streamlines over the entire tessellation using the following

relationship

$$\begin{bmatrix}\Delta x\\ \Delta y\\ \Delta z\end{bmatrix}_i = -\begin{bmatrix}\hat{S}_x\\ \hat{S}_y\\ \hat{S}_z\end{bmatrix}_i \Delta t \Leftrightarrow \Delta\vec{P}_i = \hat{S}_i(x,y,z)\Delta t \tag{2.21}$$

where Δx, Δy and Δz are spatial increments, and Δt is a time step increment (either an adaptive or a fixed time-step size can be used, e.g. a fraction of the average length of the triangulation edges). The coordinates of the next point along a given streamline, here denoted $\vec{P}_{i+1}$, are first approximated via the Euler method (i.e. the simplest of the explicit Runge-Kutta methods) which is given by the following relationship (predictor step)

$$\widetilde{P}_{i+1} = \vec{P}_i + \Delta\vec{P}_i \tag{2.22}$$

Thereafter, the trapezoidal rule (corrector step) is used in order to refine the previous estimate as

$$\vec{P}_{i+1} = \vec{P}_i + \frac{1}{2}(\Delta\vec{P}_i + \Delta\tilde{P}_{i+1}) \tag{2.23}$$

where $\Delta\tilde{P}_{i+1}$ is interpolated from the velocity vector field at the approximated location of the point $\tilde{P}_{i+1}$ computed thanks to the Euler method in Eq. 2.22. In HyFlow, the second order Runge-Kutta method is used in conjunction with a natural neighbourhood interpolation algorithm in order to interpolate the shear velocity vector field from its known value at the tessellation triangles to any point on its surface (an interpolant of the form $\hat{S}_i = f(x,y,z)$ is thus created). The natural neighbour interpolation method makes use of an area-weighting technique, i.e. based on a Voronoi tessellation of the mesh vertices – see Ref. (39), to determine a new value of the velocity vector field at any point on the surface of the tessellation.

Then, in order for the streamlines to be constrained onto the surface of the geometry, the next point along the streamline, $\vec{P}_{i+1}$, is projected onto the tessellation if the minimum distance between the point in question and the surface of the body is greater than a pre-defined tolerance (by default, set equal to 10^{-4} m in HyFlow). This projection is performed through the use of the ray-tracing algorithm mentioned in Section 2.3.5 where the unit normal vector of the closest face centroid is used to define the projection direction of the ray that originates from the streamline point given by Eq. 2.23. Finally, the coordinates of the intersection point between the ray and the tessellation is used in place of the value of P_{i+1} obtained after the correction step, and the algorithm is repeated to propagate the streamline forward until a stagnation feature is detected. An example of the

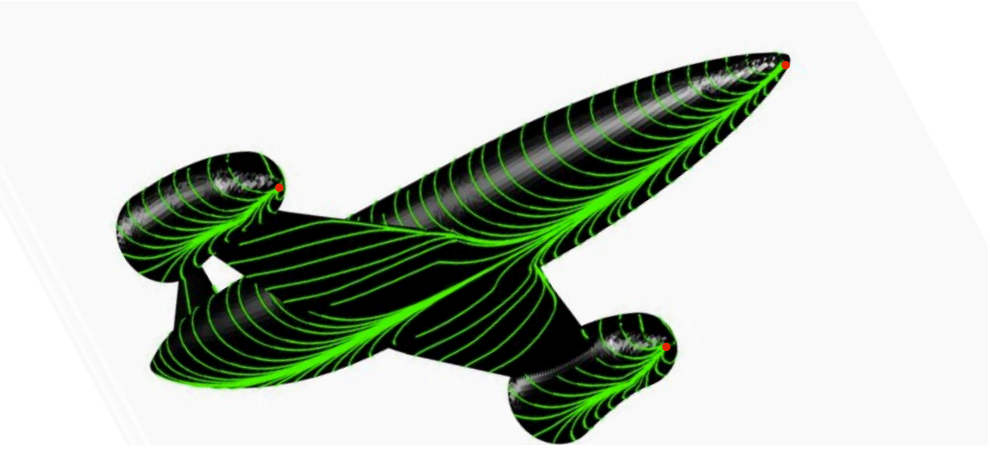

Figure 2.16: Distribution of streamlines over the Skylon SSTO vehicle at 40 degrees angle of attack.

distribution of streamlines over the surface of the Skylon SSTO configuration (i.e. without its canards) at a 40 degrees angle of attack, as computed using the previous numerical algorithm, is shown in Fig. 2.16.

Stagnation Features

The stagnation features within the flow are, in general, determined through the simple expedient of detecting those panels on which the tracking procedure fails to find a viable upstream direction in which to continue propagation of the streamlines. However, for blunt-nosed bodies (e.g. the nose tip of the fuselage of a space-access vehicle), the exact location of the stagnation point is often close to the Newtonian stagnation point (41). Therefore, coherently with the simplified streamline distribution described in this section, the location of the stagnation point can simply be determined by the panel, lying on the windward side of the vehicle, where the condition

$$\frac{\vec{V}_\infty}{\|\vec{V}_\infty\|}.\hat{n}_i = -1 \tag{2.24}$$

is fulfilled.

Running Length

The running length back along the streamline from the relevant stagnation point to the panel in question, denoted x_i, is then computed as

$$x_i = \sum_{j=1}^{n_s} \|\vec{P}_{n+1} - \vec{P}_n\|_j \tag{2.25}$$

where n_s represents the number of segments along a given streamline. The running length is then used to determine the local Reynolds number required in the computation of the local skin friction coefficients, denoted $C_{f,i}$, as will be discussed later in Section 2.4.4.

2.4.2 Boundary Layer Edge Conditions

In the current formulation, the assumption is made that the flow at the edge of the viscous boundary layer passes through the normal portion of the bow shock wave, which fixes the entropy (constant), and then subsequently undergoes an isentropic expansion from the total pressure condition $p_{0,2}$ downstream of the normal shock to the pressure which is exerted locally on each panel A_i, denoted p_i (17). Although this assumption may hold for the streamlines located outside of the viscous boundary layer, the flow within the boundary layer normally passes through a bow shock which is significantly curved (i.e. herein assumed nearly-normal), leading to significant entropy gradients normal to the wall. Nevertheless, as a means of maintaining the computational efficiency of the reduced-order approach, and also simply due to the inherent lack of information produced by the panel-based approach regarding the shape of the shock wave through which the inviscid streamlines pass, the entropy gradient normal to the wall that results from the shock curvature is generally neglected in most reduced-order aero-thermodynamic models for hypersonic vehicles (44). A simple Normal Shock Isentropic Expansion (NS-IE) flow model is thus assumed in the current implementation.

Therefore, the value of the pressure at the edge of the boundary layer at the location of the i^{th} triangular panel, denoted p_{edge_i}, is computed from the pressure coefficient obtained via the miscellaneous inviscid methods that were introduced in section 2.3 as

$$p_{edge_i} = \frac{1}{2}\rho_\infty V_\infty^2 C_{p_i} + p_\infty \tag{2.26}$$

Indeed, the thin shock layer approximation (for the region between the shock and

the body) leads to the conclusion that the pressure variation across the boundary layer can be neglected since under this assumption, the shock shape, the body shape and the streamline shapes in between are considered to be all the same, and therefore, the edge pressure is set equal to the surface pressure (i.e. which is also in agreement with the first-order boundary layer approximations where $p_{edge_i} = p_i$ since under this assumption, $\left(\frac{dp}{dy}\right)_i \approx 0$, where y is the axis normal to the body surface).

Then, since the edge flow conditions are simply determined by isentropically expanding the flow from the stagnation conditions downstream of the nearly-normal shock wave (neglecting the local curvature of the shock wave and thus the effect of a variable-entropy flow), the Mach number at the edge of the boundary layer is computed using the usual isentropic relations and the pressure ratio of the edge pressure to the total post-shock pressure (see Eq. 2.4), and is given by

$$M_{edge_i} = \sqrt{\left[\left(\frac{p_{0,2}}{p_{edge\,i}}\right)^{\frac{\gamma-1}{\gamma}} - 1\right] \times \left(\frac{2}{\gamma-1}\right)} \tag{2.27}$$

Under a similar assumption, the local temperature at the edge of the boundary layer, denoted T_{edge_i}, is given by

$$T_{edge_i} = \frac{T_0}{\left[1 + \frac{\gamma-1}{2} \times M^2_{edge_i}\right]} \tag{2.28}$$

where the free-stream total temperature, denoted T_0, is simply computed as

$$T_0 = T_\infty + \frac{V^2_\infty}{2C_{p,\infty}} \tag{2.29}$$

where $C_{p,\infty}$ is the specific heat of air at constant pressure. Then, the velocity at the edge of the boundary layer is calculated as the product of the edge Mach number (Eq. 2.27) and the local speed of sound, denoted a_{edge_i}, as

$$V_{edge_i} = M_{edge_i} \times a_{edge_i} = M_{edge_i} \times \sqrt{\gamma R T_{edge_i}} \tag{2.30}$$

Finally, the density at the edge of the boundary layer, denoted ρ_{edge_i}, is computed using the gas equation of state as

$$\rho_{edge_i} = \frac{p_{edge_i}}{R T_{edge_i}} \tag{2.31}$$

2.4.3 Reference Temperature Method

A large temperature gradient can occur across the thickness of the boundary layer on the surface of the vehicle when flying at hypersonic speed. Nevertheless, by carefully selecting an appropriate average temperature for the flow in the boundary layer, the physical properties of air under incompressible flow conditions can be extrapolated to the compressible case in order to capture the properties of the flow near the surface of the vehicle (45). It is worth mentioning that the temperature is used, in the present work, in place of enthalpy since a constant ratio of specific heats is assumed. The boundary layer reference temperature is then computed by HyFlow using the Smart-Meador method (46), derived from the boundary layer equations, for either laminar or turbulent flows, and are respectively defined for laminar or turbulent boundary layers by

$$T^*_{i,lam} = T_{edge_i}\left(0.45 + 0.55 \times \frac{T_{wall}}{T_{edge_i}} + 0.16R_f \times \frac{\gamma - 1}{2} \times {M_{edge_i}}^2\right) \tag{2.32}$$

and

$$T^*_{i,turb} = T_{edge_i}\left(0.5 \times \left(1 + \frac{T_{wall}}{T_{edge_i}}\right) + 0.16R_f \times \frac{\gamma - 1}{2} \times {M_{edge_i}}^2\right) \tag{2.33}$$

where R_f is the temperature recovery factor and is given approximately by the Pohlhausen formula (45) as $(Pr^*_i)^{1/2}$ for laminar flows, and is set equal to $(Pr^*_i)^{1/3}$ for turbulent flows (i.e. Squire's semi-empirical result (45)). T_{edge_i} and M_{edge_i} are, respectively, the temperature and Mach number at the edge of the boundary layer, and Pr^*_i is the Prandtl number evaluated at the calculated intermediate temperature. The reference density, denoted ρ^*_i, is then computed through the gas equation of state by

$$\rho^*_i = \frac{P^*_i}{RT^*_i} = \frac{P_{edge_i}}{RT^*_i} \tag{2.34}$$

where P_{edge_i} is set equal to P^*_i for the reasons explained in Section 2.4.2. Finally, temperature effects are included by assuming a wall temperature T_w, and using Sutherland's viscosity law (Eq. 2.35) in order to account for the variation of dynamic viscosity with temperature, using standard temperature and pressure as the reference values.

$$\mu(T) = \mu_0 \times \left(\frac{T}{T_0}\right)^{3/2} \times \left(\frac{T_0 + S}{T + S}\right) \tag{2.35}$$

where $\mu_0 = 1.716 \times 10^{-5}\ kg/m.s$, $T_0 = 273.15\ K$, and $S = 110.4\ K$.

2.4.4 Skin Friction Coefficients

In HyFlow, the relationships used to calculate the local skin friction coefficients, denoted $C^*_{f,lam}$ and $C^*_{f,turb}$ for laminar and turbulent flow respectively, are derived from those for incompressible flow over a flat plate and are corrected for compressibility in the flow following Eckert's procedure (as presented in Ref. (46)) as

$$C^*_{f,lam} = K_g \frac{0.664}{(Re^*)^{0.5}} \times f_1 \tag{2.36}$$

and (47)

$$C^*_{f,turb} = K_g \frac{0.02296}{(Re^*)^{0.139}} \times f_2 \tag{2.37}$$

where f_1 and f_2 are Chapman-Rubesin factors added to account for compressibility effects and are defined by

$$f_1 = \sqrt{\frac{\rho^* \times \mu^*}{\rho_{edge} \times \mu_{edge}}} \quad \text{and} \quad f_2 = \left(\frac{\rho^*}{\rho_{edge}}\right)^{0.861} \left(\frac{\mu^*}{\mu_{edge}}\right)^{0.139} \tag{2.38}$$

K_g is the Mangler transformation factor used to correct the results from two-dimensional flat plate theory to account for three-dimensionality in the flow field. Its value is empirically set equal to $\sqrt{3}$ for laminar flows while a value of 1.15 is used for turbulent flows (45), and

$$Re^*_i = \frac{\rho^* V_{edge} x_i}{\mu^*} \tag{2.39}$$

is the local Reynolds number evaluated at the reference conditions within the boundary layer. Finally, the shear stress distribution at the wall, denoted τ_w, is obtained as the product of the local skin friction coefficient and the reference dynamic pressure by

$$\tau_{w,i} = \frac{1}{2} \rho^*_i {V_{edge}}^2_i \times C^*_{f,i} \tag{2.40}$$

2.4.5 Rarefied Flows

The equation for the local free-molecular friction coefficient as a function of the local inclination angle ϕ_i, denoted by $C_{f,i\,fm}$ and derived by Probstein *et al.* (28),

is

$$C_{f,i_{fm}} = \left(\frac{\cos\phi_i}{2\sqrt{\pi}\sigma_S}\right)\left(\exp(-(\sigma_S \sin\phi_i)^2) + \sqrt{\pi}(\sigma_S \sin\phi_i)[1 + \mathrm{erf}(\sigma_S \sin\phi_i)]\right) \tag{2.41}$$

It is worth remarking that for free-molecular flows, the expression of the skin friction coefficient derived from kinetic gas theory becomes a simple function of the local inclination angle ϕ_i and the free-stream velocity (through the speed ratio σ_S) only. The local shear stress can then be computed as $\tau_{w,i_{fm}} = f_t \times C_{f,i_{fm}}$ where f_t is the tangential momentum coefficient (i.e. $f_t = 1$ to model a diffuse reflection). For the transitional regime, the bridging techniques introduced in Section 2.3.4 can be used to obtain the local transitional skin friction coefficients.

2.5 Boundary Layer Transition

It is widely accepted that the modelling of boundary layer transition is one of the most difficult outstanding challenges in fluid dynamics. No theory yet exists that can be used to accurately predict transition at hypersonic speeds (48). Indeed, most of the transition prediction techniques available for design are in the form of empirical correlations, and these, whether obtained in ground-based test facilities or in flight, have a limited range of applicability. Engineering methods often assume that transition occurs at a fixed Reynolds number: the flow is assumed laminar upstream of this point, and fully turbulent downstream. However, for the accurate prediction of the skin friction and heat transferred to a body, knowledge of the transition Reynolds number Re_t is critical. Since limited theoretical guidance exists, the appropriate value of Re_t for a given situation is generally obtained from experimental data. Any application outside the existing database, for instance for preliminary design purposes, is fraught with difficulty and requires a number of assumptions, the validity of which is always highly dependent on the expertise of the aerodynamicists. The Reynolds number at transition is usually dependent on a very large number of parameters which are either assumed, can be predicted, or are known unknowns. For instance, the Mach number at the edge of the boundary layer, M_{edge}, has a strong influence on the stability of the laminar boundary layer and, by extension, on the transitional Reynolds number

Re_t. Three-dimensionality in the flow can also have a strong effect on laminar-turbulent transition. Indeed, it was shown in a study by Chen *et al.* (49) that flows over two-dimensional flat plates have higher transition Reynolds numbers than cones at the same free-stream conditions. Hence, the Reynolds number at transition can be expressed in a functional form depending on a range of parameters, for example as

$$Re_t = f(M_{edge}, \alpha, T_w, k_R) \tag{2.42}$$

where T_w is the wall temperature and k_R is a parameter expressing the roughness of the vehicle's surface. When and if boundary layer transition occurs depends indeed on many coupled parameters and only a small sub-set is considered in the present work. Under normal conditions, transition should usually occur symmetrically on both left and right sides of the vehicle at about Mach 8 during a nominal entry trajectory for a Shuttle-sized space-access vehicle. Many parameters can potentially cause premature transition, however. Statistical analysis of the re-entry flight experience of the Space Shuttle has shown that early transition, i.e. at greater than Mach 10.9, occurred on 20% of flights, and that transition was asymmetric in 60% of those cases. Nevertheless, for lower Mach numbers, the probability of asymmetric transition reduced to only about 10% (51).

In the present work, two different mechanisms for the boundary layer transition from a laminar to a turbulent state have been modelled in HyFlow: (1) a model described in Section 2.5.1 and based on the assumption of a smooth-surface transition and (2) a model, introduced in Section 2.5.2, that can simulate asymmetric transition phenomena for example as a consequence of pre-flight maintenance errors or in-flight deterioration of the thermal shield, as shown in Fig. 2.17, as a result of asperities on the surface of the vehicle due to micro-meteorite impacts.

2.5.1 Smooth-Surface Transition Criterion

In order to define accurately the aero-thermodynamic environment of future reusable launchers during their ascent and subsequent entry into the terrestrial atmosphere, a criterion must be devised for defining when the transition of the boundary-layer from the laminar state to a turbulent state occurs. Indeed, accurate predictions of boundary layer transition are extremely important to the

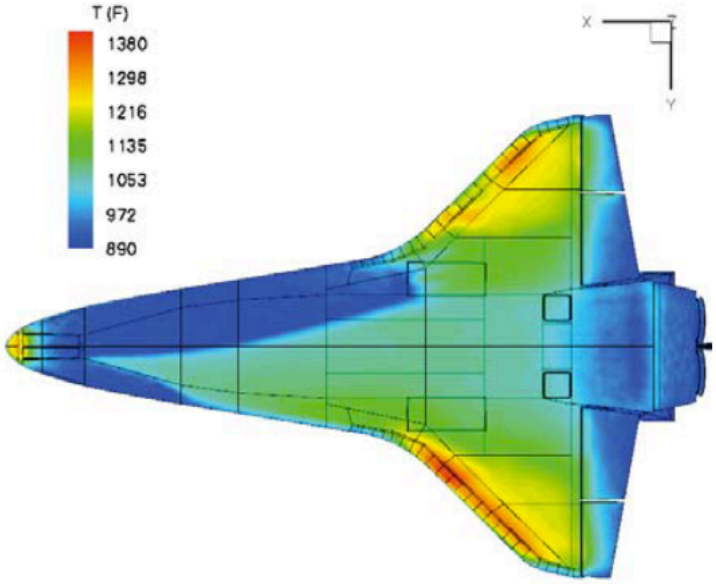

Figure 2.17: Temperature mapping over the surface of the Space Shuttle Orbiter - 3-D mapping of the temperature experienced by the underbelly of the Space Shuttle during its STS-134 flight. An asymmetric transition phenomenon occurred while the vehicle was travelling at $M_\infty = 5.8$ and inclined at 28.8 degrees angle of attack which resulted in a significant increase in local surface temperature within the turbulent wedge region that had formed downstream of a dislodged gap filler (i.e. piece of ceramic material located between the Shuttle's heat resilient tiles) (50).

design of most re-entry vehicles (16). A simple empirical correlation, based on experimental data for sharp cones at zero degrees angle of attack, and used by Bowcutt and Anderson in a study of hypersonic waveriders (52), is used in HyFlow to predict the onset of transition on those vehicle surfaces that are smooth.

$$\log_{10}(Re_t) = 6.421 \exp(1.209 \times 10^{-4}\ M_{edge}^{2.641}) \tag{2.43}$$

where Re_t is the streamline Reynolds number at which transition takes place and M_{edge} is the Mach number at the edge of the boundary layer.

Finally, it shall be remarked that, in HyFlow, the transitional region is not directly evaluated. Nevertheless, an average value between the laminar and turbulent estimates can be enforced over the panels that are adjacent to the turbulent region. This way, the transition from the laminar region to the turbulent region is smoothened in an attempt to better represent the transition phenomenon – i.e. abrupt changes in heat transfer values are thus avoided.

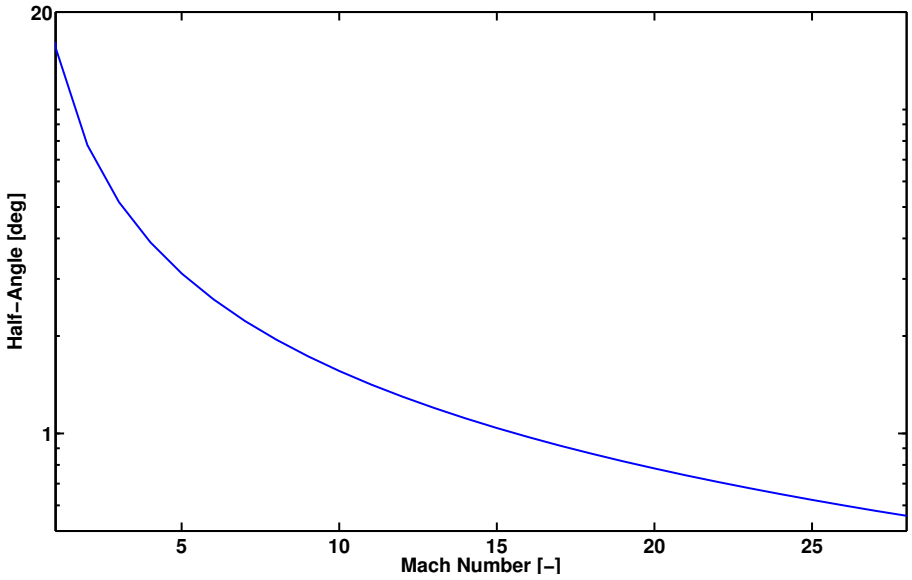

Figure 2.18: Empirical law governing the turbulent wedge angle - The variation of the turbulent wedge apex half-angle as a function of the edge Mach number (55). A logarithmic scale is used on the vertical axis.

2.5.2 Roughness-Induced Transition

Although the complexity of roughness-induced transition phenomena often requires the use of higher fidelity CFD or hybrid CFD/DSMC methods (53), taking inspiration from the work of Ryan *et al.* (54), HyFlow can also simulate some of the effects of roughness-induced boundary layer transition, such as the creation of asymmetric aerodynamic loads and increased aerodynamic heating, by introducing an isolated element of surface roughness onto the Outer Mould Line (OML) of any arbitrary three-dimensional vehicle configuration. The location of the roughness element can either be imposed, or randomized within a prescribed region of interest on the surface of the vehicle (e.g. over the windward side of the wing). The turbulent wedge that results from an isolated element of surface roughness has its apex at the location of the element and expands downstream along the surface of the vehicle. Within the turbulent wedge region, a fully turbulent boundary layer is assumed, and the apex half-angle ϕ_{wedge} of the wedge (see Fig. 2.18) is modelled by the empirical relationship of Smith *et al.* (55) as

$$\phi_{wedge} = 3^{-3/2} \times \sqrt{2} \times \frac{1}{M_{edge,kr}} \tag{2.44}$$

where $M_{edge,kr}$ is the local roughness Mach number at the edge of the boundary

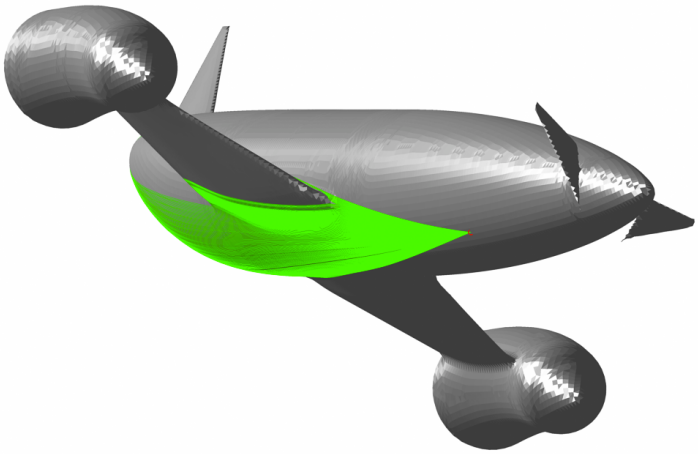

Figure 2.19: Formation of a turbulent wedge - A set of streamlines is used to define the extent of the turbulent wedge region that results from the presence of an element of surface roughness on the lower forward fuselage of the Skylon SSTO vehicle (Reaction Engines Ltd).

layer. The extent of the region of spread of the turbulence downstream of the roughness, i.e. the so-called "turbulent wedge", depends on the conditions at the edge of the boundary layer at the location of the roughness element, namely the density ρ_{kr}, the velocity U_{kr}, and the viscosity μ_{kr} of the flow. The creation of turbulent wedges can finally be triggered, during trajectory integration for instance, when the local roughness Reynolds number – written in the form of a criterion suggested by Reda (56) – and the local thickness of the laminar boundary layer satisfy a specific transition criterion (see Section 6.3.3).

Transition Model

The algorithm used in HyFlow to define a turbulent wedge on the surface of the vehicle starts by tracing its leading edge by marching downstream from its apex and calculating the boundary between the laminar flow upstream and the turbulent flow within the wedge. This is done by offsetting locally the leading edge of the wedge, with respect to the local streamline, by the wedge apex angle calculated according to Eq. 2.44. Indeed, the boundaries of the wedge are defined by the streamlines that follow the velocity vector field $\hat{S}_i$, given in Eq. 2.20, rotated about its local unit vector normal $\hat{n}_i$ by an angle $\phi \in [-\phi_{wedge}; \phi_{wedge}]$ using Rodrigues's rotation formula (see, for instance, Ref. (57)) as follows

$$\hat{S}_i^{rot} = \hat{S}_i \cos\phi + (\hat{n} \times \hat{S}_i) \sin\phi + \hat{n}(\hat{n}.\hat{S}_i)(1 - \cos\phi) \tag{2.45}$$

where $\hat{S}_i^{rot}$ represents the rotated velocity vector field induced by the element of surface roughness and used in HyFlow to determine the boundary of the turbulent wedge over the tessellated surface of the vehicle. An example of the end result of this process is shown in Fig. 2.19. Finally, the region of the surface mesh that lies beneath the turbulent wedge is then identified, and the flow is assumed to be turbulent above all panels that lie within that region.

2.6 Forces and Moments

The total force and moment acting on the vehicle can then be calculated by integrating the pressure and shear force distributions over the surface area of the vehicle. Since the reduced-order model uses a panel-based approximation to the geometry of the vehicle, this integration is approximated numerically by performing a finite summation over the total number of panels that approximate the shape of the vehicle. The aerodynamic force acting on panel i is therefore given by

$$\hat{F}_i = \{(Q_\infty C_p)_i \hat{n}_i + (Q_{ref} C_f)_i \hat{s}_i\} A_i \tag{2.46}$$

where the first term represents the inviscid contribution from Eq.2.3, and the second the viscous contribution from Eq. 2.36 (or Eq. 2.37 for turbulent flows) evaluated at the centroid of each panel, area A_i, comprising the approximation to the shape of the vehicle. $Q_\infty = \frac{1}{2}\rho_\infty \|\vec{V}_\infty\|^2$ is the free-stream dynamic pressure and $Q^* = \frac{1}{2}\rho^* \|\vec{V}_{edge}\|^2$ is the local reference dynamic pressure within the boundary layer. The overall aerodynamic force acting on the vehicle is then approximated by

$$\hat{F} = \sum_{i=1}^{N} \hat{F}_i \tag{2.47}$$

and, similarly, the aerodynamic moment about the centre of mass $\hat{x}_c$ of the vehicle is approximated by

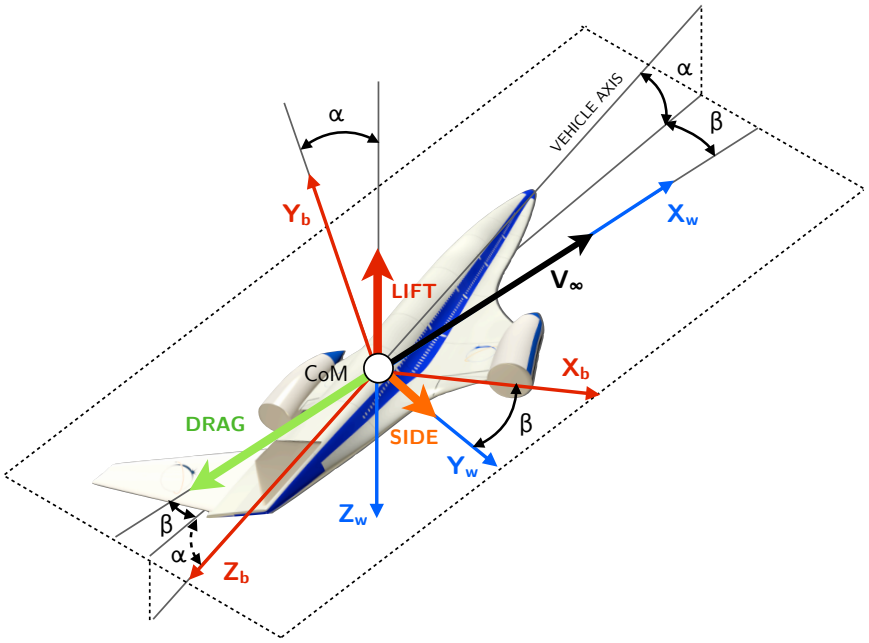

Figure 2.20: Body-fixed and wind reference frames - A schematic of the body and wind frames of reference as defined within the HyFlow model.

$$\hat{M} = \sum_{i=1}^{N} \hat{F}_i \times (\hat{x}_i - \hat{x}_c) \tag{2.48}$$

where $\hat{x}_i$ is the centroid of panel i. The centre of mass $\hat{x}_c$ of the geometry can either be arbitrarily set, or estimated by default as an area-weighted average of the centroids of its constituting panels (assuming uniform distribution of the mass over the surface of the geometry) by

$$\hat{x}_c = \frac{1}{A_{total}} \sum_{i=1}^{N} A_i \times \hat{x}_i \qquad \text{where} \qquad A_{total} = \sum_{i=1}^{N} A_i \tag{2.49}$$

Lift, Side-force and Drag

Aerodynamic forces such as lift, drag and side force are expressed in the wind axes reference frame (x_w, y_w, z_w) – i.e. w-frame. Therefore, the components of the total force and moment must be transformed from the body-fixed axes reference frame (x_b, y_b, z_b) to wind axes. In HyFlow's wind axes, x_w is orientated in the direction of the free-stream velocity vector $\vec{V}_\infty$ and is thus aligned with the drag

force, z_w is contained within the plane of symmetry of the vehicle, perpendicular to x_w and is therefore aligned with the lift force, and finally y_w is chosen in order to form a right-handed reference frame (see Fig. 2.20). The wind reference frame is obtained via two successive rotations of the body reference frame by the angle of attack α first, $C(\alpha)$, and by the angle of sideslip β then, $C(\beta)$, as follows

$$\begin{bmatrix} D \\ S \\ L \end{bmatrix}_w = C(\beta)C(\alpha) \begin{bmatrix} F_x \\ F_y \\ F_z \end{bmatrix}_b \tag{2.50}$$

with

$$C(\beta)C(\alpha) = \begin{bmatrix} -\sin\beta & -\cos\beta\sin\alpha & -\cos\beta\cos\alpha \\ \cos\beta & -\sin\beta\sin\alpha & -\sin\beta\cos\alpha \\ 0 & -\cos\alpha & \sin\alpha \end{bmatrix}_{b\to w} \tag{2.51}$$

where the angle of sideslip β and the angle of attack α are formally defined as the angle between the plane of symmetry and the direction of motion of the vehicle, and the angle between the wing aerodynamic chord and the relative air flow, respectively.

2.7 Aerodynamic Heating

Finding a successful means of maintaining the aerodynamic heating rate within acceptable limits is one of the most important drivers in the design of hypersonic vehicles (12). It is of paramount importance thus to have an accurate and time-efficient means of predicting the thermal environment to which the vehicle will be exposed along its operational trajectory. Indeed, the aero-thermal loads acting on hypersonic vehicles are used to define the overall performance requirements for various subsystems such as the Thermal Protection System (TPS) and, where appropriate, the propulsion system. In fact, mis-prediction of the aero-thermal heating environment may quite importantly impinge on the overall survivability of a given design, whereas excessive conservatism in the analyses could result in an overweight vehicle not capable of attaining orbit with a useful payload mass on board. Furthermore, it shall be remarked that for entry velocities below 9 km/s, radiative heating effects from the high temperature gas that surrounds the vehicle can often be considered negligible. Hence they are not included in the current evaluation of the overall heat transfer rates acting on space-access vehicles returning from a payload delivery mission in Low Earth Orbit (LEO). Finally,

the effects of chemistry are not accounted for in the current implementation, recognizing however that these might reduce thermal loads by as much as 20 %; e.g. see Ref. (58).

2.7.1 Acreage Heating

The HyFlow model evaluates the acreage heating based on the flat plate reference temperature method as described in section 2.4.3 for evaluating the skin friction. It then uses the well-known Reynolds analogy, taking advantage of the similarity between friction and heat transfer mechanisms, in order to estimate the non-dimensional Stanton number, denoted St_i, which corresponds to the ratio of heat transferred into a fluid to the fluid's heat capacity. The Reynolds analogy has often been used in preliminary design studies as a "*powerful tool when simple estimates of convective heat transfer rates are required*," (35) and is simply defined as

$$St_i = \frac{1}{2}\, C_{f,i}\, F_{RA} \tag{2.52}$$

In Eq. 2.52, F_{RA} is the Reynolds analogy factor which is empirically set equal to $Pr_i^{*-2/3}$ for laminar flows and 1.22 for turbulent flows (45), and Pr_i^* is a local reference Prandtl number (evaluated at the reference temperature of the boundary layer) which can either be approximated as (59)

$$Pr_i^* \approx \left[\left(\frac{T_{awi}}{T_{edge_i}} - 1\right) + \left(\frac{2}{(\gamma-1){M_{edge_i}}^2}\right)\right]^2 \tag{2.53}$$

or its value may be interpolated as a function of the edge pressure p_{edge_i} and reference temperature T_i^* using the simplified transport properties of high-temperature air provided by Hansen (60). Additionally, the local Prandtl number can also be considered fixed under the assumption of a frozen flow (i.e. where $Pr_i^* \approx 0.72$ for air). Consequently, the local convective heating rate, denoted $\dot{q}_{conv}$, can be obtained from the skin friction estimates and the chemical enthalpy difference between an adiabatic wall enthalpy and the actual wall enthalpy as

$$\dot{q}_{conv,i} = \rho_i^* V_{edge_i} St_i\, (H_{awi} - H_w) \tag{2.54}$$

where H_w is the enthalpy of the fluid at the wall and H_{awi} is the adiabatic wall enthalpy. For engineering purposes, the local adiabatic wall enthalpy, also known as the boundary layer recovery enthalpy, can be computed as

$$H_{awi} = h_{edge,i} + \frac{1}{2}\, R_f\, V_{edge,i}^2 \tag{2.55}$$

where h_{edge_i} is the local edge enthalpy (i.e. $h_{edge_i} = C_{p,\infty} T_{edge_i}$). The recovery enthalpy is such that $H_{awi} \gg H_w$, i.e. the so-called cold wall approximation. Finally, the wall enthalpy can be estimated as

$$H_w = C_{p,\infty}\, T_w \tag{2.56}$$

where $C_{p,\infty}$, assumed constant equal to 1.0045 kJ/(kg.K) in this instance is the specific heat of air at constant pressure evaluated at the conditions of the free-stream flow.

2.7.2 Stagnation Heating Method

Since the method based on the Reynolds analogy and the underlying streamline tracing algorithm is inherently invalid at the stagnation features within the flow, a mix of methods must be employed. HyFlow uses a modified version of the Fay-Riddell formula to calculate the convective heating rate for general three-dimensional stagnation points. The method is described in detail by Hamilton *et al.* (61). For an asymmetric three-dimensional stagnation point, the convective heating rates are appreciably influenced by the principal velocity gradients in both the streamwise and crosswise directions. The ratio of the crosswise velocity gradient to the streamwise velocity gradient is equivalent to the ratio of the two principal radii of curvature at the stagnation feature. Therefore, the heat flux at a general three-dimensional stagnation feature, for a wall which is cold relative to the flow (which is usually the case for hypersonic re-entry) is related to the heating rate at an axisymmetric point by

$$\dot{q}_{stag} = \sqrt{\frac{1+k}{2}}\dot{q}_{axi} \tag{2.57}$$

where the parameter k is the ratio of the principal radii of curvature of the vehicle surface at the location of the stagnation feature, estimated using the algorithm

of Cohen-Steiner *et al.* (64) (so that $k = R_1/R_2$ where $R_2 \geq R_1$), and $\dot{q}_{axi}$ is given by the well-known Fay-Riddell formula (62) as

$$\dot{q}_{axi} = 0.76 {Pr^*}^{-0.6} \times (\rho_{edge_i} \mu_{edge_i}) \times (\rho_w \mu_w) \times \sqrt{\left(\frac{dV_{edge}}{dx}\right)_i} \times (H_{awi} - H_w) \times K_c \tag{2.58}$$

where the term K_c, which accounts for the contribution of chemical reactions, is a function of the Lewis number and is approximately equal to unity for binary mixtures such as air and therefore can be neglected in preliminary analyses (i.e. the real gas effects are here neglected). Finally, the velocity gradient in Eq. 2.58, which describes the rate at which the velocity at the outer edge of the boundary layer increases along the surface away from the stagnation point, can be derived from the Newtonian flow theory as proposed by Hamilton *et al.* (61) and is given by

$$\left(\frac{dV_{edge}}{dx}\right)_i = \frac{1}{R_i} \times \sqrt{\frac{2(p_{edge_i} - p_\infty)}{\rho_{edge_i}}} \tag{2.59}$$

where the principal radius of curvature at the nose, denoted R_i, is conservatively defined in HyFlow as

$$R_i = \min(R_1, R_2) \tag{2.60}$$

Therefore, the use of the two terms $\sqrt{\frac{1+k}{2}}$ and $\left(\frac{dV_{edge}}{dx}\right)$, in Eq. 2.57 and Eq. 2.58 respectively, yields an effective velocity gradient which represents the average of the two principal velocity gradients.

Leading Edges

For an attachment line at the leading edges of the wings, Eq. 2.57 is substituted by Eq. 2.61 below to account for the reduction in heat transfer as a result of sweep.

$$\dot{q}_{LE} = \dot{q}_{cyl} \cos \Lambda^2 \tag{2.61}$$

where Λ is the sweep angle of the wings, $\dot{q}_{LE}$ is the heat flux at the leading edges of the wings and $\dot{q}_{cyl}$ is the value of heat transfer computed with the help of

an empirical formula for a long swept cylinder suggested by Bowcutt (63) and defined as

$$\dot{q}_{cyl} = 0.57 Pr^{*-0.6} \times (\rho_{edge_i} \mu_{edge_i})^{0.5} \times \sqrt{\left(\frac{dV_{edge}}{dx}\right)_i} \times (H_{awi} - H_w) \qquad (2.62)$$

Radii of Curvature

The estimates of the principal radii of curvature, evaluated by the algorithm of Cohen-Steiner *et al.* (64) for each vertex of the tessellated mesh, are greatly influenced by both the mesh quality (i.e. by the oblateness level in spheroidal sections) and the heterogeneous density of panels over the tessellation – i.e. the local mesh density (at a vertex point) may simply be measured as the number of triangles located in the close vicinity of a given vertex.

Therefore, an auxiliary method, adopting a more reliable two-step semi-automatic approach, has also been added to HyFlow: first, the stagnation points over fusiform parts of a geometry (e.g. fuselage, engine pods) are determined based on the Newtonian condition given by Eq. 2.24. Then, for each of the stagnation points, a simple ellipsoid is iteratively fitted, in a least-squares sense, to the location of these points given a sufficient number of adjacent triangles is provided – i.e. an ellipsoid is used instead of a bi-cubic surface in order to directly approximate the principal radii of curvature. If instead, the geometry contains sections where the stagnation features introduce an attachment line, such as over the leading edge of the wings and fins, the panels that lie in these regions are first identified (i.e. panels with small value of mean adjacent angles). Thereafter, a number of cross-sections in the longitudinal direction (at an arbitrary number of stations along the transversal direction) are computed and a simple ellipse is then iteratively fitted (again, in a least-squares sense). The radius of curvature of the leading edge (assigned to all its constituting panels) is then simply assumed to be the averaged value of the minor radius of the resultant ellipses (or the smallest radius if a more conservative aerodynamic heating analysis is required). Although the method may appear cumbersome at first, it is however, in practice, relatively accurate and efficient. Furthermore, this pre-processing task need to be performed only once (for a range of angle of attack) and the results then stored along with the geometry file. The result of such a process is shown in Fig. 2.21 for the blunted nose of the Space Shuttle Orbiter.

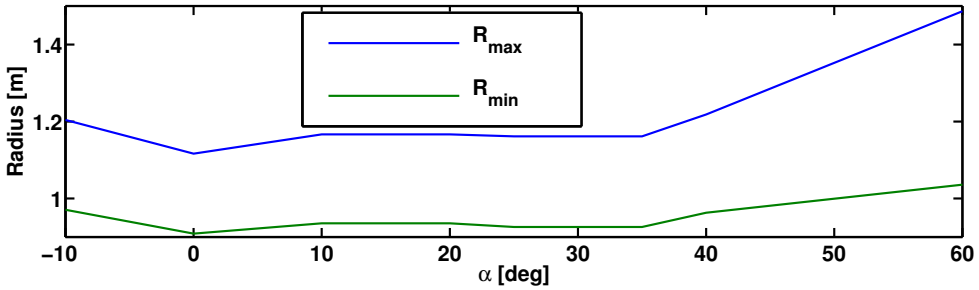

Figure 2.21: Variation of the Shuttle Orbiter nose radii with respect to the angle of attack - After identification of the Newtonian stagnation point(s) in the prescribed range of angle of attack, an ellipsoid is fitted using a sufficient number of neighbours to obtain an estimation of the radii of curvature.

2.7.3 Heating Method Integration

Since HyFlow employs two different methods for the computation of the convective aerodynamic heating transferred from the fluid to the wall of the vehicle and since the validity of the Reynolds analogy in the vicinity of the stagnation point can be called into question, the continuity between the stagnation and acreage heating methods must be ensured. As in CBAERO (21, 22), the continuity between the methods embedded within HyFlow is enforced by equating, at each of the stagnation panels, the value of the stagnation heating, here denoted $\dot{q}_{stag}$, computed via the modified Fay-Riddell formula of Eq. 2.57 (and assumed known) and the flat plate acreage heating model, $\dot{q}_{RA}|_{S_0}$, set as a function of a virtual running length S_0 as

$$\dot{q}_{stag} = \dot{q}_{RA}|_{S_0} \tag{2.63}$$

HyFlow then solves for S_0 which corresponds to the running length which would be required by the Reynolds analogy method to return the value of heat flux computed by the stagnation heating method. Nonetheless, as opposed to CBAERO where this running length is then used to offset the streamlines, in HyFlow, S_0 is instead used to define a small spherical region of influence surrounding the stagnation point in question (called stagnation zone in HyFlow's formalism) throughout which the Reynolds analogy method is considered not applicable. Indeed, the logic within Eq. 2.63, illustrated in Fig. 2.22, is required to determine a distance away from the stagnation point from which the Reynolds analogy method becomes applicable.

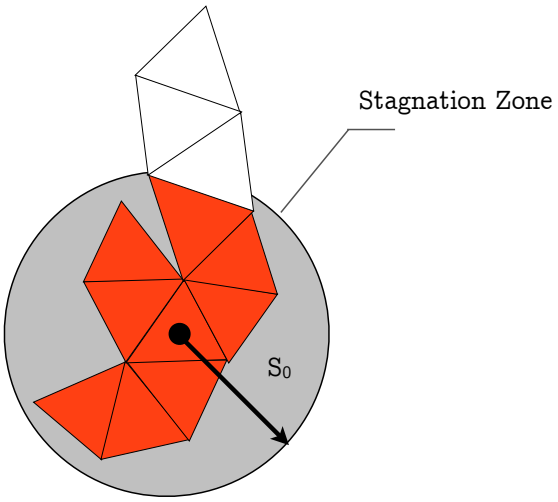

Figure 2.22: Stagnation region of influence - In HyFlow, a stagnation region of influence is defined by the minimum running length, denoted S_0, from which the Reynolds analogy method becomes applicable. All the triangles that belong to the stagnation region have their heat transfer rate value set to the stagnation heating rate value.

2.7.4 Rarefied Flows

Although the peak heating rates usually occur at lower altitudes within the continuum range (e.g. around 80 km for the CFASTT-1 vehicle), it is important to accurately characterise the aero-thermal environment of future re-usable space transportation systems when immersed in rarefied flows in order to correctly estimate the total heat load to which the vehicle is subjected. The approach used to compute the heat transfer to the surface of the vehicle via the Reynolds analogy is valid only where the slip velocities on the surface of the vehicle are negligible, in other words under conditions that are close to continuum, but can be called into question when the Knudsen number characterizing the flow over the vehicle becomes large. Similarly, as stated by Wang *et al.* (65), the Fay-Riddell formula, defined in Eq. 2.58 and used to evaluate the heating rates at the stagnation feature(s) within the flow, is dependent on the flow state at the edge of the boundary layer defined in Section 2.4.2. Therefore, the existence of an inviscid flow field is a pre-requisite to applying the Fay-Riddell equation. However, as the flow becomes more and more rarefied, viscous interactions start to predominate as a consequence of a growing boundary layer which eventually merges with

the shock layer causing the external inviscid flow field to simply disappear and the Fay-Riddell formula to become inapplicable (method breakdown). Therefore, for the transitional regime, the simple bridging technique of Eq. 2.14, which ensures continuity in the calculations of the aerodynamic heating throughout the transitional regime, is used in HyFlow in order to obtain an estimation of the transitional aero-thermal convective heating as (35)

$$\dot{q}_{trans} = \frac{\dot{q}_{cont} + K_n \dot{q}_{fm}}{1 + K_n} \tag{2.64}$$

where the free-molecular convective heating, denoted $\dot{q}_{fm}$ and derived by Probstein *et al.* (28), is given by

$$\dot{q}_{fm} = a_e p_\infty \sqrt{\frac{RT_\infty}{2\pi}} \times [\left(\sigma_S^2 + \frac{\gamma}{\gamma - 1} - \frac{\gamma + 1}{2(\gamma - 1)} \times \frac{T_w}{T_\infty}\right) \times \exp(-K_S^2) + \sqrt{\pi} K_S \times [1 + \mathrm{erf}(K_S)] - 0.5 \times \exp(-K_S^2)] \tag{2.65}$$

where a_e is the thermal accommodation coefficient and represents a measure of the extent to which the mean energy of those molecules impinging on the wall, which are then re-emitted, is accommodated to the temperature of the wall. Indeed, from a molecular point of view, wall surfaces are not smooth but instead include some asperities and imperfections (i.e. surfaces are microscopically rough). Therefore, the molecules that impinge on the wall of the vehicle are likely to be temporarily trapped by the surface before being re-emitted. The energy transferred to the wall thus becomes approximately equal to the reflected energy (28). In HyFlow, the value of a_e is thus set to unity in order to define a more realistic diffusive boundary condition.

2.8 Discussion

Although the accuracy of the current model will be demonstrated in more detail in Chapter 3, some important phenomena may require more detailed consideration in future in order to enhance the predictions of the HyFlow code for the type of complex configurations discussed within the present dissertation.

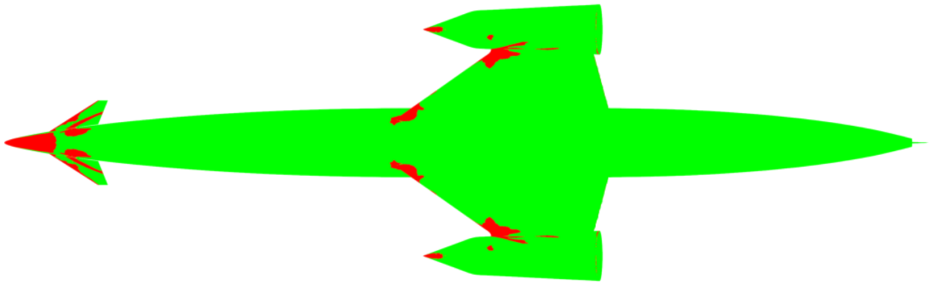

Figure 2.23: Shock-shock interaction regions over the Skylon vehicle - The regions over the windward surface of the Skylon vehicle, where the surface temperature is locally above $1,400\ K$, are shown in red (for conditions at Mach 25 and 43 degrees angle of attack) (66). The regions of particular interest are those where shock-shock interactions take place. It can clearly be noticed that, apart from the stagnation regions, only the junction between the engine nacelle and the wing, and the region of the gap between the canards and the forward fuselage, where shock impingements have occurred, present a local increase in aerodynamic heating as a result of shock-shock interactions.

Shock/Shock Interactions

In its current form, one of the crucial limitations of the model remains the lack of information about the flow field that surrounds the vehicle and therefore the lack of awareness about eventual shock interferences. Indeed, the effect of the shock, that originates from the engine pods for instance, on the leading edge of the wing remains, for now, a feature of more advanced methods such as those aforementioned CFD and DSMC numerical methods. In their numerical studies of the Skylon vehicle, partially reproduced here in Fig. 2.23, Eggers *et al.* (66) have shown that an increase of the wing leading edge temperature can be observed in the region which is directly affected by the shock produced ahead of the engine nacelle. NASA's X-15-2 flight experiment represents, in fact, the first experience with extensive structural damage (on a hypersonic configuration) as a consequence of shock impingement. Indeed, during the second flight test of the X-15, a dummy hypersonic ramjet engine was mounted on a pylon at the rear end of the vehicle's fuselage. In flight, the shock wave produced by the vehicle impinged on the pylon structure creating a zone of intense heating (67). In the reference paper, it has been reported that the level of aerodynamic heating was five to ten times greater than the nominal (undisturbed) level. The problem of shock interaction is therefore a significant one as it leads to an important increase

of local temperature, and is of major concern from preliminary studies as it can have a direct influence on the design of the vehicle's subsystems (e.g. the thermal shield or even the configuration geometry for instance). Simple geometrical methods, based on empirical models such as those overviewed in the book of Anderson, may potentially be used to derive a method to detect shock interferences at an engineering level (more particularly for level flight and flights at relatively small angle of attack) (16). Nonetheless, a much more complex analytical method derived from first principles may have to be devised for when the vehicle operates at an angle of attack.

Real-Gas Effects

In the current model, a thermally and calorically ideal gas is assumed whereas such a simple gas model may lead to discrepancies and over-estimation of the aero-thermal loads acting on hypersonic vehicles operating at very high speeds (see comments in Section 2.1). Nevertheless, it would be straightforward to either connect a solver for air in chemical equilibrium to HyFlow – such as the open-access CEA code of McBride (68) – or use a series of simplified curve-fits such as those of Tannehill and Srinivasan (69) for equilibrium air in conjunction with the procedure outlined by DeJarnette *et al.* (41) where the conservation equation for mass, momentum and energy across a normal shock wave (shown below) are solved iteratively for equilibrium air properties in order to obtain the stagnation properties aft of the normal shock-wave under an equilibrium air assumption as

$$\rho_\infty V_\infty = \rho_2 V_2 \tag{2.66}$$

$$P_\infty + \rho_\infty V_\infty^2 = P_2 + \rho_\infty V_\infty V_2 \tag{2.67}$$

$$H_s = h_\infty + \frac{V_\infty^2}{2} = h_2 + \frac{V_2^2}{2} \tag{2.68}$$

In that process, as suggested by DeJarnette, V_2 is first set to 0 m/s. Then, P_2 is solved for using Eq. 2.67. Thereafter, the value of V_2 is substituted in Eq. 2.68 to obtain h_2. Afterwards, the values of P_2 and h_2 are used in conjunction with the aforementioned simplified curve-fits for equilibrium air to evaluate the value of ρ_2 to be inserted into Eq. 2.66 in order to derive a new estimate of V_2. Finally the

process is repeated until convergence of the value of V_2 (about six iterations are required for an accuracy of the order of 10^{-5}) and P_2, h_2 and H_s are then used to compute the stagnation pressure, denoted P_s, and the stagnation density, noted ρ_s, from the previous curve-fits. Thereafter, the composition can be considered frozen and the usual isentropic equations for thermally and calorically perfect gas may be used as first approximations (those currently implemented in HyFlow) to better define the conditions at the edge of the boundary layer and account for real-gas effects without increasing significantly the computational time.

Leeward side

Finally, the computation of the pressure and heat transfer estimates as well as the streamlines in the region on the leeward side of the vehicle (the so-called "shadowed" region) may require more attention. Indeed, the flow in that particular region of the flow field might separate from the surface somewhere within it, and therefore the current streamlines that follow the geodesics of the tessellation may not fully represent these physical phenomena. Therefore, the level of accuracy provided by HyFlow in that particular region of the flow field may have to be questioned and possibly improved. Nonetheless, it is believed that the effect of eventual mis-predictions of the aerodynamics on the leeward side of the vehicle is overall quite benign.

2.9 Chapter Summary

In this chapter, a reduced-order model, used to quantify the aero-thermal environment of complex hypersonic configuration from free-molecular flow conditions at very high altitude down to the regions where the flow behaves as a continuum, has been introduced. The power of reduced order modelling, that motivated the development of HyFlow, lies in its capacity to perform fast studies in order to assess the effect of varying certain key parameters on the aero-thermodynamic behaviour of the vehicle system.

In the remainder of the thesis, it will be shown that a reduced-order model such as HyFlow can provide valuable information in the study of hypersonic vehicle configurations. Indeed, if used with care and within the limits of their applicability, reduced-order models of the type described in this chapter can yield

valuable insight into both the quantitative and qualitative aspects of the aero-thermodynamic loading on complex hypersonic configurations, as well as, by inference, form the basis of a viable computational strategy for the Multi-disciplinary Design and Optimization (MDO) of such vehicles.

Nomenclature

List of Symbols

A	Panel area
a	Speed of sound
a_e	Thermal accommodation coefficient
C	Unit axis rotation
C_f	Skin friction coefficient
C_p	Pressure coefficient
$C_{p,\infty}$	Specific heat capacity at constant pressure
D	Drag force
d_{air}	Effective diameter of the dry air particles
$\hat{F}$	Aerodynamic force
f_1, f_2	Compressibility factors
f_n, f_n	Normal and tangential momentum coefficients
F_{RA}	Reynolds analogy factor
H	Enthalpy
K_g	Mangler transformation parameter
k_B	Boltzmann constant
k_R	Roughness parameter
Kn	Knudsen number
L	Lift Force
M	Mach number
$\hat{M}$	Aerodynamic Moment
M_n	Mach number normal to the shock wave
$\hat{n}$	Local unit panel normal
n_s	Number of segments along a streamline
P	Pressure
P_B	Bridging function
Pr	Prandtl number
Q	Dynamic pressure
$\dot{q}$	Heat transfer rate
R	Individual gas constant
R_1, R_2	Principal radii of curvature
Re	Reynolds number
R_f	Temperature recovery factor
R_v	Visibility fraction per panel
S	Side Force
$\hat{S}$	Unit vector in the direction of the shear force
S_0	Virtual running length
St	Stanton number
T	Temperature
V	Velocity

$\vec{V}_{stream}$	Streamline velocity field
x	Running length along a streamline
$\hat{x}_c$	Coordinates of the centre of mass
α	Angle of attack
β	Sideslip angle
β_w	Shock wave angle
γ	Ratio of specific heats
θ	Deflection angle
Λ	Sweep angle of the wings
μ	Viscosity
ρ	Density
σ_s	Speed ratio
τ	Shear stress
ϕ	Inclination angle
ϕ_{wedge}	Apex half-angle of a turbulent wedge

Subscripts & Superscripts

0	Total Condition
2	Condition behind the shock
aw	Adiabatic wall condition
axi	Axisymmetric condition
b	Body reference frame
$cont$	Continuum regime
$conv$	Convective heat transfer
cyl	Long infinite cylinder condition
$edge$	Boundary layer edge condition
fm	Free-molecular regime
kr	Condition at the element of surface roughness
l	Local condition
lam	Laminar condition
max	Maximum
ref	Reference parameter
$stag$	Stagnation condition
t	Transition
$trans$	Transitional regime
$turb$	Turbulent condition
w	Wall condition or Wind reference frame
∞	Freestream condition
$*$	Reference condition

Chapter 3

Validation of the Aero-Thermodynamic Model

Building upon the comments made in Section 2.8 of Chapter 2, it appears prudent at this stage of the models development to revisit the assumption that the miscellaneous engineering models embedded within the HyFlow code, thoroughly described in the previous chapter, will remain valid and robust when used for the preliminary design and optimization of future hypersonic vehicles. This is particularly the case given the geometric complexity that is associated with some of the more advanced lifting body concepts that have been proposed as the foundation of a number of future space-access vehicles. Therefore, in Section 3.2, a hypersonic ballistic shape is used to validate HyFlow with a mix of experimental and numerical results. In Section 3.3, a slightly blunted nose cone geometry, known as the Re-entry F flight experiment, is used to validate HyFlow for transitional heat transfer conditions over a nearly-sharp body. Finally, some of the flight and wind tunnel data from the Space Shuttle programme are used to further validate HyFlow for a space plane-like shape in Section 3.4, while preliminary conclusions are given in Section 3.5.

3.1 Introduction

The present chapter introduces a series of validation cases encompassing various types of geometry - a combination of blunt, slender, and complex, winged, configurations - that exhibit some of the characteristic features of the hypersonic flows

that will be encountered by future space transportation systems. Throughout these test cases, miscellaneous flow conditions, spanning from the low hypersonic/supersonic regime to conditions representative of atmospheric entry are investigated using a mix of Computational Fluid Dynamics (CFD) as well as experimental and flight data whenever those are available. Nonetheless, while assessing the simplifications and assumptions inherent in the methodology embedded within such reduced-order models, it should be borne clearly in mind that the purpose of the present aero-thermodynamic model is to be used in the framework of robust optimisation, in order to examine the effect of parametric variations in the results of the conceptual design of future fully re-usable space-access vehicles. Indeed, it is important to realize that, in the context of Multi-disciplinary Design and Optimisation (MDO), the purpose of a reduced-order model is not necessarily to reproduce, to the last word in fidelity, the predictions of the more sophisticated models for which it is intended to be a surrogate. Instead, the purpose of the model is simply to rapidly yield results that are representative enough, or that embody the predictions of the more sophisticated techniques to high enough fidelity, so that the optimization process is led efficiently into the same basin of attraction within the configurational space of the system as to which the use of the more sophisticated computational techniques would lead. Indeed, the HyFlow model is required to provide only the predictive accuracy suitable for preliminary design. In this way, the more sophisticated (but computationally expensive) methods can then be relied upon in the final stages of the optimization process to further refine the search for the optimum (7).

In the validation of the aero-thermodynamic model, three different configuration geometries have therefore been considered. In Section 3.2, HyFlow is first validated against both experimental and Computational Fluid Dynamics (CFD) data for a rocket-like hypersonic configuration shape, dubbed HB-2 (Hypersonic-Ballistic shape). The HB-2 configuration, also known as the blunted-cone-cylinder-flare, was designed in 1960 as a hyper-velocity ballistic correlation model by the Supersonic Tunnel Association (STA). The HB-2 geometry is a configuration that, in the past, has attracted much interest within the hypersonic research community – see, for instance, the reference studies of Gilchrist (70), Jones (71) and Gray (72). It is therefore the well documented nature of the HB-2 geometry along with its fusiform shape (i.e. fuselage) that makes it an ideal first test case for the validation of the reduced-order aero-thermodynamic code. In fact, the hypersonic flow field around the HB-2 geometry possibly unveils some

of the major features of the flows around future space-access configurations such as the strong detached shock forming ahead of the vehicle and the oblique shock-wave/boundary layer interaction at the junction between the cylinder and the rear flare (as it will be discussed in great detail in Section 3.2) – i.e. the latter characteristic could perhaps resemble the aerodynamics of control surfaces in their deflected attitude (73).

Thereafter, the flight data of the Re-entry F configuration geometry, an experiment conducted by NASA in 1968 to study the level of aerodynamic heating in a turbulent environment, is used herein in order to provide an additional validation case for a nearly sharp geometry operating at hypersonic velocities (presented in Section 3.3). Indeed, the aerodynamics of the Re-entry F geometry resembles quite closely those of the inlet of future air-breathing engines that are foreseen to be employed by the next generation of space-access vehicles (e.g. the SABRE engine of the Skylon SSTO vehicle). Furthermore, the accuracy of the transitional model, embedded in HyFlow to simulate the boundary layer transition from a laminar state to turbulence, for those surfaces that are smooth, is investigated. This particular flow phenomenon may indeed have dramatic effects on the level of aerodynamic heating experienced by space-access vehicles in real flight conditions – consequences that might have to be dealt with during preliminary design studies from the optimisation of their performance to the scheduling of their control surface deflections (13).

Then, the ability of the reduced-order model to robustly simulate the complicated flow around a historical space-access configuration (with protrusions, wings and control surfaces), namely the American Space Transportation System (STS), will be assessed in Section 3.4 using some of the flight and wind tunnel data from its various missions and experimental work as available. The STS represents indeed the only configuration, close to those of the future generation of space transportation systems, for which an extensive amount of flight and experimental data can openly be accessed in the literature, and as such represents an excellent test case on which to compare the results provided by the reduced-order aero-thermodynamic code. Finally, all these miscellaneous validation cases may give us a grasp of the level of accuracy that can be expected from a reduced-order model such as the HyFlow code, even more so when used to evaluate the aero-thermodynamic environment of future complex space transportation system configurations. Indeed, these various test cases should provide enough confidence

Case	1	2	3
Mach Number [-]	9.59	17.8	5
Pressure [Pa]	75	29.5	3748
Temperature [K]	52	287	138.9
Angle of Attack [deg]	0-15	0	0

Table 3.1: HB-2 simulation conditions - Free-stream flow conditions for the HB-2 configuration.

in the capacity of HyFlow to be relied upon in preliminary design studies. The integration of the HyFlow code within a dedicated robust multi-disciplinary design platform will, in fact, be demonstrated in the second part of the thesis.

3.2 HB-2 Configuration

The various flow conditions considered in this validation work for the HB-2 configuration are listed in Table 3.1. Experimental data are used whenever available in the open literature. Additionally, the numerical results of a study carried out by Tissera, Drikakis and Birch are also used to provide additional means of comparison, where appropriate (74). It should also be noted that a small modification to the original shape of the HB-2 is used here. Indeed, the original slightly curved transition section from the cylinder to the rear flare was not included in the mesh used within the HyFlow environment (see region circled in red in Fig. 3.1) and may partially explain some of the discrepancies observed between the predictions of HyFlow and the results from both the CFD and the experiment in that particular region of the flow field.

3.2.1 Case 1

The first test case selected for the validation of the aero-thermodynamic model corresponds to an HB-2 configuration geometry at zero degrees angle of attack and immersed within a Mach 9.59 hypersonic flow (the free-stream conditions are presented in Table 3.1). The experimental data used in this first validation case are taken from the work of Kuchi-ishi *et al.* (75) conducted within the Japan Aerospace Exploration Agency (JAXA) test facilities. For present purposes however, a CFD simulation, using the open-source OpenFOAM CFD suite, has also

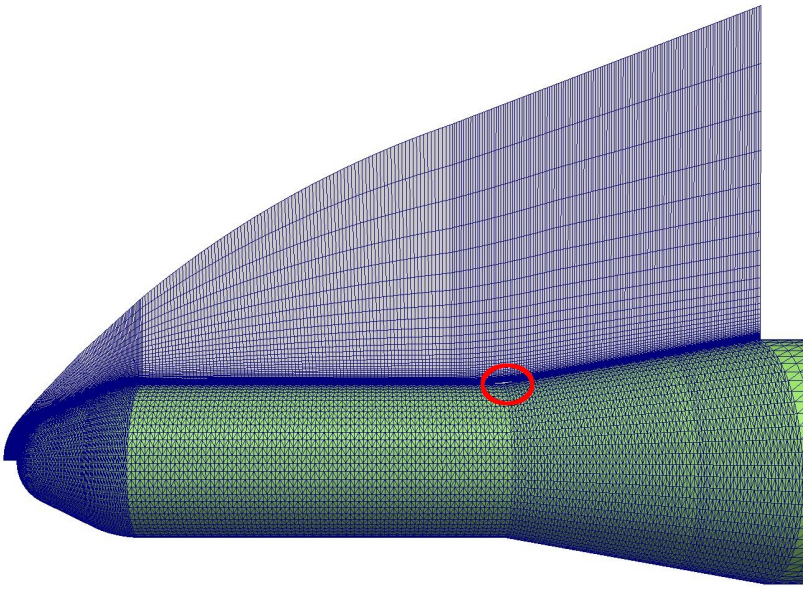

Figure 3.1: HB-2 CFD mesh - The structured mesh of the HB-2 vehicle, used in the CFD simulation with OpenFOAM, is shown. A common grid clustered near the wall of the HB-2 geometry can also be seen. Additionally, the surface mesh (in green) used in HyFlow is presented. Finally, the location of the small modification to the HB-2 mesh, at the junction between the cylinder and the rear flare, has also been marked (red circle).

been used in conjunction with both the experimental and the reference CFD results in order to waive the unavailability of data, in the literature, with reference to the wall pressure. In fact, the OpenFOAM software package has been extended and developed to contain a number of algorithms that are appropriate to the modelling of high-velocity flows (76). In doing so, the rhoCentralFoam solver of Greenshields *et al.* (77) has been upgraded to create a new solver, dubbed "rhoFoam", in which a flux scheme based on the full Riemann solver, using the Godunov approach for the first order approximation and the Weighted-Average-States (WAS) approach for the second order approximation to the flow states, has been implemented to more accurately model the complexities in terms of fluid dynamics that are inherent to hypersonic flows.

3.2.1.1 Numerical Results

Based on the length of the HB-2 configuration ($L_{HB2} = 0.49$ m) and the free-stream conditions of this first validation case, the free-stream Reynolds number is

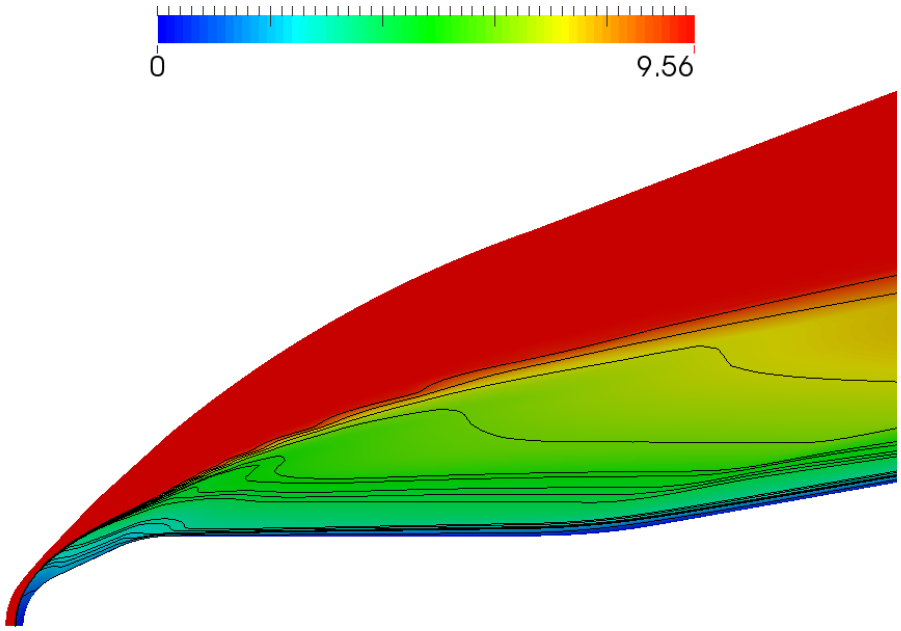

Figure 3.2: CFD mach contours for the HB-2 case 1 - Mach number contours over the fully structured fine mesh as returned by rhoFoam.

equal to $Re_\infty = 1.03 \times 10^6$. The simulation has been run assuming fully laminar flow – which is also consistent with the reference CFD study (74). Additionally, the numerical simulation assumes a constant wall temperature which was fixed to the value of 300 K to match the reference experiment – providing estimates to the cold wall convective heat flux. The computational mesh used for the CFD simulation using rhoFoam, shown in Fig. 3.1, is a two-dimensional axi-symmetric mesh composed of $550,800$ cells and fully structured with a typical cluster of cells at the wall in order to refine the estimates in the boundary layer region. Indeed, such a cluster of cells provides the best resolution in the most critical region of the flow field, where in particular high temperatures as well as high velocity gradients must be considered. Both the Mach contours and pressure distribution, shown in Figs. 3.2 and 3.3, provide an insight into the nature of the flow field that surrounds the HB-2 configuration when immersed in the flow conditions of this first test case. As can be seen, a strong shock forms upstream of the configuration while a secondary (weaker) shock is also noticeable near the location where the cylinder transitions into the flare region. Therefore, the pre-dominant features of the flow surrounding the HB-2, such as the detached bow shock wave upstream of the nose section and the shock wave/boundary layer interaction in the flare junction region, are properly resolved by the rhoFoam solver.

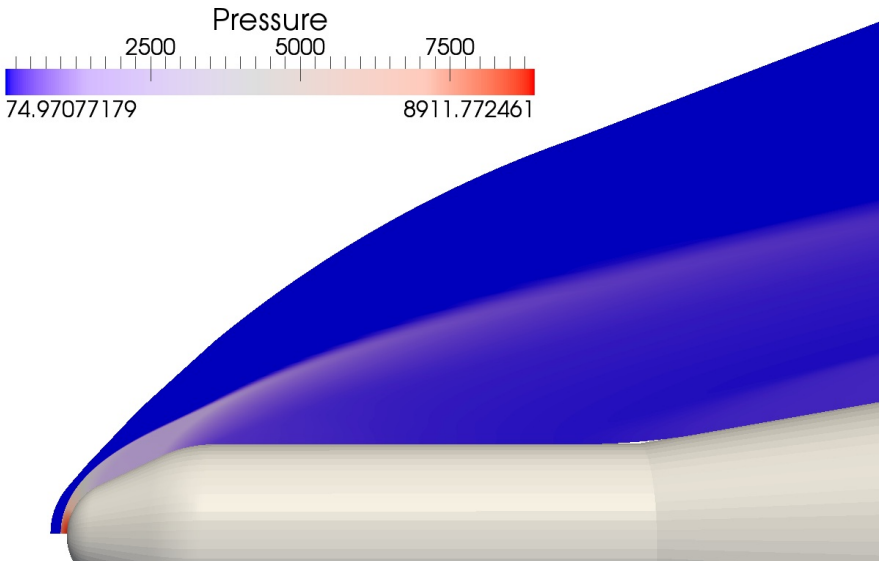

Figure 3.3: CFD pressure distribution for the HB-2 case 1 - Pressure distribution in Pascals over the fully structured fine mesh as returned by rhoFoam.

Mesh	Number of Cells
Coarse	34,425
Medium	137,700
Fine	550,800

Table 3.2: Mesh sensitivity analysis.

3.2.1.2 Mesh Sensitivity Analysis

A mesh sensitivity analysis has been carried out in order to study the influence of the mesh size on the results of the wall heat transfer rates provided by rhoFoam. The wall heat flux distribution obtained from the rhoFoam solver when used in conjunction with a coarse mesh, a medium mesh and a fine mesh (reference mesh), whose number of cells are shown in Table 3.2, has been compared to the reference experimental data in Fig. 3.4. Although the results of the three CFD simulations, in general, agree relatively well with the experimental results (when accounting for the experimental uncertainty – see error bars in Fig. 3.4), it should however be noted that the results given for all three meshes under-predict the nose stagnation heat flux value (see Fig. 3.5). In addition, the results from the coarse mesh also over-predict the level of heat flux at the conic rear-flare section of

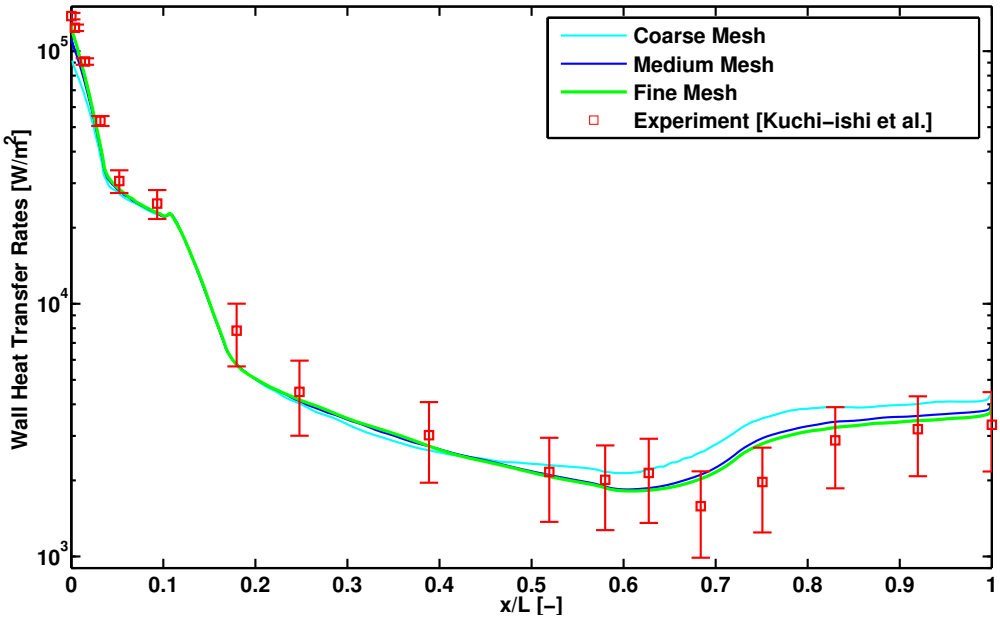

Figure 3.4: HB-2 mesh sensitivity analysis - Comparison of the wall heat flux profiles along the centreline of the HB-2 geometry as returned by rhoFoam when using a coarse (cyan curve), a medium (blue curve) and a fine (green curve) mesh. A logarithmic scale is used on the vertical axis.

the HB-2 configuration. Otherwise, a relatively good level of mesh independence is achieved even though a small difference, between the medium and the fine mesh, still subsists at the tip of the spherical nose section (see detailed nose plot in Fig. 3.5). From that point onward, only the results obtained using the most refined mesh will be considered in the remainder of this first validation case.

3.2.1.3 HyFlow Results

In HyFlow, considering the relatively high Mach number of the free-stream flow as well as the bluntness of the HB-2 geometry, the wall surface pressure is computed using the modified Newtonian theory method. The tessellation used in the present work is composed of $38,000$ panels homogeneously scattered over the surface of the geometry (i.e. relatively high resolution mesh) and is presented in Fig. 3.1 (in green). The detailed results in terms of wall pressure, boundary layer edge conditions and wall heat flux along the centreline of the HB-2 are introduced in the upcoming paragraphs.

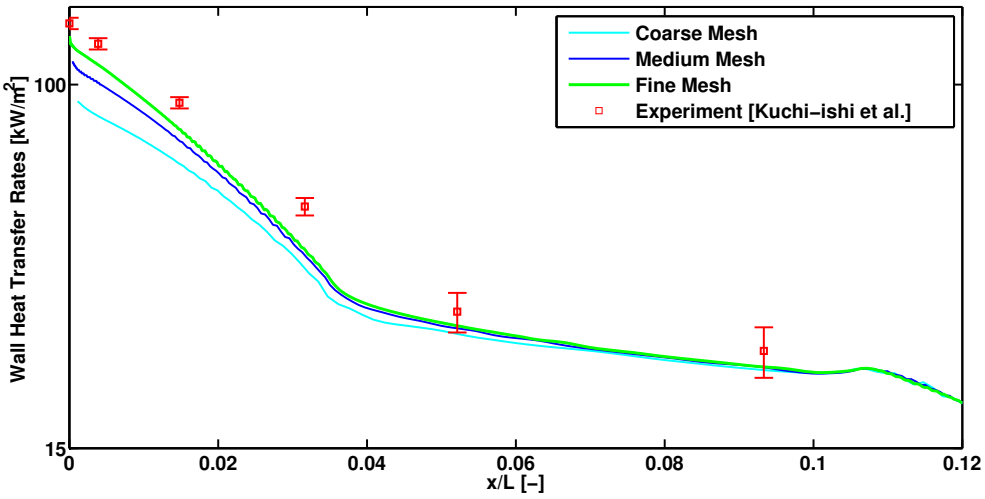

Figure 3.5: Detailed view of the mesh sensitivity analysis - Detailed comparison of the wall heat flux distribution over the blunted cone section of the HB-2 geometry as returned by rhoFoam when using a coarse (cyan curve), a medium (blue curve) and a fine (green curve) mesh. A logarithmic scale is used on the vertical axis.

Inviscid Pressure

The non-dimensional wall pressure along the centreline of the HB-2 geometry, obtained using HyFlow, are compared to those returned by the rhoFoam solver in Fig. 3.6 (i.e. the wall pressure is non-dimensionalized using the pressure at the stagnation point, denoted by P_S). From the figure in question, it appears that a very high pressure region is located at the stagnation point in the spherical nose section and is followed by a sudden drop along the subsequent conic region. HyFlow predicts a value of 8915.7 Pa at the stagnation point, while a value of 8672.1 Pa is estimated by the rhoFoam solver at the same location – which represents a very small over-estimation in the prediction of HyFlow equal to 2.8 % in that region. It should also be noticed that apart from the spherical nose where the pressure linearly decreases away from the stagnation point, a constant pressure level develops on the conic section until it transitions into the cylinder, where a constant pressure level also develops until the cylinder transitions into the flare region, and finally, a similar phenomenon occurs on the rear flare section. In fact, the Local Surface Inclination (LSI) methods embedded within the HyFlow model return identical values for all the panels that belong to a section with a constant slope. This first test case gives however confidence in the ability of

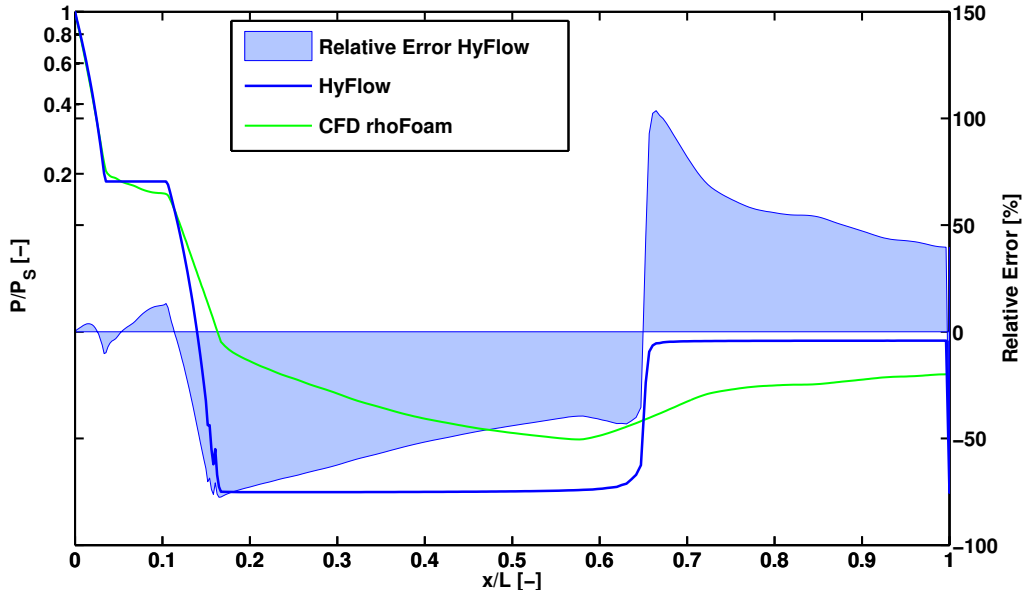

A logarithmic scale is used on the vertical axis (pressure ratio).

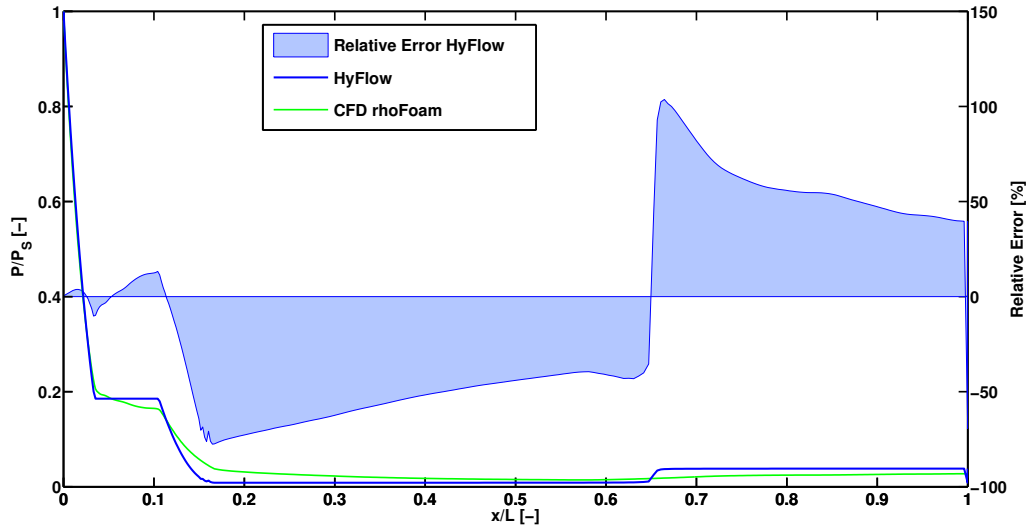

A linear scale is used on the vertical axis (pressure ratio).

Figure 3.6: Pressure profile along the centreline of the HB-2 for case 1 - Comparison of the non-dimensional pressure profiles along the centerline of the HB-2 geometry as obtained by HyFlow (blue curve) and CFD using the rhoFoam solver (green curve). Finally, the estimated continuous relative error between the results returned by HyFlow and those of the numerical simulation are also shown.

the reduced-order model to provide fairly good wall pressure estimates over the blunted cone section of the HB-2, when these are compared to the CFD results, as the two methods follow indeed the same trends in that particularly critical region of the flow field.

Nonetheless, HyFlow seems to over-estimate the wall pressure over the rear flare section of the geometry. Indeed, the relative error between the estimates from HyFlow and the CFD results (see Fig. 3.6) reduces significantly from the large value observed near the cylinder-flare junction to the end of the HB-2 geometry (partially due to the small mesh difference at the cylinder/flare junction). Recalling the inherently lower fidelity of HyFlow, it can however be concluded that this over-evaluation of the wall pressure provides a certain level of conservatism often necessary during conceptual design. This over-estimation seems however to result from the presence of the aforementioned secondary shock. Indeed, as extensively discussed in the summary and discussion section of the previous chapter, HyFlow does not provide any information about the flow field that surrounds the HB-2 configuration. Nevertheless, at the cylinder-flare junction, the interaction between the viscous boundary layer and the oblique shock wave on the flare dominates the flow field. This interaction is likely to have a non-negligible effect on the wall pressure estimates returned by the CFD solver and may explain the discrepancies, observed between the two approaches, in that particular region.

Furthermore, it can be seen that HyFlow underestimates the pressure values along the cylindrical section of the HB-2 geometry by up to 70 % at the exact location where the blunted cone transitions into the cylindrical region. The relative error reduces however down to 40-50 % at the junction between the cylindrical section and the flare. Indeed, the pressure distribution along the cylindrical section is mostly affected by the interactions between the boundary layer and the inviscid flow. In fact, the bow shock wave ahead of the HB-2 is progressively weakened as it departs from the stagnation region and thus the subsequent curvature of the bow shock produces an entropy layer where vorticity occurs. In other words, the viscous boundary layer thickens as it passes over the toroidal corner where the blunted cone transitions into the cylindrical section of the HB-2 geometry (and may even swallow part of the oncoming inviscid layer – i.e. entropy layer swallowing). The thickening of the boundary layer can thus be hypothesized as the main parameter causing the expansion to be deferred. In fact, after the expansion corner (where the blunt-nosed cone transitions into a cylinder), the pressure values returned by rhoFoam seem to be indeed slowly decaying towards

the free-stream pressure before the local change in geometry, due to the presence of the rear flare (and associated secondary shock), eventually rises again the pressure estimates. Moreover, it shall also be remarked that the cylindrical section of the HB-2 runs parallel to the free-stream flow ($\theta = 90$ degrees) and thus all of its panels have their pressure value set to the free-stream value of 75 Pa in HyFlow (recalling Eq. 2.18). This explains why the impact methods embedded in HyFlow instead transition quite abruptly whereas the rhoFoam solver gradually expands the flow around the toroidal corner.

Therefore, although the comparison between the results of HyFlow and rhoFoam indicates, thus far, a strong capacity for the reduced-order model to predict the pressure distribution on surfaces directly impacted by the oncoming hypersonic flow, some final remarks may be drawn nevertheless: the shadow region (i.e. here defined by the cylindrical region, as it is parallel to the oncoming flow direction) shows some, most probably benign, under-prediction as the pressure level in that particular region is relatively low. It should also be remarked that the miscellaneous peaks of over and under-estimation seem to coincide with the various transitions between the geometric primitives that compose the HB-2 configuration. In Hyflow, the pressure computed on a given panel does not incorporate any information regarding the pressure exerted on other panels located either upstream or downstream, and the pressure thus exhibits discrete jumps at the junctions between the various geometric primitives representing the vehicle geometry. This feature is also characteristic of CFD calculations in which the flow is assumed to be inviscid. Indeed, the smearing of the pressure distribution that is observed in reality, and that is properly represented only by the fully-viscous CFD calculations, is a well-known phenomenon associated with ability of information to propagate upstream through the subsonic near-wall region of the boundary layer.

Boundary Layer Edge Conditions

As suggested in the book of Bertin (17), the edge of the boundary layer can be determined from the results of the CFD simulation by identifying the location off-the-wall where the total enthalpy gradient goes to zero. The result of such a process is illustrated in Fig. 3.7 where the extent of the boundary layer region is plotted along the longitudinal axis of the HB-2 geometry. After post-processing the numerical results from rhoFoam using the open-source visualizer embedded

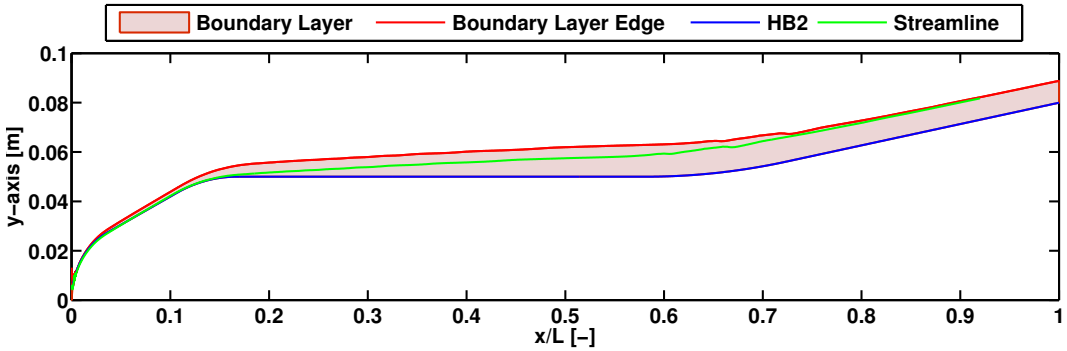

Figure 3.7: Boundary layer for the HB-2 case 1 - The thickness variation of the viscous boundary layer is illustrated over the length of the HB-2 geometry (light red zone). The path line followed by an inviscid streamline has also been depicted (green curve).

in OpenFOAM, dubbed Paraview, the physical properties at the edge of the boundary layer, namely temperature T_{edge}, density ρ_{edge} and velocity V_{edge}, can then be compared to the edge conditions resulting from the HyFlow reduced-order model in order to verify the validity of the simple (ideal gas) Normal Shock Isentropic Expansion (NS-IE) flow model, introduced in Section 2.4.2, for which the local edge conditions are obtained by simply expanding the flow from the normal shock stagnation point condition to the local pressure.

First, the laminar boundary-layer thickness, denoted δ_L, returned by HyFlow is compared to that given by the CFD simulation in Fig. 3.8. This information can indeed be used to trip a fully developed turbulent wedge when roughness-induced transition is considered as discussed in Chapter 6. As can be seen in Fig. 3.8, the boundary layer height is relatively well predicted by the reduced-order model along the centreline of the HB-2. Additionally, since δ_L is a function of the local running length used in the computation of the the skin friction coefficients, this preliminary result provides confidence in the ability of HyFlow to predict properly the viscous contribution to the overall aerodynamic loads.

Then, the comparisons of the temperature, density and velocity at the edge of the boundary layer given by HyFlow and those given by rhoFoam are presented in Figs. 3.9, 3.10 and 3.11, respectively. As a consequence of the under-prediction of the wall pressure estimates over the cylindrical region of the HB-2 geometry, the boundary layer edge conditions are also seen to be subsequently affected in that particular region. Indeed, the conditions at the edge of the boundary layer are

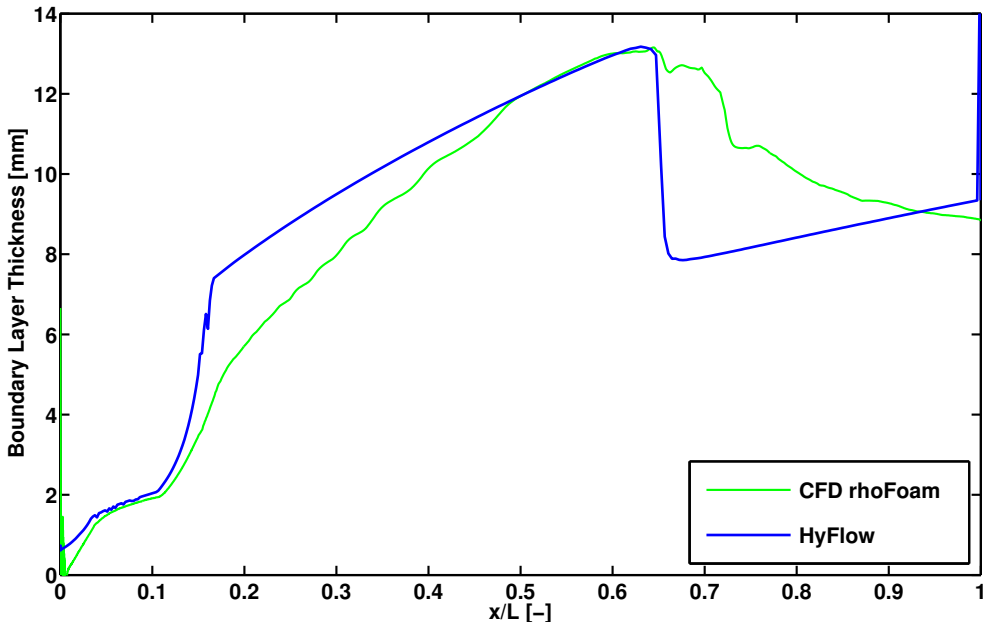

Figure 3.8: Boundary layer thickness for the HB-2 case 1 - Comparison of the laminar boundary-layer thickness along the centreline of the HB-2 geometry as obtained by HyFlow (blue curve) and rhoFoam (green curve).

directly dependent on the wall-to-post-shock pressure ratio (see Section 2.4.2). Therefore, as can be seen from Fig. 3.9 and Fig. 3.10, while the relative error is reduced as compared to the one induced in the computation of the wall pressure, the mis-predictions in terms of edge temperature and density properties seems to follow the trend observed when analysing the wall pressure in Fig. 3.6.

Furthermore, it should be remarked that the miscellaneous peaks of over and under-estimation observed (see relative error in the plots in question) also coincide with the junctions between the various geometric primitives that compose the HB-2 configuration. The 30 % and 70 % under-prediction, in the values of the edge temperature and density respectively, at the location where the blunted cone transitions into the cylindrical region seems to be again the consequence of the absence of treatment in HyFlow of the interaction between the Eulerian flow (inviscid) and the viscous flow when calculating the pressure distribution. In Fig 3.7, the importance of this phenomena can be illustrated by the path line followed by a surface streamline (green curve) that has passed across the slightly curved portion of the bow shock-wave. Indeed, that streamline is, by consequence, entrained in the viscous boundary layer with concomitant effect on the wall pressure estimates and therefore on the computed edge conditions. This

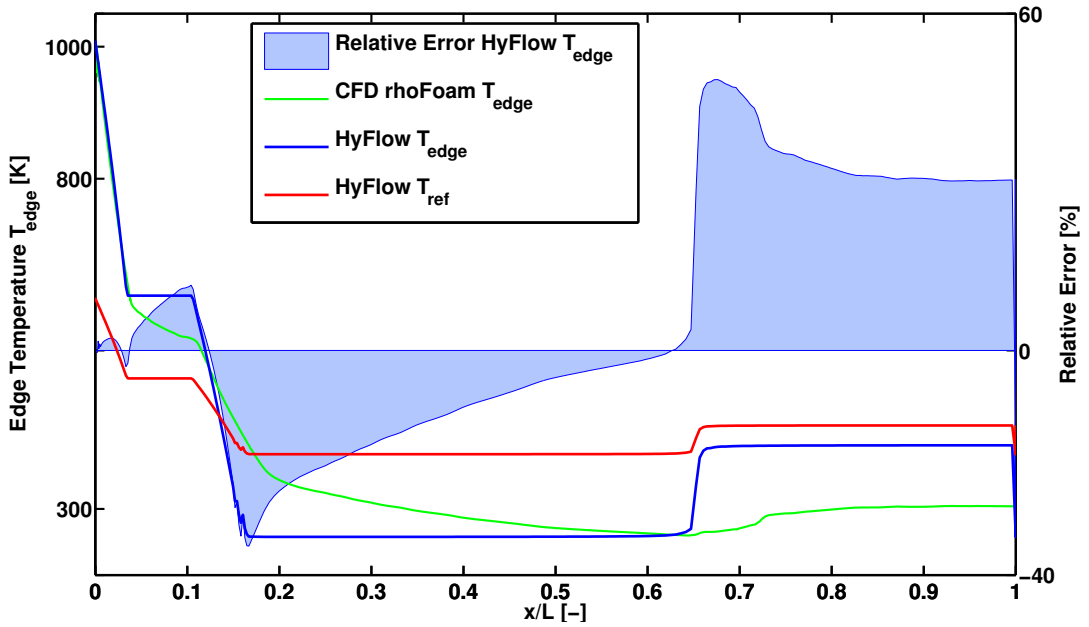

Figure 3.9: Edge temperature profile along the HB-2 centreline for case 1 - Comparison of the edge temperature profiles along the HB-2 geometry as obtained by HyFlow (blue curve) and rhoFoam (green curve). A logarithmic scale is used on the vertical axis (edge temperature) and the continuous relative error between HyFlow and the numerical results is also presented. Finally, the average temperature profile within the boundary layer, denoted T^* and computed by HyFlow, is also shown (red curve).

particular phenomenon also has an non-negligible impact on the distribution of heat transfer rates at the wall (discussed later).

Nonetheless, despite these mis-predictions in terms of temperature and density at the edge of the boundary layer, the edge velocity estimates computed by HyFlow along the centreline of the HB-2, shown in Fig. 3.11, induces only a very small error when those are compared to the numerical results. Interestingly enough, the velocity profile is slightly over-predicted over the cylindrical section of the geometry (by about 6 %) while it is somewhat under-predicted in the rear flare region by only about 4-5 %. Therefore, in the realm of the free-stream conditions corresponding to this first validation case (i.e. zero degrees angle of attack), the results of the edge conditions show a relatively small error generated by the ideal gas NS-IE flow model, considering its inherent simplicity, when compared to the CFD model employed in this validation work. The behaviour of the model is however expected to degrade at angle of attack (variable-entropy flow) (78).

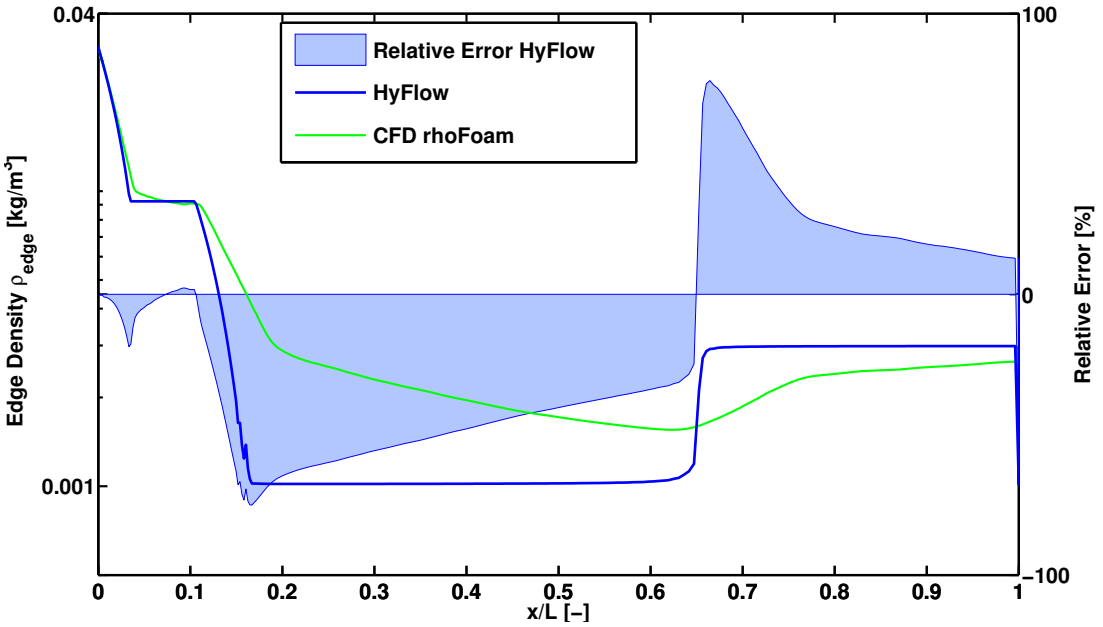

Figure 3.10: Edge density profile along the HB-2 centreline for case 1 - Comparison of the edge density profiles along the HB-2 geometry as obtained by HyFlow (blue curve) and rhoFoam (green curve). Additionally, a logarithmic scale is used on the vertical axis (edge density) and the continuous relative error between HyFlow and the numerical results is also presented.

Wall Heat Flux

Fig. 3.12 shows that the heat flux distribution at the stagnation point and on the spherical section are relatively well estimated by the reduced-order model when compared to the CFD results and experimental data – even more so in the direct vicinity of the stagnation region. According to the reference paper (75), the experimental value of the heat transfer rate at the stagnation point is equal to 137.62 ($\pm$3.991) kW/m^2. The reduced-order model estimated the stagnation heat flux as equal to 126.44 kW/m^2 while rhoFoam predicted a value of 127.94 kW/m^2. These results represent an under-prediction of 8 % and 7 % respectively with respect to the experimental results. Nevertheless, these relative errors reduce even further when accounting for the 2.9 % uncertainty in the experimental results for this level of heat flux. Moreover, it shall be noted that the relative error induced by HyFlow with regard to the CFD result is slightly less than 1.2 % and can be considered negligible. In the conic section that ends the blunted cone region however, the wall heat flux is over-predicted by HyFlow when compared to the CFD and experimental data. Nonetheless, the relative error in that particular region

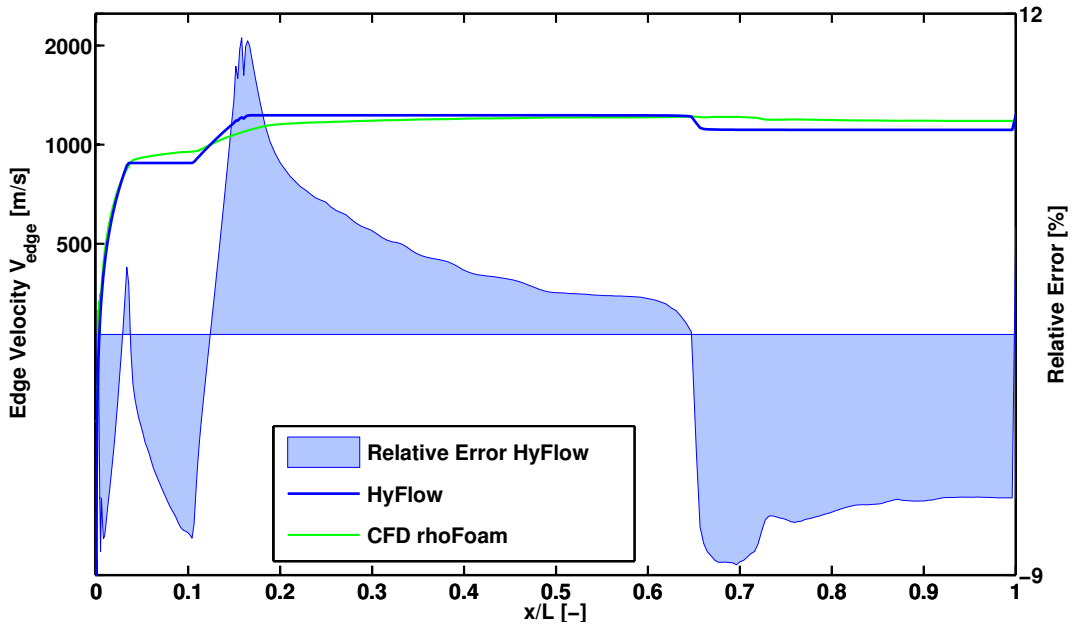

Figure 3.11: Edge velocity profile along the HB-2 centreline for case 1 - Comparison of the edge velocity profiles along the HB-2 geometry as obtained by HyFlow (blue curve) and rhoFoam (green curve). Additionally, a logarithmic scale is used on the vertical axis (edge velocity) and the continuous relative error between HyFlow and the numerical results is also presented.

is equal to about 30 %. Finally, recalling the comments made in the introductory paragraphs of the present chapter concerning the level of fidelity required of a reduced-order model such as HyFlow, the comparison with the experiment and numerical results can be considered fairly satisfactory with respect to the wall heat flux distribution (see Fig. 3.12 again).

Angle of Attack Effects

In a variant of the preceding case, the effects of a non-zero angle of attack on the resulting aerodynamic heating profile is investigated. The experimental work is also taken from the work of Kuchi-ishi *et al.* (75). While the same free-stream conditions are used (see Table 3.1), the HB-2 is inclined at a 15 degrees angle with respect to the direction of the free-stream flow. In Fig. 3.13, it can be seen that the level of aerodynamic heating over the length of the HB-2 geometry, for either the experiment or the HyFlow simulation, is substantially higher over the cylindrical and rear flare sections when compared to the results of the zero angle of attack case (see Fig. 3.12). According to the reference paper, the experimental

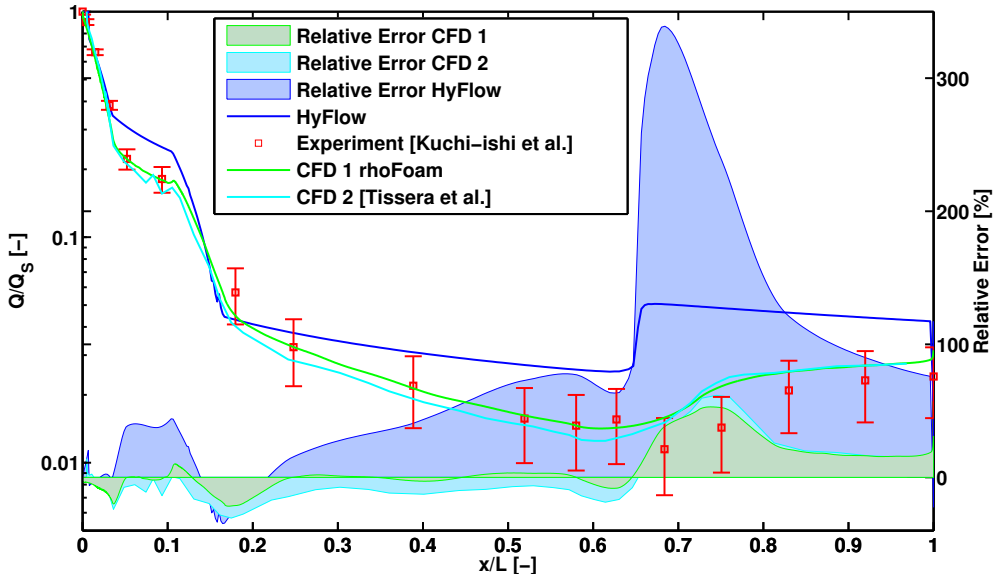

A logarithmic scale is used on the vertical axis (heat flux ratio).

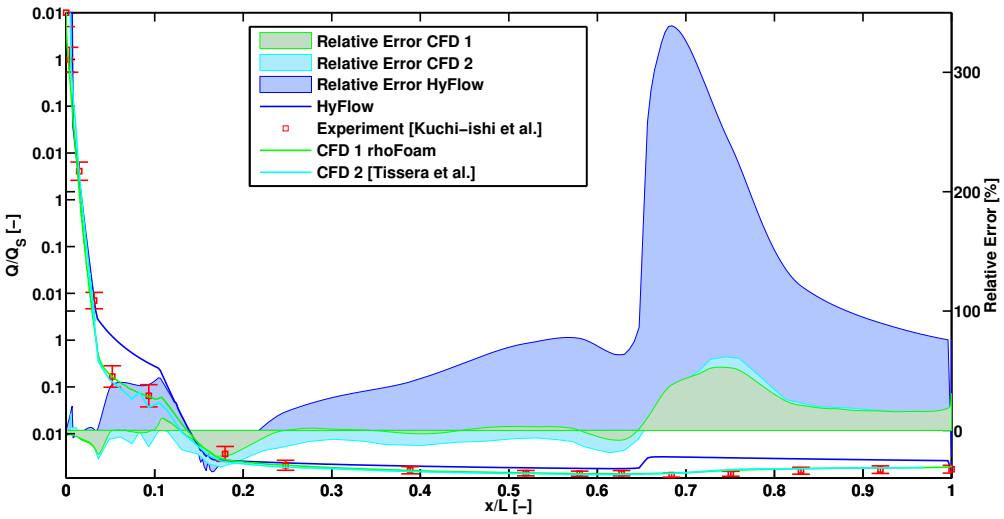

A linear scale is used on the vertical axis (heat flux ratio).

Figure 3.12: Heat transfer profile along the HB-2 centreline for case 1 - Comparison of the heat flux profiles along the HB-2 geometry as obtained by HyFlow (blue curve), by rhoFoam (green curve), CFD results of Tissera *et al.* (cyan curve) and experiment (red squares). The heat transfer is non-dimensionalized using the heat transfer value at the stagnation point.

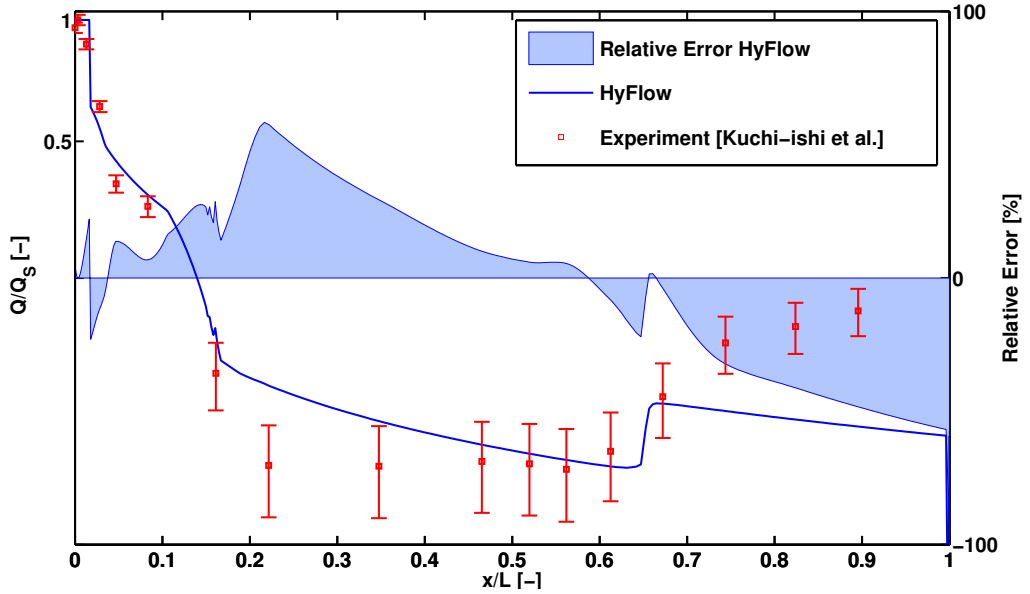

A logarithmic scale is used on the vertical axis (heat flux ratio).

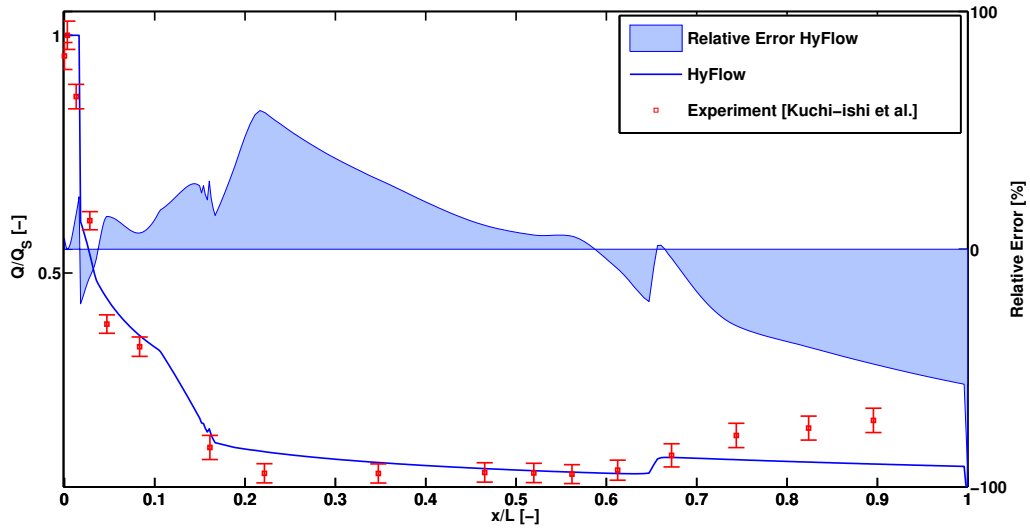

A linear scale is used on the vertical axis (heat flux ratio).

Figure 3.13: Heat transfer profile along the HB-2 centreline for case 1 at $\alpha = 15$ deg - Comparison of the non-dimensional heat flux profiles for case 1 where the angle of attack is now set to $\alpha = 15$ degrees.

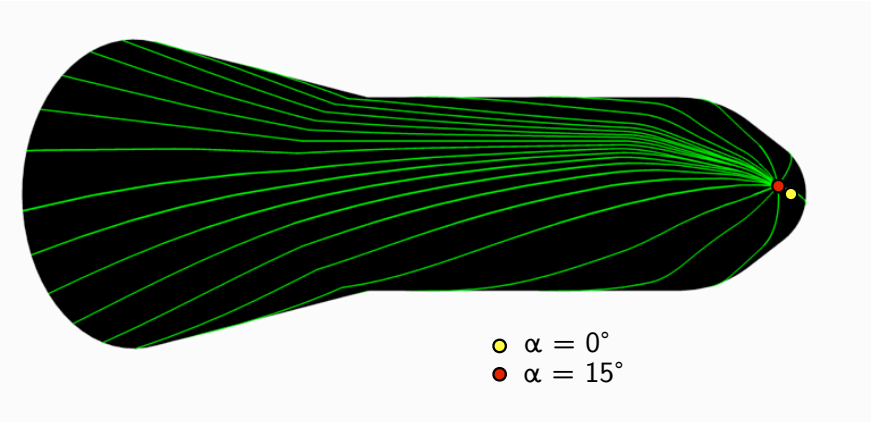

Figure 3.14: Distribution of streamlines over the HB-2 geometry at α = 15 deg - Streamlines distribution over the HB-2 geometry when inclined at a 15 degrees angle with respect to the free-stream flow. The stagnation point is shown in red and is compared to that at zero degrees angle of attack (yellow dot).

heat flux at the stagnation point is now equal to 140.29 ($\pm$4.068) kW/m^2 (average heat flux value over the three different experimental runs). The value predicted by HyFlow was found to be similar to that of the previous axi-symmetric case and is thus equal to 126.44 kW/m^2 (i.e. the relative error at the stagnation point is slightly over 7 % when accounting for the 2.9 % experimental uncertainty for this level of heat flux). In HyFlow, at a 15 degrees angle of attack, the Newtonian stagnation point over the blunt-nosed HB-2 geometry shifts from its axial location to slightly underneath the spheroidal section as shown in Fig. 3.14 (but remains in the 3-cm-diameter spherical section of the geometry). Therefore, a constant heat flux profile is returned by HyFlow at the tip of the HB-2 geometry as shown in Fig. 3.13. Indeed, in Hyflow, a stagnation region of influence is defined around the stagnation point in which the stagnation point heating value is imposed (see Section 2.7.3). The experimental uncertainty provided in the work of Kuchi-ishi *et al.* has been interpolated over the range of heat flux experienced by the HB-2 configuration and the resulting error bars have been added to the experimental results in Fig. 3.13. It shall be remarked that the trend obtained via HyFlow follows well the experimental data in the blunted-cone and cylindrical sections (when accounting for the experimental uncertainty). However, as opposed to the zero degrees angle of attack case, the (relatively benign) values of wall heat flux are slightly under-predicted in the rear flare section with an average relative error of about 35 % over that region. Nonetheless, while the reason can only be hypothesized, it is thought that the pressure level resulting from the presence

of a secondary oblique shock (at the cylinder-flare junction) could explain the discrepancies observed between HyFlow and the experimental data.

3.2.2 Case 2

The experimental data for this second validation case are taken from the experimental work of Gray conducted within the Von Kármán Gas Dynamics Facility (VKF) (72). The hypersonic conditions of the free-stream flow are presented in Table 3.1. This particular case provides free-stream conditions (at Mach 17.8) that are very close to those that will be experienced by future space-access vehicles during the first part of their atmospheric entry trajectory. In this case, the HB-2 geometry remains at zero degrees angle of attack. The results of the numerical study accomplished by Tissera *et al.* (74) are again used to provide a fair comparison with regards to the accuracy of the results provided by the HyFlow reduced-order model. The results from their second-order (DD limiter) MUSCL scheme was used here for comparison as the method was reported to provide the best results for the heat transfer distribution in the reference numerical work. For the same reasons given in the previous case (see Section 3.2.1), the wall pressure is estimated by HyFlow using the modified Newtonian theory. Additionally, the mesh in Fig. 3.1 is also used for this second case and the results in terms of wall pressure and wall heat flux will be presented in the next paragraphs.

Inviscid Pressure

As can be seen in Fig. 3.15, while the trend of the dimensionless pressure curve returned by HyFlow over the cylindrical section is similar to that observed in the preceding HB-2 test case, the estimates of the wall pressure over the conic section of the blunted-cone seem to have however improved. As a matter of fact, HyFlow returns fairly good results when those are directly compared to the experimental data. Indeed, the wall pressure estimated by HyFlow, while slightly over-predicting the results of the experiment by nearly 10% (albeit most likely within the unknown uncertainty bounds), may give a better representation than that given by the results from the numerical simulation reported in the work of Tissera *et al.* (as their results somewhat underestimate the pressure over that particular section of the HB-2 geometry). In the preliminary design

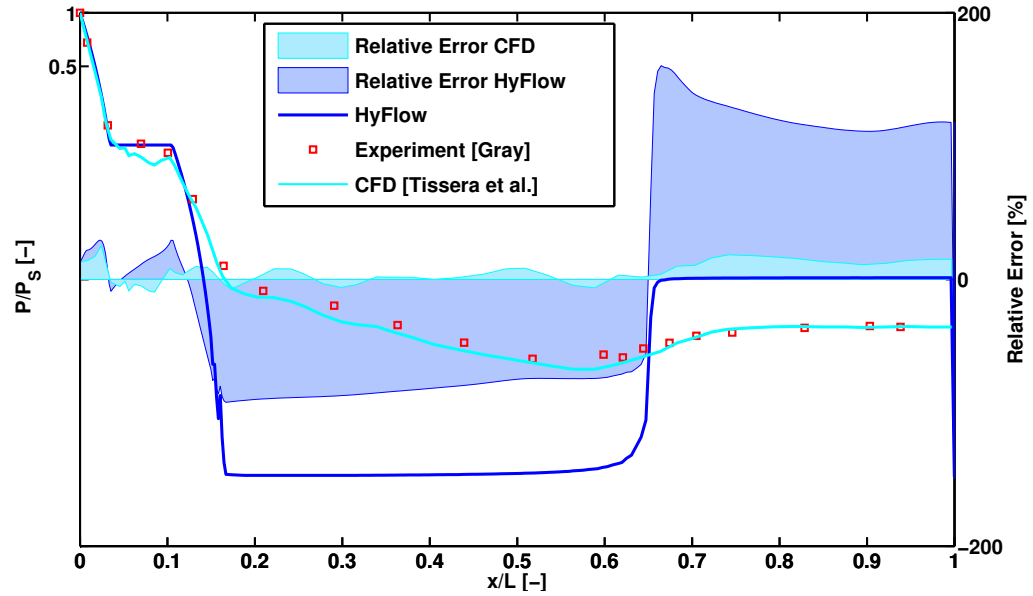

A logarithmic scale is used on the vertical axis (pressure ratio).

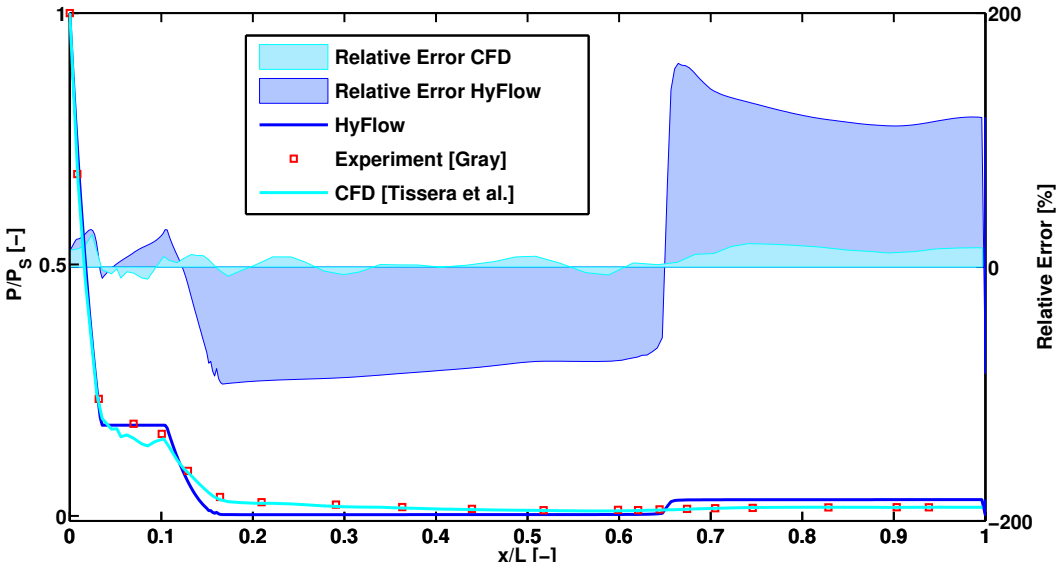

A linear scale is used on the vertical axis (pressure ratio).

Figure 3.15: Pressure profile along the centreline of the HB-2 for case 2 - Comparison of the pressure profiles along the HB-2 geometry as obtained by HyFlow (blue curve), CFD (cyan curve), and experimental work (red squares). The relative errors for each method with regards to the experimental data are shown too.

of hypersonic vehicles, over-estimation would, in fact, always prevail over under-prediction. However, the wall pressure distributions returned by HyFlow over the rear-flare section and in the cylindrical region are, once again, over-predicted and under-predicted, respectively, by the reduced-order model whereas the CFD model seems to provide an excellent surrogate to the experimental data.

Wall Heat Flux

As reported in the study of Tissera *et al.* (74), the experimental stagnation values are not readily available in the open literature. However, the stagnation heat flux of the reference CFD results, obtained via their second order (DD) MUSCL scheme, is reported to be equal to $4,260$ kW/m^2 while HyFlow provides a relatively close value of $4,538$ kW/m^2 (which represents a relatively small over-prediction of 6.5 %).

Additionally, as can be seen from the dimensionless heat flux profiles reported in Fig. 3.16, HyFlow seems to capture very well the heat flux distribution over the blunted-cone region. Indeed, the estimates provided by HyFlow seem to better follow the trend of the experimental results than those of the numerical study – i.e. when relative errors are compared. This fairly good behaviour, in what represents the most critical region of the HB-2 geometry, is likely to originate from the relatively good estimates of wall pressure presented in the previous paragraph. Indeed, as already explained in the preceding case, those may have a considerable influence on the conditions at the edge of the boundary layer subsequently used in the computation of the wall heat transfer rates.

3.2.3 Case 3

In a third case, the initial conditions are representative of the supersonic-hypersonic boundary region with a free-stream flow at Mach 5 (see Table 3.1). In this speed range, it may be attempted to use other Local Surface Inclination (LSI) methods in order to resolve the wall pressure over the surface of the HB-2 geometry. In Fig. 3.17, the pressure distribution along the centreline of the HB-2 geometry as computed by the Tangent-Wedge method (grey curve), the Tangent-Cone method (orange curve) and the modified Newtonian theory (blue curve) are shown and compared against both experimental data and the CFD results from the reference work of Tissera *et al.* (74). It is interesting to notice that the estimates

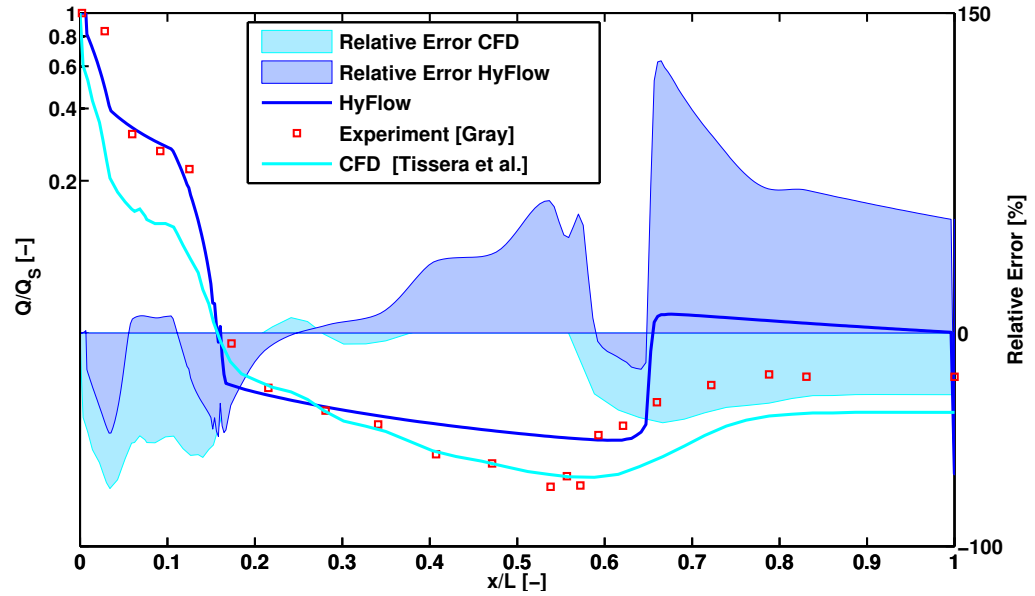

A logarithmic scale is used on the vertical axis (heat flux ratio).

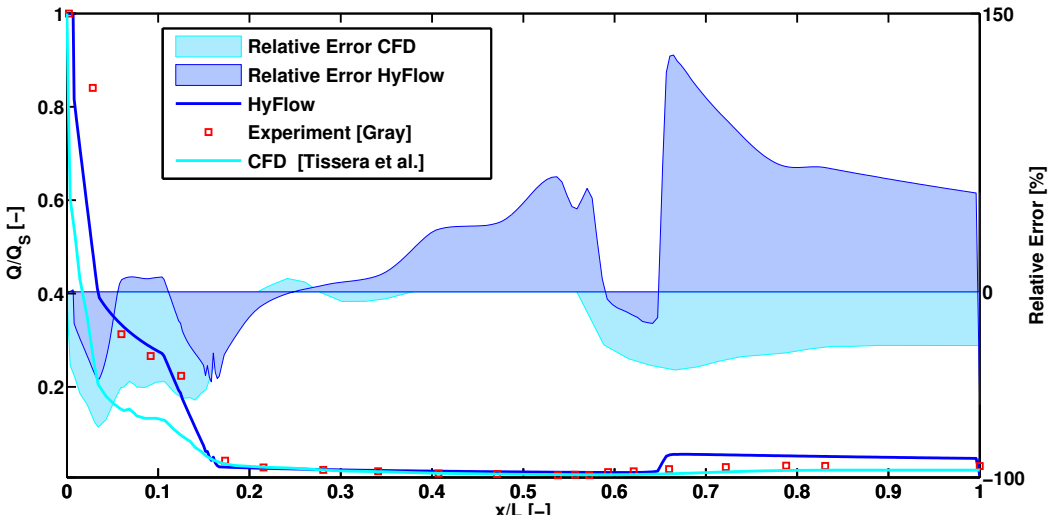

A linear scale is used on the vertical axis (heat flux ratio).

Figure 3.16: Heat transfer profile along the HB-2 centreline for case 2 - Comparison of the heat flux profiles along the HB-2 geometry as obtained by HyFlow (blue curve), by rhoFoam (green curve), CFD results of Tissera *et al.* (cyan curve) and experiment (red squares).

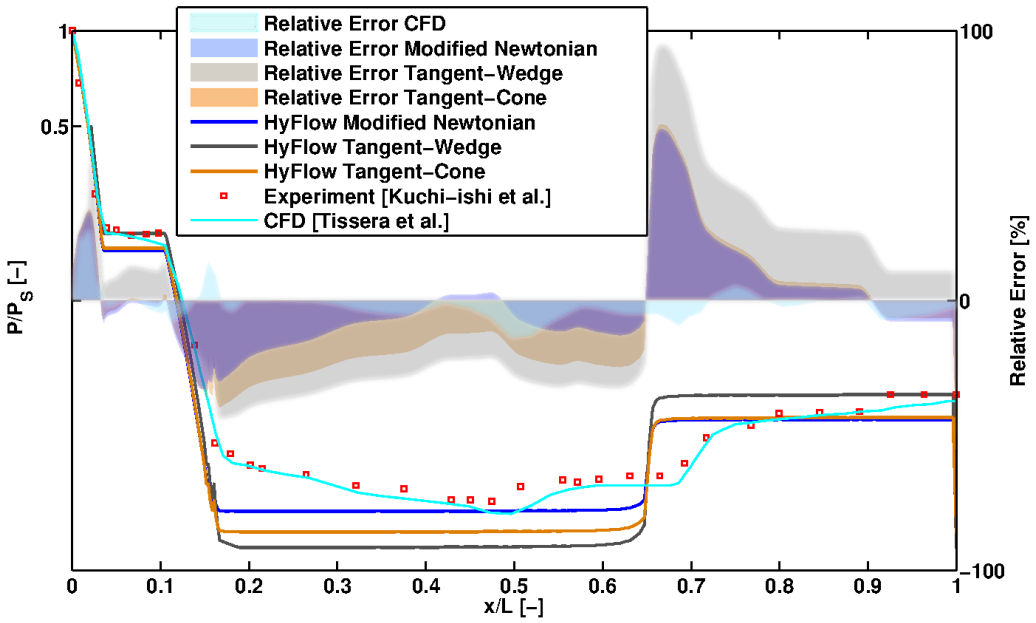

Figure 3.17: Pressure profile along the centreline of the HB-2 for case 3 - Comparison of the pressure profiles along the HB-2 geometry as obtained by HyFlow's LSI methods: modified Newtonian (blue curve), tangent-cone (orange curve) and tangent-wedge (grey curve). Additionally, the CFD results of Tissera *et al.* are also plotted (cyan curve) along with the experimental data from Kuchi-ishi *et al.* (red squares). A logarithmic scale is used for the vertical axis (heat flux ratio).

from the Tangent-Wedge method match relatively well the trend followed by the experimental data all over the blunted-cone region and at the end of the rear-flare section but has the highest relative error over the cylinder and the beginning of the rear-flare section (as those are scaled from the stagnation pressure value which is found to be greater when using the Tangent-Wedge method). As reported in the paper of Tissera *et al*, the interaction between the oblique shock wave and the viscous boundary layer in the cylinder-flare junction induces flow separation. The intersection between the separation shock and the re-attachment shock defines a common corner shock well captured by the reference CFD results as opposed to HyFlow where this phenomenon is completely neglected. Indeed, as thoroughly discussed in the previous cases, HyFlow does not provide information either about the flow field that surround the configuration (no secondary oblique shock is detected) nor it is capable of accounting for the effect of viscous interactions on the pressure estimates.

3.2.4 Discussion

Concerning the heat transfer results, the accuracy of the reduced-order model for Case 2 is overall more satisfactory than for the first HB-2 test cases ($\alpha = 0$ deg and $\alpha = 15$ deg). As expected, the accuracy of the HyFlow code (and the modified Newtonian theory) improves as the Mach number increases in the region directly impacted by the hypersonic free-stream flow. Indeed, at very high hypersonic speeds, the bow shock wave moves closer to the body, a phenomenon which leads to the shock layer becoming thinner. This assumption of a thin shock layer, which forms the basis of the method embedded within the reduced-order model, becomes consequently more accurate in describing the physics involved. Additionally, even though additional investigations may be required to clarify the small discrepancies observed in terms of wall heat flux in the blunted-cone section for cases 1 and 2, as this section of the HB-2 configuration represents the most critical region of the flow field (i.e. where the highest heat transfer rates are located during hypersonic flight), the estimates in terms of wall pressure and heat flux, when compared to CFD and experimental data, are overall fairly satisfactory for all three HB-2 cases given the level of fidelity and required computational time of the present reduced-order approach: about two minutes if the streamlines need to be calculated, around a second if a database of streamlines has been pre-computed. Nevertheless, as suggested by Tissera *et al.* (74) in their numerical study, it may be interesting to re-run cases 1 and 2 under chemically reacting gas conditions to see if there is any improvement in the predictions of the stagnation heat flux. Indeed, the Lewis number is assumed equal to one in HyFlow since a binary mixture is considered to model the gas surrounding the vehicle (see Section 2.7.2). However, at the free-stream conditions of Case 2 (and perhaps to a much lesser extent Case 1), dissociation of the gas molecules is very likely to have occurred.

3.2.5 HB-2 Aerodynamic Loads

The variation of the aerodynamic coefficients, namely axial force coefficient C_A (in body axes), normal force coefficient C_N (in body axis again) and pitching moment coefficient C_m with respect to the angle of attack (for the free-stream conditions of Case 1) are compared to the results of two experimental runs from the work of Kuchi-ishi *et al.* (75) in Fig. 3.18 (i.e. these particular runs were selected to

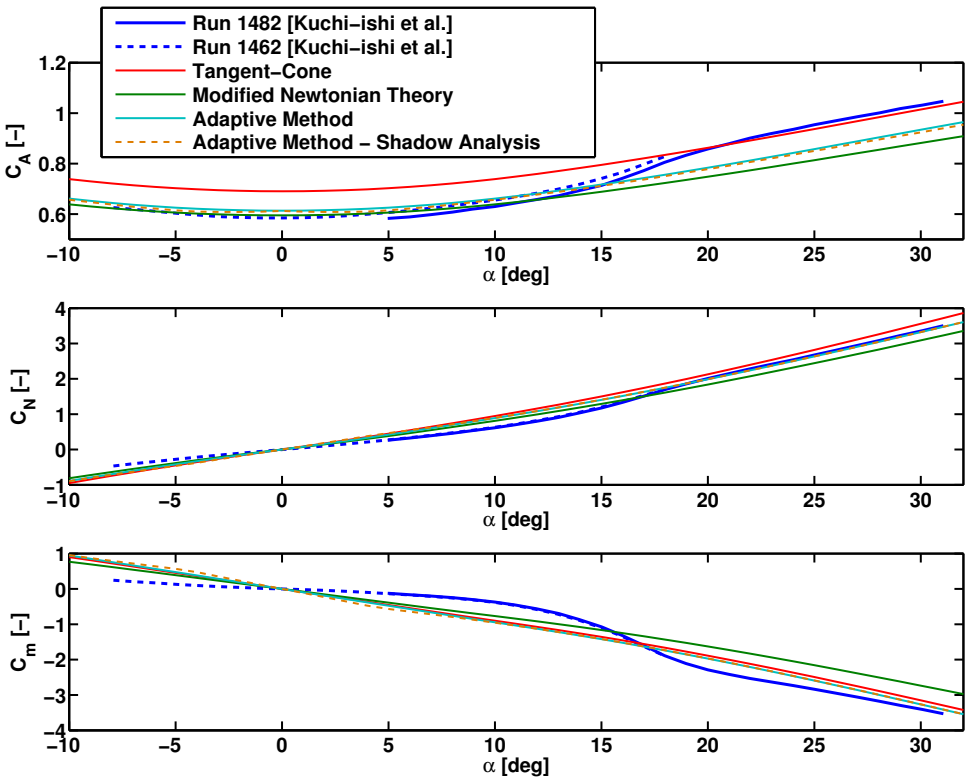

Figure 3.18: HB-2 Aerodynamic Coefficients - The variation of the three-components of the aerodynamic coefficients with respect to the angle-of-attack is depicted. The results from HyFlow using various Local Surface Inclination (LSI) methods are compared against two of the experimental runs from the reference paper.

cover the range of $-10 \leq \alpha \leq 32$ deg). Several Local Inclination Methods (LSI) have been employed, amongst others, the Tangent-Cone method and the Modified Newtonian Theory yielded the best results. As can be seen in the figure in question, the level of accuracy in the predictions of HyFlow, considering the relative simplicity of the present reduced-order model, can be considered satisfactory. Nonetheless, although these results demonstrate that the well-proven LSI methods are powerful tools in the preliminary design of hypersonic vehicles, they however confirm the eventual lack of consistency in the range of application of these methods (i.e. what method to apply where). Indeed, it can be observed that the modified Newtonian theory seems to predict better the components of the aerodynamic coefficients for small angles of attack (i.e. $\alpha \leq 15 - 16$ deg), whereas the empirical Tangent-Cone method increases the quality of its predictions (compared to experimental data) when the angle of attack is in the range

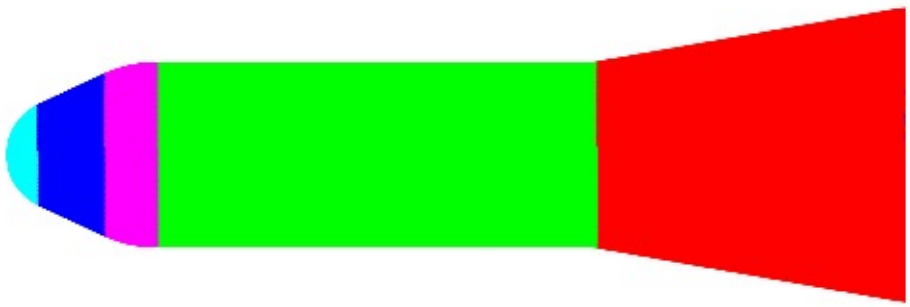

Figure 3.19: HB-2 mesh partitioning - The HB-2 mesh has been partitioned into five regions: a spherical nose tip (cyan), a nose cone (blue), a toroidal corner (magenta), a cylindrical region (green) and a rear-flare (red).

of $18 \leq \alpha \leq 32$ deg (i.e. beyond its normal application). Therefore, in an attempt to improve the predictions of HyFlow, the ballistic configuration has been partitioned into several geometric primitives using the growing region algorithm discussed in Section 2.3.2.4 of Chapter 2: a conical rear-flare, a cylindrical region and a spherical-nose cone were first defined. Thereafter, a *region-adapted scheme* can be employed using HyFlow by assigning a given method to each of the previously identified geometrical regions. In the present analysis, following the guidelines often suggested in the literature, the modified Newtonian theory has been applied onto the windward panels of the blunted cone (since a strong bow shock must form ahead of the nose tip), and a Tangent-Cone method has been applied to the other two regions (i.e. more particularly at the rear flare because of the presence of a secondary weaker conical shock). As can be seen in Fig. 3.18, the geometry-adapted method seems overall to return the most consistent and accurate results. Additionally, for demonstration purposes, the aerodynamic loads have been re-computed using the same *region-adapted* method in conjunction with a shadow analysis (these results are also shown in Fig. 3.18 for context). Nonetheless, as expected, the associated increase in computational complexity has little benefit on the results of an aerodynamic study performed with such a high resolution convex tessellation.

Finally, in order to challenge the established "*intuitive logic*" that often dictates the use of a specific method and since experimental results are available, the

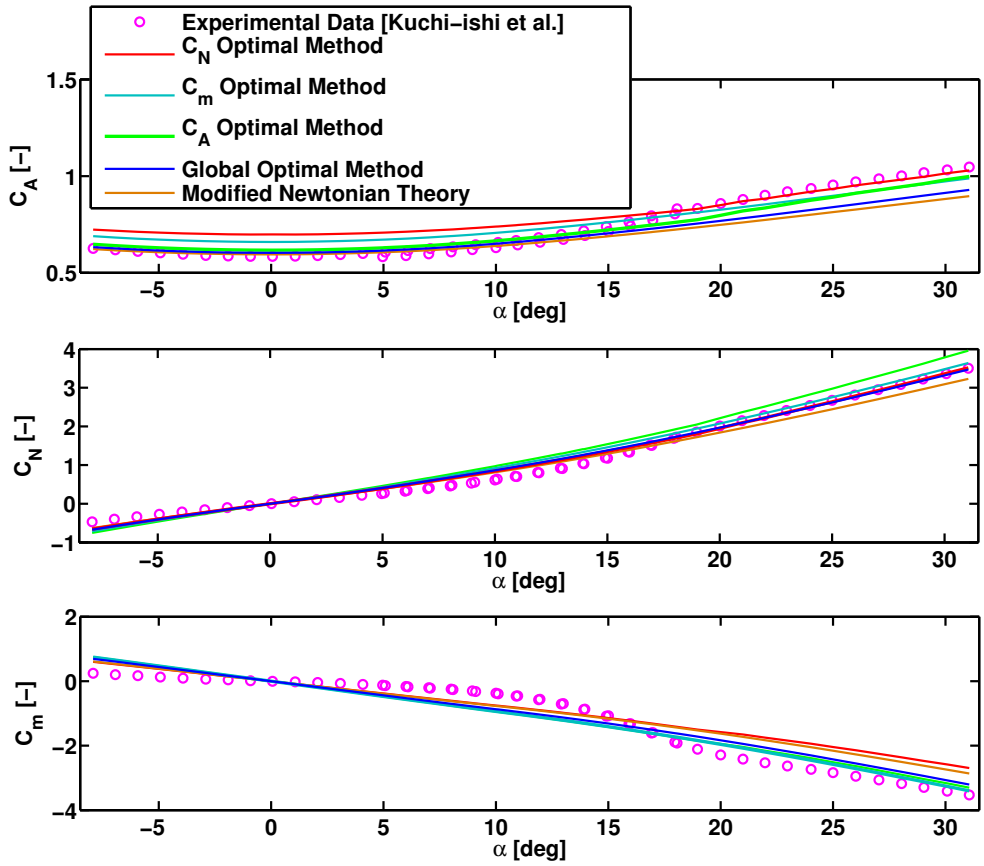

Figure 3.20: HB-2 aerodynamic coefficients - The variation of the three-components aerodynamic coefficients with respect to the angle-of-attack is depicted. The results from HyFlow using various Local Inclination Methods are compared against two of the experimental runs from the reference paper.

adequate set of LSI methods that would lead to results that better match the wind tunnel data may be obtained via an "optimization process": this way an optimal combination of methods can be determined. To solve this problem, the HB-2 geometry has been manually partitioned into five zones, first the cylindrical and conical flare regions mentioned earlier, and then, the nose-cone region has been further split into three parts: a spherical nose, a conical region and a toroidal corner (see Fig. 3.19). Since four methods are considered, namely Tangent-Cone, Tangent-Wedge as well as both the modified and classic Newtonian Theory, there is a total of $4^5 = 1024$ possible combinations of methods. Here, the optimal set of methods is simply assumed to be the combination, m_c, that minimizes the total integrated relative error (over the range of angle of attack), denoted ϵ_R, in all three components of the aerodynamic coefficients. The fitness function is therefore defined as

Optimal Method	Cone	Flare	Cylinder	Corner	Nose Tip
Global	MN	CN	CN	MN	MN
C_A	MN	TC	TW	CN	MN
C_N	MN	MN	TC	MN	TW*
C_m	MN	TC	TC	MN	TC

Table 3.3: HB-2 LSI methods optimization results - Modified Newtonian (MN) - Classic Newtonian (CN) - Tangent-Wedge (TW) - Tangent-Cone (TC) – *It shall be remarked that, as discussed in Section 2.3.2.2 of Chapter 2, when the local inclination angle is greater than the maximum wedge angle for the given free-stream condition (here, when $\phi \geq 44.3$ deg) – i.e. detached shock condition – the tangent-wedge method embodied in the HyFlow code switches to the Modified Newtonian Theory, which is most likely to be the case on the spherical nose section.

$$\min_{\mathbf{m_c}} \sum_{i=1}^{3} \left(\epsilon_R = \int_{-10}^{32} \| C_{wt}(\alpha) - C_{Hy}(\alpha) \| \, \mathrm{d}\alpha \right) \tag{3.1}$$

where $C_{wt}(\alpha)$ and $C_{Hy}(\alpha)$ are, respectively, the experimental and HyFlow-returned three components of the aerodynamic coefficients. The results from the optimization procedure are summarized in Table 3.3 and shown in Fig. 3.20. Interestingly enough, it appears that the global optimal set of methods that best describes all three aerodynamic coefficients is a mix of Modified and Classic Newtonian Theory, respectively applied to the full nose cone for the former, and to the cylinder and rear flare for the latter. The modified Newtonian theory is indeed often suggested as the method of choice for blunt bodies while the classic Newtonian theory is, in general, preferred to analyze slender geometries (which may explain why it has been optimally applied here onto the conical flare region). Additionally, the optimal solutions for each individual coefficient, independently of the others, are also introduced in Table 3.3 for context. Although a more in-depth study than that presented here would be necessary to draw additional conclusions, the previous results show that the geometry-adapted optimization approach adopted in the present section may reveal itself to be quite beneficial in maturing our understanding concerning those well-proven engineering methods and might, in turn, improve the way those are used in engineering models.

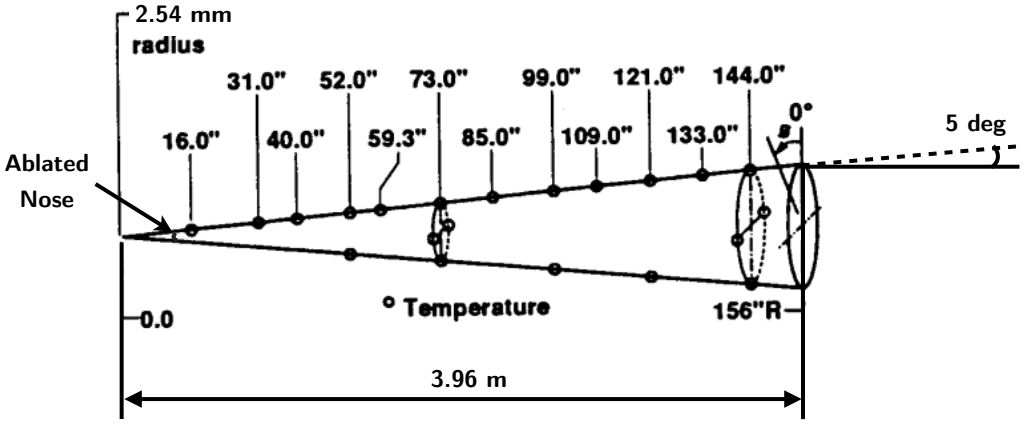

Figure 3.21: Re-entry F vehicle - Temperature measurement locations on Re-entry F vehicle (modified from Ref. (79)).

3.3 Re-entry F Configuration

This second validation case is based on both the experimental work (flight test) conducted by NASA in 1968 – the results from the flight experiment were presented by Zoby *et al.* (79) – and the numerical work carried out by Barnhardt and Candler (80) concerning the Re-entry F configuration geometry. The slightly blunted conic configuration consists of a 3.96 m long cone, shown in Fig. 3.21, with a 5 degrees half-apex angle and a very small blunted nose tip made out of ablative graphite material designed to survive its ballistic hyper-velocity trajectory ($R_N = 2.54$ mm). The results from the experimental flight have been used extensively to benchmark theoretical models as well as ground test data. The two points along the original ballistic trajectory, considered in this validation work, are listed in Table 3.4. These specific cases have been selected due to the availability of the results from the numerical simulation conducted by Barnhardt and Candler (also based on a number of previous investigations). In this second validation test case, the emphasis is on the capability of HyFlow to properly predict the level of turbulent aerodynamic heating while correctly predicting the extent of the turbulent region. Indeed, the accurate prediction of the boundary layer status is paramount for the design of most re-entry vehicles and those of the configuration discussed in the present dissertation are no exceptions. In this validation case, the effect of the effective angle of attack on the transition heating profile is also investigated.

Since the leading edge radius of the Reentry-F configuration is so small compared to its length, the flow over the majority of the vehicle should resemble that

Case	1	2
Altitude [km]	24.38	21.34
Mach Number [-]	20.01	19.93
Density [kg/m^3]	0.043523	0.07092
Temperature [K]	221	218
Effective Angle of Attack, η [deg]	0-0.2	0.3-0.6

Table 3.4: Re-entry F simulation conditions - Free-stream flow conditions for the Re-entry F configuration.

over a slender, sharp cone. The most obvious surface inclination-based approach within Hyflow for calculating the pressure on its surface should ostensibly be the Tangent-Cone method. It is commonly held however that the validity of this approach should be called into question at high Mach numbers. For this reason, both this method and classic Newtonian theory were used to estimate the properties of the flow required for the prediction of the thermal transfer to the surface of the vehicle. The results, in terms of wall heat flux, for a case at zero degrees angle of attack and another at a very small effective angle of attack, are presented in the upcoming paragraphs.

3.3.1 Case 1

In Fig. 3.22, the transition heating profile along the centreline of the Re-entry F configuration is presented for the 24-km-altitude case at zero degrees angle of attack. It can be seen that transition occurs symmetrically on both left and right sides of the vehicle (therefore, there is no clear distinction between leeward and windward sides). As shown in the figure in question, the CFD simulation seems to correctly predict the level of both laminar and turbulent aerodynamic heating – but only since the location of the boundary layer transition has been fixed in order to match the flight experiment. The uncertainty in the location of boundary layer transition has been reported by Schneider (81) as being of the order of 300 %. On the other hand, although the laminar heat transfer rates are well predicted by the reduced-order model (albeit slightly under-predicted by 15-20 %), HyFlow is not able to capture the full magnitude of the turbulence heating and thus fails to provide accurate predictions of the values of heat rate within the turbulent region located aft of the Re-entry F configuration. Indeed, since at a free-stream

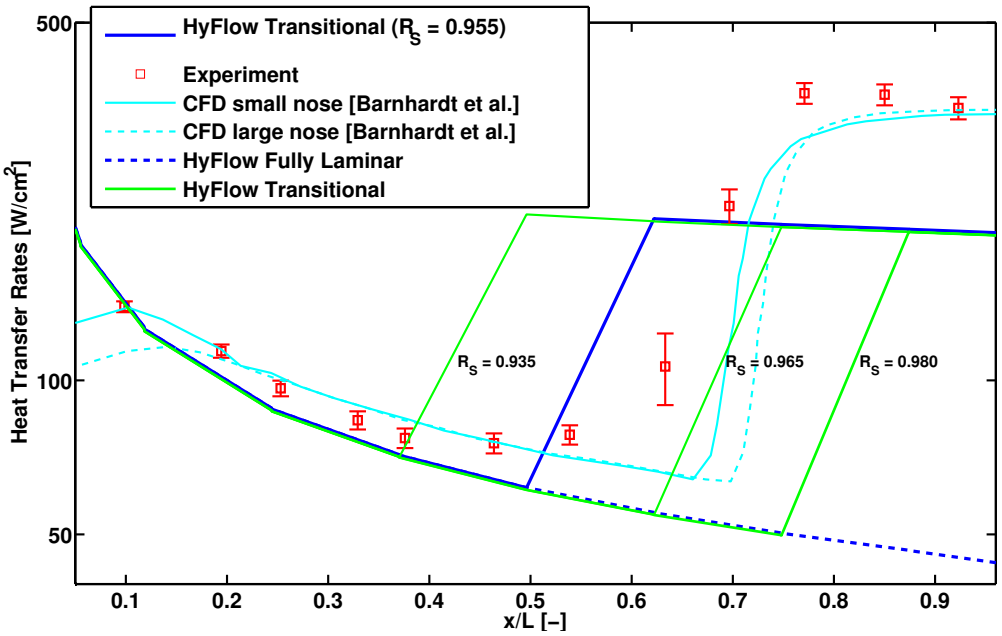

Figure 3.22: Heating profile along the centreline of the Re-entry F experiment for case 1 - $\eta = 0$ deg - Comparison of the transitional heat flux profiles given by the flight experiment (red squares), HyFlow (blue curves) and CFD data for two different nose tips (cyan curves). The experimental uncertainty at each point is also shown. A logarithmic scale is used on the vertical axis (Heat Transfer Rates).

Mach number of about 20, the total enthalpy was reported to range from 18.3 to 16.9 MJ/kg (81), the experiment can thus be considered as a hot hypersonic flow test with real chemistry effects which might explain the discrepancies observed in the level of aerodynamic heating in the turbulent region (and perhaps also in the laminar region). Nonetheless, the location and extent of the transitioned boundary layer region can accurately be predicted by HyFlow if the smooth-surface transition model described in Section 2.5.1 is correctly configured to match the results of the flight experiment (through the use of a scaling parameter, herein denoted R_s, employed in the computation of the effective Reynolds number at transition given by $Re_t^* = R_s \times Re_t$). In that particular case, a very small correction to the original transition Reynolds number, given by $R_s = 0.945$, is used to better define the location of the boundary layer transition. In Fig. 3.22, the effect of varying this scaling parameter on the location of the transition from a laminar state to turbulence is also shown for context. In the laminar region close to the blunted nose tip, the observed discrepancies, between the results from both HyFlow and the reference CFD, are not understood with great certitude,

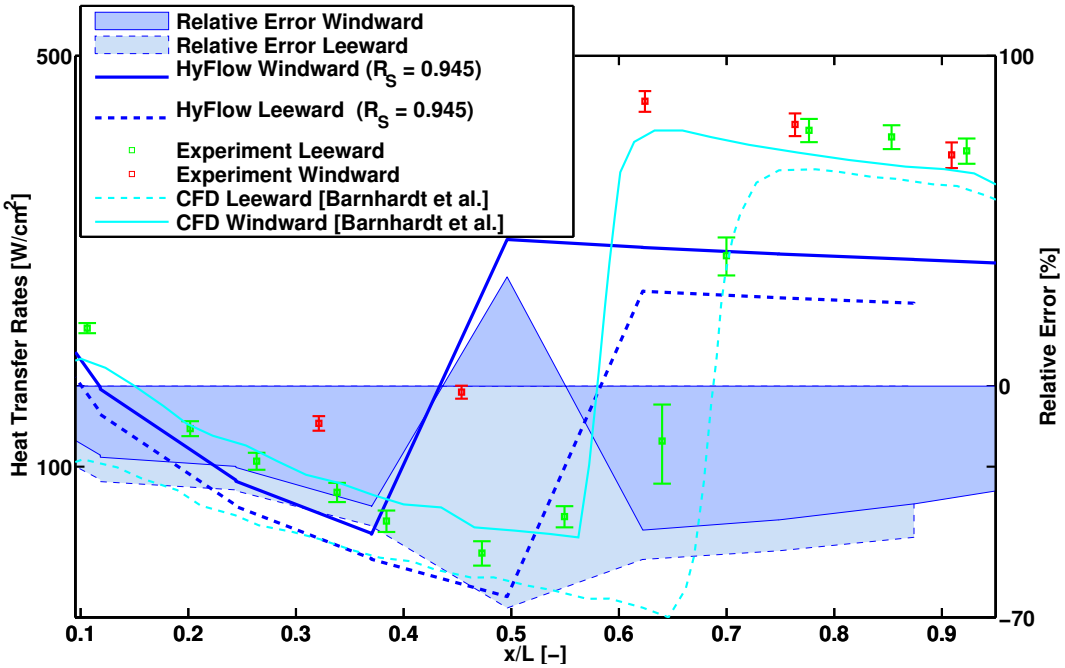

Figure 3.23: Heating profile along the centreline of the Re-entry F experiment for case 1 - $\eta = 0.2$ deg - Comparison of the transitional heat flux profiles given by the flight experiment (red squares), HyFlow (blue curves) and CFD data for two different nose tips (cyan curves). The experimental uncertainty at each point is also shown. A logarithmic scale is used on the vertical axis (Heat Transfer Rates).

however. Indeed, in the reference study of Barnhardt and Candler (80), only the qualitative mention of a large and small ablated nose, without additional information, is provided. Nevertheless, the reason for that particular treatment of the nose region is related to the obvious lack of measurements in the ablated nose section – i.e. logically confirmed in Fig. 3.21 where the location of the temperature measurements is shown (the first sensor was located along the longitudinal axis of the vehicle at a station corresponding to $x/L = 0.1$).

Additionally, as confirmed in a study by Schneider, there is "*[an additional] uncertainty in the local conditions due to problems involved in estimating the nose radius as a function of time during ablation*" (81). In HyFlow however, the blunted nose tip is defined by its non-ablated state. Thus the value of heat transfer rate returned by HyFlow at the blunt-nosed tip of the configuration is, by consequence, extremely high ($Q_S = 16.3$ kW/cm^2), justifying the use of an ablator for the flight experiment.

Effect of a Small Angle of Attack

In Fig. 3.23, the effect of a small effective angle of attack equal to 0.2 degrees, on the transition heating profile and the extent of the turbulence region, is investigated. As already referred to in the study of Barnhardt and Candler (80), the smallest effective angle of attack has a non-negligible effect on the extent of the region of turbulence over the fore-body conic configuration. Indeed, in their study, Bernhardt and Candler have shown that the boundary layer transitioned asymmetrically as a result of this small effective angle of attack. From Fig. 3.23, the distinction between the leeward and windward side of the vehicle is indeed clearly shown in the results from both the CFD simulation and HyFlow. The turbulent region over the windward side of the vehicle is longitudinally located further upstream than the region of turbulence on the leeward side. The location of the onset of transition on both leeward and windward sides predicted by the reduced-order model, once the transitional model is slightly scaled (the same scaling scaling factor of 0.945 is used here as in the previous case), is in agreement with the experimental results. The limits of the turbulence region seem to be even more accurately defined by HyFlow when compared to the results from the reference CFD simulation. Indeed, the CFD simulation shows a delay before the onset of transition on either side of the Re-entry F configuration is triggered – i.e. since transition was not the main focus of the CFD study, it appears to be poorly treated. Additionally, while the level of heat flux in the laminar region is still slightly under-predicted by HyFlow with regard to the results of the flight experiment, it should however be noticed that the heat transfer rates on the leeward side of the vehicle are favorably comparable to those provided by the CFD simulation. Nonetheless, the level of heat flux in the turbulent region is still under-predicted by the reduced-order model (and, to a much reduced degree, by the CFD simulation) for either the leeward or windward side of the vehicle.

3.3.2 Case 2

In this second test case of the Re-entry F flight experiment, for which the free-stream conditions of the simulation are given in Table 3.4, two small effective incidence angles have been considered. The results from HyFlow are compared to both the reference numerical and experimental results in Fig. 3.24. In the figure in question, the results on both windward side (left graph) and leeward

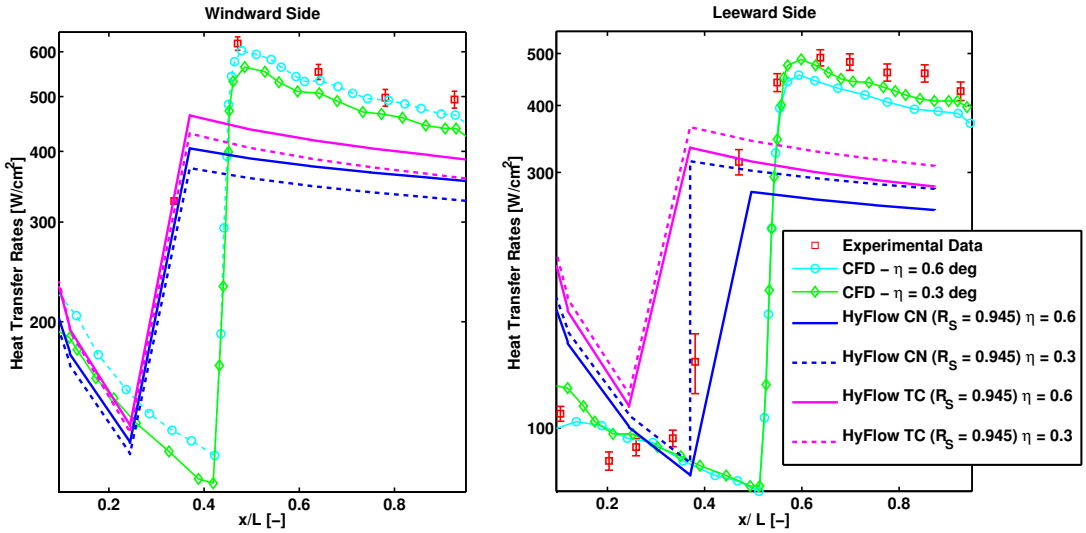

Figure 3.24: Heating profile along the centreline of the Re-entry F experiment for case 2 - Comparison of the transitional heat flux profiles given by the flight experiment (red squares), HyFlow (blue and magenta curves) and CFD data for two different effective angles of attack (cyan and green curves). The experimental uncertainty at each point is also shown. A logarithmic scale is used on the vertical axis (heat transfer rates).

side (right graph) of the vehicle, with the two different effective angles of attack, are depicted. The asymmetry in boundary layer transition between the leeward and windward sides of the vehicle is clearly apparent in the predictions of both the CFD simulations and the HyFlow reduced-order model. The smooth-surface transition model within Hyflow (see Section 2.43) is indeed sensitive to asymmetries in the flow and, when the classic Newtonian theory is used to predict the properties of the flow on the surface of the vehicle (blue curves), predicts rather accurately the difference in transitional behaviour between the leeward and windward sides of the vehicle once the critical Reynolds number within the model is properly tuned to the experimental conditions (the effective Reynolds number at which transition occurs has been decreased using the same scaling factor as in the previous case). In contrast, if the Tangent-Cone approach is used to calculate the flow properties (magenta curves), then the asymmetry in transition is quite seriously under-predicted, revealing a rather disconcerting sensitivity within the analysis to the details of the modelling procedure that is used.

Although the heat transfer rates in the region of laminar flow on the forward part of the body are predicted reasonably well by both incarnations of the reduced-

order model, HyFlow significantly under-predicts the heat flux within the turbulent region on the aft portion of the Reentry-F configuration. It should be borne in mind however that, as in the preceding case, the presence of real-gas effects and chemical reactions under these 'hot' conditions cannot be discounted (81) and this might explain some, if not all, of the discrepancies between the observed and predicted levels of aerodynamic heating of the surface of the vehicle.

3.3.3 Discussion

From the present validation case, it appears that the HyFlow reduced-order model is capable of predicting the asymmetric nature of the turbulent boundary-layer region if the transitional Reynolds number is slightly scaled (i.e. symmetric turbulent regions too). Nevertheless, it seems that HyFlow is not entirely capable of estimating the level of turbulent heating in both the leeward and windward regions of the flow geometry. Thus, although the results may be satisfactory enough considering the lower fidelity level of HyFlow, further investigations are however necessary in order to identify the source of these observed discrepancies to see whether those are the result of the nature of the geometry being discussed in this section (nearly sharp cone) or are the results of the simplistic ideal gas model considered thus far given the fact that chemical reactions must indeed be taking place in the surrounding flow field at such hyper-velocities.

3.4 Space Shuttle Orbiter Configuration

In this final validation study, a combination of pre-flight wind tunnel tests and flight data from the Space Shuttle programme along with the results from numerical studies will be used to establish with more certitude the relevance of the HyFlow model in the context of the preliminary Multi-disciplinary Design and Optimisation (MDO) of the future generation of heavy-lift space transportation systems. Herein this section, the ability of HyFlow to accurately estimate the aerodynamic loads, wall pressure and wall heat transfer rates over a space plane-like geometry will indeed be verified. The mesh used in the present work is pictured in Fig. 3.25. The tessellation is composed of about $15,000$ panels and was obtained from the 3D CAD models repository on NASA's website. Although the mesh has undergone important modifications mainly in order to remove a

Property	Value	Remark
Reference Area $[m^2]$	249.441	S_{ref}
Reference Length [m]	12.0579	L_{ref} – Mean Chord
Wingspan [m]	23.7871	–
Centre of Mass	$[0, 0.8224, 21.335]$	fixed at 65% of the length

Table 3.5: Reference parameters of the Space Shuttle Orbiter

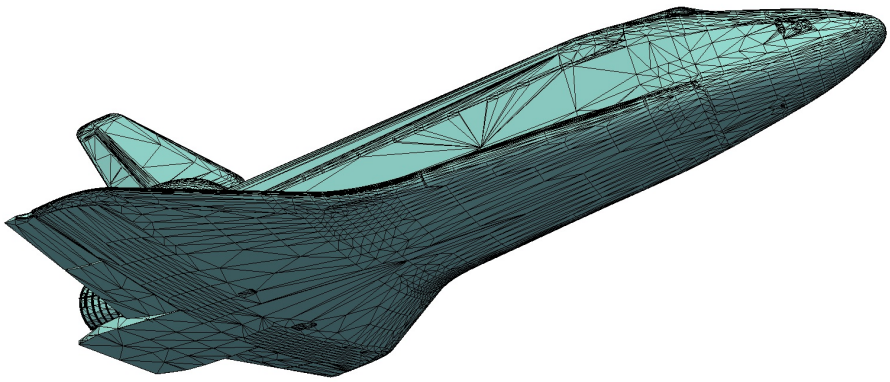

Figure 3.25: Surface mesh of the Space Shuttle Orbiter - The figure illustrates the surface mesh used in HyFlow to describe the Space Shuttle Orbiter geometry.

large number of internal panels (payload bay, Reaction Control System (RCS) thrusters, windscreen and other details) as well as overlapping triangles, the mesh remains however of relatively low quality (as a result of both the non-uniformity in the size of its constituting triangles as well as the persistence of small details) and will thus provide a good measure of the robustness of the present reduced-order model. The reference quantities, taken from the Shuttle Orbiter Aerodynamic Design book (36) and used in the present work, are summarized in Table 3.5.

3.4.1 Orbiter Aerodynamic Loads

Taking inspiration from the validation work of Dirkx (23) performed with the help of a fully inviscid engineering model, named the Re-entry Aerodynamics Module (RAM), a series of wind tunnel tests (36) have been used in the present work to evaluate the accuracy of the aerodynamic loads returned by the HyFlow code

Case	Mach Number [-]	Angle of Attack [deg]
1	5	[0:40]
2	20	[0:40]

Table 3.6: Simulation Conditions for the Analysis of the Aerodynamic Coefficients

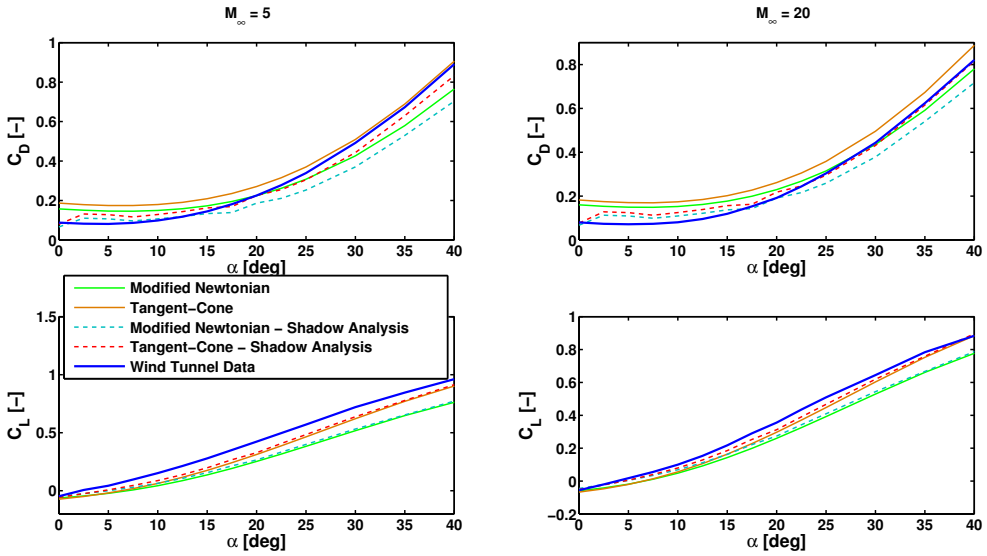

Figure 3.26: Lift and drag coefficients for the Space Shuttle Orbiter - Comparison between the lift and drag coefficients provided by HyFlow and some of the experimental work (in blue) from the Space Shuttle programme for a free-stream Mach number of 5 and 20. Both the tangent-cone (in green) and modified Newtonian (in red) methods have been used in the computation of these aerodynamic forces.

for complex shapes. As discussed by Dirkx in his paper, these data contain however some known discrepancies with flight data, mainly in the predictions of the pitching moment – i.e. the so-called pitching moment anomaly mentioned earlier – and care must therefore be taken when analyzing the quality of the present results. However, this unprecedented wind tunnel effort provides access to a large set of experimental work that can be used to compare various components of the aerodynamic coefficients such as lift, drag and pitching moment predicted by the HyFlow code at various angles of attack with non-deflected control surfaces – i.e. body flap and elevons (see Table 3.6). The results of the evaluation of the aerodynamic loads presented in this section, using the modified Newtonian theory and the Tangent-Cone methods, will be presented with and without shadowing

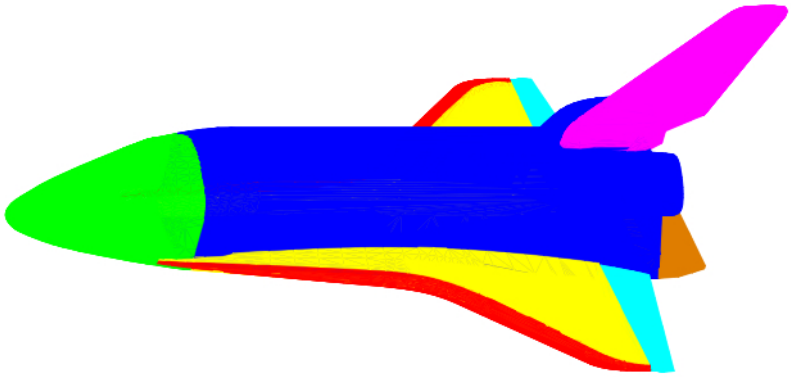

Figure 3.27: Space Shuttle Orbiter mesh partitioning - The Shuttle Orbiter mesh has been partitioned into seven regions: a canopy-nose (green), a fuselage (blue), wings (yellow), leading edges (red), body flap (brown), elevons (cyan) and a vertical tail (magenta).

analysis (see Section 2.3.5 of Chapter 2). When comparing the lift and drag coefficients in Fig. 3.26, it can be seen that the method described here provides a satisfactory reproduction of the wind tunnel coefficients. Indeed, given the aforementioned problems related to the quality of the tessellated mesh, the effect of shadowing on the aerodynamic force coefficients appears to be non-negligible, almost in all cases improving the estimates. The degradation of the Newtonian solution with shadow analysis for $\alpha \geq 20$ deg as compared to that without is however thought to be the fortuitous result of an increase in drag partly resulting from a few remaining internal panels and shadowed portion of the geometry, notably in the area of the rear booster pods, whose contribution to the overall drag coefficient increases with increasing angle of attack – see circled region in Fig. 2.10. In the study of Dirkx (23), the booster arrangement at the rear of the vehicle was, supposedly, not part of the mesh used in his validation work, and only the Orbital Maneuvering System (OMS) pods main structure were. This difference may explain the relatively small deviations in the predictions of the lift and drag coefficients with and without shadow analysis observed by the author in his study.

Optimal Set of Methods

A similar analysis as that presented in Section 3.2.5 for the HB-2 configuration has been repeated here for the Space Shuttle Orbiter. The mesh has thus been

Mach 5					
Optimal Method	Leading Edges	Controls	Fuselage	Nose	Wings
Global	TW*	TC	TC	MN	TC
Mach 20					
Optimal Method	Leading Edges	Controls	Fuselage	Nose	Wings
Global	TW*	TW*	TC	MN	TW*
	Mach 20	&	**Mach 5**		
Optimal Method	Leading Edges	Controls	Fuselage	Nose	Wings
Global (shadow)	TW*	TC	TC	MN	TC
Global (non-shadow)	MN	MN	TC	MN	TC

Table 3.7: Shuttle Orbiter LSI methods optimisation results - Modified Newtonian (MN) - Classic Newtonian (CN) - Tangent-Wedge (TW) - Tangent-Cone (TC). *It shall be remarked that, as discussed in Section 2.3.2.2 of Chapter 2, when the local inclination angle is greater than the maximum wedge angle for the given free-stream condition (here, when $\phi \geq 44.3$ deg) – i.e. detached shock condition – the tangent-wedge method embodied in the HyFlow code switches to the Modified Newtonian Theory, which is most likely to be the case on the spherical nose section.

split into several regions: canopy-nose, fuselage, wings, leading edges, body flap, elevons and vertical tail. Before performing the analysis, all the control surfaces have been gathered into a single region in order to identify a unified method for the controls (for a total of five distinct regions). Thereafter, the optimization process, with shadowing analysis, has been performed: an optimal set of methods that minimizes simultaneously the error for both Mach 5 and Mach 20 cases has been identified and is shown in Table 3.7. The global optimal set of methods for both Mach 5 and Mach 20 with and without shadowing are also shown for context and the resulting aerodynamic coefficients are depicted in Fig. 3.28. As expected, the predictions for both Mach 5 and Mach 20 are greatly improved thanks to the choice of an optimal set of methods.

The choice of the optimal scheme, albeit difficult to justify as it may appear counter-intuitive at first, is however illuminating. First, the wall pressure over the leading edges of the wings appears to be best represented by the two-dimensional Tangent-Wedge method (before it switches to the modified Newtonian theory at high angle of attack). Then, the pressure distribution over the control surfaces is defined by a Tangent-Cone approximation (the Tangent-Wedge and Tangent-

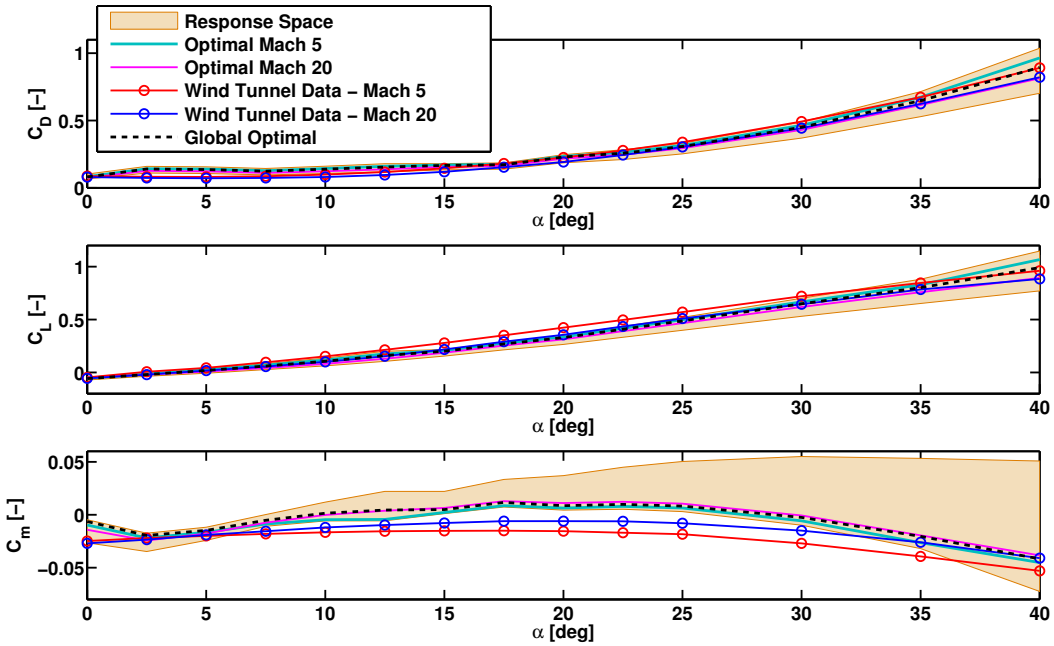

Figure 3.28: Lift, drag and pitching moment coefficients for the Space-Shuttle Orbiter obtained with the optimal set of methods - Comparison between the drag, lift and pitching moment coefficients provided by the identified optimal zone-based schemes and some of the wind tunnel results for a free-stream Mach number of 5 and 20 (red and blue circles respectively).

Cone methods are here, at Mach 20, applied beyond their usual domain of application). The local pressure forces and moments over the fuselage and the wings (i.e. whose undersurface is blended into the fuselage underbelly) are optimally solved using the same LSI method, namely the Tangent-Cone method again. Finally, the method of choice for the nose-canopy region is the modified Newtonian theory as it is usually favored for blunt bodies.

Overall, the predictions provided by the HyFlow model (with shadowing analysis), despite the relatively poor quality of the mesh, are more than satisfactory. The evaluation of the pitching moment coefficient presented here, albeit over-predicted, follow the trend of the wind tunnel test and their comparisons with the experiment data should however be analyzed in a broader context: there is possibly a mismatch between the experimental centre of mass and that used in the present study as there is, most likely, a difference between the geometry defined by the tessellation employed here and the wind tunnel model. Additionally, it has been shown that pre-flight wind tunnel results under-predicted the pitching moment acting on the vehicle at high Mach number (see full explanation in the

Case	1	2	3	4
Altitude [km]	73.2	74	46.7	45.1
Mach Number [-]	24.2	23.4	9.15	7.19
Pressure [Pa]	3.40	3.4	100.3	180.42
Temperature [K]	207	206	260	252.47
Angle of Attack [deg]	39.4	39.4	34.8	30.1

Table 3.8: Shuttle Orbiter simulation conditions - Free-stream flow conditions for the Shuttle Orbiter configuration.

study of Dirkx (23)) These results give therefore a good measure of the robustness of the HyFlow code. To conclude the present analysis, although the approach adopted here may not improve the evaluation of the pressure force and moment at each single point along the operating envelope of the vehicle (where better local optima possibly exist - see response space in Fig. 3.28 resulting from all possible combinations of LSI methods), this method may nevertheless become extremely valuable for the preliminary planning of both ascent and entry trajectories where a unified method is often sought for – of course, the reproducibility of the results may have to be first verified with additional data. Nonetheless, some similitudes with the HB-2 analysis can readily be noticed: for instance, the pressure force and moment over the blunted nose cone of the HB-2 were also optimally derived using the Modified Newtonian Theory (as for the nose-canopy here).

3.4.2 Pressure and Heat Transfer Comparisons

In this validation effort, four different simulation conditions have been considered. The first validation case is based on the numerical study conducted by Kleb and Weilmuenster to analyze the flow on the leeward (and windward) side of the Shuttle Orbiter during a re-entry condition (82). This numerical study was performed with the help of the LAURA (Langley Aero-thermodynamic Upwind Relaxation Algorithm) code. The simulation conditions of Case 1, presented in Table 3.8, represent a point along the first part of the STS-28 mission re-entry flight – i.e. albeit located at the boundary between the continuum and rarefied regimes, this particular case was run under a continuum assumption to match the reference numerical simulation. Additionally, numerous flight data from various STS missions with approximately the same flight conditions provided in the

reference study, have also been used here to maximize the amount of data for comparison. The third validation case is based on the work of Hamilton, Greene and DeJarnette (83) as well as on the work of Zoby *et al.* (84) (see Table 3.8). In the study of Hamilton *et al.* (83), the authors validate an engineering method, dubbed LATCH (which stands for Langley Approximate Three-Dimensional Convective Heating), against flight data from the STS-2 mission at an altitude of 46.7 km. The LATCH engineering code is based on the axisymmetric analogue for three-dimensional boundary layers and employs the inviscid flow field solution from the LAURA code to define the local conditions. The second and fourth cases are exclusively based on the aforementioned work of Zoby *et al.* where an approximate method, also based on the axi-symmetric body analogue, is validated against both STS-2 and STS-1 flight data (84). In this fourth and last validation case, the flow along the windward centreline undergoes a transition from a laminar state to turbulence. As mentioned in the paper of Hamilton *et al.* (83), the flow over the windward surface of the Space Shuttle Orbiter has been reported to remain in chemical non-equilibrium down to an altitude of approximately 50 km. Therefore, discrepancies can obviously be expected in the evaluation of the heat transfer for Case 1 and Case 2.

Case 1: Pressure Distribution

The results for the non-dimensional wall pressure along the windward and leeward centreline of the Shuttle Orbiter, obtained using HyFlow, are compared to those from the reference study as well as various flight measurements from the STS-3 and STS-5 missions in Fig. 3.29 (i.e. the pressure values are non-dimensionalized here using the free-stream dynamic pressure Q_∞). The pressure has been estimated using both the modified Newtonian theory and the optimal set of methods defined in the previous section for comparison. On the windward side, the modified Newtonian theory overall predicts very well the centreline pressure distribution over the blunted nose of the Orbiter whereas it slightly under-predicts the pressure distribution over the rest of the vehicle's fuselage (from a fuselage station $x/L = 0.2$). Unlike the modified Newtonian theory, the optimal set of methods predicts with surprising fidelity the pressure distribution over the entire windward centreline of the vehicle. Indeed, as seen in Table 3.7, the pressure over the blunt-nosed region is computed using a mixed approach: the Tangent-Wedge

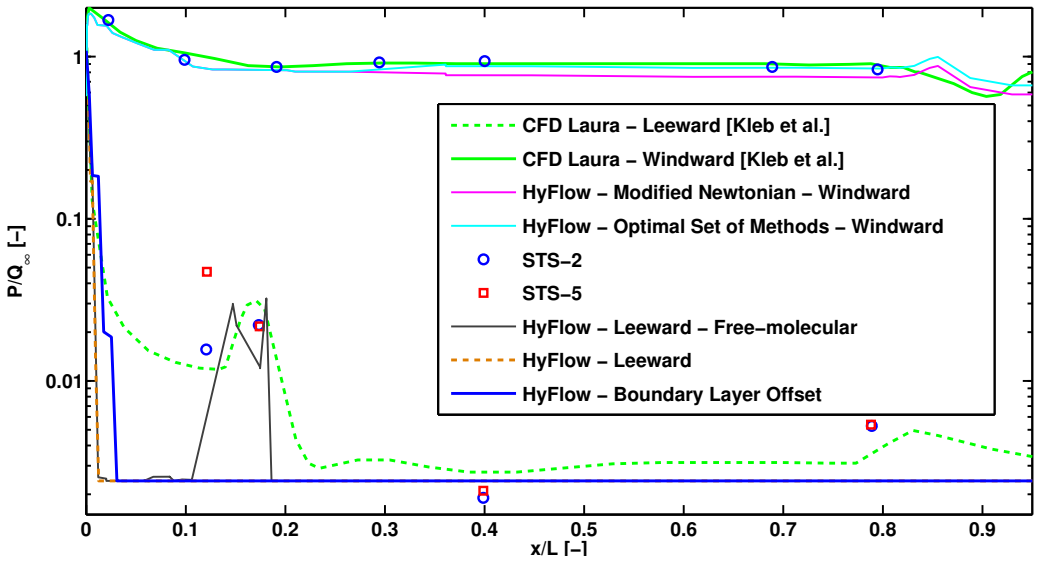

Figure 3.29: Windward and leeward centreline pressure comparisons - Non-dimensional pressure profile along the windward and leeward centerline of the Shuttle Orbiter. The results returned by the reduced-order model are compared to those of the reference CFD study and actual flight data. A logarithmic scale is used on the vertical axis (pressure ratio).

method is used at low angle of attack and the Modified Newtonian theory is instead employed at higher angle of attack. Here, the modified Newtonian theory has clearly been used, between the nose tip and a fuselage station located at $x/L = 0.2$, as it follows the trend of the full Newtonian method over that portion of the windward centreline. Thereafter, in the remainder of the fuselage region, the Tangent-Cone (empirical) method is then used to quantify the wall pressure over that particular region of the flow geometry. Surprisingly, given its application beyond its common speed range, the results follow relatively well the trend of both flight data and numerical results and may thus encourage even further the use of the optimal approach previously described. On the leeward side however, the centreline pressure distribution is slightly under-predicted (albeit, again, the apparent discrepancies are exacerbated by the logarithmic scale employed on the vertical axis), especially over the canopy, at a fuselage station between $x/L = 0.15$ and $x/L = 0.20$, where a "*pressure bump*" is seen. Nonetheless, in order to model the presumed non-continuum effects related to the re-circulation region on the leeward side of the vehicle as the Shuttle Orbiter operates at hyper-velocity and adopts a high angle of attack attitude, a free-molecular flow with diffusive reflections of the impinging molecules has been enforced on the leeward side for

context. The results have been plotted in Fig. 3.29. Interestingly, the local increase in pressure in the region of the canopy seems to be very well predicted. Additionally, the pressure distribution at the ten percent fuselage station has been compared to the numerical and flight data in Fig. 3.30 – i.e. at a fuselage cross-section that belongs to the nose region of the vehicle where pressure estimates are exclusively provided by the modified Newtonian theory. The wall pressure has been plotted against the circumferential angle, denoted ϕ, which is measured from the leeward side symmetry plane (where $\phi = 0$ deg) to the windward symmetry plane (where $\phi = 180$ deg). As can be seen in the figure in question, the transition between the leeward and windward side is marked by an abrupt change in the pressure estimates from those provided by the modified Newtonian theory in the compression region to those in the shadow region where the free-stream pressure value has been enforced. Although the pressure results on the leeward side of the vehicle properly represent the physics involved in that specific region (i.e. an expansion is modelled as a result of a decrease in density and an increase in velocity as the flow passes from the windward to the leeward side of the geometry), the quantitative estimates are however, as already discussed, under-predicted. Finally, a comment is required since at such angle of attack, the flow is expected to be of variable entropy. As suggested in the study of Zoby *et al.* (84), a flow of variable entropy can be approximated by estimating the inviscid flow conditions at a distance away from the wall equal to the local boundary-layer thickness. In HyFlow, the geometry has therefore been offset by the (empirical) laminar boundary-layer thickness and the resulting geometry has then been used in the computation of the wall pressure. For demonstration purposes, the results of such a process has been added in Fig. 3.29 for the leeward side (as the estimates obtained over the windward side only slightly changed compared to the previous results). The resultant effect is to slightly delay the flow expansion over the leeward side of the vehicle.

Case 1: Wall Heat Flux Distribution

In Fig. 3.31, the heat flux profile along the windward and leeward centerline of the Shuttle Orbiter is depicted and compared against several STS missions flight data as well as the reference CFD study. As can be seen, the predictions are quite satisfactory on the windward side of the vehicle. Small scatters in the predictions can be identified, however. Indeed, rearwards of the fuselage station

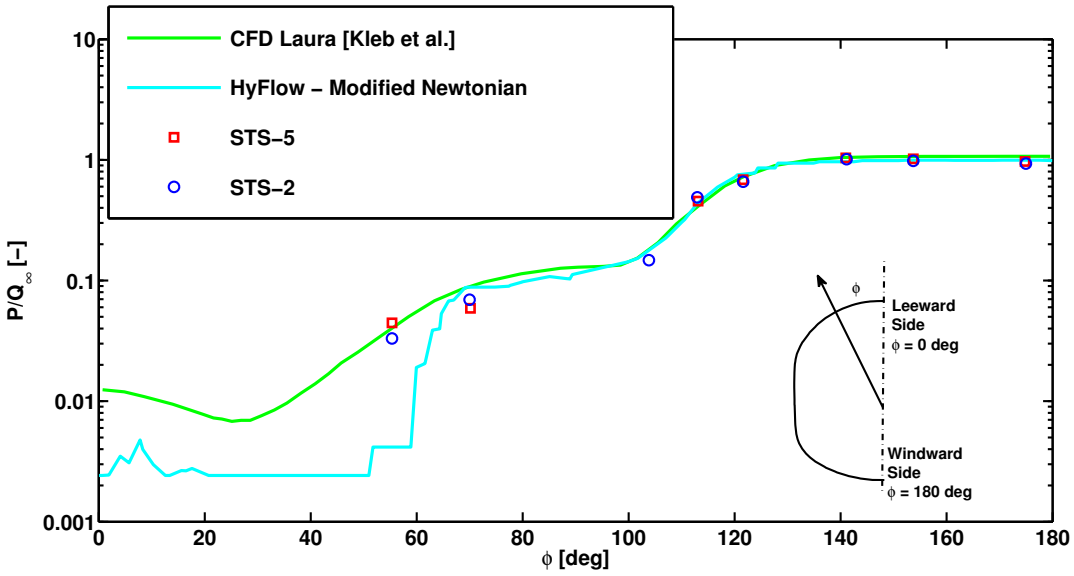

A logarithmic scale is used on the vertical axis (pressure ratio).

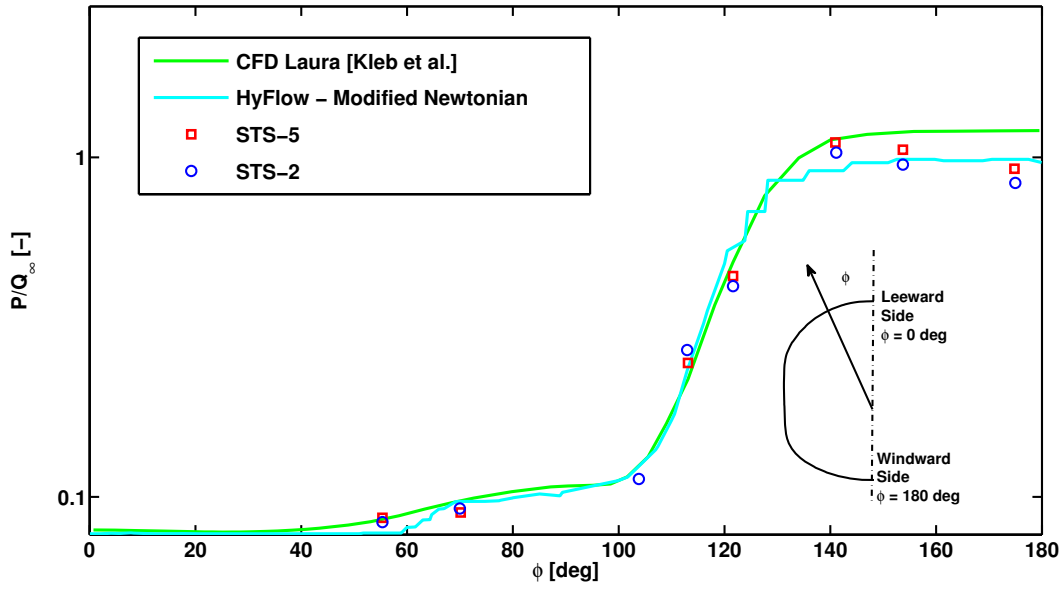

A linear scale is used on the vertical axis (pressure ratio).

Figure 3.30: Lateral pressure distribution at a fuselage station x/L = 0.1 - It shall be remarked that, as in the reference numerical study, the meridional angle, here denoted ϕ, is measured from the leeward side symmetry plane (where $\phi = 0$ deg) around to the windward symmetry plane (where $\phi = 180$ deg).

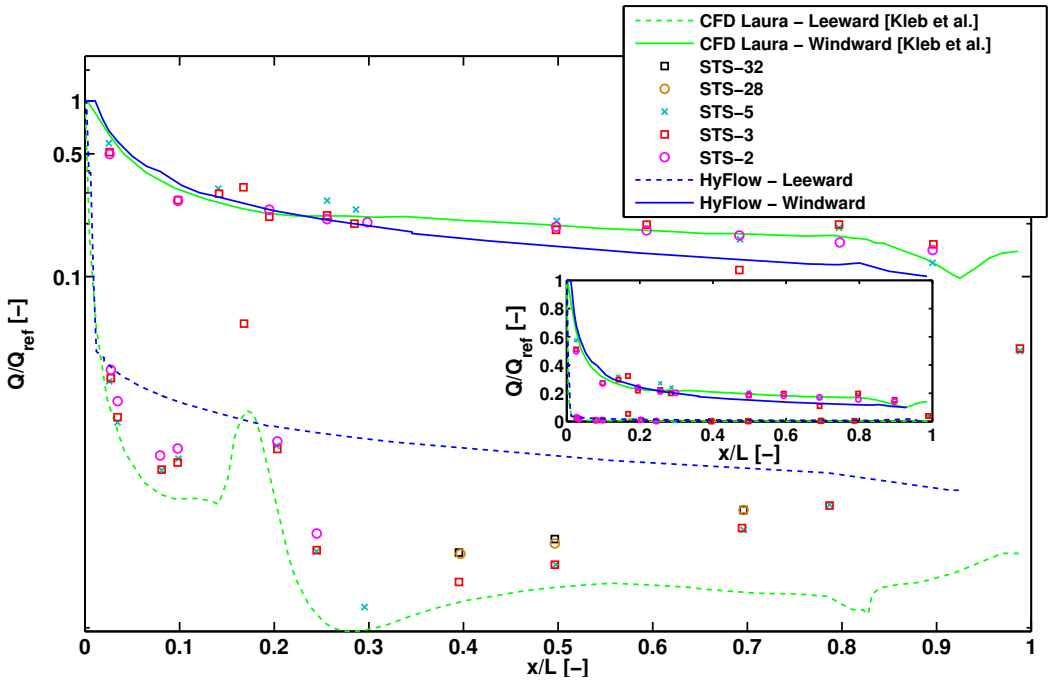

Figure 3.31: Non-dimensional heat flux profile along the windward and leeward centerline of the Shuttle Orbiter for case 1 - The results returned by the reduced-order model are compared to those of the reference CFD study and actual flight data. A logarithmic scale is used on the vertical axis (heat flux ratio).

at $x/L = 0.3$, the accuracy of the estimates deteriorates as the trend provided by the HyFlow code seems to "*plunge*" under that of both the flight data and the results from the reference study. Nonetheless, although it appears at first that HyFlow slightly under-predicts the heat transfer over the rear fuselage of the Orbiter, a flight data point at a station $x/L = 0.7$ confirms that the results provided by the reduced-order model may approximate the actual heat-transfer more closely than can be seen from the figure in question. On the leeward side of the vehicle, the heat transfer estimates appear to be quite over-predicted by the reduced-order model. However, discrepancies are once again exacerbated by the logarithmic scale: a thumbnail of the exact same plot using a linear vertical axis instead is also depicted in the middle of Fig. 3.31 for context.

Cases 2 and 3

In Fig. 3.32, the heat flux profile along the windward centreline of the Shuttle Orbiter is depicted and compared against both flight data from the STS-2 mission as well as the results from the reference approximate method of Zoby *et al.* (84).

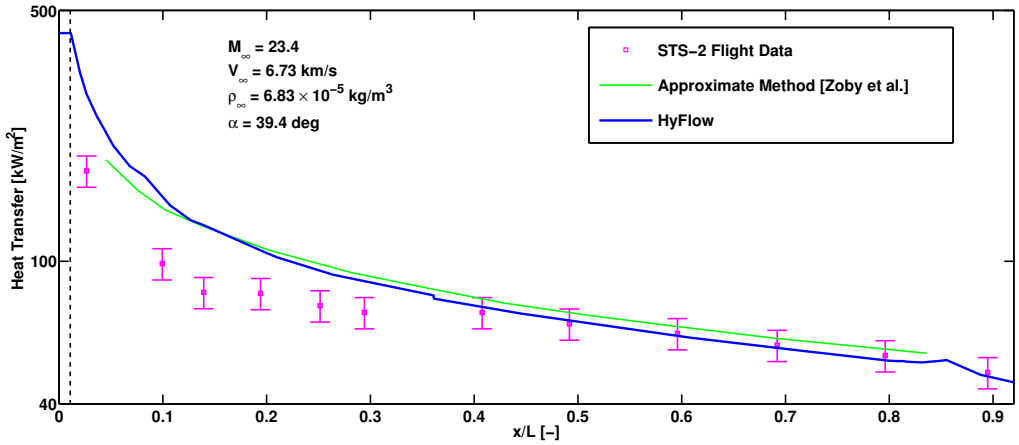

Figure 3.32: Heat flux profile along the windward centerline of the Shuttle Orbiter for case 2 - The results returned by the reduced-order model are compared to those of the reference approximate method and actual flight data. A logarithmic scale is used on the vertical axis (heat flux). It shall also be remarked that the dotted vertical line in the figure represents the extent of the stagnation region of influence as defined in Chapter 2.

Additionally, an uncertainty bound of ± 10 % around the values extracted from the STS-2 mission has been added to each experimental point (84). The level of heat flux along the windward centreline is clearly well captured by HyFlow. HyFlow indeed follows the results from the approximate method over all fuselage stations where a direct comparison is possible (between $x/L = 0.06$ and $x/L = 0.84$). As for the reference approximate method, the largest discrepancies can be observed from the nose-tip to a station $x/L = 0.4$ along the fuselage of the Orbiter where it can clearly be noticed that both engineering methods appear to over-estimate the flight data.

In Fig. 3.33, the heat flux profile along the windward centreline of the Space Shuttle Orbiter is depicted and compared against the flight data from the STS-2 mission along with the results from the reference approximate method of Zoby *et al.* as well as the results from the LATCH engineering code. Although the predictions from HyFlow seem to very slightly over-predict the flight data, these estimates are however very satisfactory (i.e. as a small amount of conservatism is often required in preliminary design studies). Additionally, it can be seen that from a fuselage station $x/L = 0.4$, HyFlow appears to follow the trend of the results provided by the LATCH code whose inviscid local conditions are obtained via the high-fidelity LAURA CFD code. Furthermore, a series of cross-

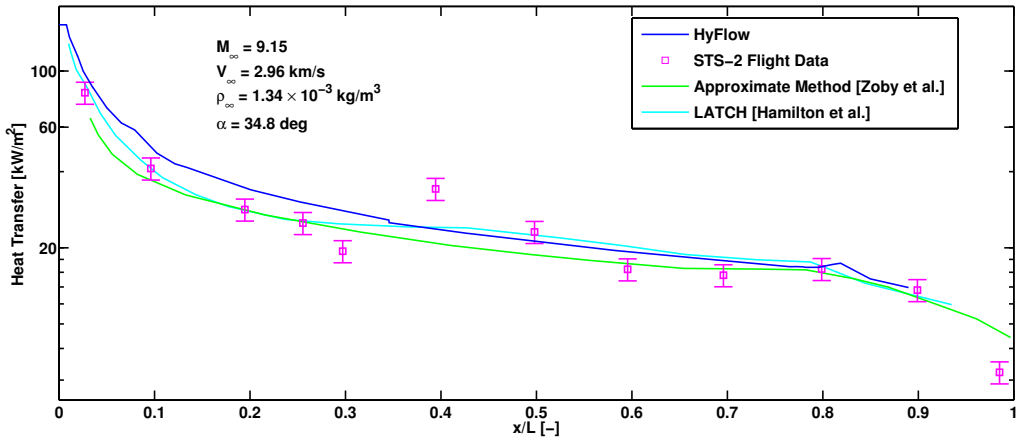

Figure 3.33: Heat flux profile along the windward centerline of the Shuttle Orbiter for case 3 - The results returned by the reduced-order model are compared to those of the reference approximate methods and actual flight data. A logarithmic scale is used on the vertical axis (heat flux).

sections along the fuselage of the vehicle for Case 3 have been defined and the lateral heating distribution on the Shuttle Orbiter obtained via HyFlow has been compared against the reference study of Hamilton *et al.* (83) in Figs 3.34 and 3.35. At a fuselage station $x/L = 0.1$, the estimates from the HyFlow code seem to follow quite closely the trend defined by the flight data over the windward side of the fuselage. At a fuselage station $x/L = 0.4$, the small increase in heat flux over the tip of the forward strakes is not predicted by HyFlow (i.e. resulting in about 30% error in the predictions), otherwise, the results are in agreement with both those from the reference LATCH method as well as from the flight data closer to the symmetry plane. At a fuselage station $x/L = 0.6$, the increase in local heat flux at the leading edges of the wings is well predicted by HyFlow but not to the extent depicted by both the LATCH code and the experimental data. At a fuselage station $x/L = 0.7$, the level of heat flux over the leading edges of the wings is very well predicted by the reduced-order model. Finally, it shall also be remarked that for all these cross-sections, the heat transfer over the leeward side of the vehicle is slightly over-predicted by HyFlow.

Case 4

In Fig. 3.36, the heat flux profile along the windward centerline of the Shuttle Orbiter is depicted and compared against a series of flight data as well as the

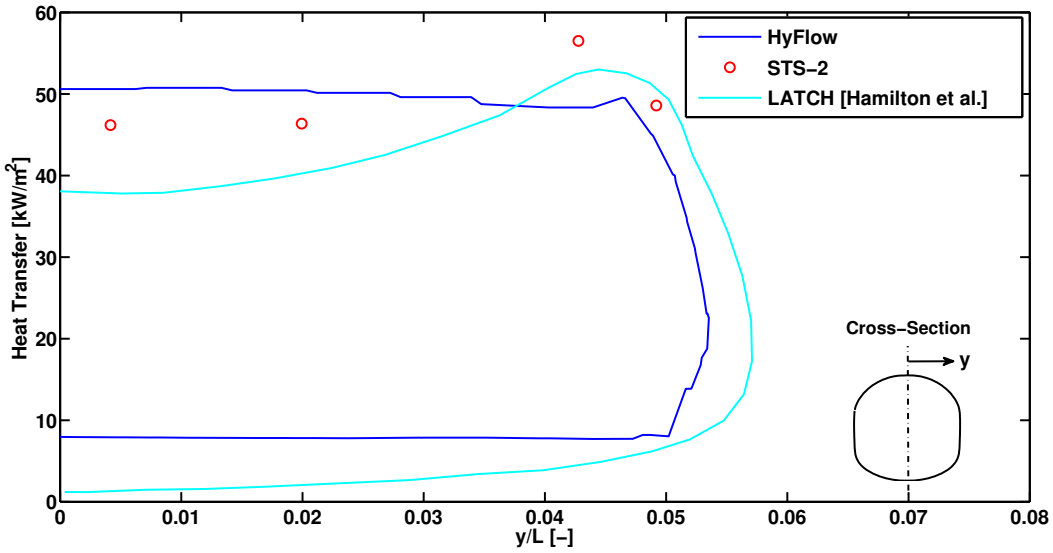

Fuselage Station x/L = 0.1

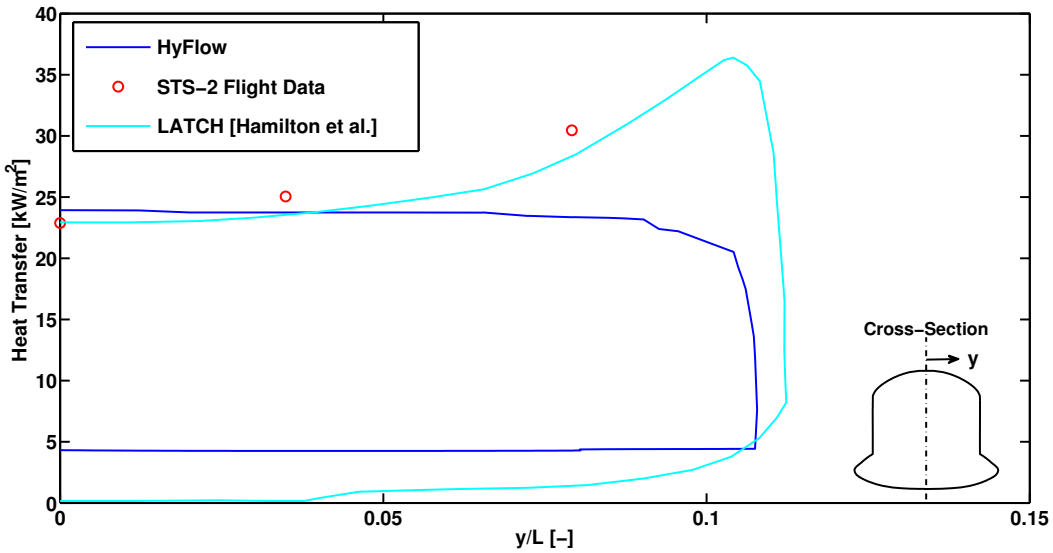

Fuselage Station x/L = 0.4

Figure 3.34: Lateral heating distribution on the forward fuselage of the Space Shuttle Orbiter for case 3.

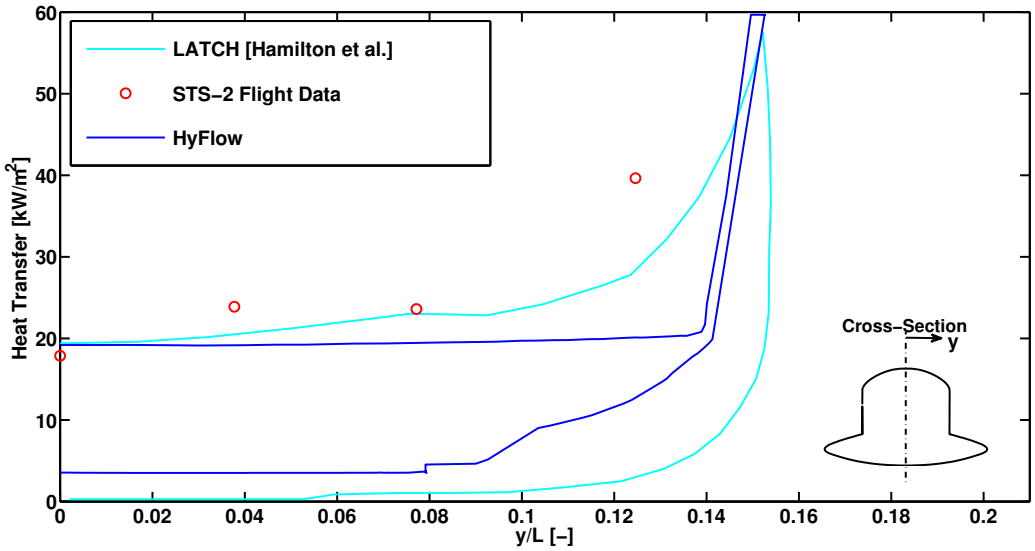

Fuselage Station x/L = 0.6

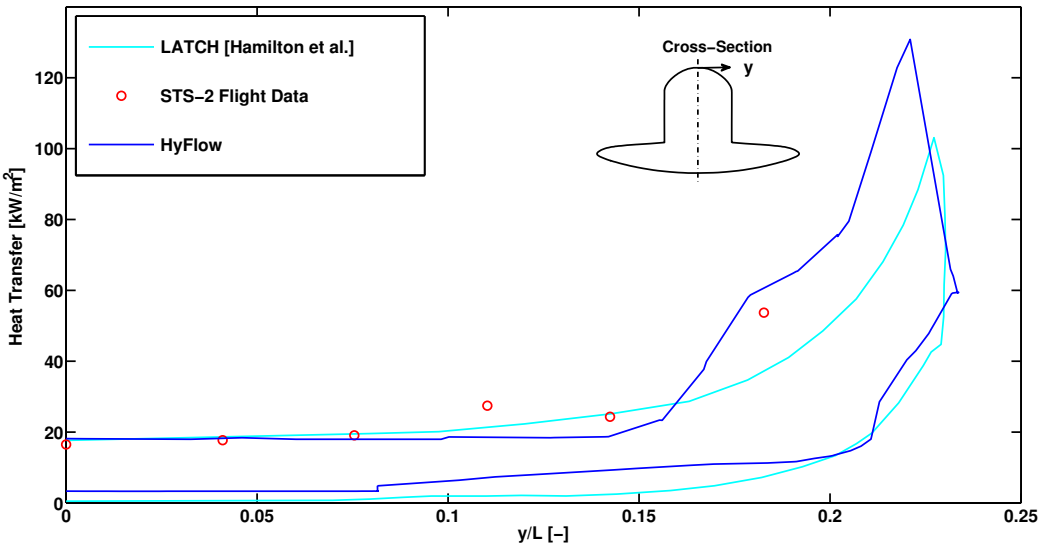

Fuselage Station x/L = 0.7

Figure 3.35: Lateral heating distribution on the rear fuselage of the Space Shuttle Orbiter for case 3.

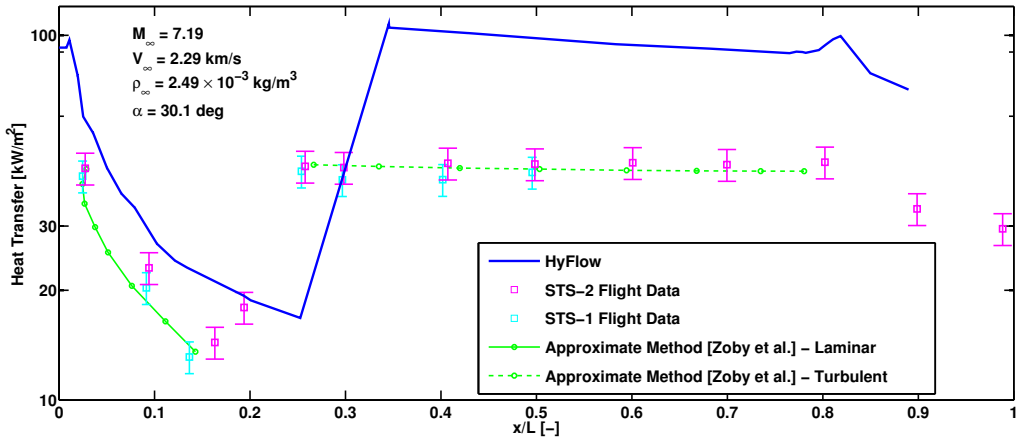

Figure 3.36: Heat flux profile along the windward centerline of the Space Shuttle Orbiter for case 4 - The results returned by the reduced-order model are compared to those of the reference approximate method and actual flight data. A logarithmic scale is used on the vertical axis (heat flux).

reference approximate method of Zoby *et al.* (84). While the results in the laminar section are representative of those provided in previous cases, those in the turbulent region show an important over-prediction in the level of heat transfer provided by the HyFlow code (i.e. by about a factor 2). Nonetheless, the extent of the turbulent region over the windward side of the vehicle is well predicted by the engineering code (i.e. here, the effective Reynolds number at which transition occurs has not been scaled).

3.4.3 Discussion

The aerodynamic load coefficients as well as the wall pressure and heat transfer distribution over both the windward centreline and a series of fuselage cross-sections returned by the engineering code for a range of simulation conditions can be considered fairly satisfactory given the low fidelity level intended by the model as well as its reduced computational effort (i.e. about a minute). Nonetheless, as it was expected (see discussion in Section 2.8 of Chapter 2), the leeward side of the vehicle appears here to be poorly treated and will thus require further investigations in order to properly model the flow physics in that often neglected region of the flow field. To conclude, the miscellaneous test cases for the Shuttle Orbiter provide a sufficient proof that the HyFlow code can be used and form the

basis of a suitable method for the study of the aero-thermodynamic environment of future re-usable winged configurations at a preliminary design level.

3.5 Chapter Summary

In this chapter, a number of geometries have been used to validate the HyFlow engineering code for a range of simulation conditions spanning from high-altitude re-entry conditions down to the low hypersonic regime. It has been shown that the present reduced-order model can provide valuable information in the study of hypersonic vehicle configurations if used within the limits of its applicability. Indeed, the various results obtained throughout this series of validation cases give confidence in the ability of HyFlow to provide predictions that are reasonably satisfactory. In fact, HyFlow predicted well crucial properties such as the wall pressure, aerodynamic loads and surface heating (i.e. especially in terms of the location and extent of the regions of maximal heating on the surface of the vehicle). HyFlow can also simulate accurately complex flow phenomena such as the boundary layer transition from a laminar state to turbulence, phenomena that are essential to model correctly when globally optimizing the aero-thermal design of future re-usable winged launchers (85).

Finally, these various results could, for instance, be corrected by reference to the predictions of a more sophisticated numerical analysis – i.e. mapping of the local edge properties similar to the process used by the LATCH code or anchoring the estimates provided by the reduced-order model at a number of representative conditions using high-fidelity CFD results. An anchoring process was presented by Kinney in order to derive a database of aero-thermodynamic properties for the Orion capsule-like vehicle using CBAERO in conjunction with the LAURA code (22). In doing so, it is believed that the present reduced-order method would most likely be capable of reproducing the results of the more complex methods, and thus of acting as their exact surrogate in MDO studies.

Nomenclature

List of Symbols

C	Aerodynamic coefficient
L	Body length
M	Mach number
P	Pressure
Q	Heat transfer rate
q	Dynamic pressure
Re	Reynolds number
R_N	Nose radius
R_s	Scaling factor
S	Surface area
T	Temperature
V	Velocity
x	Distance along the longitudinal axis
y	Distance along the transversal axis
α	Angle of attack
η	Effective angle of attack
ρ	Density
ϕ	Circumferential angle

Subscripts

A	Axial force
D	Drag force
$edge$	Boundary layer edge condition
L	Lift force
m	Pitching moment
N	Normal force
ref	Reference parameter
s	Stagnation condition
t	Transition
wt	Wind tunnel results
Hy	HyFlow results
∞	Freestream condition

Chapter 4

System Modelling

This chapter marks the transition from a fluid-based view of the formulated hypersonic problem to its intended more global "*system*" perspective. In doing so, this chapter introduces a novel multi-disciplinary design approach developed to assist in the rapid preliminary design of some of the critical system components of the next generation of re-usable space-access vehicles. Section 4.1 gives an overview of the various challenges encountered in the modelling of such complex aerospace systems and introduces the general organization of the system model. From Section 4.2 to Section 4.5, each of the aforementioned subsystem models, presently used to evaluate the overall performance of a Re-usable Launch Vehicle (RLV) during concept exploration, is presented. Then, Section 4.6 provides a definition and possible means of coping with some of the major couplings between system components. Finally, the present chapter finishes with some preliminary conclusions in Section 4.7.

4.1 Introduction

The multi-disciplinary design of future Space Transportation Systems (STS) is characterised by a large number of technical challenges that require a simultaneous attack using the full range of engineering disciplines. Exposure to the severe heating environment that always accompanies hypersonic flights is a source of particular concern for the designers when assessing the performance of this new generation of vehicles. Additionally, it is fundamental that the safety and reliability of the vehicle are assured when planning the trajectories of such vehicles.

For example, the controls of the vehicle have to steer the re-entry trajectory along a corridor that is heavily constrained by both structural and aerodynamic heating considerations. Indeed, future trans-atmospheric vehicles will, by means of a complex hybrid propulsion system (e.g. Rocket-Based Combined Cycle), accelerate up to orbital speed when still within the denser part of the terrestrial atmosphere. The high velocity of the vehicle, when combined with the high air density in the lower atmosphere, will expose it to a severe heating environment. By contrast, during atmospheric entry at very high speeds, the same vehicle will most likely follow an un-powered gliding trajectory during which deceleration to lower velocities will occur at high altitude where the density of the air is relatively low. Although it may be possible to design the trajectory of the vehicle so that the peak heating during descent may be somewhat lower than that experienced during ascent, the integrated heat load that will need to be dissipated or absorbed by the vehicle will not be very much different between the ascent and descent phases of its mission. Nonetheless, despite the severe heating conditions to which future space-access vehicles will be exposed, there will be strict emphasis on their full re-usability in order to ameliorate their acquisition cost over multiple missions. Part of this strategy will also be to limit costs by reducing the amount of maintenance and refurbishment that is required between flights. Indeed, a careful balance needs to be struck between the robustness of the Thermal Protection System (TPS) and the resultant mass of the vehicle without incurring later penalties in terms of operational cost and maintenance time. In fact, as mentioned previously, one of the many lessons learned from the Space Shuttle programme was how sensitive the economics of a re-usable vehicle could be to the robustness and maintainability of its TPS.

4.1.1 Thermal Control Challenge

The design of efficient thermal structures, that are capable of long-life operations even in the severe heating environment associated with the vehicle's ascent and subsequent entry, is an extremely complicated task. Designers will thus, in all likelihood, find themselves forced to employ a new approach to the design of the vehicle's TPS. This will almost certainly result in a switch from the classic insulated aircraft approach, *à la* Space Shuttle, to the use of a combination of passive, semi-passive, and active TPS (86). The resulting thermal shield will most likely make use of both lightweight protective materials and a complex Active

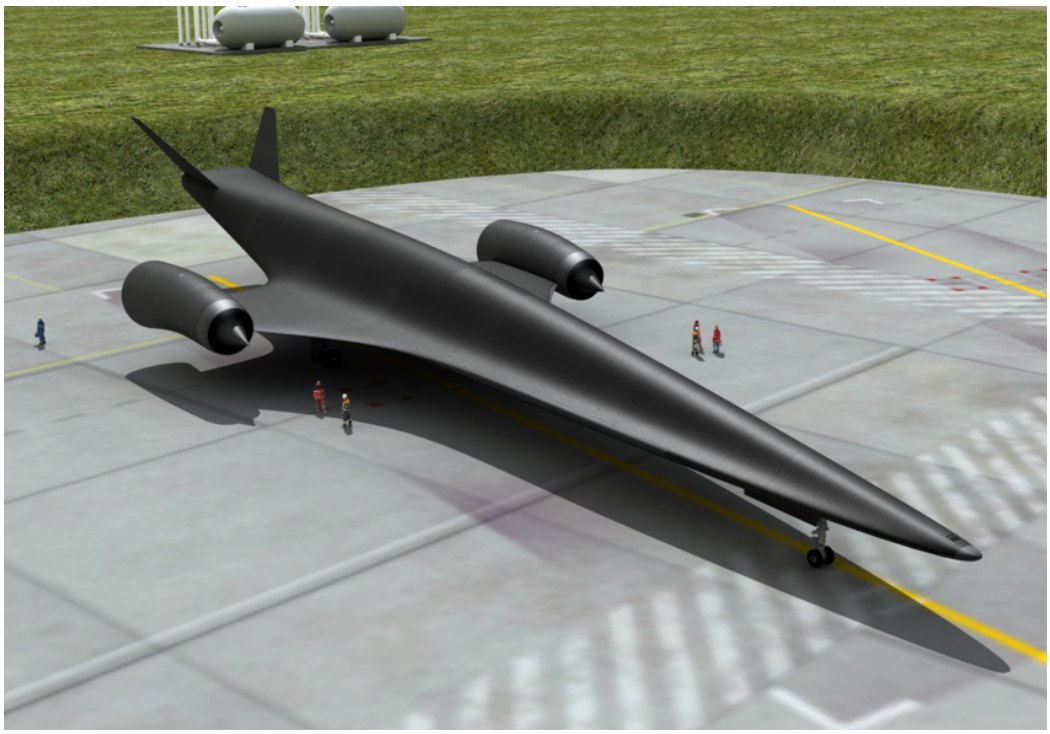

Figure 4.1: The CFASTT-1 SSTO vehicle during maintenance operations - Artist impression of the CFASTT-1 launch concept during ground-hold operations (original graphic by Adrian Mann).

Cooling System (ACS) involving the re-circulation of a coolant through the most severely heated parts of the structural skin (e.g. leading edge of the wing, blunted nose etc.). The most plausible thermal management strategy might indeed result from a marriage between the active cooling approach and the radiative heat shield technology that was originally developed for advanced re-entry vehicles (e.g. Space Shuttle's reinforced carbon-carbon tiles). Thermal shields of either kind often end up occupying a sizable proportion of the vehicle's weight (i.e. reduce payload-to-mass ratio), not to mention being the focus of maintenance and repair efforts during the operational life of the vehicle. Therefore, the careful selection of an optimal and adequate thermal methodology (most likely to be a structurally integrated thermal protection system), that could potentially ensure that the concept of "full re-usability" becomes, in fact, technically and economically within the realms of possibility, offers a large number of technical (and technological) challenges to the thermal designer. Additionally, sizing the TPS exclusively for the high-temperature conditions to which the vehicle might be exposed during its mission may not necessarily ensure that the vehicle will meet all of its performance requirements. Indeed, future re-usable space-access vehicles

will be held at a spaceport for a short period of time between missions in order to fill their cryogenic propellant tanks and perform necessary maintenance tasks as illustrated in Fig. 4.1 (i.e. mission preparation phase). Therefore, during these ground-hold operations, the vehicle will be exposed to ambient sea-level conditions, as opposed to the very high temperatures that characterize their in-flight mission profile. Heat transfer from the atmosphere to the surface of the vehicle will thus be primarily convective and take place at a much lower rate than when the vehicle is in flight. The materials that cover the cryogenic tanks might then need to be sized to prevent the formation of ice on the outer surface of the vehicle prior to launch. Ice formation has the potential to be extremely hazardous, of course, given the aerodynamic and mass penalties that it would induce. In fact, ice or frost accumulations over the surface of these vehicles could also represent a threat to future space-access vehicles as a result of their uniquely complex shape and the possibility that brittle materials (such as ceramic materials) might be used for their TPS. Indeed, ice chunks may detach from the vehicle's surface and hit other downstream parts of the vehicle at take-off; in fact, this prospect was a source of critical concern in the early design of NASA's Space Shuttle (87).

4.1.2 Hybrid Propulsion Systems

This new generation of space-access vehicles is also foreseen to make use of hypersonic air-breathing engines, in particular ramjets or scramjets, in order to achieve the performance required for practical attainment of a Single-Stage-To-Orbit (SSTO) capability. Indeed, supersonic combustion is widely accepted to be the most promising alternative to the use of conventional rocket engines in this context. Instead of carrying separate tanks for fuel and oxidizer during take-off, scramjet-powered vehicles will theoretically need only to carry the fuel, using atmospheric oxygen for combustion. Although air-breathing engines are characterized by a much higher specific impulse than rockets, scramjets are subject to strong engine-airframe coupling, adding significant complexity to the design of the vehicle (12). Furthermore, in the realm of hypersonic systems, high specific impulse cryogenic propellants such as liquid hydrogen, liquid methane, and possibly liquid oxygen are envisioned to be utilised. The various handling problems related to the storage of these cryogenic propellants inside of the fuselage of future re-usable space-access vehicles is another major concern. The choice of propellant can indeed have a significant influence on both the geometry of the configuration

and the approach to the propulsion system employed by this new generation of hypersonic vehicles. In fact, the low density of liquid hydrogen propellant, often regarded as the option of choice for space transportation applications as a result of its high energy per unit mass (i.e. 116.7 MJ/kg) (88), requires a large volume for storage and therefore necessitates a large fuselage which, in turn, leads to a reduction in the ratio of lift-to-drag (89). This instance tends to justify why recent research worldwide is looking at a number of approaches that might possibly increase the density of hydrogen propellants – for instance through processes such as sub-cooling, metal addition and gelling. Additionally, cryogenic tanks will most likely be attached directly to the structural skin of the vehicle (integral tank configuration) and will then serve an additional load bearing function. Since the cryogenic propellant may also be used to regeneratively cool parts of the vehicle (such as the leading edge of the wing and the structure of the air-breathing engine), the entire structure may then be subjected to quite significant loads as a result of thermal cycling. Therefore, new materials such as fibre composites are necessary to provide both the required additional structural strength and to decrease the weight of current cryogenic fuel-tanks, i.e. to obtain an economically competitive payload-to-mass ratio. Therefore, the development of flight-weight cryogenic tanks represents an additional technological challenge, and the behaviour of re-usable fuel tanks, in their broader context – when these are subjected to both sub-cool temperatures due to cryogenic fuels and to hypersonic aerodynamic heating – must thus be carefully analyzed from early in the development programme.

4.1.3 Vehicle System Modelling

These various characteristics, inherent to this future class of hypersonic vehicles, emphasize the need to derive and employ a very robust methodology that both embeds a sufficient amount of detail and covers the number of critical disciplines required to design and optimise future trans-atmospheric configurations efficiently at a system level. A multidisciplinary design methodology must perforce be used and applied for both the ascent and re-entry phases of the vehicle's mission in order to optimize concurrently the various subsystem components to a point where the SSTO concept may become technically feasible. In fact, the successful multi-disciplinary design of future trans-atmospheric vehicles requires the development of an integrated multi-disciplinary environment that is itself

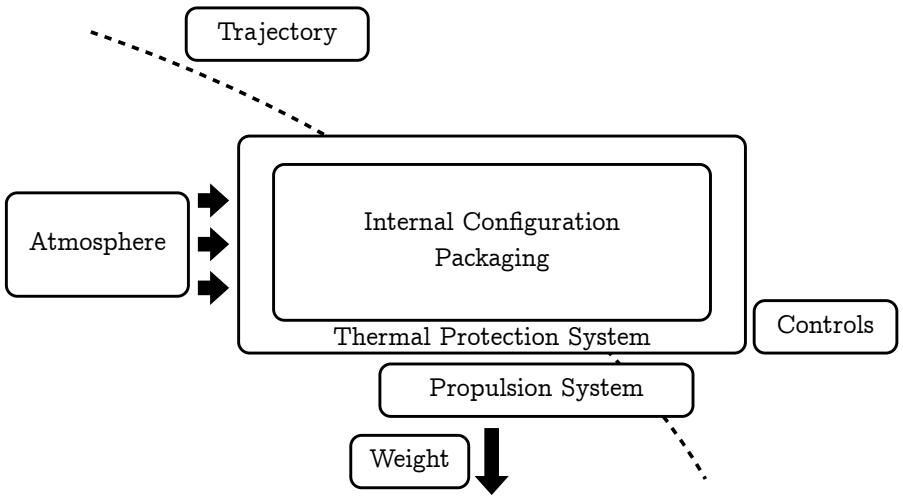

Figure 4.2: Architecture of the system model - The diagram represents the various system components used to represent the overall configuration of the vehicle. Each of these models are described in detail in the present chapter.

highly optimized and specialised for the modelling, design and, in turn, the optimization of the hypersonic vehicles to which it will be applied. To be efficient when used for concept exploration, multi-disciplinary optimisation or preliminary design, such preliminary modelling environment must emphasize computational *efficiency*, *modularity* and *accuracy* of its performance predictions. An integrated multi-disciplinary design environment, implemented in the context of Matlab's Object-Oriented Programming (OOP) framework and solely dedicated to the design of re-usable space-access vehicles, has therefore been developed and combined with the HyFlow reduced-order model for the analysis of hypersonic vehicle configuration at a conceptual design level. The hypersonics literature reports similar attempts at designing integrated design environments, such as the design/analysis methodology for rapid assessment and optimization of scramjet-powered vehicles of Starkey *et al.* (90) called the University of Colorado Vehicle Design and Analysis Code (UCDA). Their design environment connects a series of *in-house* tools together with third-party software to provide full Aero-Servo-Thermo-Propulso-Elastic (ASTPE) analysis capabilities for the preliminary design of waveriders. NASA's IDEA (which stands for Integrated Design and Engineering Analysis) environment (10) is another example of such integrated design platform tailor-made for the preliminary design of future launch system configurations, i.e. from staged launchers to advanced TSTO (Two-Stage-To-Orbit) and SSTO concepts. Their design environment relies in parts on reduced-order modelling with plans

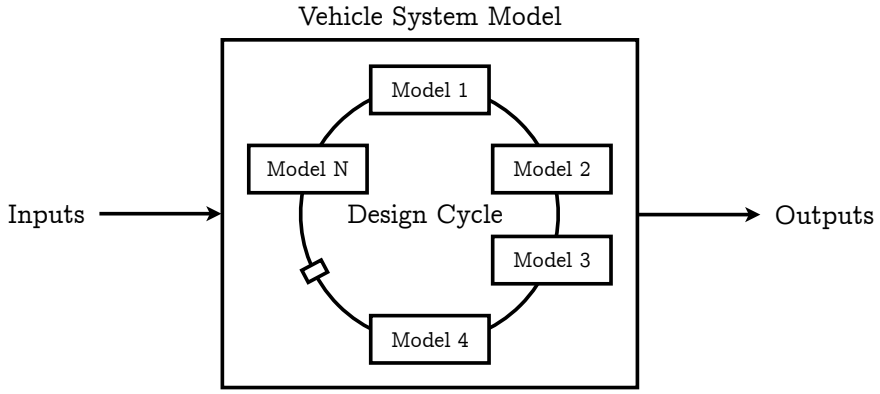

Figure 4.3: Black-box approach - The vehicle is defined as a *black box* composed of a series of inter-connected subsystem models also adopting the self-contained *black-box* type of organization.

to combine tools with different levels of fidelity.

In the present work, a spaceplane is conceptually represented by a system model discretized into a series of inter-connected system components (illustrated in Fig. 4.2). The resulting design environment can be used to predict the overall performance, mass and trajectory of the vehicle, to concurrently size the active and passive thermal shields, organize the internal configuration of the vehicle, and finally to evaluate the performance of the propulsion system as well as the overall mass of the system as required. This systemic and synergistic platform has been implemented and prototyped in the framework of OOP in order to provide modularity and versatility to the overall computer code and thus to facilitate the various couplings between the embedded models that are often required when dealing with such complex aerospace systems (see discussion in Section 4.6). In fact, all the vehicle system components have been organized into self-contained *black boxes*. This particular type of software architecture can be used efficiently to facilitate the communication between the system components during the design process (see Fig. 4.3). Therefore, although the system model has been conceived to be used in a fully integrated framework, the intrinsic modularity and flexibility of the object-oriented structure allows it to easily be modified so that new features and/or subsystems may ulteriorly and conveniently be added without having to alter the underlying architecture of the software. In doing so, the hybrid propulsion system model, dubbed HyPro and described in Section 4.4 (76), developed in C++ as a stand-alone external tool, could successfully be connected to the rest of the relevant set of subsystem models – e.g. in the study of Wuilbercq,

Mogavero, Pescetelli, Minisci and Brown (14), HyPro has been connected to the present flight model along with the HyFlow engineering code for the study of the ascent trajectory planning of re-usable space-planes (see Section 5.3 of Chapter 5). Here, the system model has been divided into four core modules (i.e. five with HyFlow) defined as critical in the study of hypersonic vehicles and includes

- a *Flight Simulation Model*, presented in Section 4.2, that can be used to compute the trajectory and corresponding performance of space-planes over their ascent and entry missions. The model can be used to run simulations in three Degrees-of-Freedom (3 DoF). The model can also be used determine an adequate schedule of control surface deflection angles,
- a *Thermal Protection System Model*, introduced in Section 4.3, that can be used to create (hybrid) active and passive thermal shields employed to protect future re-usable space-access vehicles from the severe heating environment that develops at hypersonic speeds,
- a *Propulsion System Model*, presented in Section 4.4, that can be utilized to define hybrid engines such as Rocket-Based Combined-Cycle engines (RBCC),
- and a *Mass Model*, discussed in Section 4.5, that can deal with both the internal arrangement of the vehicle and estimate the individual contribution of major system components to the overall weight of the system.

Since, in general, both the ascent and subsequent entry trajectories of future re-usable space-access vehicles must first be ascertained before both the heat transfer rates and aerodynamic loads can be evaluated (35), the flight model is the first *subsystem component* (or discipline) to be described in Section 4.2.

4.2 Flight Simulation Model

The next generation of re-usable launchers is foreseen to employ the lifting body principle which implies that their resulting configurations will, in all likelihood, be aircraft-like and make use of wings (see Chapter 1). As a result, these vehicles will be capable of greatly modifying their entry and ascent trajectories throughout the various layers of the terrestrial atmosphere and will also be able

to re-enter at smaller negative flight path angles, i.e. resulting in a reduction of the integrated thermal load (91). These lifting configurations are therefore endowed with the ability to have a greater control over their landing site (critical for range modulation) but will also be provided with the unique ability to fly back to their launch site in case of an adverse abort mission scenario which is a significant requirement for securing airworthy operations. For instance, in July 2014, the UK government's Review of Commercial Spaceplane Certification and Operations technical report (92) ascertained that abort events that "*can occur within the air-breathing mode, during transition to rocket mode, during the rocket mode within the atmosphere and finally an abort to orbit could be carried out*" and therefore, such mission scenarios need, in general, to be addressed from early within the development programme (albeit those may be beyond the scope of the present dissertation work).

Hence, the type of re-entry approach discussed here, first adopted by NASA's Space Shuttle, makes use of a manoeuvring re-entry flight corridor. Indeed, historically, the Space Shuttle has demonstrated that through a series of sharp banking manoeuvres (during which the spaceplane is rolled to create a side force) - also known as s-turns - the vehicle may be able to increase its deceleration rate and change its heading. On the other hand, these repeated banking manoeuvres increase both the heat transfer rates as well as the normal acceleration (i.e. load factor) acting on the vehicle. However, the resulting increase in surface heating that accompanies this series of manoeuvres can be spread out over a larger portion of the trajectory by an optimal modulation of the bank angle, here denoted by μ, in order to maximize the vehicle's deceleration while preventing it from exceeding either the temperature and structural limits of its constituting material or the maximum allowable heat transfer rate. Therefore, the preliminary modelling and optimisation of the dynamic motion of future space transportation systems (trajectory planning) must account for the possibility to modulate the bank angle and angle of attack throughout the vehicle's trans-atmospheric path in order to allow for flight manoeuvres and aerodynamic control, i.e. out-of-plane motion.

In the present section, the environment in which space-access vehicles will be operating is first introduced in Section 4.2.1. Then, the equations used to describe the translational motion of winged RLVs will be discussed in Section 4.2.2. Finally, the approach adopted here to model the control surfaces will be explicated in Section 4.2.3.

4.2.1 Atmosphere and Planet

The static atmospheric characteristics (namely temperature T_∞, pressure P_∞, density ρ_∞ and speed of sound a_∞) follow the 1976 US Standard Atmosphere model (93) up to an altitude of $1,000$ km (see Fig. 4.4). In the present model, the atmosphere is assumed to be composed of two distinct regions: the lower atmosphere below 86 km altitude and the upper atmosphere from 86 km to $1,000$ km altitude. It should also be remarked that the model does not account for the effects of wind and the Earth is represented by the equipotential World Geodetic System 84 (WGS 84) ellipsoid model.

Lower Atmosphere

The lower part of the terrestrial atmosphere is partitioned into a number of different regions expressed in terms of geo-potential height and the model assumes a perfect mixing of the air constituents. From sea-level to 86 km, it is further assumed that air is composed of the same gases in similar proportions. These two assumptions, which imply that the molecular weight of the air is the same at all altitudes (i.e. constant mean molecular weight M_{air}), allow the use of the simple hydrostatic equation to compute both free-stream pressure and density as

$$dP = -g(h)\rho dh \tag{4.1}$$

where $g(h)$ is the altitude-dependent acceleration of gravity later introduced in Eq. 4.2.

Upper Atmosphere

For the upper atmosphere however (i.e. above 86 km), the approximations made for the lower atmosphere become invalid. Indeed the process of dissociation of air molecules in this region constitutes one of the main reasons for the breakdown of these intrinsic assumptions. This is because in the upper atmosphere, the diatomic gases that compose atmospheric air, namely oxygen and nitrogen, are constantly breaking apart into separate atoms and continually combining back into molecules. Therefore, above 86 km altitude, most of the oxygen is to be found in its atomic form unlike nitrogen which seems to be less sensitive to molecular

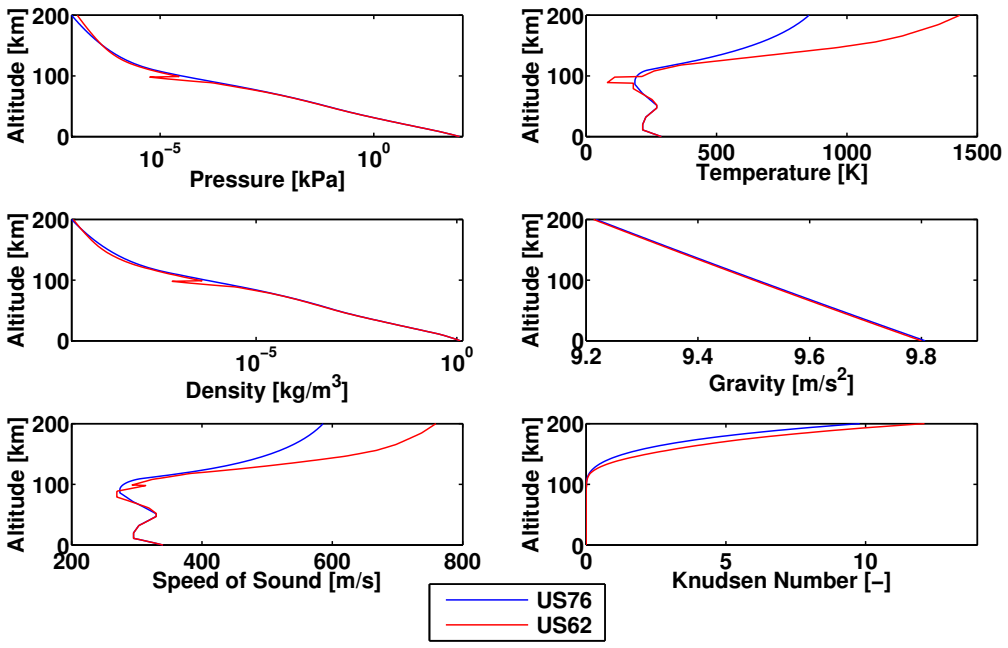

Figure 4.4: US76 and US62 atmosphere models - A comparison between the most recent US Standard 76 atmosphere model used in the current system model up to 1,000 km (red line) and the US Standard 62 atmosphere model (blue line, i.e. also included in the system model). The two models differ above 32 km altitude. The Knudsen number plot (bottom-right) was obtained using the mean aerodynamic chord of a representative STS as the reference length.

dissociation. Furthermore, in the upper atmosphere, that non-uniformity of the composition of the atmosphere is also the result of molecular diffusion. Indeed, without the turbulence and mixing that takes place in the lower regions of the atmosphere (also known as "regions of mixing"), the lighter gases have the tendency to rise while the heavier ones fall. In the upper atmosphere, atomic oxygen becomes therefore more plentiful than diatomic nitrogen as a result of its lighter weight - i.e. atomic oxygen has a molecular weight of 16, while the diatomic nitrogen possesses a molecular weight of 28. Therefore, the treatment of the upper atmosphere requires numerical integration to determine the number densities of the major constituents of atmospheric air, namely diatomic nitrogen, atomic oxygen, diatomic oxygen, argon, helium, and hydrogen. Taking inspiration from the work of Pietrobon and his original computer code (94), the number density of each air constituent, denoted n_i, is numerically integrated using Simpson's rule with a 10 m integration step – i.e. which gives an accuracy within 0.05 % – from which the remaining atmospheric properties can be computed. The number density, n_i, corresponds to the number of atoms or molecules in a mass m_i of

the i^{th} constituent of air (whose molecular weight is equal to M_i) and is given by $n_i = \frac{m_i \mathcal{N}_{av}}{M_i}$ (where $\mathcal{N}_{av}$ is the Avogadro's number).

Gravity Model

Finally, the gravitational acceleration, denoted g, is assumed to vary with altitude according to an inverse square law as

$$g(h) = g_{sea} \left(\frac{h}{R_e + h} \right)^2 \tag{4.2}$$

where h denotes the geodetic altitude above mean sea-level, $R_e = 6378.137$ km is the mean radius of the Earth, and $g_{sea} = 9.80665$ m/s^2 is the gravitational acceleration at sea-level.

4.2.2 Equations of Motion

As opposed to commercial airplanes, operating within the upper layer of the troposphere at approximately 10-12 km altitude, thereby permitting the use of the flat Earth reference frame approximation (and simplified atmospheric models) to perform preliminary trajectory analyses, trans-atmospheric vehicles will operate from sea-level conditions to space across a range of altitudes at which the flat Earth approximation can no longer be employed. In fact, preliminary trajectory analyses must account for both the curvature and angular rotation of the planet in order to model accurately the motion of space transportation systems during both their ascent-to-orbit and subsequent entry missions. The first step in examining the trans-atmospheric trajectory of future RLVs is to develop a set of equations to describe their motion. The set of equations derived here is similar to that described in the book of Vinh, Busemann and Culp (95) for the motion of a vehicle around a spherical, rotating planet. The translational motion of the vehicle along its trajectory is governed by a set of three kinematic equations and three dynamic equations. Here, the vehicle is dynamically represented by a simple point with varying mass. The derivation of these equations is well presented in the aforementioned reference and therefore, only some major steps are provided herein.

First, a number of key mathematical concepts used in the subsequent derivation of the dynamical system are briefly introduced. However, for more detail, the interested reader is referred to the referenced textbook (95) as well as the very comprehensive technical report of Mooij (96). Here, the transformation from one frame to another is expressed by means of individual unit axis-rotations, denoted $C_k(\eta)$ where k corresponds to a given unit axis (i.e. index 1 for a rotation around the x-axis, 2 for a rotation around the y-axis and 3 for a rotation around the z-axis attached to the frame of reference) and η is an arbitrary angle used in the definition of the rotation. This system of notation is directly taken from the work of Mooij (96). Therefore, the three unit rotations are defined as

$$C_1(\eta) = \begin{bmatrix} 1 & 0 & 0 \\ 0 & \cos\eta & \sin\eta \\ 0 & -\sin\eta & \cos\eta \end{bmatrix} \tag{4.3}$$

$$C_2(\eta) = \begin{bmatrix} \cos\eta & 0 & -\sin\eta \\ 0 & 1 & 0 \\ \sin\eta & 0 & \cos\eta \end{bmatrix} \tag{4.4}$$

$$C_3(\eta) = \begin{bmatrix} \cos\eta & \sin\eta & 0 \\ -\sin\eta & \cos\eta & 0 \\ 0 & 0 & 1 \end{bmatrix} \tag{4.5}$$

Any rotation from a frame i to a frame j can be defined by a sequence of unit axis-rotations which defines a transformation matrix, noted $T_{j,i}$. The transformation from frame j to frame i is simply defined as the inverse matrix: $T_{i,j} = {T_{j,i}}^{-1} = {T_{j,i}}^{T}$. Transformation matrices can also be combined to transform from two or more frames. Additionally, the derivative of a unit vector, denoted $\hat{i}$, in a rotating reference frame is given by

$$\frac{d\hat{i}}{dt} = \vec{\omega} \times \hat{i} \tag{4.6}$$

where $\vec{\omega}$ corresponds to the angular rotation of the moving frame with respect to an inertial frame of reference, e.g. R-frame and I-frame in Fig. 4.5. The derivation of the equations that govern the translational motion of spaceplanes around a spherical, rotating planet usually requires an inertial frame of reference. Indeed, in flight mechanics, the principal governing equation is the well-known second law of motion of Newton which is defined with respect to the I-frame as

in Eq. 4.7.

$$m\frac{d^2\vec{r}}{dt^2} = \Sigma\vec{F} = \vec{F}_a + \vec{F}_n + m\vec{g} \tag{4.7}$$

where $\vec{F}_a$ and $\vec{F}_n$ are, respectively, the sum of both the axial propulsive and drag forces acting on the vehicle, and the sum of the forces such as the lift and thrust component normal to the vehicle's direction of motion. However, for convenience, those dynamic equations can be adjusted and can be expressed with regard to a rotating reference frame fixed to the centre of mass of a celestial body and rotating with the same angular rate as that of the central celestial body, denoted $\vec{\omega}_E$, to which is it is attached, i.e. again with respect to the inertial frame of reference (see Fig. 4.5). Considering the Earth, this reference frame is also known as the Earth-Centred Earth-Fixed (ECEF) frame, here denoted the R-frame. Furthermore, an additional navigation frame (n-Frame) attached to the centre of mass of the vehicle can conveniently be defined, i.e. often referred to as the North-Oriented Local Level (NOLL) frame of reference (97) (see Fig. 4.5). The navigation frame of reference rotates and moves with the position of the vehicle. The position vector of the vehicle with respect to the I-frame and R-frame (since they are both planetocentric and thus share the same origin) is here denoted $\vec{r}$. The axes x_n and y_n are both tangent to the plane passing through the origin and oriented along the generic meridian and parallel (x_n is directed towards the local North and y_n is oriented towards the local East), and the z_n axis is perpendicular to the surface of the Earth and directed towards its centre (see Fig. 4.5 again), i.e. the origin of both the I-frame and R-frame. The translational motion of an RLV during its trans-atmospheric flight is governed by the time variation of its position vector $\vec{r}$, its velocity vector $\vec{v}$ and its mass $\vec{m}$. Referring to Fig. 4.5, the vehicle's position vector can be expressed in the n-frame simply as

$$\vec{r} = -r\hat{k}_n = -(R_e + h)\hat{k}_n \tag{4.8}$$

Furthermore, the rate of change in position of the spaceplane with respect to time is governed by the well-known kinematic equation (Eq. 4.9) obtained by taking the time derivative of the position vector in Eq. 4.8.

$$\vec{v} = \frac{d\vec{r}}{dt} = -\frac{dr}{dt}\hat{k}_n - r\frac{d\hat{k}_n}{dt} = -\frac{dh}{dt}\hat{k}_n - r\frac{d\hat{k}_n}{dt} \tag{4.9}$$

Then, substituting Eq. 4.6 into Eq. 4.9 to evaluate the time derivative of the unit

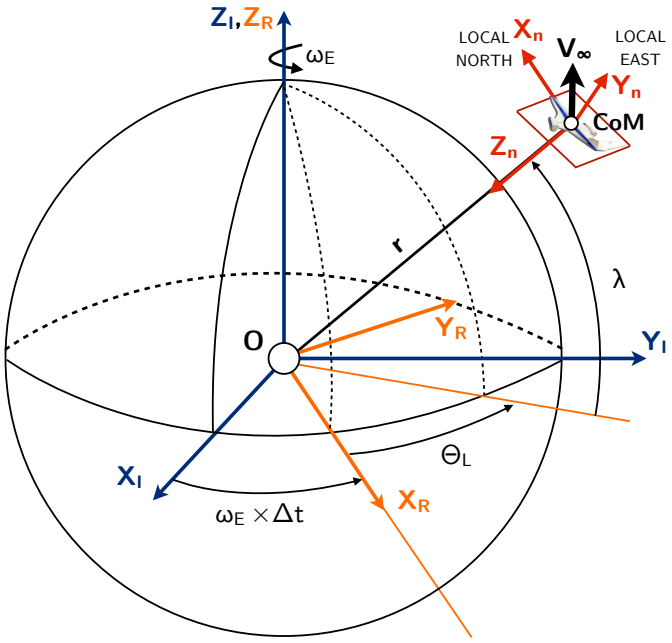

Figure 4.5: Illustration of the inertial, rotational and navigational reference frames - Relationship between the inertial and rotating planetocentric frames (index I and R, respectively) as well as the navigation frame (index n).

vector $\hat{k}_n$, the expression for the velocity becomes

$$\vec{v} = -\dot{h}\ \hat{k}_n - \vec{r} \times (\vec{\Omega}_{n/R} \times \hat{k}_n) \tag{4.10}$$

where $\vec{\Omega}_{n/R}$ represents the angular rate of the n-frame with respect to the R-frame and is dependent on the position of the vehicle, i.e. namely its longitude, denoted θ_L, and its latitude, noted λ. Thus

$$\vec{\Omega}_{n/R} = -\dot{\lambda}\hat{j}_n + \dot{\theta_L}\hat{k}_R \tag{4.11}$$

where $\vec{k}_R$ is the unit vector along the z-axis of the R-frame whose components must be expressed in the n-frame. Indeed, as depicted in Fig. 4.5, the transformation matrix from the R-frame to the n-frame is obtained by two successive rotations and is defined as follows. First, the R-frame is rotated about its z-axis with the help of the unit axis-rotation, $C_3(\theta_L)$, in order to reach an intermediate frame, i.e. it is here simply denoted as the R_{in}-frame for convenience. Finally, a

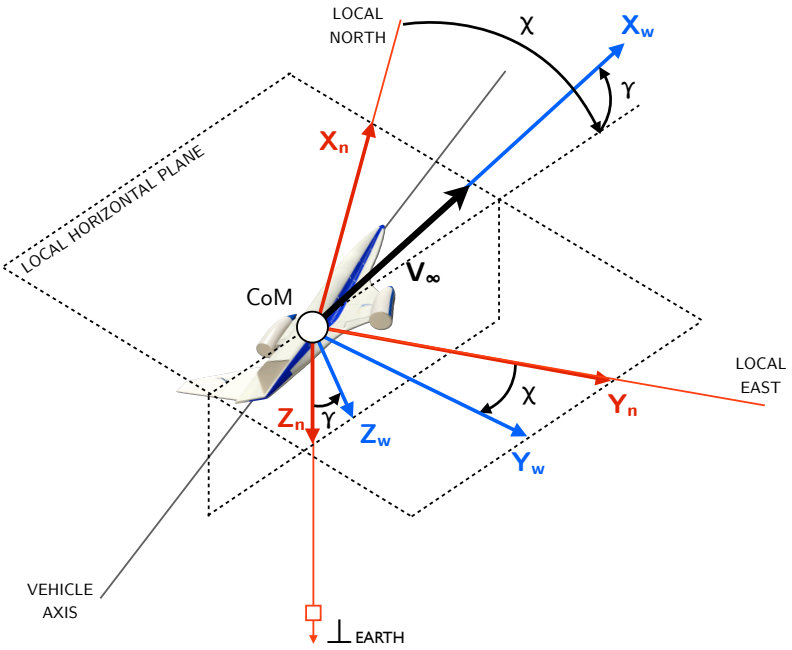

Figure 4.6: Illustration of the navigation reference frame and the wind reference frame - Relationship between the navigation frame (index n) and the wind frame (index w). The diagram is inspired by that of Mooij (96).

second rotation is performed about the y-axis of the resulting intermediate R_{in}-frame – i.e. which, in turn, corresponds to the the y-axis of the n-frame (see Fig. 4.5). The unit axis rotation matrix is thus defined as: $C_2(-\pi/2 - \lambda)$. Applying the resulting transformation matrix, $T_{n,R}$, would align the R-frame with the n-frame. Thus, the unit vector $\hat{k}_R$ can be expressed in the n-frame as

$$\hat{k}_R = \cos\theta_L \hat{i}_n - \sin\theta_L \hat{k}_n \tag{4.12}$$

An expression for $\vec{\Omega}_{n/R}$ can finally be obtained. Indeed, substituting Eq. 4.12 into Eq. 4.11 yields

$$\vec{\Omega}_{n/R} = \dot{\theta_L} \cos\lambda \ \hat{i}_n - \dot{\lambda} \ \hat{j}_n - \dot{\theta_L} \sin\lambda \ \hat{k}_n \tag{4.13}$$

Thereafter, the second term on the right-hand side of Eq. 4.10 can readily be evaluated as

$$\vec{r} \times (\vec{\Omega}_{n/R} \times \hat{k}_n) = r\dot{\theta_L} \cos\lambda \ \hat{i}_n + r\dot{\lambda} \ \hat{j}_n \tag{4.14}$$

The velocity vector in Eq. 4.10 can finally be expressed as

$$\vec{v} = (R_e + h)\dot{\theta_L} \cos\lambda \; \hat{i}_n + (R_e + h)\dot{\lambda} \; \hat{j}_n - \dot{h} \; \hat{k}_n \tag{4.15}$$

Additionally, as depicted in Fig. 4.6, the velocity vector is collinear with the x-axis of another frame of reference, namely the wind frame, i.e. w-frame, index w. In the w-frame, the velocity can simply be expressed as

$$\vec{v} = v \; \hat{i}_w \tag{4.16}$$

where v is the magnitude of the velocity vector. The unit vector $\hat{i}_w$ can then be defined in the n-frame by two successive rotations (see Fig. 4.6 again). The first unit axis-rotation, given as $C_2(-\gamma)$, rotates the w-frame about its y-axis by an angle, noted γ and termed the flight path angle, which is the angle between the velocity vector and its projection onto the local horizontal plane defined as $\mathcal{P}_n : (\hat{i}_n, \hat{j}_n)$, i.e. the plane passing across the vehicle and perpendicular to the surface of the local meridian. The second rotation involves the angle between the x-axis of the n-frame (i.e. the local parallel of latitude) and the projection of the velocity vector onto $\mathcal{P}_n$, i.e. $C_3(-\chi)$ where χ is the heading or azimuth angle. The transformation matrix is given by $T_{n,w} = C_3(-\chi)C_2(-\gamma)$. As a result, the unit vector along the x-axis of the wind frame, $\hat{i}_w$, can be expressed in the n-frame as

$$\hat{i}_w = \cos\gamma\cos\chi \; \hat{i}_n + \cos\gamma\sin\chi \; \hat{j}_n + \sin\gamma \; \hat{k}_n \tag{4.17}$$

Therefore, substituting Eq. 4.17 into Eq. 4.16, the velocity vector can be expressed in the n-frame as

$$\vec{v} = (v\cos\gamma\cos\chi) \; \hat{i}_n + (v\cos\gamma\sin\chi) \; \hat{j}_n - (v\sin\gamma) \; \hat{k}_n \tag{4.18}$$

By comparing Eq. 4.18 and Eq. 4.15, the three kinematic equations describing the change in position of the vehicle over time can then be defined as follows

$$\dot{h} = v\sin\gamma \tag{4.19}$$

$$\dot{\lambda} = \left(\frac{v}{R_e + h}\right)\cos\gamma\sin\chi \tag{4.20}$$

$$\dot{\theta}_L = \left(\frac{v}{R_e + h}\right)\frac{\cos\gamma\cos\chi}{\cos\lambda} \tag{4.21}$$

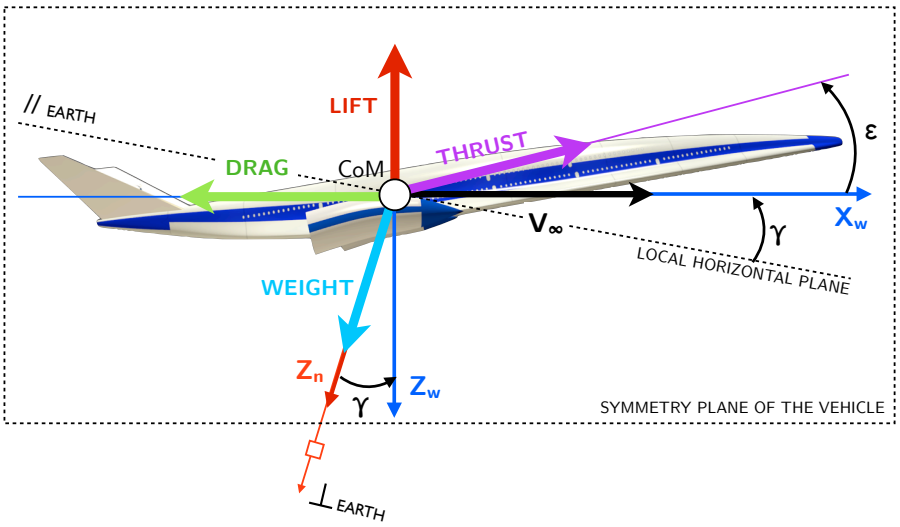

Figure 4.7: Aerodynamic forces and thrust components – The figure depicts all the external forces acting on a space-access vehicle in its symmetry plane.

Thereafter, the three dynamic equations can be derived. First, Eq. 4.7 can be re-written in the rotational R-frame as

$$m\frac{d}{dt}\left(\frac{d\vec{r}}{dt}\right) = \vec{F}_A + \vec{F}_N + m\vec{g} = \vec{D} + \vec{L} + \vec{F}_T + \vec{G} \tag{4.22}$$

which, when combined with the formula for the time derivative of a unit vector in a rotating frame (see Eq. 4.6), becomes equivalent to

$$m\left[\dot{\vec{v}} + 2\vec{\omega_E} \times \vec{v} + \vec{\omega_E} \times (\vec{\omega_E} \times \vec{r})\right] = \Sigma\vec{F} \tag{4.23}$$

Indeed, substituting twice Eq. 4.6 into 4.22 and recalling that the R-frame rotates with a constant angular velocity about its z-axis ($\omega_E\ \hat{k}_R$ and thus $\dot{\omega_E} = 0$), the second law of motion simplifies into Eq. 4.23. Now, the final steps consist in expressing all the components of Eq. 4.23 into a consistent rotating frame of reference. Both sides of the equation can then be equated to define the three dynamic equations: the w-frame is selected here.

Firstly, all the external forces exerted on the vehicle need to be expressed consistently in the w-frame, i.e. a transformation matrix could then resolve their components in any appropriate frame. First, if it is assumed that the thrust vector, here noted $\vec{F}_T$, belongs to the symmetry plane of the vehicle as depicted in Fig. 4.7 – i.e. there is no out-of-plane thrust component – then, the thrust vector

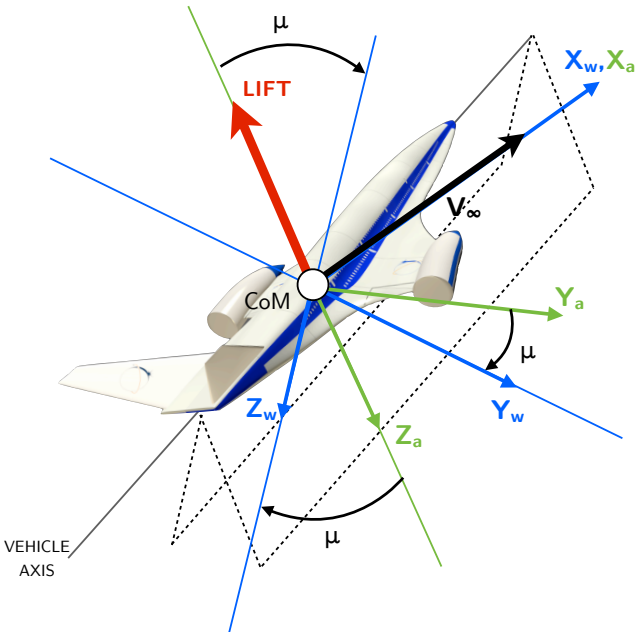

Figure 4.8: Definition of the bank angle – Relation between the aerodynamic frame (index a) and the wind frame (index w). The diagram is inspired by that of Mooij (96).

can simply be resolved in the w-frame as

$$\vec{F_T} = F_T \cos\epsilon \; \hat{i}_w - F_T \sin\epsilon \; \hat{k}_w \tag{4.24}$$

If it is then assumed further that the lift force exerted on the vehicle, $\vec{L}$, can be controlled via the modulation of both the angle of attack and bank angle to provide the capability for the vehicle to perform horizontal manoeuvres, an intermediate frame of reference (here, called the aerodynamic frame) can therefore be created for the sake of clarity (see Fig. 4.8), i.e. the a-frame, index a. The components of a vector in the a-frame can be expressed in the w-frame via a single rotation about the x-axis of the a-frame (which is collinear with the velocity vector and therefore with the x-axis of the w-frame) by an amount corresponding to the bank angle, i.e. recalling its notation μ, noted: $T_{w,a} = C_1(\mu)$. Therefore, the lift force has two components in the w-frame, its expression is given by

$$\vec{L} = -L \sin\mu \; \hat{j}_w - L \cos\mu \; \hat{k}_w \tag{4.25}$$

Furthermore, it shall be remarked that the drag force, noted $\vec{D}$, is collinear and

opposite to the velocity vector (again, refer to Fig. 4.7). The drag force can therefore readily be expressed in the w-frame as

$$\vec{D} = -D\ \hat{i}_w \tag{4.26}$$

Similarly, the gravitational force, here denoted $\vec{G}$ for convenience and collinear with the z-axis of the n-frame, can thus be expressed in the w-frame as (see Fig. 4.7)

$$\vec{G} = -mg\hat{k}_n = -mg\sin\gamma\ \hat{i}_w + mg\cos\gamma\ \hat{k}_w \tag{4.27}$$

Therefore, the right-hand side of Eq. 4.23 can be expressed in the w-frame using Eqs. 4.24, 4.25, 4.26 and 4.27 as

$$\begin{aligned} \Sigma\vec{F} = \quad & (F_T\cos\epsilon - D - mg\sin\gamma)\ \hat{i}_w \\ + \quad & (-L\sin\mu)\ \hat{j}_w \\ + \quad & (mg\cos\gamma - L\cos\mu - F_T\sin\epsilon)\ \hat{k}_w \end{aligned} \tag{4.28}$$

Secondly, the several acceleration terms on the left-hand side of Eq. 4.23 must be resolved in the w-frame before either side of the reference system of equations can be compared. Recalling that the expression of the angular rotation in the reference n-frame (i.e. using $T_{n,R}$, thus Eq. 4.12) is given by

$$\vec{\omega}_{E,n} = T_{n,R}\ \omega_E\ \hat{k}_R = \omega_E\cos\lambda\ \hat{j}_n - \omega_E\sin\lambda\ \hat{k}_n \tag{4.29}$$

and that $\vec{r} = r\ \hat{k}_n$, then the apparent transport acceleration of the vehicle due to the angular rate of the rotating R-frame given by $\vec{\omega_E} \times (\vec{\omega_E} \times \vec{r})$ can be resolved first in the n-frame as

$$\vec{\omega_E} \times (\vec{\omega_E} \times \vec{r}) = \omega_E^2 r\sin\lambda\cos\lambda\hat{j}_n + \omega_E^2 r\cos\lambda\cos\lambda\hat{k}_n \tag{4.30}$$

Thereafter, by application of the transformation matrix $T_{w,n}$, the expression of the apparent acceleration term in the w-frame becomes

$$\begin{aligned} \vec{\omega_E} \times (\vec{\omega_E} \times \vec{r}) = \quad & \omega_E^2 r\cos\lambda(\sin\lambda\sin\chi\cos\gamma - \sin\gamma\cos\lambda)\ \hat{i}_w \\ + \quad & \omega_E^2 r\cos\lambda(\sin\lambda\cos\chi)\ \hat{j}_w \\ + \quad & \omega_E^2 r\cos\lambda(\sin\lambda\sin\chi\sin\gamma + \cos\gamma\cos\lambda)\ \hat{k}_w \end{aligned} \tag{4.31}$$

Subsequently, in Eq. 4.23, the rotation of the R-frame introduces an apparent acceleration into the equation, known as the Coriolis acceleration term and defined as $2\vec{\omega_E} \times \vec{v}$. Using both Eq. 4.16 (i.e. the velocity vector expressed in the w-frame) and an expression of the angular rate of rotation (Eq. 4.29) resolved in the w-frame as

$$\begin{aligned} \vec{\omega_{E,w}} = T_{w,n}\omega_{E,n} = \quad & \omega_E(\cos\lambda\sin\chi\cos\gamma + \sin\lambda\sin\gamma)\ \hat{i}_w \\ + \quad & \omega_E\cos\lambda\cos\chi\ \hat{j}_w \\ + \quad & \omega_E(\cos\lambda\sin\chi\sin\gamma - \sin\lambda\cos\gamma)\ \hat{k}_w \end{aligned} \tag{4.32}$$

Then, the Coriolis acceleration term can also be expressed in the w-frame as

$$2\vec{\omega_E} \times \vec{v} = 2\omega_E v[(\cos\lambda\sin\chi\sin\gamma - \sin\lambda\cos\gamma)\ \hat{j}_w + (cos\lambda\cos\chi)\ \hat{k}_w] \tag{4.33}$$

Lastly, an expression for the relative acceleration term can be obtained. Rewriting Eq. 4.15 as $\vec{v}_n = v_{\theta_L}\hat{j}_n + v_\lambda\hat{i}_n - v_r\hat{k}_n$ for the sake of simplicity, the relative acceleration then becomes

$$\dot{\vec{v}} = \begin{bmatrix} \dot{v}_{\theta_L} \\ \dot{v}_\lambda \\ -\dot{v}_r \end{bmatrix} . \begin{bmatrix} \hat{i}_n \\ \hat{j}_n \\ \hat{k}_n \end{bmatrix} + \begin{bmatrix} v_{\theta_L} \\ v_\lambda \\ -v_r \end{bmatrix} . \begin{bmatrix} d\hat{i}_n/dt \\ d\hat{j}_n/dt \\ d\hat{k}_n/dt \end{bmatrix} \tag{4.34}$$

where, once again using Eq. 4.6, an expression for the unit vector derivatives can be determined as

$$\begin{bmatrix} d\hat{i}_n/dt \\ d\hat{j}_n/dt \\ d\hat{k}_n/dt \end{bmatrix} = \begin{bmatrix} 0 & -\dot{\theta}_L\sin\lambda & \dot{\lambda} \\ \dot{\theta}_L\sin\lambda & 0 & \dot{\theta}_L\cos\lambda \\ -\dot{\lambda} & -\dot{\theta}_L\cos\lambda & 0 \end{bmatrix} . \begin{bmatrix} \hat{i}_n \\ \hat{j}_n \\ \hat{k}_n \end{bmatrix} \tag{4.35}$$

Then, substituting Eq. 4.35 into Eq. 4.34 would yield the expression of the relative acceleration in the n-frame (i.e. not shown here for the sake of clarity). Thereafter, the transformation matrix used to pass from the n-frame to the wind frame of reference, namely $T_{w,n}$, could finally be used to obtain the relative acceleration term as expressed in the w-frame. Both sides of Eq. 4.23 are now expressed consistently in the w-frame. Therefore, comparing both sides of Eq. 4.23 and rearranging for $\dot{\chi}$, $\dot{\gamma}$ and $\dot{v}$, the so-called dynamic equations used in the present

work can finally be obtained as

$$\begin{aligned}
\dot{v} = & \quad \frac{F_T \cos\epsilon - D}{m} - g\sin\gamma \\
& + \quad \omega_E^2 \left(R_E + h\right)\cos\lambda(\sin\gamma\cos\lambda - \cos\gamma\sin\chi\sin\lambda) \qquad (4.36) \\
\dot{\gamma} = & \quad \frac{F_T \sin\epsilon + L}{mv}\cos\mu - \left(\frac{g}{v} - \frac{v}{R_E + h}\right)\cos\gamma + 2\omega_E\cos\chi\cos\lambda \\
& + \quad \omega_E^2 \left(\frac{R_E + h}{v}\right)\cos\lambda\left(\sin\chi\sin\gamma\sin\lambda + \cos\gamma\cos\lambda\right) \qquad (4.37) \\
\dot{\chi} = & \quad \frac{F_T \sin\epsilon + L}{mv\cos\gamma}\sin\mu - \left(\frac{v}{R_E + h}\right)\cos\gamma\cos\chi\tan\lambda \\
& + \quad 2\omega_E(\sin\chi\cos\lambda\tan\gamma - \sin\lambda) \\
& - \quad \omega_E^2 \left(\frac{R_E + h}{v\cos\gamma}\right)\cos\lambda\sin\gamma\cos\chi \qquad (4.38)
\end{aligned}$$

where, to summarize, v is the speed of the vehicle as measured in an Earth-centred reference frame (assumed to have a mean rotation rate $\omega_E = 7.292115 \times 10^{-5}$ rad/s as given by the WGS 84 model). In these equations, γ indicates the flight path angle, χ is the path directional angle (also known as the azimuth angle), μ is the bank angle, and λ and θ_L denote respectively the latitude and the longitude of the vehicle at time t. The mass of the vehicle is m, F_T is the magnitude of the thrust produced by its engines, and L and D denote the aerodynamic lift and drag forces, respectively. The angle between the thrust vector and the velocity vector is ϵ (see Fig. 4.7). Finally, the mass variation of the vehicle due to its fuel consumption, denoted $\dot{m}_v$, can also be accounted for as

$$\dot{m}_v = -\dot{m}_{fuel} \qquad (4.39)$$

where $\dot{m}_{fuel}$ represents the amount of fuel consumed during the ascent-to-orbit phase of the mission of the space-access vehicle (this term is also known as the fuel mass flow rate or throttle). Thereafter, a numerical integration of these highly non-linear differential equations – kinematic equations Eqs. 4.19-4.21 and dynamic equations Eqs. 4.36-4.38 – using a variable step Runge-Kutta method (i.e. *ode45* in matlab) can be performed without requiring any further simplifications to the previous set of equations.

4.2.3 Control Surfaces

The deflections of the controls are obtained by accounting for the rotational motion of the vehicle as follows. Firstly the components p, q and r in body axes of the rate of rotation of the vehicle about its centre of mass (i.e. roll, pitch and yaw, respectively) can be related to the rates of change of the pitch angle θ (i.e. $= \alpha + \gamma$), bank angle μ, and heading angle χ at any point along the trajectory via the Euler angle transformation (97) given by

$$\begin{bmatrix} p \\ q \\ r \end{bmatrix} = \begin{bmatrix} \frac{\partial \mu}{\partial t} - \frac{\partial \chi}{dt} \sin\theta \\ \frac{\partial \theta}{\partial t} \cos\mu + \frac{\partial \chi}{\partial t} \cos\theta \sin\mu \\ -\frac{\partial \theta}{\partial t} \sin\mu + \frac{\partial \chi}{\partial t} \cos\theta \cos\mu \end{bmatrix} \tag{4.40}$$

Indeed, the Euler angles can be used to describe the orientation of the vehicle with respect to the navigational reference frame described previously in Section 4.2.2. These components can then be differentiated with respect to time, numerically or otherwise – for instance using the following central-difference scheme

$$f_i' = \frac{f_{i+1} - f_{i-1}}{2\Delta t_i} + o(\Delta t_i^2) \tag{4.41}$$

in order to obtain the angular accelerations $\dot{p}$, $\dot{q}$ and $\dot{r}$ of the vehicle about its centre of mass (again in body axes). These accelerations can then be related via Euler's law to the body-axis components M_x, M_y and M_z of the aerodynamic moment $\hat{M}$ (see Eq. 2.49) required to generate these accelerations by

$$\begin{bmatrix} M_x \\ M_y \\ M_z \end{bmatrix} = \begin{bmatrix} I_v^b \end{bmatrix} \begin{bmatrix} \dot{q} \\ \dot{r} \\ \dot{p} \end{bmatrix} \tag{4.42}$$

where the matrix $[I_v^b]$ contains the body-axis components of the inertia tensor of the vehicle. Finally, the set of control surface deflections required to produce the desired moments (Eq. 4.42), denoted δ_i, can then be obtained (see Section 5.2.2 of Chapter 5).

4.2.3.1 Aerodynamic Effects

Since the reduced-order aero-thermodynamic model does not require surface continuity (except in the assessment of the viscous loads as a result of the computation of the surface streamlines), the aerodynamic effects of changing the

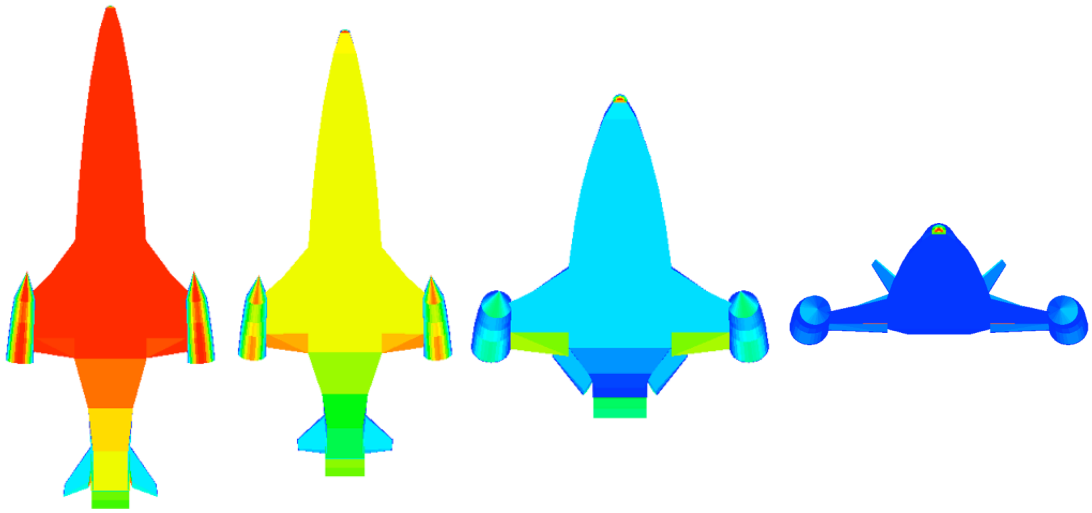

Figure 4.9: Deflection of the control surfaces during re-entry - The figure shows the pressure distribution over the surface of the CFASTT1 re-usable vehicle concept with its rotated controls along a representative re-entry trajectory (starting from re-entry attitude on the left-hand side).

deflections of the control surfaces are simply obtained by applying the appropriate three-dimensional affine transformations to the mesh defining the surface of the vehicle in order to rotate these controls about a prescribed hinge line – i.e. Rodrigues's rotation formula (57) is again used here to define a rotation about arbitrary axis (see Eq. 2.45). It shall also be remarked that the pattern of streamlines as well as the aero-thermal solutions are based on the geometry with un-deflected controls which is consistent with other industry-standard codes such as CBAERO (21). For example, Fig. 4.9 shows the pressure distribution (computed using HyFlow) over a CFASTT-1 SSTO vehicle at a number of points along its terrestrial entry trajectory with its controls correctly oriented in their trimmed attitude.

Additionally, the model must account for the controls being aerodynamically "shadowed" (partially or entirely) by upstream-located portions of the vehicle's surface. Indeed, in Fig. 2.9, it has been shown that the pen-nib shape of the fuselage at the rear of the vehicle introduces a slope in the fuselage geometry that could lead to the beaver tail (i.e. rear body flap) being completely shielded from the oncoming hypersonic flow at small angles of attack (e.g. confirmed by the rightmost figure in Fig. 4.9). Therefore, the efficiency of the controls, denoted $\eta_{\alpha i}$, must be derived as a function of the angle of attack using the method presented in

Section 2.3.5. Indeed, a database of efficiency, which represents fundamentally the area fraction of a given control surface that is visible by the oncoming hypersonic flow, can thus be built up prior to performing the control analysis (i.e. after the geometry of the controls has been defined). This area-weighted efficiency factor can then be used to correct the set of individual aerodynamic contributions from the deflected control surfaces, denoted by P_i, as

$$P_i = \eta_\alpha P_{ws,i} \frac{A_i}{A_{total}} \tag{4.43}$$

where the terms $P_{ws,i}$ and P_i are, respectively, representative measures of the aerodynamic performance of the control surfaces without the "shadowing effect" being accounted for (index ws), and where deviations from these conditions, when the control surface efficiency is taken into account, might possibly require the controls to be deflected by an additional amount (index i).

Thereafter, these corrected aerodynamic contributions can then be added to the overall force and moment acting on the vehicle during the control scheduling design process.

4.2.3.2 Geometry Effects

During trajectory integration, the tensor of inertia, $[I_v^b]$, can either be considered fixed or variable. In the latter case, the inertia tensor must be computed at each time-step, Δt, in order to account for the change in deflection angle of the control surfaces. Based on the assumed gross take-off mass of the vehicle, denoted m_{gross}, and further assuming a uniform distribution of the vehicle's structural density, the components of the inertia tensor can then be approximated by assigning an area-weighted lumped-mass to each face of the tessellation (if no better description of the vehicle's mass distribution is provided). Each lumped-mass, located at a distance Δx_i ($= \|\hat{x}_i - \hat{x}_c\|$) from the centre of mass of the vehicle, is given by

$$m_i = m_{gross} \frac{A_i}{A_{total}} \tag{4.44}$$

Finally, the components of the inertia tensor in body axes can be estimated as follows

$$I_v^b = \sum_{i=1}^{N} m_i \left(\Delta x_i^2 I_3 - \hat{x}_i \, \hat{x}_i^T \right) \tag{4.45}$$

where I_3 denotes the three-by-three identity matrix and m_{gross} is the gross take-off mass of the vehicle.

4.3 Thermal Protection System Model

The thermal survival of the severe aerodynamic heating environment that accompanies hypersonic flights has always been the source of serious concern for both the ascent and subsequent re-entry of space-access vehicles. In fact, the problem of aerodynamic heating becomes even more critical in the context of re-usable vehicles as these will have to repeat this performance mission after mission. For instance, during re-entry, the large kinetic energy of the vehicle must be dissipated and converted into thermal energy in order to decelerate the vehicle to near-zero velocity. Nonetheless, although the heat that goes into the surface of the vehicle through the boundary layer (i.e. that which is primarily transferred by convection), here denoted Q_w, and expressed as

$$Q_w = A\left(k_{air}\frac{\delta T}{\delta y}\right)_w = St\rho V A(H_0 - H_w) \tag{4.46}$$

is quite significant (where k_{air} is the thermal conductivity of the surrounding air, St is the Stanton number and H_0 is the total enthalpy), the fraction of this flow rate of thermal energy that instead goes into the flow field that surrounds the space-access configuration, here simply denoted Q_{air} for convenience, and given by

$$Q_{air} = \dot{m}_{air} H_0 = \rho A V H_0 \tag{4.47}$$

is much more important (where $\dot{m}_{air}$ represents the air mass flow rate). Indeed, the ratio of these two heating terms can simply be approximated by (35)

$$\frac{Q_w}{Q_{air}} = \frac{St\rho AV(H_0 - H_w)}{\rho A V_{edge} H_0} \approx St \tag{4.48}$$

since, in general, the cold-wall approximation dictates that $H_0 \gg H_w$ (and therefore $H_0 - H_w \approx H_0$). Consequently, by application of the Reynolds analogy, previously discussed in Section 2.7.1, this ratio finally becomes equivalent to

$$\frac{Q_w}{Q_{air}} \approx \frac{C_f}{2} \approx 0.001 \quad \text{if } Pr \approx 1 \tag{4.49}$$

Eq. 4.49 corroborates the fact that the heat transferred to the surface of hypersonic vehicles is approximately of the order of a thousand times lower than that

of the heat transferred to the surrounding atmosphere (i.e. which absorbs most of the thermal energy resulting from hyper-velocity flight). Nevertheless, while a physical "*thermal barrier*" as such does not exist, the aerodynamic heating problem still remains the foremost design driver for this class of re-entry vehicles (12). Indeed, the aerodynamic heating distribution varies roughly according to

$$\dot{q}_{conv} \propto \frac{1}{2}\rho_{\infty}V_{\infty}^{3} \tag{4.50}$$

As a result, at hypersonic speeds, the heat transfer rates are quite substantial and adequate thermal control strategies in order to repeatedly absorb and dissipate part of the thermal energy transferred to the wall, must thus be devised. Throughout the mission profile of future re-usable space transportation vehicles, a Thermal Protection System (TPS) – also known as thermal shield – is then required to maintain the temperature of the structural skin within its operating temperature limits. The pre-eminent requirement that future re-usable launchers must emphasize light weight and serviceability together with resistance to high temperatures will most likely require that the passive use of light weight insulation materials be augmented, at least on the most exposed parts of the vehicle (such as over the leading edges of the wings, and in the nose region), by a complex Active Cooling System (ACS) involving the flow of a coolant - possibly part of the vehicle propellant – through actively cooled surface panels by means of a process, known as convective cooling, which is similar to that currently employed in liquid fueled rocket engines for the regenerative cooling of metallic thrust chambers and nozzles. However, despite a considerable number of studies in the literature since the 1960s and 1970s (see, for instance, the exhaustive literature review gathered by Shore (98)), such as the comprehensive studies provided by Helenbrook *et al.* (99, 100, 101), the active cooling of entire parts of the vehicle's airframe remains, to date, only on paper as a promising technology that could potentially help to achieve the full re-usability concept. Nonetheless, the successful design of an ACS requires a challenging and adequate balance between low weight and simplicity on the one hand, and a combination of reliability, long life and maintainability on the other.

The various active thermal system strategies, discussed in the present section, circulate a coolant in a closed loop in order to absorb incident aerodynamic heating before transferring it to either (1) the tankage – where the process is known as direct cooling (described in Section 4.3.1.2) – or (2) to a heat exchanger through

a process known as indirect cooling (described in detail in Section 4.3.1.4), where in both cases the absorbed heat is rejected to the on-board propellant (e.g. liquid Hydrogen). Nevertheless, since future space transportation vehicles will also make use of insulation layers on those parts of the body that are less exposed to the critical aero-thermal environment (such as hot structures), the thermal model must be versatile enough in order to accommodate and combine the use of the two TPS technologies – active and passive – during the preliminary design process. Such an attempt to define a rapid engineering model that combines the use of passive and active convective cooling systems has, to the author's knowledge, not been addressed in any prior multi-disciplinary design studies of re-usable space transportation systems. This particular type of thermal protection strategy may be designated as hybrid TPS by analogy to hybrid or combined-cycle propulsion systems that embed different modes of operations (those will be discussed in Section 4.4).

In the present section, an engineering methodology, dubbed HyTPS and based on the thermal network analogy, is thus presented in Section 4.3.1. In Section 4.3.2, the use of the thermal model in order to analyze the ground-hold phase of the mission of future space-access vehicles is discussed. Finally, a preliminary validation of the thermal model is proposed in Section 4.3.3.

4.3.1 Hybrid Thermal Protection System (HyTPS)

In the open literature, a multi-disciplinary design study performed by Tröltzsch *et al.* (102) involved the modelling of a water cooling system for the most exposed regions of the DLR Spaceliner Concept via an *in-house* tool dubbed *CalCoolAid*. The modelling approach adopted by the authors, which appears rather simplistic at first, is however efficient: the regions requiring an ACS are those where the radiative equilibrium temperature is such that $T_{rad,eq} \geq T_{max}$. Then, the structural skin of the vehicle is assumed to be maintained at a targeted constant temperature, denoted T_t, by the water ACS. Thereafter, the trajectory is re-run assuming an isothermal wall boundary condition in the actively cooled regions. Finally, the total heat load that goes into the wall is integrated along the trajectory and the heat of vaporization of water is used to evaluate the volume of water required to actively cool those surfaces. Additionally, an ACS optimization study performed by Valdevit *et al.* (103) is, to the author's knowledge, the only example of a study

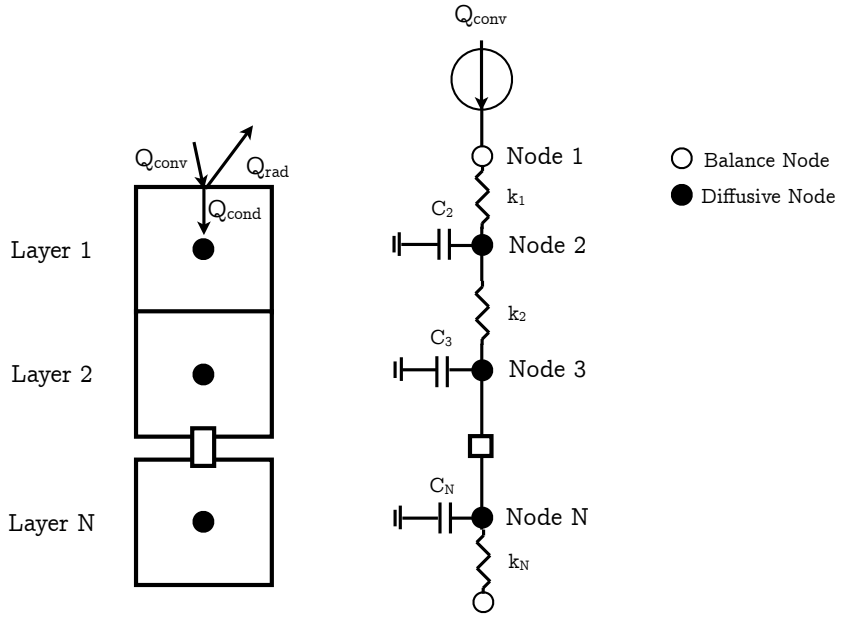

Figure 4.10: Thermal network concept.

of ACS conducted with the help of an analytical two-dimensional thermal network with rectangular channels (i.e. successfully validated with Finite Elements Analysis (FEA)). In their design study, a thermal management system has been designed to actively cool the combustion chamber as a result of the extreme thermal loads associated with supersonic combustion under structural and thermal constraints.

Within the present work, the preliminary design of a structurally integrated hybrid TPS is aided by adopting an electrical analogy to create an Equivalent Resistive Network (ERN) as shown in Fig. 4.10, also known as a Lumped Capacitance Network (LCN), where the temperature assigned to a series of nodes within the system is taken to represent the average temperature of the corresponding sub-volume (i.e. isothermal volumes where the variation of temperature within each "material lump" can be assumed negligible) (104). Additionally, a thermal capacitance, denoted C_i and assigned to each of the network nodes, is computed from the material properties evaluated at the temperature of the node (depending on the availability of material/coolant properties) and is assumed to be concentrated at the nodal centre of the associated sub-volume. In the modelling of thermal networks, the link that allows heat to flow from one node to another is represented by an equivalent thermal resistor that can either be

- *conductive* and is characterised by its thermal conductivity k_i,
- *radiative* and is characterised by its thermo-optical properties ϵ_i (i.e. surface emissivity),
- *convective* and is characterised by the heat transfer coefficient that results from the movement of a fluid (air) past the wall of the vehicle h_i.

In the current implementation, each node of the thermal network can be modelled as either

- a *diffusive node* which describes a node with a finite thermal capacitance, capable of absorbing and storing part of the heat flowing through it,
- a *balance node* (also known as an *arithmetic node*), associated with zero thermal capacitance, which thus responds instantaneously to its surroundings – e.g. this type of node may be used to model the surface wall of a re-entry vehicle (where it is assumed that the wall temperature remains close to its radiation equilibrium value),
- or, a *boundary node* which is characterised by an infinite capacitance and therefore models a constant temperature node. This type may be used to represent a fully loaded cryogenic tank during servicing on ground (see Section 4.3.2).

Additionally, three basic thermal networks, depicted in Fig. 4.11, can be considered as the backbone of the TPS model currently being discussed. Those three elementary networks can indeed be combined to create any complex hybrid TPS arrangement. Although the heat exchanger resistive network model, whose application will be discussed in great detail in Section 4.3.1.4, can more precisely be used to connect two different thermal networks together, both the insulator and convective cooling channel type of networks can indeed be combined and assembled to form hybrid TPS models. For instance, the schematic of such simplified Active Thermal Management Unit (ATMU), that can be modelled using the two basic equivalent thermal networks, is depicted in Fig. 4.12. In Section 4.3.1.1, the detailed methodology used in the present work to design such hybrid thermal shields is introduced.

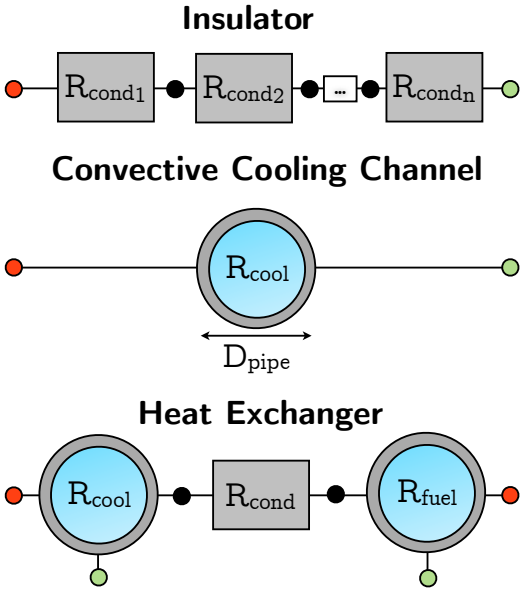

Figure 4.11: Elementary thermal networks - The three basic thermal networks that are used to define any complex combination of passive and active thermal protection systems are presented. The number of input (red dots) and output (green dots) points are also depicted. The heat exchanger model can actually be used to connect two different equivalent resistive networks together and to provide a physical model for the heat exchange between networks.

4.3.1.1 Modelling of Active Cooling Panels

In the process of sizing the hybrid TPS, the geometry of the vehicle is first partitioned into a number of self-consistent thermal zones (where an arbitrary number of zones can be specified). Within each of these zones, the convective heating profile (obtained using both the flight model described in Section 4.2 and the HyFlow reduced-order model) on the panel that is most severely heated along the trajectory of the vehicle is used to size the thickness of the insulation layer, or the properties of the ACS that is required, as appropriate. Additionally, it is assumed that the structural skin of the re-usable launch vehicle is itself made of a thermally resilient material (such as titanium) and thus that surface insulation is not required in those areas where the surface temperature does not exceed a pre-determined threshold. The mass flow rate of coolant, denoted $\dot{m}_{cool}$, which is required to actively cool the vehicle can then be evaluated from the coolant mass flow rate that must perforce be designed in order to maintain the structural skin of the vehicle below a prescribed threshold temperature (see Eq. 4.51 below).

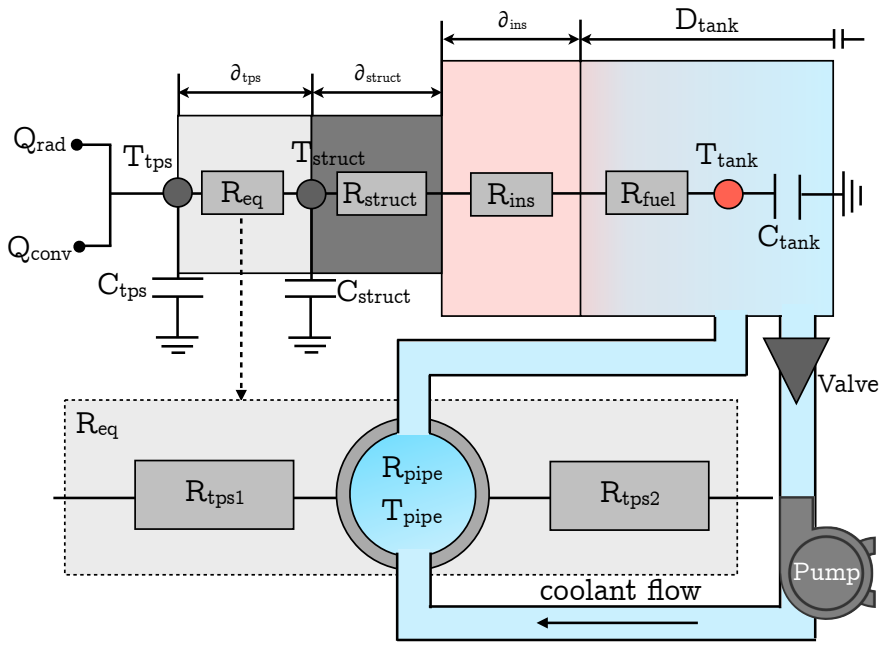

Figure 4.12: Hybrid active and passive thermal management unit - Schematic of a proposed conceptual thermal network for the active thermal protection of future re-usable space-access vehicles. A coolant flows from the propellant tank through an actively cooled surface panel which is schematically represented as an equivalent thermal resistance (see diagram at the bottom).

$$\dot{m}_{cool} = \rho_{cool} A_{pipe} U_{cool} \tag{4.51}$$

where ρ_{cool} is the density of the cooling fluid, $A_{pipe} = \pi(D_h^2/4)$ is the cross-sectional area of the cooling lines (i.e. D_h is the hydraulic diameter of the pipelines), and U_{cool} is the velocity of the pumped coolant flowing through the piping system.

A more accurate representation of the previous TPS arrangement, first introduced in Fig. 4.12, is given in Fig. 4.13 where the left-hand surface node (of the balance node type) is assumed to be directly exposed to the external flow. The associated nodal temperature is thus dependent on the convective heating from the flow at the surface of the vehicle and the radiative cooling of the surface of the vehicle during its passage through the terrestrial atmosphere. These effects are modelled as external power sources to the thermal network, first as

$$Q_{conv} = \dot{q}_{conv} A_i \tag{4.52}$$

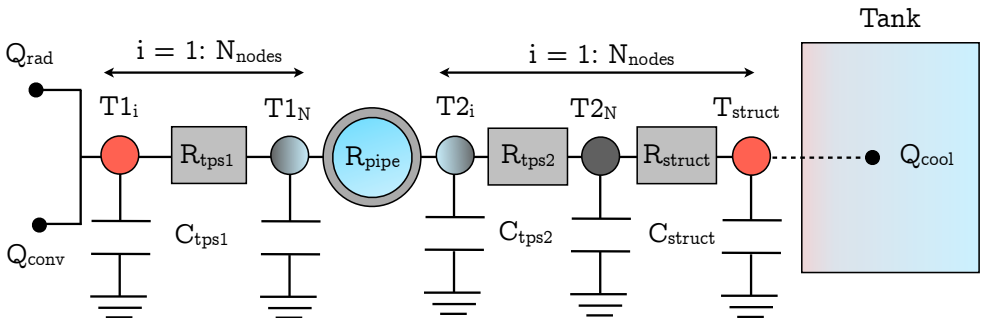

Figure 4.13: Hybrid cooling system model - Simplified schematic of the TPS thermal network which is composed of several layers of RSI and a cooling duct simply modelled as a circular pipe. The left-hand side of the ACS is exposed to the thermal environment associated with hypersonic flight while the right-hand side is subjected to a cryogenic boundary for those surface areas that are in close thermal contact with cryogenic tanks, otherwise no thermal source is added to that end of the TPS.

and then using the Stefan-Boltzmann law as

$$Q_{rad} = \epsilon_{tps} \sigma A_i T_1^4 \tag{4.53}$$

where A_i represents the surface area of the thermal zone being sized, $\dot{q}_{conv}$ represents the transient convective heat transfer profile experienced by the thermal zone along the vehicle's trajectory, and ϵ_{tps} and σ are, respectively, the emissivity of the surface coating and the Stefan-Boltzmann constant. In the case of the surface node, a thermal balance that includes the convection from the flow field, the radiation from the surface and the conduction through the material is solved for its nodal temperature, T_1, using a rapid Newton-Raphson iterative process. This thermal balance is given by

$$Q_{conv} - Q_{rad} = Q_{cond} \tag{4.54}$$

Additionally, the regions of the vehicle that are located in close thermal contact with the cryogenic tanks may also account for the natural convective cooling effect due to the presence of a large reservoir of cryogenic propellant at the beginning of the ascent-to-orbit phase (i.e. when the propellant tanks are fully loaded) and is modelled as an additional power source to the structural skin node (right-hand

node) as

$$Q_{cool} = h_{tank} A_i (T_{tank} - T_{struct}) \tag{4.55}$$

where h_{tank} is the natural convective heat transfer coefficient – computed using an empirical formula (104), and T_{struct} and T_{tank} are, respectively, the structural skin temperature and the temperature of the cryogenic liquid propellant. Then, the various sub-volumes that comprise the entire insulation layers can be modelled by defining an arbitrary number of material nodes whose finite capacitances are given as

$$C_i = \rho_i c_i V_i \tag{4.56}$$

where the density and specific heat of the TPS material (or fluid) are, respectively, ρ_i and c_i, and V_i is the volume of material/fluid available to absorb the thermal load. Each layer of TPS is also assumed to be made out of a material whose conductivity is a thickness-weighted average of the conductivity of both the current and subsequent thermal nodes and is thus computed as

$$k_i = \frac{\delta_i k_i + \delta_{i+1} k_{i+1}}{(\delta_i + \delta_{i+1})} \tag{4.57}$$

As depicted in Fig. 4.13, two protective layers of either similar or dissimilar materials (of thickness δ_1 and δ_2 respectively), can be located on either side of the ACS feeder lines. The conductive resistance of these thermal insulation layers, denoted R_{tps}, can be modelled by

$$R_{tps} = \frac{0.5(\delta_i + \delta_{i+1})}{k_i A_i} \tag{4.58}$$

Additionally, the last node of the first insulation layer and the first node of the second insulator are considered to be in direct contact with the ACS feeder lines over an equivalent area that is simply assumed to be equal to the surface area A_i of the thermal zone under consideration (see Fig. 4.13). Indeed, the coolant is presumably distributed to panels through a network of feeder and return lines composed of a large number of coolant passages (101). Furthermore, the conductivity of the cooling passages, through which the coolant flows, is neglected

on the assumption that they would be made of a thin layer of highly conductive material in order to enhance the cooling of the most severely heated parts of the skin of the space-access vehicle (thus assuming fully integrated cooling passages). Moreover, the model assumes the second layer of Re-usable Surface Insulation (RSI) to be directly attached to the underlying structural skin of the vehicle (again structurally integrated TPS configuration). Then, the set of integral feeder lines located between the two insulation layers is modelled as an equivalent convective resistance as introduced in Eq. 4.59.

$$R_{pipe} = \frac{1}{h_{fuel}\, A_i} \tag{4.59}$$

where h_{fuel} is the convective heat transfer coefficient, thus allowing the cooling of the TPS by the forced convection of the pumped coolant within the pipe to be accounted for. The forced convective heat transfer coefficient of the coolant depends on the nature of the flow – i.e. on whether it is laminar or turbulent. Assuming a turbulent flow (since the fluid Reynolds number is generally such that $Re_{fuel} \geq 2300$), the average Nusselt number within the pipe lines is obtained using Gnielinski's correlation (105) as

$$\bar{Nu}_{pipe} = \left(\frac{\chi}{8}\right) \frac{(Re_{fuel} - 1000) Pr_{fuel}}{1 + 12.7\sqrt{(\chi/8)}(Pr_{fuel}^{2/3} - 1)} \times \left[1 + \left(\frac{D_{pipe}}{L_{pipe}}\right)^{2/3}\right] \tag{4.60}$$

where the equivalent length of the feeder lines is simply estimated equal to $L_{pipe} = \sqrt{A_i}$, D_{pipe} is the hydraulic diameter of the cooling passages (a measure of the ACS equivalent thickness, denoted δ_{acs}), and the friction factor, denoted χ, is given by the well-known Petukhov correlation (105) for smooth tubes as

$$\chi = (1.82 \log Re_{fuel} - 1.64)^{-2} \tag{4.61}$$

Thereafter, using the definition of the average Nusselt number, which is the ratio of the convective to conductive heat transfer normal to the cooling lines, the convective heat transfer coefficient can be estimated as

$$h_{fuel} = \frac{k_{fuel} \bar{Nu}_{pipe}}{D_{pipe}} \tag{4.62}$$

where k_{fuel} represents the thermal conductivity of the cooling fluid.

Then, by application of a thermal energy balance, whereby the energy flowing into each node must equal the sum of the heat flowing out together with the amount of thermal energy stored at each node, the time evolution of the nodal temperatures within the prescribed ACS scheme can simply be obtained as

$$\text{Heat Out} + \text{Heat Stored} = \text{Heat In} + \text{Source} \tag{4.63}$$

$$\Leftrightarrow C_i \frac{dT_i}{dt} + \frac{T_i - T_{i+1}}{R_{i+1}} = \frac{T_{i-1} - T_i}{R_{i-1}} + Q_{source} \tag{4.64}$$

Finally, the resulting system of differential equations can then be integrated (numerically or otherwise) in order to evaluate the variation of the nodal temperatures throughout both the ascent and subsequent re-entry trajectories (e.g. using Matlab's *ode45* routine).

Therefore, after careful selection of the various materials to be employed within the hybrid TPS, a combination of parameters such as the mass flow rate $\dot{m}_{fuel}$, the pipe equivalent diameter D_{pipe} (i.e. ACS thickness δ_{acs}), and the thickness of the RSI layers $\{\delta_i\}$ must perforce be designed to prevent the structural temperature from rising above a pre-determined threshold in order to guarantee that the thermal and structural integrity of the vehicle is conserved while the overall weight of the actively cooled panel system is minimized. Hence, the system may be designed such that each actively cooled thermal zone receives only the flow-rate of coolant that is required to absorb the thermal load acting on that particular area of the vehicle. In the remainder of this section, the two different active cooling strategies will be further discussed.

4.3.1.2 Direct Convective Cooling

For direct convective cooling systems, the re-usable space-access vehicle is actively cooled over critical parts of its airframe surface by the residual heat-sink of the liquid hydrogen fuel. It is assumed that, during the ascent of the vehicle, any fuel that is used within the ACS will be sent directly to the propulsion system where it will be mixed with the main fuel supply and fed into the engines where the coolant flow rate is equal to the fuel flow rate – such a process is called a Direct Cooling System (DCS). No other provision thus has to be made to store or dissipate the energy that is extracted from the TPS during this phase of the mission.

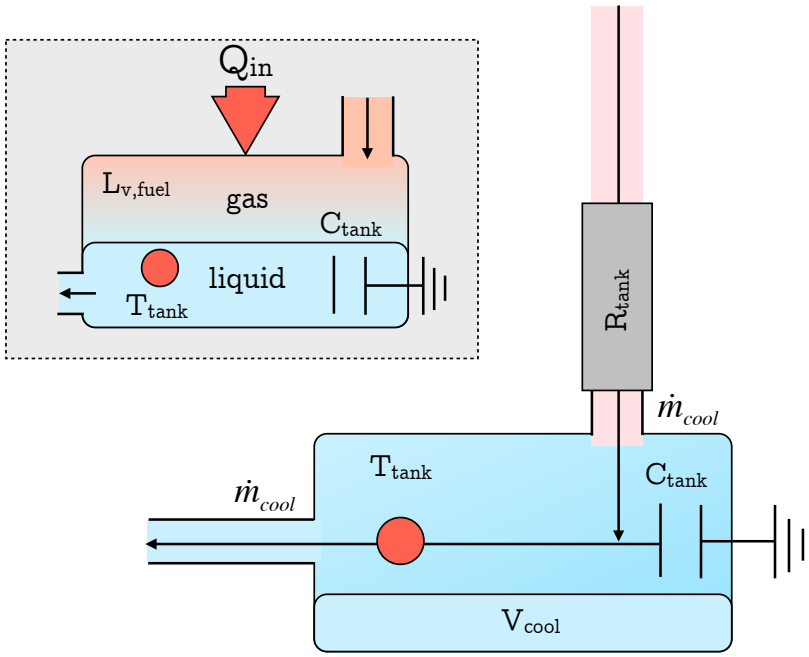

Figure 4.14: Tank thermal network - Schematic of the thermal energy balance at the cryogenic tank. The resistance models the mass flow rate of heated coolant which is purposely re-circulated through the cryogenic tank in order to dissipate extra thermal energy..

Nevertheless, during re-entry, the situation becomes more difficult, since some means must be found to absorb or dissipate, within the system, the energy that is absorbed by the ACS. It is assumed that a residual amount of propellant has been held within the main fuel tanks with the express purpose of using it within the ACS during re-entry. The coolant is thus re-circulated to the tank after use within the ACS, where its thermal energy is dissipated firstly by increasing the temperature of the fluid within the tank and subsequently, once the boiling point of the fluid is reached, by vaporising the contents of the tank. The re-circulation of the cryogenic fuel through the tank during re-entry has been accounted for by modelling a thermal network for the tank system as shown in Fig. 4.14. This network is then coupled to that for the active cooling panel described previously in Section 4.3.1.1. The thermal resistance

$$R_{tank} = \frac{1}{\dot{m}_{cool} c_{cool}} \tag{4.65}$$

models the mass flow rate of cryogen that re-circulates from the cooling pipes into the tank, where c_{cool} is the temperature-dependent specific heat of the coolant

(again if this information is known, otherwise the specific heat is assumed constant). A differential equation governing the variation of the fuel temperature within the cryogenic tank, denoted T_{tank}, as a result of this heated coolant being returned to the tank can therefore be obtained using the following energy balance

$$Q_{in,tank} = Q_{stored,tank}$$

in other words

$$\dot{T}_{tank} = \begin{cases} \dot{m}_{cool} c_{cool} \left(\frac{T_{out} - T_{tank}}{C_{tank}} \right) & \text{if} \quad T_{tank} < T_{liq} \text{ and } V_{cool} > 0 \\ 0 & \text{if} \quad T_{tank} \geq T_{liq} \text{ and } V_{cool} > 0 \end{cases} \tag{4.66}$$

where

$$C_{tank} = \rho_{cool} c_{cool} V_{cool} \tag{4.67}$$

is the capacitance of the tank, with V_{cool} being the remaining volume of fuel within the tank, and T_{out} is the temperature of the heated cryogen at the outlet of the pipelines (and thus at the inlet of the tank). The logic within Eq. 4.66 is required to account for the possibility that the propellant in the tank might boil. Indeed, the volume of fuel within the tank is assumed to vary with time during ascent as the on-board fuel is consumed, and during re-entry as the coolant boils off, according to

$$\dot{V}_{cool} = \begin{cases} -\dot{m}_{fuel} / \rho_{fuel} & \text{during ascent} \\ -\dot{V}_{boil} & \text{during re-entry} \end{cases} \tag{4.68}$$

where $\dot{V}_{boil}$ is the fuel boil-off volume rate, and is defined simply as

$$\dot{V}_{boil} = \begin{cases} 0 & \text{if} \quad T_{tank} < T_{liq} \\ Q_{in} / (\Delta H_{fuel}\, \rho_{fuel}) & \text{if} \quad T_{tank} \geq T_{liq} \end{cases} \tag{4.69}$$

where ΔH_{fuel} represents the latent heat of vaporization of the fuel, evaluated at the pressure that exists within the tank. Indeed, if the fuel inside the tank is warmed to the extent that it reaches its vapour-liquid phase equilibrium (liquefaction) temperature T_{liq} at the corresponding pressure within the fuel system, then the temperature of the fuel does not continue to rise until all the fuel has changed from a liquid to a vapour.

4.3.1.3 Cooling Channels

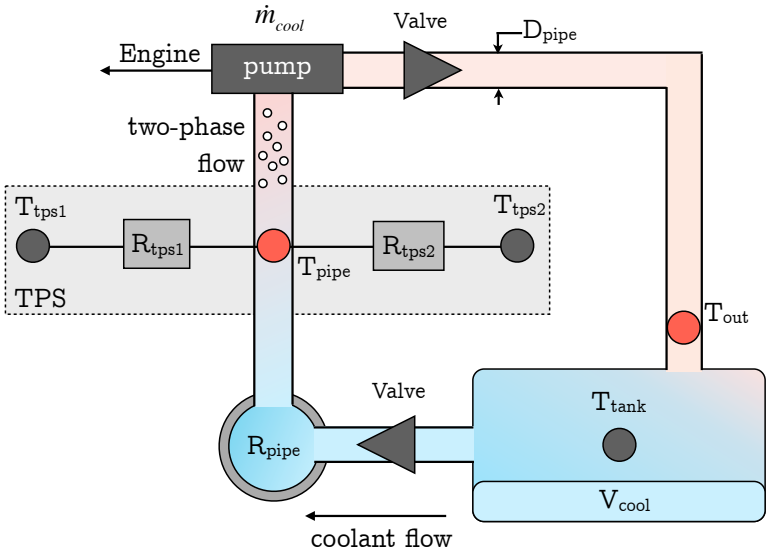

Figure 4.15: Thermal balance at a cross-section of the pipeline - Simplified schematic of the thermal balance at a cross-section of the cooling channels.

The effects due to the vaporization of the cryogenic propellant within the cooling ducts are accounted for by monitoring the formation of a two-phase flow using a method similar to that described in Section 4.3.1.2. The heat input into each section of the ACS feeder lines is a result of the heat conducted from the wall and absorbed by the coolant, and is given by

$$Q_{in,pipe} = \frac{T_{tps1} - T_{pipe}}{R_{tps1}} \tag{4.70}$$

Additionally, the heat leaving each section of the pipe is computed as

$$Q_{out,pipe} = \frac{T_{pipe} - T_{tps2}}{R_{tps2}} + \dot{m}_{cool} c_{cool} (T_{out} - T_{tank}) \tag{4.71}$$

where T_{out} is the temperature of the fluid leaving the feeder lines, and the temperature T_{pipe} of the fluid within the feeder lines is approximated as the average temperature between the inlet and outlet of the system, i.e.

$$T_{pipe} = \frac{T_{out} + T_{tank}}{2} \tag{4.72}$$

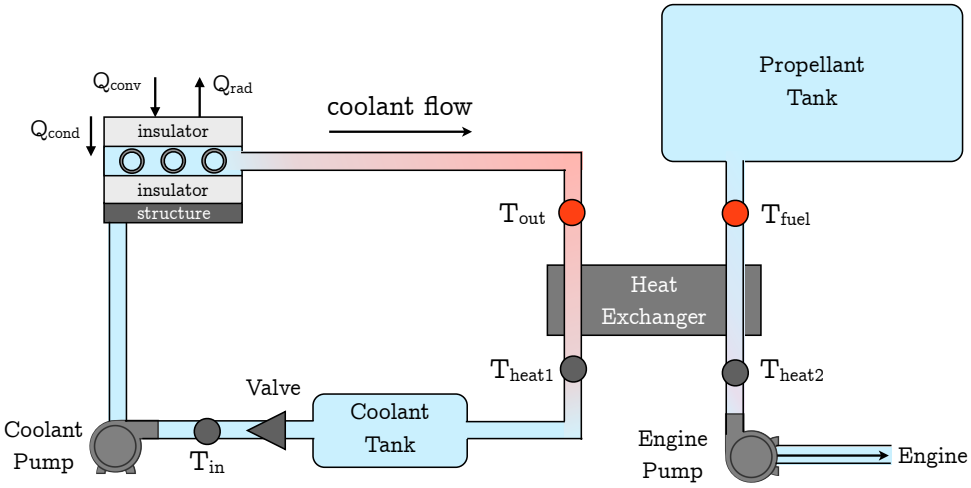

Figure 4.16: Illustration of a regenerative cooling system - Before being fed into the engine, the propellant partially dissipates the heat absorbed by the coolant when flowing through actively cooled panels. A regenerative cooling system requires the use of a heat exchanger.

An energy balance at the pipe node, as shown in Fig. 4.15, allows the temperature inside the coolant feeder lines to be estimated as

$$T_{pipe} = \frac{2\dot{m}_{cool}c_{cool}R_{eq1}R_{eq2}T_{tank} + R_{eq1}T_{tps2} + R_{eq2}T_{tps1}}{2\dot{m}_{cool}c_{cool}R_{eq1}R_{eq2} + R_{eq1} + R_{eq2}} \tag{4.73}$$

where R_{eq1} and R_{eq2} are the sum of the convective resistance of the feeder lines and the conductive resistance of the layers of insulation respectively.

4.3.1.4 Indirect Convective Cooling

For indirect convective cooling systems, a secondary coolant, which could potentially be another liquid instead of hydrogen – e.g. silicon fluid, water-glycol or lithium – circulates in a closed loop through convectively cooled panels and then through a heat exchanger to transfer the absorbed heat to the propellant before being fed into the propulsion system as shown in Fig. 4.16. Since the heat absorbed by the coolant is re-used rather than being discarded, such a cooling method is often referred to as a regenerative cooling approach. While the additional heat transferred to the fuel has beneficial effects on the combustion process and minimizes the vaporization of the fuel within the coolant tank, Regenerative

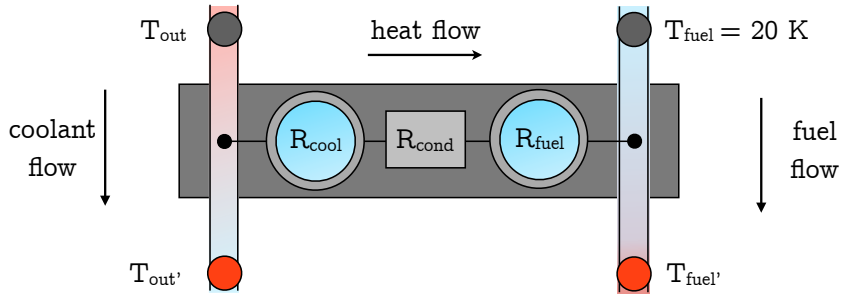

Figure 4.17: Equivalent thermal network for a heat exchanger - Schematic of a simple thermal circuit for a heat exchanger where the fuel (e.g. hydrogen) is used as the cooling fluid in order to dissipate part of the heat absorbed by the coolant (hot fluid).

Cooling Systems (RCS) requires an additional pump, a heat exchanger and possibly a dedicated coolant tank. Despite the additional complexity and mass, these extra devices are essential if an actively cooled structure is required to accommodate the aerodynamic or combustion heating loads associated with hypersonic flight. As shown in Fig. 4.16, the heat exchanger device is added to the regenerative cooling configuration in order to efficiently transfer thermal energy (enthalpy) between the two fluids - i.e. coolant and fuel - that are at different temperatures and in thermal contact.

A detailed view of a simple thermal network used to model the RCS heat exchanger is presented in Fig. 4.17. In the steady state, heat is transferred from the hot fluid (coolant) to the cold fluid (propellant) by three distinct thermal processes: (1) convection from the coolant to the hot fluid wall, (2) conduction through the wall of the heat exchanger, and (3) convection from the wall to the cold fuel. In practice, a foulant film, defined as an accumulation of un-wanted deposits on heat transfer surfaces, may form on both sides of the heat exchanger wall and might therefore result in an additional resistance to heat transfer. These fouling films often induce a reduction in exchanger efficiency and a pressure drop across it. Neglecting the pressure drop, the effect of the foulant layer(s) can therefore be modelled as a resistive factor, denoted k_{foul}, which can serve as a scaling factor (i.e. for hydrogen, $k_{foul} = 0.00176$ m^{2}K/W), intended to increase the required surface of the heat exchanger in design studies. The temperature of the coolant at the outlet of the actively cooled area, denoted T_{out}, is obtained through a combination of Eq. 4.72 and Eq. 4.73. Indeed, while Eq. 4.73 is used to determine the temperature of the coolant flow in the pipe at the location of

the actively cooled panel, Eq. 4.72 is then used to compute the temperature of the coolant at the inlet of the heat exchanger as

$$T_{out} = 2T_{pipe} - T_{tank} \tag{4.74}$$

Thereafter, since the temperature of the fuel flow is assumed constant equal to the operational temperature of the fuel before it passes through the heat-exchanger device, both the temperature of the coolant and the fuel after heat exchange, respectively $T_{out}^{'}$ and $T_{fuel}^{'}$, may be computed through an additional thermal balance applied at each of these two nodes. Then, as mentioned in the introduction of Section 4.3.1, the heat exchanger thermal network is simply used to couple the fuel feeder line network to that of the actively cooled panel. Finally, the parameters of the heat exchanger (namely area and conductivity of the heat exchanger wall) may therefore be sized in order to provide a certain temperature at the outlet of the engine lines (to improve combustion efficiency for instance) while ensuring that the boil-off of the fluid in the coolant tank is minimized.

4.3.1.5 ACS Controller

A simple bang-bang controller, i.e. on/off controller such as that used in a domestic refrigerator, has been modelled where the switching times between ACS on and off can be determined from a condition that is based on the temperature of the underlying structural skin of the vehicle. The threshold temperature used to switch between the two states can also include a 10 % margin below the material's critical temperature in order to account for thermal inertia within the structure (i.e. as thermal energy spreads across the structure of the vehicle). Then, this two-state optimal control strategy consists of two distinct phases: an initial phase during which the hybrid TPS simply serves as a passive thermal shield until the temperature of the structure has reached a prescribed limiting temperature, and then a second phase during which an intermittent flow of coolant is activated within the cooling channels in order to maintain the structural skin temperature below the temperature limit. The optimal control law, denoted u, can therefore be modelled as

$$u = \begin{cases} 0 & \text{if} \quad T_{struct} < T_{max} \\ 1 & \text{if} \quad T_{struct} \geq T_{max} \end{cases} \tag{4.75}$$

where T_{max} represents the threshold temperature and depends on the thermal properties of the structural material. It is important to note that during the first

passive phase, since the narrow cooling passages are assumed to have no influence on the thermal response of the structure (ACS is off), the pipe node is modelled as a neutral node (or ghost node). Indeed, a start-off condition based on the temperature of a specific node within the TPS can be added to any node of the thermal network in order to force it to switch between its on and off states during the numerical integration as appropriate.

4.3.2 Ground-hold Phase

In addition to the problem posed by the extreme heating environment to which the vehicle is subjected along both its ascent and re-entry trajectories, and taking inspiration from the work of Izon (106), the present work also considers the necessity of avoiding the generation of ice at the surface of the vehicle during ground-hold operations between successive missions. Indeed, the fuel inside the cryogenic tank will be maintained at a very low temperature before launch (20.4 K for liquid hydrogen, 90.2 K for liquid oxygen), heat will therefore be extracted from the tank structure as well as from the TPS materials that are directly in contact with it, causing temperatures to decrease throughout. If the temperature of the outer surface of the TPS, T_{tps}, decreases below the freezing point of water in the ambient atmosphere ($T_{ice} = 274.15$ K under sea-level conditions), for instance during adverse weather conditions or when humidity levels in the atmosphere are high, then the surface of the vehicle could develop a layer of ice prior to launch. The presence of ice on the surface of the vehicle during operations carries with it the potential to be extremely hazardous, and could lead to serious damage to the thermal shield of the RLV as well as increasing the vehicle's mass and potentially reducing its aerodynamic performance. Consequently, it must be ensured that the TPS, especially on those parts of the vehicle that are in close thermal contact with the cryogenic tanks and their insulation, is designed as far as possible to prevent the formation of an ice layer on the surface of the vehicle. It is indeed very important to ensure that the overall optimal TPS thickness does not only satisfy in-flight aero-thermodynamic heating constraints, but is also robust to other considerations that, somewhat ironically given past experience (e.g. ice covered foam on the Space Shuttle external tank), have traditionally been regarded as of secondary importance during the preliminary design phase. The problem of calculating the performance of the TPS during ground-hold operations is represented by the simplified thermal network shown in Fig. 4.18.

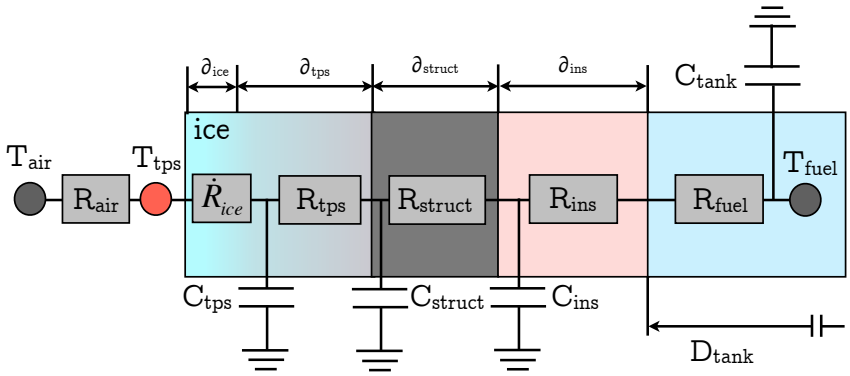

Figure 4.18: An illustration of the thermal shield during ground-hold - The diagram represents the state of the thermal management unit during pre-flight preparations such as after the cryogenic tank has been filled. A dynamic resistance has been added to model the formation of an ice layer on the surface of the vehicle when the TPS is subject to standard sea-level atmospheric conditions.

Ice Growth Model

On the ground, the vehicle is exposed to humid air at the ambient temperature. The time evolution of the wall temperature, denoted T_{wall}, can be obtained via a simple energy balance. Indeed, if the heat input at the wall is assumed to be due to the natural convection of the atmospheric air (e.g. neglecting solar radiation, for instance), then

$$Q_{in} = \frac{T_{air} - T_{wall}}{R_{air}} \tag{4.76}$$

and the convective resistance R_{air} is given by

$$R_{tps} = \frac{1}{h_{air} A_i} \tag{4.77}$$

where the convective heat transfer coefficient for still air, h_{air} is assumed equal to 5.6785 W/m^2 K under standard sea-level atmospheric conditions where $T_{air} =$ 293.15 K. Then, the thermal energy that leaves the surface due to the combined effects of conduction through the layer of ice, the TPS, the structural skin and the tank insulation layer, and heat transfer from the tank due to natural convection, can be computed as

$$Q_{out} = \frac{T_{wall} - T_{fuel}}{R_{eq}} \tag{4.78}$$

where T_{fuel} represents the temperature of the cryogenic fuel, and the equivalent resistor, R_{eq}, is given by

$$R_{eq} = \frac{\delta_{ice}(t)}{k_{ice}A_i} + \frac{\delta_{tps}}{k_{tps}A_i} + \frac{\delta_{struct}}{k_{struct}A_i} + \frac{\ln\left(1 + 2\delta_{ins}/D_{tank}\right)}{k_{ins}\pi D_{tank}} + \frac{1}{h_{fuel}A_{tank}} \tag{4.79}$$

where D_{tank}, δ_{ice}, δ_{tps}, δ_{struct} and δ_{ins} are, respectively, the diameter of the tank, the transient thickness of the ice layer with temperature-dependent conductivity k_{ice}, the thickness of the TPS layer with conductivity k_{tps}, the thickness of the underlying structural skin with conductivity k_{struct}, and the thickness of the tank-age insulation layer with conductivity k_{ins}. The term h_{fuel} represents the natural convective heat transfer coefficient of the fuel, and is based on empirical formulas. The differential equation governing the time evolution of the wall temperature during ground-hold operations can thus be written as

$$\dot{T}_{wall} = \frac{T_{air} - T_{wall}}{R_{air}C_{tps}} + \frac{T_{fuel} - T_{wall}}{R_{eq}C_{tps}} \tag{4.80}$$

Finally, the rate of growth of the layer of ice on the surface of the vehicle can be modelled by

$$\dot{\delta}_{ice} = \frac{Q_{in}}{\Delta H_f^0 \times \rho_{ice}} \tag{4.81}$$

where Q_{in} is the total heat flux flowing through the layer of ice, ΔH_f^0 is the heat of formation of ice from a vapour (assumed constant equal to -285.825 kJ.mol^{-1} for standard conditions), and ρ_{ice} is the density of ice which can vary with the temperature at the surface of the vehicle. This ground-hold analysis can then be used as a constraint of the TPS optimization problem verifying that ice would not build up during ground-hold given a TPS arrangement.

4.3.3 Verification of the HyTPS Thermal Model

The capabilities of the present TPS modelling approach will now be demonstrated for a series of test cases performed for two different types of passive TPS subject to both constant and transient thermal loads. Indeed, while it would be difficult to validate the present methodology for the modelling of an ACS (as a result of

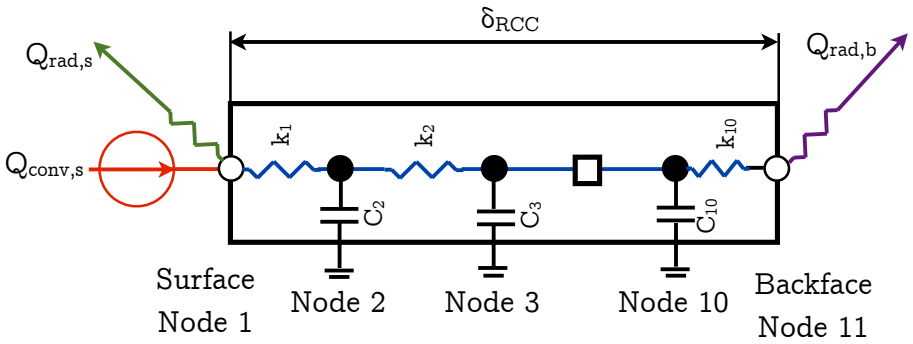

Figure 4.19: Thermal network for test cases

the lack of such experimental studies with all necessary data in the open literature), the present approach will however be verified for its use in the design of a passive thermal shield subject to both constant heat source and trajectory-based thermal loads, and composed of a single or multiple layers of insulation materials. The two first validation cases are taken from the work of Cowart and Olds (107), and the results of the present model are thus compared against a finite-difference model called the Thermal Calculation Analysis Tool (TCAT) which has been benchmarked against a commercial code called SINDA with excellent results. The thermal network modelled using HyTPS and employed to simulate the two first test cases is presented in Fig. 4.19. The third and last validation case attempts to replicate the study of Jones, Braswell and Richie (108) concerning the development of a fail-safe system for actively cooled supersonic and hypersonic aircraft. Additionally, the *pdepe* solver of Matlab, used to solve initial-boundary value problems for parabolic-elliptic Partial Differential Equations (PDEs) in one dimension, is also employed here (where appropriate) to solve the transient one-dimensional heat-conduction equation and thus to provide additional results for comparison. This Matlab solver has been used by Garbers (109) to perform the preliminary design of the TPS for the long-range hypersonic rocket-powered vehicle concept of DLR called the Spaceliner. The design method has been validated for the sizing of the TPS over the entire surface of the Space Shuttle and its results compared favorably with data found in the literature.

Constant Heat Source Analysis

For the first test case, a tile of 0.1016 m thickness and made out of Re-inforced Carbon-Carbon (RCC) material (similar to that used for the Space Shuttle),

Property	Value	Unit
Density	1580	kg/m^3
Specific Heat	770	J/(kg.K)
Thermal Conductivity	4.3	W/(m.K)
Emissivity	0.79	-

Table 4.1: Material properties of an RCC tile - Material properties of a Reinforced Carbon-Carbon (RCC) tile, at a temperature of 300 K, are presented.

whose properties are presented in Table 4.1, is considered (hot structure). It shall be noted that the material properties have been held constant throughout the simulation. The tile is subjected to a constant convective heat transfer rate set equal to 200 kW/m^2, applied to the top surface of the thermal shield structure for a period of 2000 seconds. Furthermore, as the tile is assumed to be in a vacuum, a conductive and radiative boundary condition at the backface node is also assumed in order to match the reference simulation (see thermal network in Fig. 4.19). Finally, the initial temperature of the tile is assumed equal to 300 K.

The comparison between the results provided by the HyTPS thermal model and the reference data are presented in Fig. 4.20 along with the results from the *pdepe* solver. As can be seen from the figure in question, the qualitative and quantitative results for the tile's backface and surface nodes seem to be very well predicted by the present reduced-order model when these results are compared to those from the finite difference code. In fact, the temperatures of both the surface and backface nodes reach a steady-state value equal to $1,400$ K and 800 K, respectively, which simply indicates that all modes of heat transfer also reach steady state as shown in Fig. 4.21. In this figure, it can be seen that most of the convective heat is re-radiated away from the surface of the tile. Overall, the results provided by HyTPS are very satisfactory.

Trajectory-Based Analysis

A second test case is presented in order to validate the HyTPS engineering code for trajectory-based analyses as this capability represents indeed the main reason for the development of the model in the first place. Therefore, for this second validation case, the data of the convective heat flux profile experienced by the Space-Shuttle STS-1 flight have been extracted from the reference paper and used

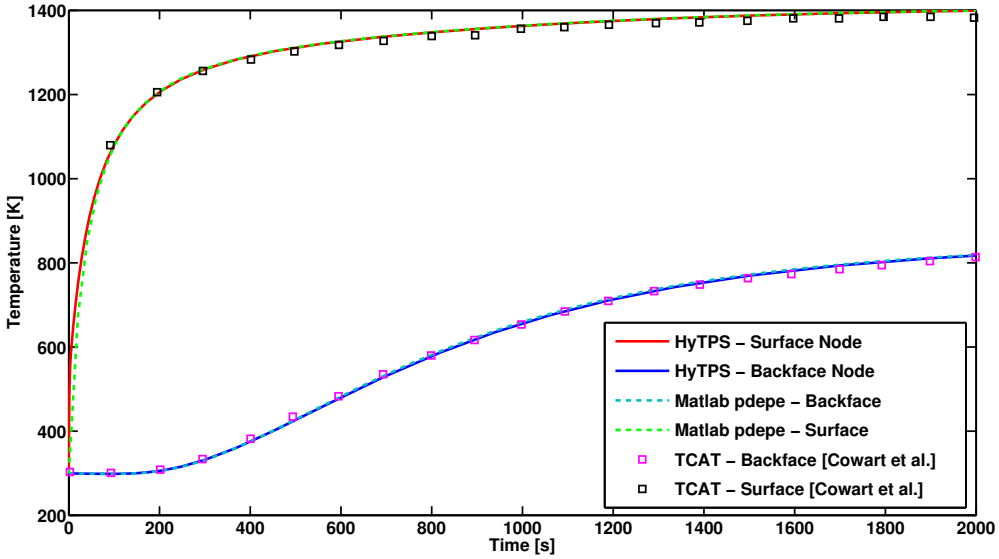

Figure 4.20: Steady-state thermal analysis - Validation of the capabilities of the present thermal model to perform steady-state calculations. The temperature profile of the backface node as predicted by HyTPS is shown in blue, while that of the surface node is shown in red.

in order to provide the transient heat flux required for the sizing of an RCC tile (see Fig. 4.22). Initial conditions similar to that of the previous test case are also assumed here, except that an *adiabatic* boundary condition is now assumed at the backface node. Nonetheless, it is not clearly stated in the reference paper whether the thickness of the tile is similar to that of the previous steady-state condition case. Moreover, the difference observed between the reference data and the results from the present model assuming a 10-cm-thick tile is rather dubious. Consequently, two different tile thicknesses are considered in the work presented here: a 10-cm-thick tile as before and a 15-cm-thick tile. The thermal response from the present TPS model (see again Fig. 4.19) is then compared with regard to the reference data obtained by Cowart *et al.* (107) using their one-dimensional finite-difference code. Additionally, the *pdepe* solver of Matlab is also used to provide a verification of the previous suspicion regarding the thickness of the tile and to corroborate the results given by HyTPS. These results are finally presented in Fig. 4.23. It can clearly be seen from the figure in question that, in either case, the surface node temperature peaks at a value of $1,600$ K after about 500 seconds of simulation, and then falls (at about $1,000$ seconds) before that of the backface reaches its peak value: slightly less than 700 K for a 15-cm-thick tile (experienced

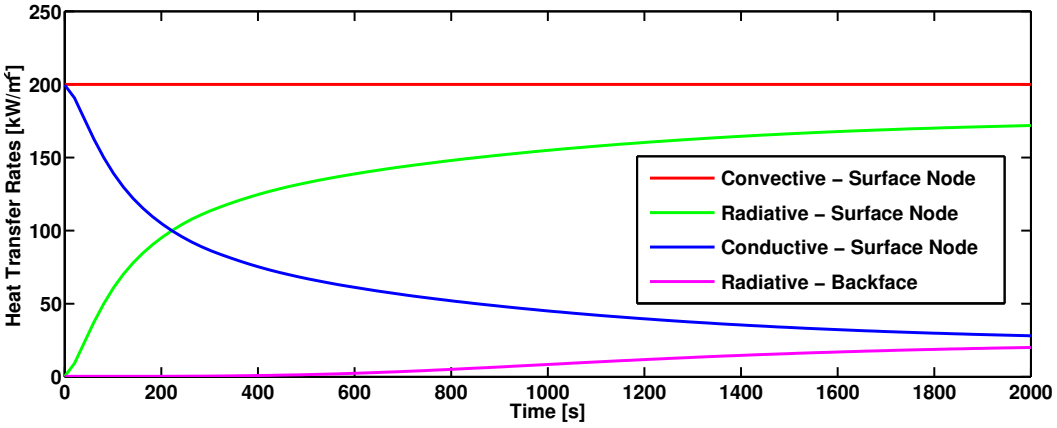

Figure 4.21: Heat transfer rates history for the steady-state case - The figure shows the various modes of heat transfer predicted by HyTPS: convective (red), surface radiative (green), conductive (blue), backface radiative (magenta). All modes of heat transfer reach approximately steady-state by the end of the simulation.

at the end of the simulation), and around 1000 K for a 10-cm-thick tile at about 1,500 seconds after the beginning of the simulation. The results from the *pdepe* solver confirm the trend provided by the results of the HyTPS code in both cases.

The present thermal analysis provides confidence in the ability of the present reduced-order model to properly describe the physics involved in heat transfer problems as the results confirm that the RCC tile indeed acts as an insulator – i.e. as it takes longer for the heat acting on the surface node to be transferred through the layer of material to the backface node. It shall also be noted that, in the case of a 10-cm-thick tile, the surface temperature reaches a temperature lower than that of the backface node at the end of the simulation, a phenomenon that results from the thermal inertia that subsists in the material (see Fig. 4.23). Furthermore, the level of peak temperature at the surface of the TPS seems to have been well predicted by both the HyTPS engineering model and the *pdepe* solver, in either case. The rise in temperature at the backface node seems to be well anticipated by both the thermal network model and the *pdepe* solver in the case of a 10-cm-thick layer of RCC. This instance, however, confirms the suspicions concerning the reference tile thickness. Indeed, the temperature profiles returned by both the HyTPS code and the *pdepe* solver follow exactly the results of TCAT in the case of a 15-cm-thick tile. The results provided by the HyTPS code (as those have been corroborated by those provided by the *pdepe* solver) are again reasonably satisfactory. The next validation case will however attempt to lift the veil on

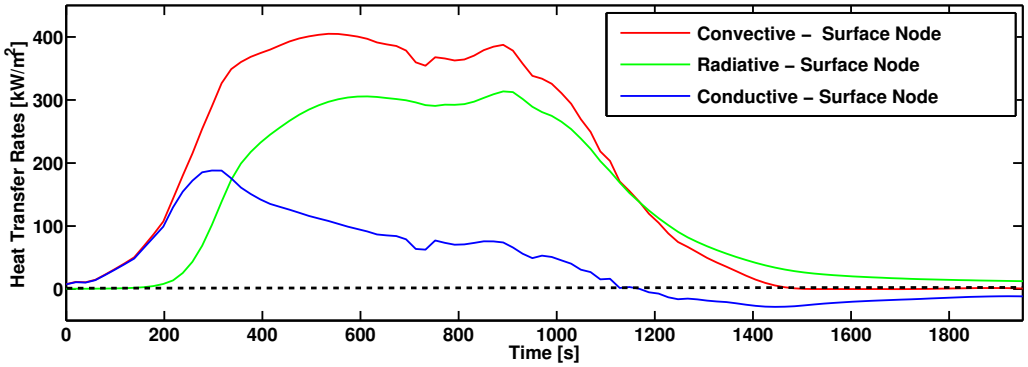

Figure 4.22: Stagnation point heating history along the STS-1 descent trajectory - The figure shows the various modes of heat transfer predicted by HyTPS: convective (red), radiative (green) and conductive (blue).

the remaining doubts concerning the validity of the present thermal model in transient-based simulations and will provide an additional validation for the heat transfer problem through a two-layer stack of disparate materials.

Multi-layer Insulator

A final test case is necessary to provide a proof of concept for the modelling of a TPS composed of layers of dissimilar materials. Here, the study of Jones and Braswell (108) is used for context. In the reference study, the authors derived an abort manoeuvre for the vehicle to provide a low-heat-load descent from nominal Mach 5 cruise conditions in case of a malfunction within the ACS (see Fig. 4.24) and subsequently sized a passive TPS for the aircraft skin to survive the resulting abort heat load without exceeding the allowable temperature limits of the materials. This strategy was conceived as an alternative to the use of a secondary redundant active cooling system (for reliability purposes). In the reference study, an average bare skin thickness of 0.508 cm (i.e. t_{ref}) is reported to be required for the vehicle to survive the abort manoeuvre from Mach 5 if the skin is made out of aluminium material ($T_{max} \leq 422$ K) and if the initial temperature at cruise condition is equal to 366 K (i.e. resulting in a surface mass of 11.564 kg/m^2). The HyTPS code has been used to reproduce this case: Fig. 4.25 depicts the results obtained from HyTPS if a 0.508-cm-thick aluminium skin is assumed and subjected to the abort heat transfer rates of Fig. 4.24. It shall be remarked that the exact value of surface emissivity is not provided in the reference study. However, it is assumed to be quite low and of the order of $\epsilon \leq 0.2$ (as is usually the case

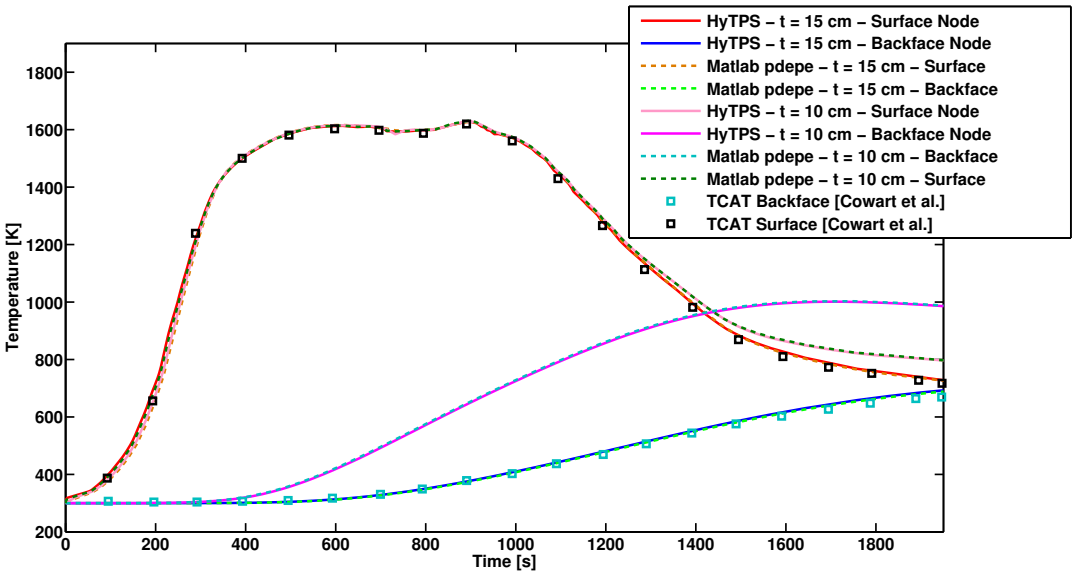

Figure 4.23: Trajectory-based transient thermal analysis - Validation of the capabilities of the present thermal model to perform trajectory-based calculations.

Property	Value	Unit
Density	2198	kg/m^3
Specific Heat	1046	J/(kg.K)
Thermal Conductivity	0.0049	W/(m.K)
Emissivity	0.2-0.8	-

Table 4.2: Material properties of the overcoat - Thermal properties of an insulating overcoat material.

for aluminium material). Nonetheless, a series of different values of emissivity has been considered for context – i.e. this figure thus illustrates the effectiveness of radiation cooling. For a reasonable estimate of the surface emissivity (i.e. $\epsilon = 0.2$), HyTPS predicts very well the result of the reference study. Indeed, an aluminium layer of thickness set to the value of t_{ref} maintains its temperature below 422 K as was desired.

Finally, in the reference paper, an overcoat TPS concept is sized. Indeed, because of the relatively low-heat-load descent, a layer of insulation (with a lower weight than aluminium) can be used to overcoat the structural skin layer and provide a reduction of both the heat load that goes into the ACS and the overall weight of the system. The thermal properties of the overcoat material are given in Table 4.2. Again, the surface emissivity of the material is unknown, however, considering

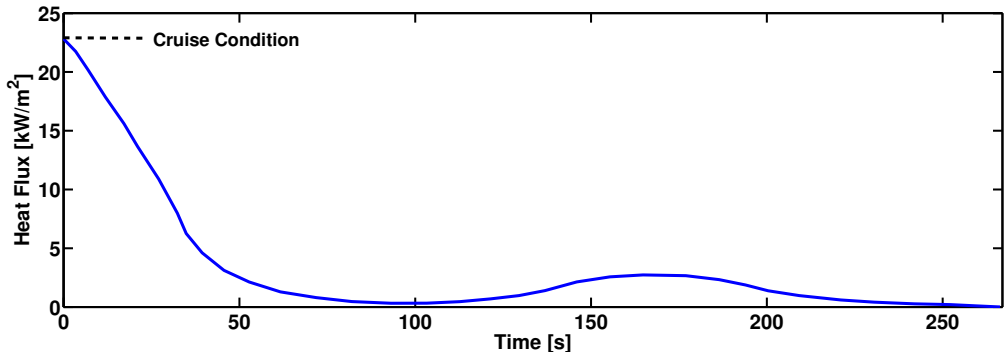

Figure 4.24: Low-heat-load descent heat transfer rates from Mach 5 cruise.

its relatively good insulation properties (very low thermal conductivity), it is assumed that the material is of the insulation type (i.e. foam) and should have a relatively low surface emissivity (as it is certainly not a hot structure like an RCC tile whose emissivity is of the order of 0.79). Nonetheless, two extreme values have been considered (i.e. $\epsilon = 0.2$ and $\epsilon = 0.8$) for comparison.

Then, a TPS arrangement consisting of a two-layer stack of disparate materials (i.e. a thin overcoat layer attached to an aluminium skin) can be optimized to reduce the total weight of the skin structure under thermal constraints. Indeed, the surface temperature must be prevented from exceeding a temperature equal to 700 K during cruise and equal to 811 K during abort. Additionally, the temperature of the skin must remain below 422 K throughout the flight profile. Here, the temperature distribution at the beginning of the abort manoeuvre must be the steady-state distribution at cruise. During cruise, the skin node has been modelled as a boundary node since the ACS is assumed to maintain efficiently the temperature of the structural skin constant at 366 K in the original study. Finally, a gradient-based optimizer (i.e. Matlab's *fmincon*) has been used to size the two layers of material. In the original study, the total weight is reported to be equal to 9.61 kg/m^2. Here, HyTPS returns a value of 10.62 kg/m^2 if $\epsilon = 0.2$ and 4.50 kg/m^2 if $\epsilon = 0.8$. The thermal response for either case is presented in Fig. 4.26 and Fig. 4.27, respectively. This final test case terminates the series of validations for the HyTPS engineering code: overall, the results provided by the reduced-order model appear promising.

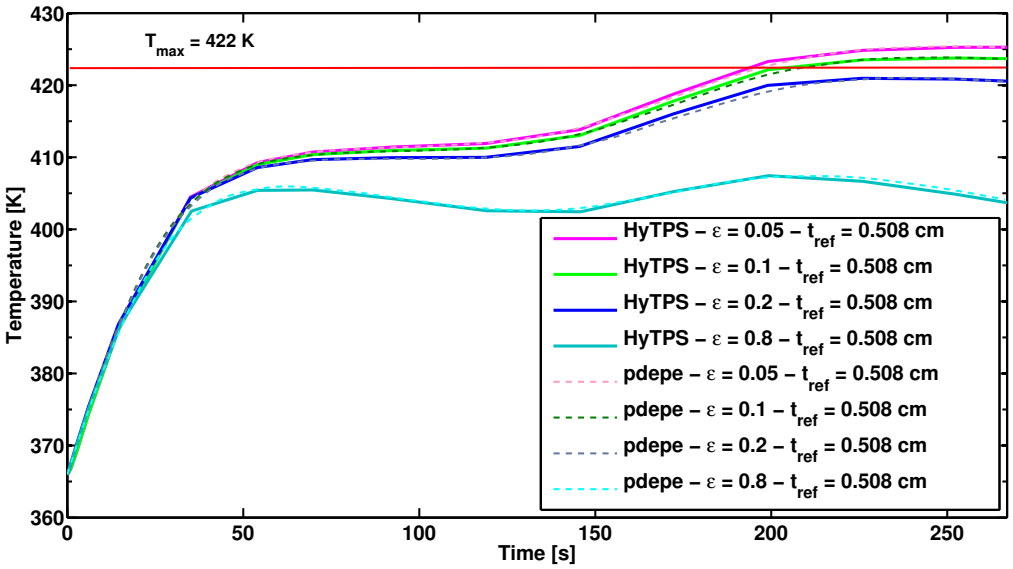

Figure 4.25: Temperature history of the structural skin during abort - The figure shows the thermal response of a 0.508-cm-thick aluminium skin exposed to an abort manoeuvre for different values of surface emissivity.

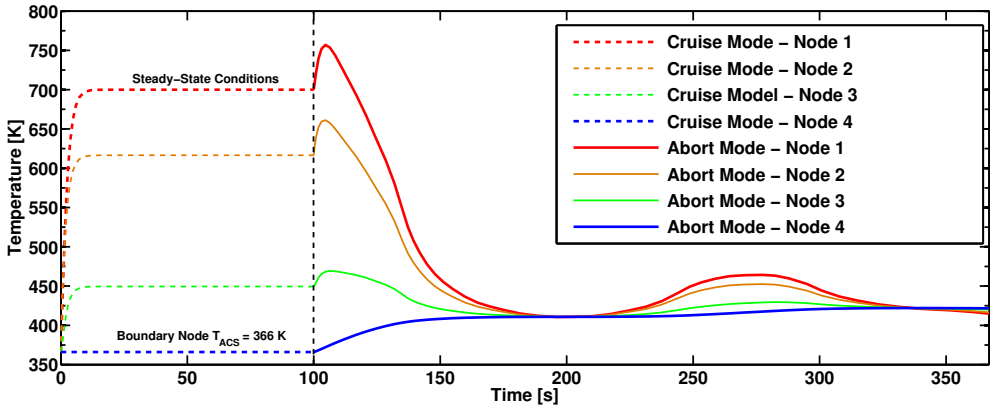

Figure 4.26: Temperature history during abort for an emissivity of 0.2.

4.4 Hybrid Propulsion Model

As discussed in Section 4.1, the new generation of space-access vehicles is foreseen to employ air-breathing engines, such as ramjets or scramjets, in order to achieve the performance required for practical attainment of a Single-Stage-To-Orbit (SSTO) capability. Unlike turbo-machinery-based engines, ramjets and scramjets do not have, theoretically, any moving parts. These engines are, in fact, simply composed of the following four basic engine components: intake, iso-

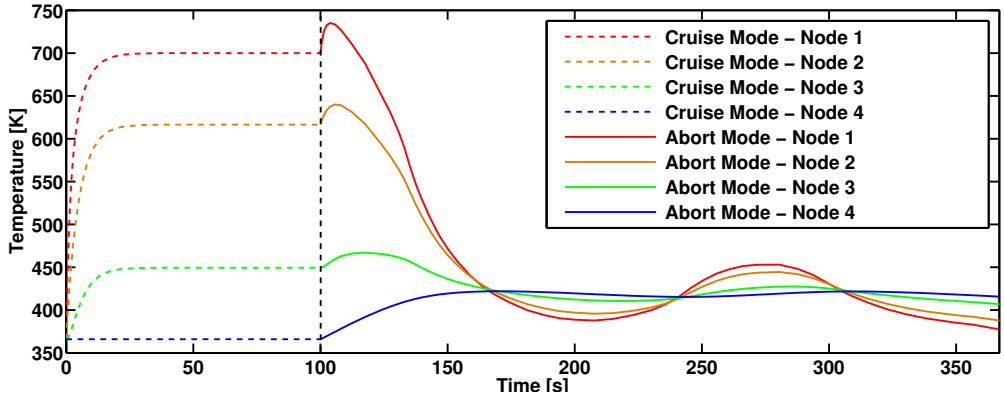

Figure 4.27: Temperature history during abort for an emissivity of 0.8.

lator, combustor, and nozzle. However, to support the flight of future re-usable space-access vehicles from subsonic to hypersonic speeds, those structurally simple air-breathing engines will have to be augmented into a propulsive configuration, often referred to as either a composite or combined-cycle device, that is of a much more complex nature. Indeed, air-breathing engines such as ramjets and scramjets would not be sufficient to propel a space-access vehicle from a standstill as they require an initial forward motion prior to being employed. This instance justifies the necessary requirement that future RLVs must, in all likelihood, make use of a more complex engine architecture, often referred to as hybrid engines, such as the promising Rocket-Based Combined-Cycle (RBCC) propulsion systems.

4.4.1 The HyPro Code

The propulsion model, described throughout this section, has been developed by Mogavero (76) as a stand-alone program successfully coupled and integrated into the system model – i.e. the engine model also adopts the self-contained *black-box* approach briefly introduced in Section 4.1.3. It shall be remarked that, while it is not the present author's intention to claim credit for the propulsion model being described in this section, a description of the combined-cycle propulsion model as well as some additional information concerning its intrinsic concepts are however necessary as these are paramount in the modelling of the next generation of future re-usable space transportation systems. Part of the present propulsion model will therefore be used in some of the design applications later introduced in Chapter 5. The propulsion model, called HyPro (which simply stands for "Hy-

brid Propulsion Optimizer"), has been developed using the C++ programming language. The model is similar in capabilities to other reduced-order propulsion models such as the Simulated Combined-Cycle Rocket Engine Analysis Module (SCCREAM) software developed at Georgia Institute of Technology by Bradford and Olds (110) as a preliminary analysis tool specifically crafted for the design of hybrid propulsive systems. Here, the HyPro computer code has a structure that benefits from the intrinsic modularity of the Object-Oriented Programming (OOP) formalism embodied within the C++ environment. Its modular structure allows it to be configured to easily model many different types of propulsion systems: from a pure rocket engine to a complex composite propulsion device. The architecture of the software also makes it possible to implement each module in terms of a pre-defined set of properties and parameters that can easily be changed during runtime. For example, it is possible to define a particular schedule of operation used to switch between the various operational modes of the system during a trajectory integration/optimisation procedure. This feature makes it particularly suitable for multi-disciplinary design studies. Additionally, the HyPro code has been validated against published scramjet CFD data with promising results. Its predictions have also been compared against those of the industry-standard SCCREAM code with reasonably satisfactory results, demonstrating its potential in modelling engines with relatively complex internal configurations. In Fig. 4.28, an illustration of the HyPro model, structured in order to represent a scramjet/ramjet engine, is depicted. This set of modules could be changed and re-arranged to represent a different engine configuration. Hybrid engines can be modelled by collating and inter-connecting all the required modules, then switching on or off certain of the modules according to a proposed schedule of operation.

Section 4.4.2 presents the gas dynamics involved within each of the miscellaneous engine modules. Thereafter, each individual component of the engine is presented from Section 4.4.3.1 through Section 4.4.3.6. Finally, the overall engine system model, used to assemble a given configuration, is introduced in Section 4.4.4.

4.4.2 Gas Dynamics Equations

In HyPro, the equations for the conservation of mass, momentum and energy along a duct with constant section area, given in Eq. 4.82 through Eq. 4.84, are required to be solved.

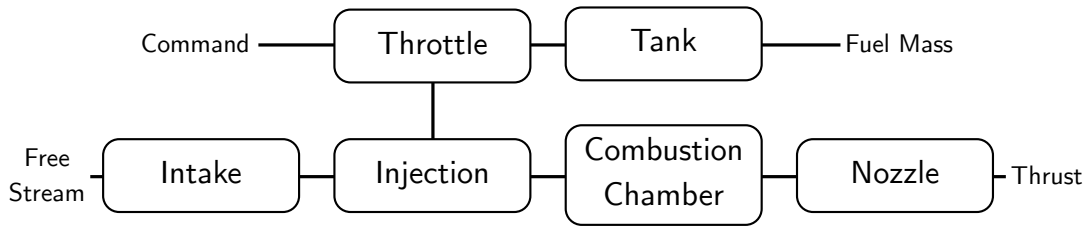

Figure 4.28: An illustration of the modularity of the HyPro model – The diagram shows an example of the modular structure of the HyPro propulsion model. The modules are arranged here to define a Scramjet/Ramjet configuration.

$$\rho_1 U_1 - \Delta G = \rho_2 U_2 \tag{4.82}$$

$$P_1 + \rho_1 U_1^2 - \Delta I = P_2 + \rho_2 U_2^2 \tag{4.83}$$

$$h_1 + \frac{U_1^2}{2} - \Delta H = h_2 + \frac{U_2^2}{2} \tag{4.84}$$

Nonetheless, before being solved, these equations may be re-written in the following form

$$\rho_1 U_1 - \Delta G = \rho_2 U_2 \tag{4.85}$$

$$P_1 + \rho_1 U_1^2 - \Delta I = (1 + \gamma^* M_2^2) P_2 \tag{4.86}$$

$$h_1 + \frac{U_1^2}{2} - \Delta H = h_2 + \frac{\gamma^* M_2^2 R T_2}{2} \tag{4.87}$$

where the subscripts 1 and 2 denotes, respectively, the conditions at the beginning and at the end of a given module, and ΔG, ΔI and ΔH are, respectively, the flux of mass, momentum and energy across the walls of the duct. Therefore, assuming the conditions at the beginning of a module as well as the corresponding lateral fluxes, the gas dynamics solver within HyPro evaluates the conditions at the end of the module. Here, it is assumed that the gas can be modelled by a calorically and thermally ideal gas where γ^* represents the effective ratio of specific heats of the gas mixture and is considered to vary with temperature. As described in the reference study of Mogavero *et al*, the solver requires first an initial guess for the value of M_2 to be made before it proceeds through the solution of each element of the system of equations. The solution process is defined by the following steps:

1. First, Eq. 4.87 is solved in terms of the static temperature T_2 using a simple bisection algorithm.

2. Then, Eq. 4.86 is used to determine the static pressure P_2.

3. Finally, Eq. 4.85 is used to determine whether the initial value of the Mach number at the end of the module is correct or not.

Finally, this iterative process is repeated until a pre-specified level of convergence is obtained.

4.4.3 Engine System Components

The following section introduces the miscellaneous engine components (i.e. modules) of the HyPro code that can be used and combined together to model the type of hybrid engines foreseen to equip the future generation of RLVs.

4.4.3.1 Intake Model

The first component of an air-breathing engine (either ramjet or scramjet) will always be the intake (also known as inlet). The primary function of the inlet is to decrease the Mach number of the oncoming hypersonic flow and to compress the inlet air to a desired state before it is fed into either an isolator or directly into the combustion chamber. The intake geometry of future air-breathing engines will most likely be of a variable nature and may possibly be adjustable during the vehicle's ascent to support the flight of the vehicle from supersonic to hypersonic speeds. The intake of future air-breathing engine is thus likely to become a critical component of the overall vehicle system due to its complex area-changing capability and size. Indeed, if we assume an ascent flight at constant dynamic pressure (often assumed for the ascent-to-orbit of air-breathing engine-powered vehicles), the mass flow rate of air captured by the inlet area, noted $\dot{m}_{air}$, is given by

$$\dot{m}_{air} = \rho_\infty V_\infty A_{in} = q_\infty \frac{A_{in}}{V_\infty} \tag{4.88}$$

where A_{in} is the inlet area. It can clearly be seen from Eq. 4.88 that as the flight velocity increases, the amount of air swallowed by the engine's intake is then reduced. Therefore, the inlet area will most probably require to be adaptable to the flight conditions if the range of applicability of these engines is to be extended to sustain a high level of thrust throughout the operational envelope of the vehicle. The previous comment emphasizes even further the importance of a

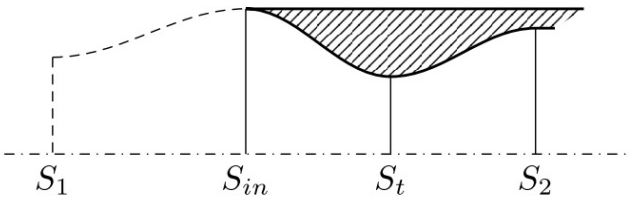

Figure 4.29: Engine intake model - Definition of the miscellaneous stations for the intake model embedded within HyPro.

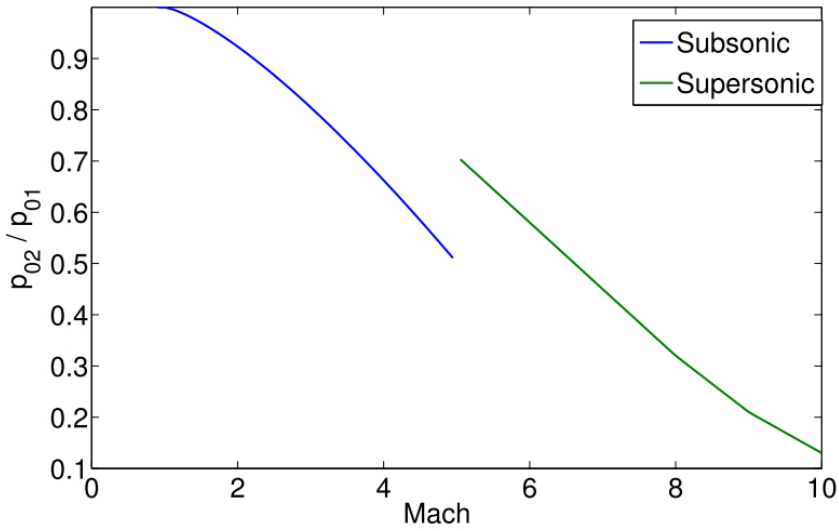

Figure 4.30: Intake pressure drop - Intake total pressure drop as a function of Mach number.

proper modelling of the intake considering the impact it may have on the overall engine performance.

In HyPro, the inlet model is composed of four different stations as depicted in Fig. 4.29. It should be remarked that the conditions at the first station, denoted S_1 in the figure in question, can be assumed to be different from those at the intake station, designated as S_{in}, in order to give the possibility to model non-adapted types of intakes. Indeed, in the case of a non-adapted intake, the external flow path is assumed to be isentropic if the external flow is subsonic, whereas if the external flow is supersonic then a strong normal shock is assumed to form ahead of the module and is considered to be sufficiently strong to fully adapt the intake to the external flow. When the intake is not fully adapted, an additional term, used to model the corresponding intake drag, D_T, can be computed using

Eq. 4.89 below (111).

$$D_T = \dot{m}_{in}(U_{in} - U_1) + A_{in}(p_{in} - p_1) \tag{4.89}$$

This extra drag can then be subtracted from the total thrust delivered by the engine, denoted F_T. Thereafter, the flow within the intake is computed by assuming a total pressure drop across the convergent part of the duct while the flow in the expanding part of the intake's duct is assumed to be isentropic. The pressure drop in the converging portion of the intake is given by the military specification MIL Spec E-5007D in the case of subsonic conditions at station S_{in} (112) and by fitting to a prescribed curve otherwise (see Fig. 4.30) (113). Indeed, another method was required for when the inlet flow Mach number increases beyond Mach 5 as it has been shown that the MIL Spec E5007D predicts a very high pressure loss beyond that speed limit – values that are believed to be far too conservative (112). In fact, an intake must, in theory, retrieve much of the free-stream stagnation pressure if its design is to be considered successful.

4.4.3.2 Fan and Compressor Model

In HyPro, a relatively simple model for fans and compressors is also included. The model takes as input the total pressure ratio and considers the compression to be isentropic. The stagnation conditions at the end of the compressor are thus determined as

$$P_{0,2} = R_p P_{0,1} \qquad \rho_{0,2} = R_p^{\frac{1}{\gamma^*}} \qquad T_{0,2} = \frac{1}{R}\frac{P_{0,2}}{\rho_{0,2}} \tag{4.90}$$

where R_p represents the aforementioned compression pressure ratio. The static conditions and the Mach number at the end of the compressor are then calculated by imposing a mass balance across the compressor. This balance equation is then solved iteratively using the Mach number as the guessed "*known*" variable.

4.4.3.3 Mixer Model

The mixer module permits the modelling of the mixing of two flows. In HyPro, it is therefore modelled with the help of an additional module composed of an

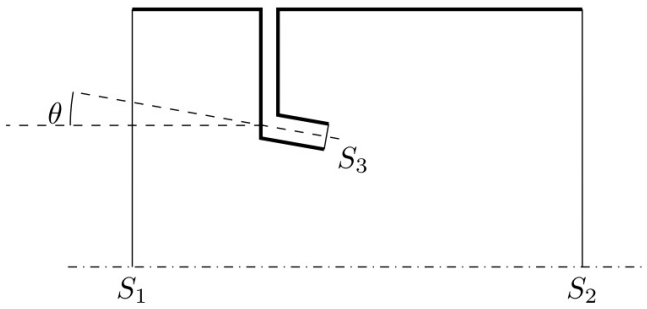

Figure 4.31: Mixer model - Definition of stations for the mixer module.

internal node (denoted S_3 in Fig. 4.31). This particular module can then be concatenated into any other module of the HyPro model. This module can typically be used when the momentum contribution of the flow out of the module (here attached to the internal node S_3) cannot be neglected: e.g. in modelling an ejector system, the plume of a rocket mixes with the airflow coming from the inlet and thus its contribution is modelled in HyPro using the mixer module. Again, the mixer module makes use of the gas dynamics solver described in Section 4.4.2, where the lateral fluxes of Eq. 4.85 through Eq. 4.87 are, here, given by

$$\Delta G = -\frac{A_3}{A_1}\rho_3 U_3 \tag{4.91}$$

$$\Delta I = \eta\left[\Delta G U_3 - \frac{A_3}{A_1}(P_3 - P_1)\right]\cos\theta \tag{4.92}$$

$$\Delta H = \Delta G\left(\frac{U_3^2}{2} + h_3\right) \tag{4.93}$$

where η represents the mixer efficiency and θ is the angle at which the flow is injected into the mixer at the location of the module's internal node (see Fig. 4.31). The previous equations are derived under the assumption that the pressure surrounding the injected flow is equal to the pressure at the inlet station S_1 – this is true if it is further assumed that the mixer module is defined in such a way that its inlet (S_1 in the figure in question) is close enough to the point of injection.

4.4.3.4 Injector Model

The injection module takes care of the mixing between the injected fuel and the main air flow. In HyPro, two models are available: both add the fuel flow to the main air flow and do not consider the possibility of any reaction between the fuel and the incoming air at the point of injection. The most basic of the two models

accounts for the addition of the fuel mass to the main air flow through the simple expedient that the pressure at the exit of the module is increased as compared to that at the entrance by

$$P_2 = \frac{P_1}{1 - X_{fuel}} \tag{4.94}$$

where X_{fuel} represents the molar fraction of the fuel. In that model, the temperature and velocity are considered constant along the length of the module. Although this assumption is not physically valid, its sole purpose however was to be used during the validation of the model. For the second injector model, the gas dynamics solver described in Section 4.4.2 is once again used. The module takes as input the equivalence ratio, denoted ϕ (also known as the fuel/oxidizer ratio), along with the fuel properties such as its temperature and composition, and then calculates the lateral fluxes required in Eq. 4.85 through Eq. 4.87 according to

$$\Delta G = -(\phi\Phi)\frac{M_f}{M_1} X_{ox1}\rho_1 U_1 \tag{4.95}$$

$$\Delta I = 0 \tag{4.96}$$

$$\Delta H = \Delta G h_f \tag{4.97}$$

where Φ is the stoichiometric composition of the fuel (i.e. proportions of reactants and products), M_f and M_1 are, respectively, the molecular mass of fuel and that of the incoming air-stream, and X_{ox} is the molar fraction of oxidizer. Hence, the main assumption in Eq. 4.96 is that the momentum of the injected fuel, ΔI, is negligible compared to that of the principal flow.

4.4.3.5 Combustor Model

The combustion chamber, where the air flow is heated by combusting some of the fuel, is likely to be the most complex part of the whole engine sub-system for modelling. If a scramjet is considered, interactions between several distinct physical phenomena all need to be concurrently accounted for, leading to complications when attempting to provide a modular model. In addition, the high temperatures in the combustion chamber and the associated changes in composition of the gas mean that real gas effects cannot be neglected. Moreover, in the case of supersonic combustion, heat-exchange and friction phenomenon are important processes that need to be accounted for. For these reasons, in the

current version of HyPro, the solver described in Section 4.4.2 is employed once again when the composition of the gas at the end of the combustion chamber has been calculated assuming complete combustion.

If needed, the heat flux exchanged through the chamber walls and the momentum loss due to friction can be added to the model. The momentum loss due to friction is given by

$$\Delta I = \tilde{\tau}\frac{A_w}{A_1} \quad \text{where} \quad \tilde{\tau} = \frac{1}{2}(\tau_1 + \tau_2) \tag{4.98}$$

where the shear stress τ_i, computed as in Eq. 2.40, assumes a constant friction coefficient C_f along the length of the module. Since the variation of shear stress along the combustion chamber's wall is not linear, Eq. 4.98 is only a first order approximation (a good compromise between accuracy and computational complexity). Finally, the heat exchange with the wall can then be evaluated as

$$\Delta H = \frac{\tilde{q}}{\dot{m}}\frac{A_w}{A_1} \quad \text{where} \quad \tilde{q} = \frac{1}{2}(\dot{q}_1 + \dot{q}_2) \tag{4.99}$$

where $\dot{q}_i$ is the wall heat flux and is computed as in Eq. 2.54 where the Stanton number, St, is obtained via the Reynolds analogy as $St = C_f/2$ (see Section 2.7.1 in Chapter 2 for more explanation).

4.4.3.6 Nozzle Model

Finally, the last part of an air-breathing engine corresponds to the nozzle. For scramjet engines, the nozzle should be a divergent duct that is used to expand the flow (convergent-divergent duct for ramjet engines). Since these engines require a large nozzle pressure ratio (even more so for scramjet engines), the nozzle will most probably use the entire vehicle's aft fuselage to expand the engine's outflow. Since the thrust of the engine is only slightly greater than the drag acting on the vehicle at hyper-velocities, a good efficiency as well as an adequate design of the nozzle are paramount to the success of these engines (114). In HyPro, a simple model based on isentropic expansion is used under the assumption that the flow passing through the nozzle can accurately be modelled as being frozen (110). The dissipation of the flow through the nozzle can also be modelled simply by expressing it in terms of a constant stagnation pressure drop.

4.4.4 Engine System Model

The main underlying design philosophy in the development of the HyPro reduced-order model was, above all, to provide flexibility in the creation of fully integrated single engine systems that are composed of a combination of different propulsive technologies. Indeed, the various models presented in the previous section may be combined, collated and connected in order to form the basis for the propulsion approach required in the present work for the planning of the ascent-to-orbit phase of the mission of future re-usable space planes. Therefore, as for the rest of the other components of the vehicle model, HyPro's main module is a self-contained subsystem model that can be used to organize the overall topological configuration of the propulsive device in order to model any kind of engine (from a pure rocket to a complex combined-cycle engine) while ensuring the communication between the various inter-connected modules without interfering with any other external subsystem components. The engine system model thus also manages the interface with the overall vehicle system (transfer the output). Whenever a configuration is set up, the solution state of each module is determined sequentially starting upstream from the intake down to the nozzle at the rear of the configuration. Most of the time, the solution proceeds in that direction unless choking occurs within the system. In that particular case, the information has to be propagated upstream to let the flow path of those forward modules adapt to that choking phenomenon. For instance, whenever choking is detected in the mixer module then the intake model has to adapt by spilling out part of the incoming air flow, while if choking is detected in the combustion chamber then the injection process has to adapt to reduce the amount of injected fuel (76). In general, whenever choking is detected in one of the engine modules, then an iterative procedure is begun in order to converge the flow properties within all upstream modules on those conditions which allow the exact conditions for choking to be established within the affected module. Once the flow path has fully been determined, the global thrust of the engine can be evaluated by performing a momentum balance across a control volume as

$$F_T = \dot{m}_2 U_2 - \dot{m}_1 U_1 + (P_2 - P_1) A_2 - D_T \tag{4.100}$$

The main advantage of this self-contained black-box approach is that the thrust value, F_T, internally computed in the propulsion model, can then be directly used during trajectory integration by the flight model without having any cognizance of

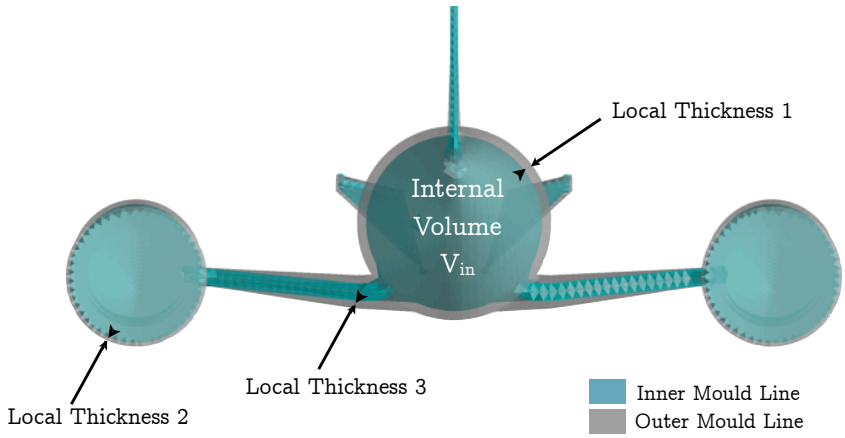

Figure 4.32: Definition of the Inner Mould Line (IML) - The surface mesh of the Skylon vehicle (shown in light grey) is extruded inward in order to obtain a physical representation (mesh) of the internal space available for the accommodation of the vehicle's subsystems (which is shown in cyan blue).

the various computations that have been conducted within the engine model itself. This is the same for the switching between operative modes, these parameters as well as the prescribed schedule of operation are directly defined inside the propulsion model. This software architecture provides therefore an excellent setup for parametric studies (see, for example, Section 5.3.3 of Chapter 5)

4.5 Mass Model

The mass model can be used to accomplish two different tasks: firstly, the model includes a packaging module that can be used to deal with the internal configuration of the vehicle. The mass model can indeed be employed to organize the internal subsystems of the vehicle in order to fulfill some pre-defined requirements that may be based on conditions such as the location of the Centre of Mass (CoM) of the vehicle. This packaging module is introduced in Section 4.5.1. Then, the present mass model can also be used to estimate the weights of major subsystem components such as the TPS, the tanks and the propulsion system. It can then calculate the location of the overall Centre of Mass (CoM) by superimposition of the CoM of all the system components. These miscellaneous weight models are described in Section 4.5.2.

4.5.1 Internal Configuration

First, the packaging module is responsible for the arrangement of the various system components within the internal space of the vehicle – i.e. a relative position between adjacent subsystems is therefore defined. The internal arrangement can be based on an order that is pre-defined by the user or might, for instance, be automatically set to maximize the forward location of the centre of mass of the vehicle for considerations of longitudinal stability during re-entry with empty tanks. Then, the packaging module also provides a means of verifying that all of the internal components, such as the tanks, subsystems and payload can be accommodated within the Inner Mould Line (IML) of the vehicle (see Fig. 4.32). The IML is obtained by offsetting the external mesh of the vehicle by the local TPS thickness. The method consists in displacing the vertices of the mesh, associated with a TPS thickness δ_i, in the direction normal to the surface of the tessellation as

$$v_i^{new} = v_i - \delta_i \hat{n}_i^v \tag{4.101}$$

where $\hat{n}_i^v$ is the outward vertex unit normal, v_i is the location of the original vertex and v_i^{new} are the new coordinates of the displaced vertex. For the vertices that are located at the boundary of two different *thermal zones*, the maximum thickness between the two zones is used to offset the vertices (i.e. conservative assumption). The internal volume, denoted V_{in}, can then be computed through the use of Gauss's Divergence theorem, where the vector field flowing through each triangular panel is here assumed to be the z-component of the local outward unit normal, denoted n_i^z, as

$$V_{in} = \sum_{i=1}^{N} A_i \; \tilde{c}_z \; n_i^z \tag{4.102}$$

where $\tilde{c}_z$ is the z-component of the i^{th} face centroid – i.e. conceptually, this method simply adds up the volumes of the pyramids defined by each of the panels used to describe the tessellated mesh. Finally, if the internal configuration of the vehicle does not fit within the surface boundary defined by the IML, the model then automatically scales the vehicle so that it does by using a transformation matrix, herein denoted T_s, given by

$$T_s = \begin{bmatrix} S_x & 0 & 0 \\ 0 & S_y & 0 \\ 0 & 0 & S_z \end{bmatrix} \Rightarrow v_i^{new} = T_s v_i \tag{4.103}$$

where S_x, S_y and S_z are the necessary scaling factors along the x, y and z axis respectively – i.e. these factors are set equal for photographic scaling along the x, y and z directions. In fact, two options can be used here: first, if the component systems are physically represented by their respective volume (but are not modelled using a CAD software or otherwise), a simple test is performed to verify whether the total volume of the components can be accommodated within the internal space. If it is not, a uniform scaling factor can simply be determined as

$$S_x = S_y = S_z = \frac{V_{req}}{V_{in}} \tag{4.104}$$

where V_{req} is the volume required to fit all the system components (i.e. sum of the volume of all components) and then Eq. 4.103 can be applied. Otherwise, if the subsystems have been modelled and their relative positions defined, the packaging module can perform a test to identify whether the vertices of the mesh of a given subsystem are located inside or outside of the boundary defined by the vehicle's triangulated surface. To perform this test, a number of rays, whose origins corresponds to each vertex point of a given subsystem mesh, are traced in the positive and negative x, y and z directions. A vertex is considered enclosed within the tessellation of the vehicle if the number of ray/surface intersections is equal to the number of rays, otherwise the point is located outside of the IML and the vehicle requires to be scaled up. The scaling factor(s) in Eq. 4.103 are then simply computed using a rapid iterative Newton-Raphson method. These factor(s) are required to fit the internal configuration within the physical boundary of the IML.

4.5.2 Weight Models

The weight model allows the mass of each individual component of the vehicle to be estimated once its flight performance, the dimensions and shape of its subsystems, and the amount of cryogenic fuel required for both the propulsion system and its ACS is known. Here, some elements of the Hypersonic Aerospace Sizing Analysis (HASA) method have been used in order to estimate the vehicle's mass, denoted m_v, also known as the Gross Take-Off Mass (GTOM) of the vehicle (115). This method has been used extensively in MDO studies (116, 117). The HASA method adopts a statistical weight approximation technique which

has been shown to approximate reasonably well the GTOM for a number of hypersonic vehicles, including the American Space Shuttle (115). It should finally be noted that the payload mass, denoted m_{pay}, can either be assumed to be part of the mission requirements (and is therefore maintained constant throughout the design process) or can become a parameter of a design study. This section introduces the method to compute the weight of the major system components of the vehicle.

Propulsion System

Here, the total mass of the propulsion system is considered to be the sum of the mass of the thrust structure, noted m_{thrust}, used to support the engines and the mass of the propulsion system itself, denoted $m_{engines}$. The equations for computing these values are taken directly from the HASA method where m_{thrust} is assumed to scale with the maximum thrust produced by the combined effect of all the engines, denoted F_{Tmax}, and is, in fact, the result of an equation which is a slightly modified version of that used in the original HASA method as

$$m_{thrust} = \frac{1}{3}(m_{rocket} + 2m_{ab}) \tag{4.105}$$

where m_{rocket} and m_{ab} represent, respectively, the result of the corresponding HASA equation for the mass of the support structure of a rocket engine and that of the structure of an air-breathing engine. The logic in Eq. 4.105 is required to account for the fact that the structure of hybrid engines will, most likely, resemble more closely that of an air-breathing engine rather than that of the historical rocket engines on which the original HASA equation is based on. Finally, the mass of the engines, denoted $m_{engines}$, is itself based on a characteristic length of the hybrid engines (i.e. the height of the module in the original HASA equation) as well as the number of engines used to propel the vehicle.

Thermal Protection System

The total mass of the thermal protection system can be evaluated as the sum of the masses of the RSI layers applied to the vehicle's surface together with the

mass of the ACS. The mass of an insulation layer is given by

$$m_{tps} = \rho_{tps} A_i \delta_i \tag{4.106}$$

where δ_i is the thickness of the insulator, A_i represents the surface area covered by the RSI in the corresponding *thermal zone*, and ρ_{tps} is the density of the insulation material. Similarly, the mass of the ACS - given by Eq. 4.107 - is approximated as the sum of the masses of its component layers of RSI, calculated using Eq. 4.106, a basic system mass m^0_{acs} (i.e. that must include any pump, valves etc.), a term proportional to the length of piping and the number of pipes used within the system, and the total mass of coolant, noted m_{cool}, that passes through the system during the mission (from $t = 0$ s to t_f).

$$m_{acs} = \sum_{i=1,2} \rho_{tps,i} A \delta_i + m^0_{acs} + k_{acs} L_{pipe} N_{pipe} + \int_0^{t_f} \dot{m}_{cool} dt \tag{4.107}$$

Load Bearing Structure

The total mass of the structural skin of the vehicle, denoted m_{skin}, can simply be determined by the following relationship

$$m_{skin} = \rho_{skin} A_v \delta_{skin} \tag{4.108}$$

where δ_{skin} represents the thickness of the structural skin of the vehicle and is assumed to be of the order of a few millimeters (i.e. aerospace standard), A_v is the total area covered by the vehicle's inner mould line surface (since the TPS will directly be attached to the underlying structural skin) and finally ρ_{skin} is the density of the structural material that composes the load bearing structure of the vehicle.

Cryogenic Tanks

The mass of each propellant/coolant tank, denoted m_{tank_i}, can simply be computed as the sum of its structural mass, the mass of its insulation layer and the total mass of its propellant load. Therefore, the total mass of liquid fuel on board

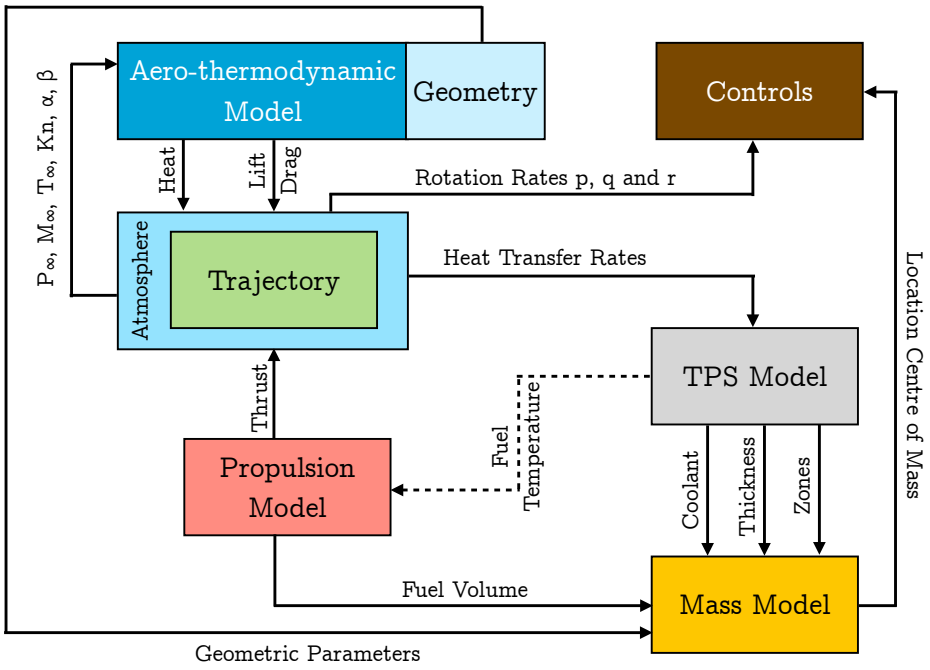

Figure 4.33: An illustration of the various couplings between subsystem models - The diagram summarizes the various connections between the miscellaneous system components introduced in this chapter.

of the vehicle is simply given by

$$m_{tank} = \sum_{i=1}^{n_{tank}} [\delta_i \rho_i A_{tank,i} + \delta_{ins,i} \rho_{ins,i} A_{tank,i} + \rho_{fuel,i} V_i] \tag{4.109}$$

where δ_i and $\delta_{ins,i}$ are, respectively, the thickness of the tank structure (with density ρ_i) and the thickness of the insulation layer (e.g. foam or aerogel) whose material's density is equal to $\rho_{ins,i}$, $A_{tank,i}$ is the total surface area of the tank, $\rho_{fuel,i}$ is the density of the fluid contained within the tank and V_i is the tankage volume.

4.6 Couplings between Models

As opposed to the design of conventional aircraft, future winged RLVs are highly integrated aerospace systems. Indeed, it appears trivial that all the subsystems presented in this chapter are connected, in one way or another. These tight interconnections between component systems need to be evaluated and accounted for

during the preliminary design assessment of any new hypersonic vehicle concept. Indeed, while some of these connections can lead to synergistic requirements, others lead to competing objectives that need to be addressed during the preliminary design process as the latter can have dramatic consequences on the resulting final design. The various couplings between these models are summarized and conceptualized in the diagram shown in Fig. 4.33. Although some of the various couplings presented below have already been implemented in the current version of the software, others are simply discussed here as suggestions for future works.

Propulsion System and Aerodynamics

In the design of future air-breathing engine-powered vehicles, the very strong coupling that exists between the aerodynamic surfaces and the propulsion system is a good example of strongly "*coupled and shared system functions*" (118). The entire undersurface of the vehicles will, in fact, become part of the air-breathing engine used to accelerate up to orbital speeds. Indeed, the inlet of future air-breathing engines will be fully integrated into the fuselage design as a means to accommodate the long compression ramps that are often required for this type of engine. Furthermore, the aft-body of the vehicle will serve as part of the nozzle expansion system and the engine system itself will provide a sizable fraction of the aerodynamic loads, such as the lift and pitching moment, required by the vehicle. Additionally, the exhaust plume which is expanded at the rear of the propulsion system may also modify the external aerodynamic loads acting on surfaces located further downstream and may, as a result, increase the drag acting on the vehicle and, by consequence, modify the performance of the vehicle during its ascent-to-orbit phase. For instance, the pressure distribution along the afterbody surface (the portion of the body directly impacted by the engine plume), denoted $P_{aft,i}$, might be estimated with the help of the simple relationship introduced in Eq. 4.110 in the absence of a better approximation (119).

$$P_{aft,i} = \frac{P_{exit}}{1 + \frac{d_z}{L_{aft}} \left(\frac{P_{exit}}{P_i} - 1 \right)} \tag{4.110}$$

where P_{exit} is the pressure at the engine exit, d_z is the distance, along the longitudinal z-axis, from the engine exit to the panel in question, L_{aft} is the length of the vehicle's afterbody (which can be computed as the distance between the nozzle and the rear tip of the vehicle's fuselage) and P_i is the surface pressure

as estimated by HyFlow. The logic in Eq. 4.110 is required to account for the effect of the plume in the direct vicinity of the nozzle. From the equation in question (and more particularly its denominator), the effect of the pressure at the engine exit decreases as the distance between the nozzle and the panel in question increases.

Finally, the input conditions at the beginning of the engine's inlet module, namely Mach number and pressure, may also be computed from HyFlow (instead of being assumed) and then inserted into the inputs of HyPro. This can be achieved by identifying the panels that define the inlet of the engine prior to performing the vehicle aerodynamic analysis (this analysis obviously requires the physical mesh of the engine to be modelled).

ACS and Propulsion Model

Furthermore, the regenerative cooling system will be used to absorb and dissipate the aerodynamic heating and combustion loads acting on space-access vehicles but may also be used to enhance the combustion process within the propulsive device (see Section 4.3.1.4). In fact, the same could be done if the direct cooling method discussed in Section 4.3.1.2 is employed instead. Indeed, the heated coolant (assumed to be part of the fuel) and the propellant that originates directly from the fuel tank (the fraction of it that does not pass through actively cooled panels) will be mixed together before being fed into the engine's combustion chamber – i.e. increasing the temperature of the propellant while mixing. Therefore, either of these two methods may have to be optimized in order to fulfill both the heat protection requirements (based on the trajectory of the vehicle) and the enhancement of the engine's efficiency by providing a suitable temperature rise in the fuel that is subsequently fed into the engines. Indeed, this condition can be met by correctly conceiving the heat exchanger in the case of the regenerative cooling method or by optimizing for the flow rate of coolant which is required for mixing with the flow rate of fuel if the direct cooling method is being used instead.

TPS and Controls

Additionally, the type of TPS – which can either be brittle (and thus easily subject to damage) or might introduce a repeated pattern of surface asperities

due to tiling for example (56) – may be more inclined to trigger an early onset of transition (see Section 2.5.2). This phenomenon affects the aerodynamic heating environment in which space-access vehicles will be operating. An early onset of transition can also have a non-negligible effect on the scheduling of control surface deflections as a result of an increase in viscous drag (see Section 6.3.3 of Chapter 6) (13). In fact, the resulting turbulent region may develop asymmetrically and therefore might induce unbalanced aerodynamic moments that require corrective control measures.

Fuel Consumption, Internal Configuration and Controls

Additionally, when assessing the controls during the ascent-to-orbit phase, the fuel consumption and internal arrangement of the vehicle may be employed as additional aerodynamic trimming devices in order to move slightly forward or backward the centre of mass of the space-access vehicle, as appropriate – i.e. active centre of mass management. Indeed, the mass model described in Section 4.5.2 can be used to compute the shift of the location of the centre of mass of the vehicle as the on-board fuel is consumed: this is, in fact, an important consideration when the longitudinal stability and controllability of the vehicle is being assessed. Indeed, the location of the centre of mass has obviously a great influence on the aerodynamic moment acting on the vehicle, and therefore, it has a direct impact on the optimal scheduling of the control surface deflection angles as discussed in Section 4.2.3.

Therefore, taking inspiration from the work of Yokoyama *et al.* (116), it may be further assumed that it is possible to control the proportion of fuel consumption that originates from either the forward or rearward tanks. The tanks can therefore be used as additional trim devices, moving forward or backward the centre of mass of the vehicle along the ascent trajectory. The differential equation that dictates the mass flow rate of fuel for each tank is then given by

$$\dot{m}^i_{fuel} = \left(\frac{F^j_T}{I^j_{sp}} + \frac{1}{1+\nu} \frac{F^k_T}{I^k_{sp}} \right) \frac{\epsilon_R}{g} \tag{4.111}$$

where m^i_{fuel} is the mass flow rate of the i^{th} tank, j and k are indices used to represent, respectively, the air-breathing and rocket modes of the engine powerplant,

ν is the liquid hydrogen/liquid oxygen mixture ratio of the rocket engines, and ϵ_R is the proportion of liquid propellant consumption in the i^{th} tank.

Finally, these additional equations (whose number depends on the number of tanks) can thus be used in conjunction with the flight model described in Section 4.2. Therefore, the mass variation of the vehicle due to its fuel consumption, denoted $\dot{m}_v$, can now be derived as

$$\dot{m}_v = -\sum_{i=1}^{N_{tanks}} \dot{m}^i_{fuel} \tag{4.112}$$

4.7 Chapter Summary

An engineering design environment has been developed to model some of the complex physics that needs to be considered and properly accounted for in the design of the next generation of space-access vehicles, particularly in terms of the characteristics of their propulsion systems, the properties of their thermal protection systems and of their internal configurations. Indeed, the complexity of such vehicles requires the integration of all technological disciplines from a conceptual design stage standpoint. As such, some of the challenges that will be faced by the designers of the next generation of re-usable launch vehicles, particularly as they aim to address and overcome the many complications that are introduced into the design and optimisation process through the very tight coupling between the various component systems of the vehicle, have been discussed. In fact, it is hoped that reduced-order methods such as those described throughout the present chapter will play a significant role in addressing the many conflicting demands on their performance that will need to be successfully balanced in order for these vehicles to eventually become a practical reality.

Therefore, in the present chapter, both the environment and the three degrees-of-freedom dynamical equations for a point mass travelling around a spherical rotating planet, used in the present work to evaluate the ascent and subsequent entry trajectories of re-usable space-access vehicles, have first been comprehensively described. These equations, used only to define the translational motion of the vehicle, have been augmented by partially accounting for rigid body dynamics. Indeed, a reverse-engineering method to design the control surfaces that

are used to steer the vehicle into a prescribed trajectory has been derived in Section 4.2.3. Additionally, a method has been presented in order to robustly assess the efficiency of those control surfaces.

Thereafter, a novel engineering approach for the modelling of hybrid TPS has been presented. The novelty comes from the modularity and flexibility of the thermal network approach described in Section 4.3. Indeed, the HyTPS model can simulate the complex thermal management systems of future space-access vehicles (i.e. by connecting a number of thermal networks together). The model can be used to rapidly model active cooling panels as well as passive insulators and thus provides an excellent framework for the parametric optimization of thermal protections sytems (see Section 5.2.3 of Chapter 5). Furthermore, a certain amount of engineering detail can also be added to the thermal analysis, e.g. concurrent thermal networks can be coupled to monitor fuel boil off. Additionally, the use of the present model to solve problems that are usually regarded as of secondary importance and that are often neglected in preliminary design studies has also been investigated, e.g. the formation of ice or frost during the mission preparation operations. The importance of this ground-hold phase will be demonstrated later in Section 5.4 of Chapter 5. Finally, a preliminary verification of the capabilities of the hybrid TPS model, based on the very limited amount of data available in the literature, has also been performed.

Additionally, an external reduced-order propulsion toolbox, dubbed HyPro and developed by Mogavero *et al* (76), has been integrated into the present system model to provide the capability to model any complex air-breathing propulsive device and thus to analyze the ascent-to-orbit phase of an SSTO mission.

Furthermore, a simple mass model, that can be used to arrange the internal configuration and estimate the GTOM of the vehicle, has briefly been introduced.

All the models presented in this chapter are capable of communicating with the rest of the vehicle system model to provide an efficient means of performing the preliminary design analysis of future fully re-usable space-access vehicles. Finally, further considerations in terms of subsystem couplings that may be the source of possible future work and improve the current capabilities of the system model have been discussed in Section 4.6.

Nomenclature

Flight Simulation Model

List of Symbols

A	Panel area
a	Speed of sound
$C_k(\eta)$	Individual unit axis rotation
D	Drag force
$\vec{F}$	Aerodynamic force
F_T	Thrust
G	Gravitational force
g	Gravitational acceleration
h	Altitude
I	Tensor of inertia
I_3	Three-by-three identity matrix
L	Lift force
M	Molecular weight
M_x, M_y, M_z	Control moments
m	Mass
$\dot{m}_{fuel}$	Fuel mass flow rate
n	Number density
$\mathcal{N}_{av}$	Avogadro's number
P	Pressure
$\mathcal{P}_n$	Local horizontal plane
p, q, r	Rate of rotation of the vehicle about its centre of mass
R_e	Earth mean equatorial radius
$\vec{r}$	Position vector
T	Temperature
t	Time
$T_{j,i}$	Transformation matrix from a frame i to a frame j
$\vec{v}$	Velocity vector
γ	Flight path angle
δ	Deflection angle of the control surfaces
ϵ	Angle between the thrust vector and the velocity vector
η_α	Efficiency of the control surfaces
θ_L	Longitude
λ	Latitude
μ	Bank angle
ρ	Density
χ	Heading angle
Ω	Relative angular rate
ω	Angular rotation
ω_E	Angular rotation of the Earth

Subscripts & Superscripts

a	Axial force or Aerodynamic frame of reference
b	Body frame of reference
$gross$	Gross Take-Off
i	Inertial frame of reference
n	Normal force
r	Rotational frame of reference
sea	Sea-level condition
v	Vehicle
w	Wind frame of reference
∞	Freestream condition

Thermal Protection System Model

List of Symbols

A	Panel area
A_{pipe}	Cross-sectional area of the cooling pipelines
C	Thermal capacitance
C_f	Skin friction coefficient
D_{pipe}	Hydraulic diameter of the cooling lines
D_{tank}	Diameter of the tank
H	Enthalpy
h	Heat transfer coefficient
k	Thermal conductivity
k_{air}	Thermal conductivity of the surrounding air
L_{pipe}	Length of the pipelines
$\dot{m}$	Mass flow rate
Nu	Nusselt number
Q	Heating term
$\dot{q}$	Heat transfer rate
R	Thermal resistance
Re	Reynolds number
St	Stanton number
T	Temperature
T_{liq}	Liquefaction temperature
V	Volume
$\dot{V}_{boil}$	Fuel boil-off volume rate
U_{cool}	Coolant axial velocity
ΔH_{fuel}	Latent heat of vaporization of the fuel
ΔH_f^0	Heat of formation of ice from a vapour
δ	Layer thickness
ϵ	Emissivity of the material

ρ	Density
χ	Friction factor

Subscripts & Superscripts

0	Total Condition
acs	Active cooling system
cond	Conductive heat transfer
conv	Convective heat transfer
cool	Coolant
edge	Boundary layer edge condition
eq	Equilibrium condition or Equivalent
in	Influx
ins	Insulation
max	Maximum
out	Outflux
rad	Radiative heat transfer
struct	Structural skin
tps	Thermal protection system
w	Wall condition
∞	Freestream condition

Propulsion Model

List of Symbols

A	Section area
C_f	Skin friction coefficient
D_t	Ram Drag
F_T	Thrust
G	Mass flow
H	Total Enthalpy
h	Enthalpy
I	Momentum flow
M	Mach number
$\dot{m}$	Mass flow rate
P	Pressure
q	Dynamic pressure
$\dot{q}$	Heat transfer rate
R_p	Compression pressure ratio
St	Stanton number
V	Axial velocity
W	Molecular weight

X	Molar fraction
γ	Ratio of specific heats
η	Efficiency
θ	Injection angle
ρ	Density
τ	Shear stress
Φ	Stoichiometric ratio
ϕ	Equivalence ratio

Subscripts & Superscripts

0	Total Condition
1	Beginning of the module
2	End of the module
3	Third node of the module
$fuel$	Fuel
in	Intake condition
ox	Oxidizer
w	Wall condition
∞	Freestream condition

Mass Model

List of Symbols

A	Panel area
$\tilde{c}_z$	Longitudinal coordinate of a panel
F_T	Thrust
k	Thermal conductivity
L	Length
m	Mass
m^0_{acs}	Basic ACS system mass
$\dot{m}$	Mass flow rate
N_{pipes}	Number of pipes
$\hat{n}$	Local unit panel normal
S_x, S_y, S_z	Scaling factors
t	Time
T_s	Transformation Matrix
V	Volume
v	Vertex coordinates
v^{new}	New vertex coordinates
V_{in}	Internal volume
V_{req}	Required volume

δ	Layer thickness
ρ	Density

Subscripts & Superscripts

ab	Air-breathing engine
acs	Active cooling system
$cool$	Coolant
f	Final condition
ins	Insulation
max	Maximum
$pipe$	Cooling pipelines
$skin$	Structural skin
tps	Thermal protection system

Couplings between Models

List of Symbols

d_z	Distance along the longitudinal axis from the engine exit to a panel
F_T	Thrust
g	Gravity acceleration
I_{sp}	Specific impulse
L_{aft}	Length of the vehicle's afterbody
$\dot{m}_{fuel}$	Fuel flow rate
m_v	Vehicle mass
N_{tanks}	Number of fuel tanks
P	Pressure
ϵ_R	Proportion of liquid propellant consumption
ν	Liquid hydrogen/liquid oxygen mixture ratio of the rocket engines

Subscripts & Superscripts

$exit$	Exhaust condition of the engine
j	Air-breathing mode of the engine
k	Rocket mode of the engine

Chapter 5

System Design Applications

The present chapter demonstrates the relevance and usefulness of the integrated design strategy, explored in the previous chapter, for vehicle system level trade-offs in the early design of a Re-usable Launch Vehicle (RLV). In doing so, a review of the different mission phases along with the miscellaneous optimal control problems that need to be solved will be outlined, where appropriate. First, a brief discussion about the key issues in the design of the new class of Single-Stage-To-Orbit (SSTO) vehicles is given in Section 5.1. Then, in the subsequent Sections 5.2 and 5.3, the various models used to plan or design some of the system components during the re-entry and ascent trajectory missions of future space-access vehicles is discussed. Thereafter, in Section 5.4, the ground-hold phase of the mission (i.e. when the vehicle is being serviced between successive missions) is briefly presented along with possible future extensions of the model. Finally some preliminary conclusions are given in Section 5.5.

5.1 Introduction

A large number of the challenges associated with the design of hypersonic vehicles have already been covered in precedent chapters (e.g. Section 4.1). Nonetheless, it appears appropriate to comment further on the design process required to conceive those complex aerospace systems. In the present chapter, the CFASTT-1 SSTO configuration will be used in all the computations to demonstrate the use of the miscellaneous engineering models in the modelling and design of future fully re-usable launchers. The CFASTT-1 is a derivative of the Skylon SSTO

Property	Value	Remark
Length [m]	83	–
Reference Area [m^2]	300	S_{ref}
Reference Length [m]	16	L_{ref} – Mean Chord
Wingspan [m]	20	–
Centre of Mass	$[0, -14.7, 7.5]$	–
Leading Edges [cm]	10	radius
Dry Mass [tons]	60	–
Take-off Mass [tons]	260	–

Table 5.1: Reference parameters of the CFASTT-1 vehicle.

vehicle intended to examine a number of aerodynamic features for future SSTO configurations. The vehicle has a fuselage with the same volume as that of the Skylon vehicle, but with its forward underside flattened to allow better thermal characteristics during re-entry. The vehicle has an elliptical, flattened nose blending in two forward strakes to give forebody lift and nose-up pitching moment so that canards are not required. The rear fuselage has been flattened into a pen-nib shape to allow for a rear beaver-tail control surface, *à la* Space Shuttle, for pitch attitude control during re-entry. The wings are similar to those of the Skylon vehicle but blended into the fuselage and forward strakes. Finally, the engines have been toed in slightly to reduce their moment arm about the centre of gravity. The reference quantities associated with the CFASTT-1 SSTO configuration are provided in Table 5.1.

In the design of future re-usable launchers, their ascent and subsequent re-entry trajectories (intrinsically related to a measure of their performance) must first be ascertained before other subsystems can be designed (35). Nonetheless, it shall be remarked that the selection of an appropriate set of optimisation tools for the design of vehicle trajectories is never a particularly straightforward process. The convergence of conventional, simple gradient-based optimisation routines is often severely hampered by particular features that are embedded within the model for the system's performance. Changes in behavioural mode or other discontinuities embedded within the model cause particular problems in this respect. The choice of optimisation algorithm can thus influence the outcome of the design process considerably, and it can be difficult, if not impossible, to find the true, globally-optimal design solution even if a good initial guess is available. In the

present chapter, it shall be remarked that the re-entry and ascent trajectory of the reference representative aerospace plane will be controlled by a slightly modified version of the schedule of bank angle and angle of attack first derived in the work of Pescetelli *et al.* (120, 121).

Another major problem when designing fully re-usable space-access vehicles concerns the careful selection and combination of materials and structures that can withstand the repeated aero-thermal loads associated with hyper-velocity flights during the air-breathing-powered ascent (i.e. high instantaneous heat flux phase) and the subsequent atmospheric re-entry (i.e. large integrated heat load phase). For instance, Allen and Eggers (122) have demonstrated that bluntness is often required to survive entry from orbit (which proved that a "*thermal barrier*" does not exist). In fact, they have proven that the heat load acting on a re-entry vehicle was inversely proportional to the drag coefficient, denoted C_D – i.e. the greater the drag, the lower is the heat load acting on the re-entry vehicle. Indeed, the effect of bluntness is to provoke the detachment of the bow shock (by a stand-off distance Δz) that forms ahead of the re-entry vehicle with concomitant effect on the amount of convective heat transferred to the wall of the system. Therefore, since re-entry vehicle design is, in general, primarily concerned with slowing the vehicle as it re-enters into the Earth's atmosphere, blunt leading edges have, historically, usually been employed both for deceleration purposes and to mitigate the severe heating environment to which the vehicle is exposed. For instance, the Space Shuttle Orbiter used a leading edge radius of about 600 mm (123). In contrast, supersonic ramjets will have to accelerate through the denser regions of the terrestrial atmosphere and therefore must make use of smaller leading edge radii to reduce the resulting aerodynamic drag (124). For example, the HyFly program scramjet inlet design considered a 3 mm leading edge radius (125) (which is 200 times smaller than that of the Space Shuttle). Sharp leading edges will result in dramatic thermal challenges (i.e. see the level of heat flux for the Re-entry F flight experiment in Section 3.3 where the use of an ablator was necessary). However, the use of ablative materials will, most likely, be proscribed due to obvious re-usability issues. Therefore, the design of thermal shields require innovative solutions such as hybrid Thermal Protection Systems (TPS).

In this chapter, three phases of the mission profile of a typical re-usable space-access vehicle will be covered. In Section 5.2, the re-entry phase of an SSTO mission is first discussed where the optimal control problem used to plan the atmospheric entry of the vehicle through the definition of an optimal schedule

of bank angle and angle of attack is presented in Section 5.2.1. Then, in Section 5.2.2, a schedule of control surface deflection angles based on a nominal entry trajectory is derived. Finally, the modelling and design of an Active Cooling System (ACS), in the context of the re-entry trajectory of the CFASTT-1 vehicle, is discussed in Section 5.2.3. Thereafter, in Section 5.3, the ascent-to-orbit phase of the mission is introduced. A demonstration of the capability of the HyPro propulsion model coupled to the rest of the system model is presented via the modelling of a Rocket-Based Combined-Cycle (RBCC) engine in Section 5.3.1. Then, the optimal control problem for the ascent phase of the mission is described in Section 5.3.2. The effect of varying certain key parameters in the engine model on the ascent-to-orbit trajectory of the CFASTT-1 vehicle is presented in Section 5.3.3. Finally, the ground-hold phase of the mission is illustrated in Section 5.4 where the formation of ice on the Outer Mold Line (OML) of the vehicle is monitored.

5.2 Atmospheric Entry Phase

As first proposed by Chapman in 1959 (126), a composite (or again hybrid) type of re-entry, which combines some of the features of lifting and non-lifting trajectories, is necessary in order for the vehicle to enter first *without lift* but with instead a *drag device* to rapidly decrease the vehicle's speed in the most rarefied regions of the planetary atmosphere. Then, once the velocity has been reduced to a desired value, the *drag device* could either be jettisoned or retracted, leaving a winged vehicle for the remainder of the descent phase. Although such a trajectory, sometimes referred to as a *feathered re-entry* (a type of trajectory whose feasibility has recently been demonstrated by the sub-orbital Space Ship One of Virgin Galactic as it adopts a shape-changing airfoil, retracting the tip of its wings in the first part of its descent), would possibly lead to a more complex vehicle configuration (as it may involve some sort of moving parts) and reveal itself to be quite unpractical for the type of application discussed in the present work (for instance, if some parts of the vehicle would have to be jettisoned in flight), this type of hybrid descent trajectory may however be mimicked by the type of aerospace planes discussed here.

Indeed, a high angle of attack attitude could first be employed to introduce the flat-bottom surface of our representative winged configuration to the free-stream

flow during the first part of the entry trajectory. This entry strategy would ensure a reduction of the vehicle's speed when it operates at high altitude in the upper regions of the terrestrial atmosphere (i.e. where the air density is reduced), therefore decreasing the heat transfer rates acting on it. In fact, since the level of aerodynamic heating affects quite significantly the selection of the TPS type, size and weight, the re-entry trajectory of re-usable space-access vehicles has to be optimized in order to maintain the aerodynamic heating level below an acceptable value. Indeed, blunt bodies yield minimum TPS due to their large local radius of curvature and minimum ballistic coefficient (122). Finally, the lifting capabilities of the vehicle can then be used in the final portion of the entry trajectory in order to steer the vehicle towards its targeted final point (e.g. its spaceport).

5.2.1 Entry Trajectory Planning

During re-entry, although a shallow trajectory and a rapid bleeding of the entry speed through banking manoeuvres will, in all likelihood, be necessary features of the strategy employed by future RLVs (as discussed in Section 4.2), great care must be taken not to violate both the maximum normal acceleration and heat transfer rate limits when planning the entry trajectory of these vehicles. Furthermore, since these space-access vehicles should be allowed to perform out-of-plane motion through a series of banking manoeuvres, during both their ascent to orbit and the re-entry phase that follows, the control law should account for both the angle of attack, denoted α, and the bank angle, noted μ (see the definition of the bank angle in Fig. 4.8).

Optimal Control Problem

In the present work, it is assumed that the CFASTT-1 re-usable launcher will, most likely, follow an un-powered, gliding trajectory controlled by the angle of attack α and the bank angle μ. The nominal control law $c(t)$ is then obtained as the solution of the optimisation problem which aims to minimize the integrated heat load at the nose stagnation point as

$$\min_{\mathbf{c}\in D} \int_{t_0}^{t_f} \dot{q}_{stag}(t)dt \tag{5.1}$$

or possibly, in future studies, over the entire surface of the vehicle (using the

HyFlow panel method) as

$$\min_{\mathbf{c}\in D} \int_{t_0}^{t_f} \left(\sum_{i=1}^{N} \dot{q}_i A_i \right) (t) dt \tag{5.2}$$

subject to the dynamics described in Section 4.2 and initial conditions (i.e. at $t = 0$) set to start in the hypersonic regime: $h_0 = 120$ km, $v_0 = 7.8$ km/s, $\gamma_0 = -1$ deg, $\chi_0 = 90$ deg, $\lambda_0 = 1$ deg, $\theta_{L0} = 0$ deg. The terminal conditions (i.e. at $t = t_f$) are $h_f = 24$ km, $v_f = 0.8$ km/s, $\gamma_f = -30\,\text{deg}$, $\chi_f = 90$ deg, $\lambda_f = 40$ deg, and $\theta_{Lf} = 0$ deg – i.e. these conditions are the same as those used for the guidance of the American Space Shuttle. Additional path constraints are imposed on the peak heat flux at the nose stagnation point $\dot{q}_{stag} < 500,000$ W/m^2, and the maximum acceleration along the normal body axis so that $a_y(t) \leq 28$ m/s^2. The numerical optimization method, that has been adopted by Pescetelli *et al.* (121) in order to solve for the optimal control problem previously introduced and thus derive the nominal control law used in the present work (see Fig. 5.1), was based on a mixed optimization approach.

Nonetheless, since this optimization process is beyond the scope of the present thesis work, it will only briefly be described here for the sake of completeness: a population-based stochastic algorithm was used first to explore the design space and to identify a set of neighbourhoods in which candidates for the global optimum of the system might exist. A gradient-based approach was then used in each such neighbourhood to refine the solution and to ensure that the constraints on the system are accurately met. Following this, the highest ranked solution according to its cost function is accepted as the global optimum.

To optimise the re-entry trajectory of the CFASTT-1 concept, a direct collocation method based on the Finite Elements in Time (FET) approach and using a spectral basis (127) is applied: in this approach, the trajectory is discretized into a large but finite number N of sub-intervals, and the design space is then the matrix product of the unit vector of dimension N and a suitable control vector c for the vehicle along its trajectory. The resultant non-linear programming (NLP) problem (128) is then solved using the MOPED algorithm (129) to search for candidate optima; these solutions are then refined using the gradient-based IDEA optimisation method (130).

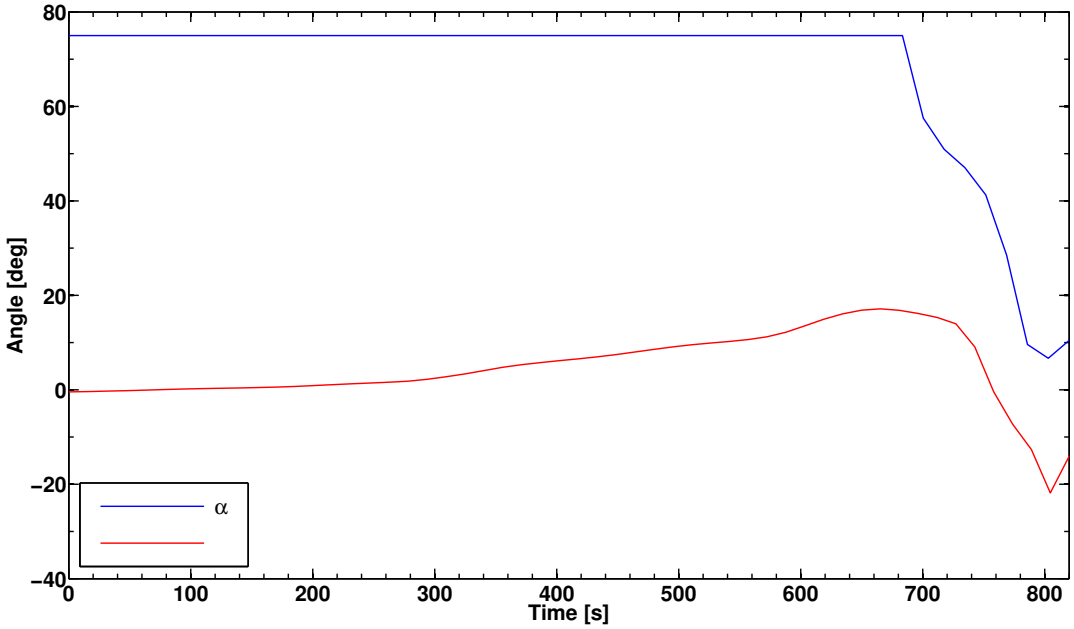

Figure 5.1: Nominal control law during re-entry - Nominal schedule of bank angle and angle of attack.

Re-entry Aero-thermodynamics

To perform the re-entry trajectory planning, the HyFlow engineering code has been coupled to the flight simulation model described in Section 4.2. For present purposes, the modified Newtonian theory method embedded within the HyFlow code (see Section 2.3.2.1) has been used to calculate the inviscid aerodynamic environment over the entire surface of the CFASTT-1 representative winged system when it operates in the continuum regime, starting from a high angle of attack at entry and ending at the onset of the Terminal Area Energy Management (TAEM) regime at supersonic speed – the TAEM interface corresponds to the transition from a high angle of attack attitude to a controlled supersonic flight. The use of this local inclination method can be justified by the nature of the re-entry trajectory of the vehicle. Indeed, as a means to reduce the total heat load along the trajectory, the vehicle maintains a high angle of attack during a significant portion of the descent, and its aerodynamics thus resemble very closely those of a blunt body for most of the duration of its flight (see Fig. 5.1 again). Additionally, it shall be noted that the free-stream Knudsen number, K_n^∞, was used to switch between rarefied and continuum flow methods. Furthermore, the smooth-surface boundary layer transition criterion was employed to determine the onset of transition during the integration of the re-entry trajectory.

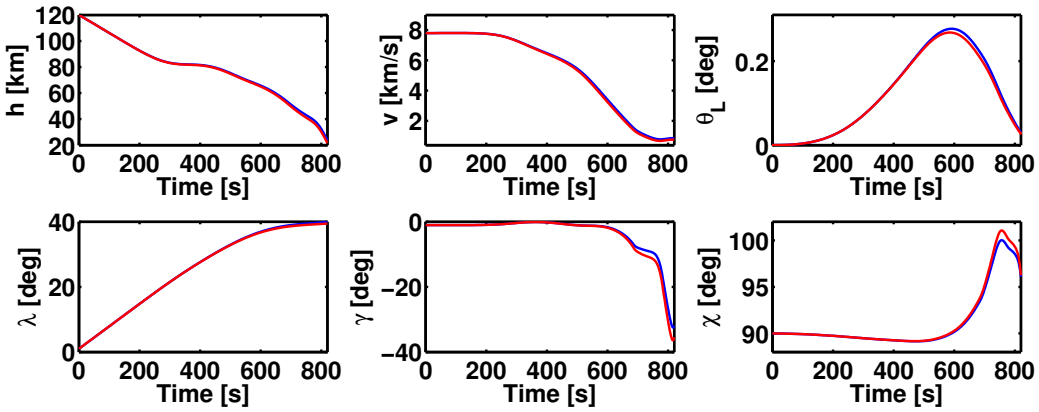

Figure 5.2: Nominal re-entry trajectory - Evolution of the states, where the bold red line refers to the nominal trajectory when only inviscid forces are accounted for, and the blue line refers to the same trajectory but this time with viscous loads added.

Nominal Re-entry Trajectory

The resulting nominal trajectory of the vehicle is shown in Fig. 5.2. As expected, during the first phase of the atmospheric entry, the vehicle maintains its descent at a constant 75 degrees angle of attack (which corresponds to the upper bound of α in the optimization process) as a means of decelerating within the upper, less dense, regions of the terrestrial atmosphere (see Fig. 5.1). The vehicle is subjected to a maximum level of aerodynamic heating at its nose stagnation region shortly after crossing the Mesopause at about 80 km altitude (i.e. $\dot{q} \approx 450$ kW/m^2). The scheduled angle of attack is then promptly reduced in order to guarantee the structural integrity of the vehicle as its normal acceleration increases towards the design threshold (set to 28 m/s^2) at about 600 seconds after the beginning of the re-entry phase. A final set of combined pitch/roll inputs are then required to turn the vehicle onto its correct heading during the terminal manoeuvres that bring it to the prescribed final latitude and longitude of the TAEM interface (as will be shown in Section 5.2.2).

5.2.2 Controls Scheduling for the Nominal Trajectory

The controls of the CFASTT-1 vehicle – see Fig. 5.3 – are comprised of two fins arranged in a butterfly configuration at the rear of the fuselage, which are used both for yaw and roll control, as well as for pitch control in low-speed flight.

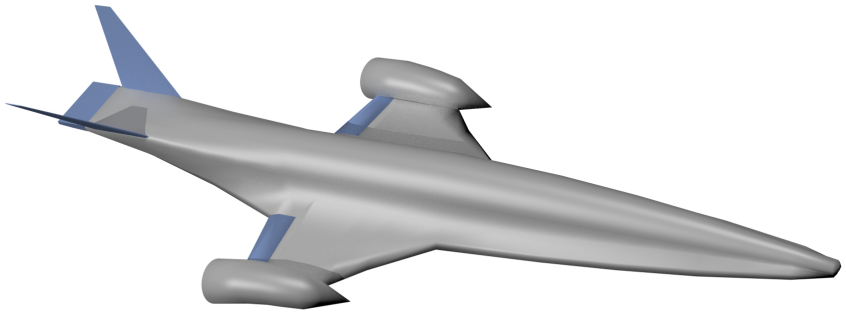

Figure 5.3: The CFASTT-1 vehicle and its control surfaces - The CFASTT-1 space-access vehicle with its control surfaces (in blue).

The rear fuselage, flattened into a pen-nib shape, accommodates a rear beaver-tail control surface *à la* Space Shuttle for pitch attitude control during re-entry. Finally, two elevons are attached to the trailing edge of the wings for additional pitch and roll control.

Optimal Control Problem

Since the performance of the vehicle along its atmospheric re-entry trajectory is known (i.e. the process would be equivalent in the case of an ascent trajectory), the rate of change along the nominal trajectory of the components $\dot{p}$, $\dot{q}$ and $\dot{r}$ in body axes of the angular acceleration of the vehicle about its centre of mass (shown in Fig. 5.4) can be computed from the set of angles $\{\chi, \gamma, \mu, \alpha\}$. Following the procedure summarized in Section 4.2.3 of Chapter 4, the *control moments* that need to be generated in order to rotate the vehicle into the desired attitude can then be obtained from Eq. 4.42. The variation of these moments along the nominal trajectory of the vehicle are shown in Fig. 5.5. Then, the schedule of control surface deflection angles can finally be determined. In order to evaluate the variation of control surface deflection that is required along the re-entry trajectory, the control vector, c_δ, is first defined as

$$c_\delta = \{\delta_1, ..., \delta_5\} \tag{5.3}$$

where δ_1 and δ_2 correspond to the rotation angles of the rear fins, δ_3 and δ_4 correspond to the rotation angles of the elevons, and δ_5 controls the rotation

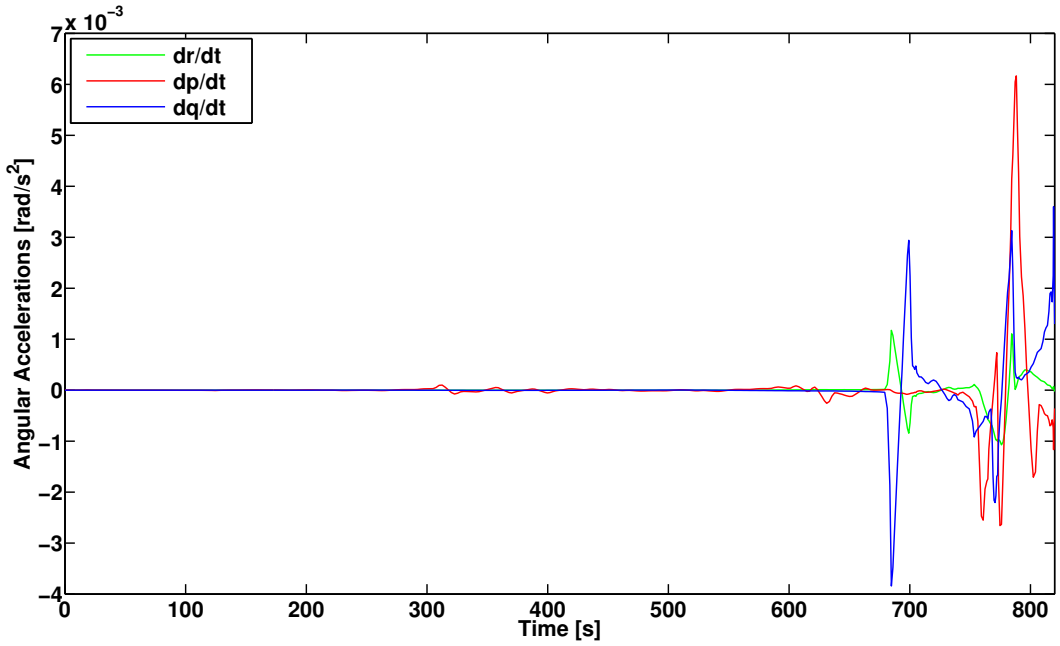

Figure 5.4: Angular rotation rates - Angular accelerations in pitch ($\dot{q}$), yaw ($\dot{r}$), and roll ($\dot{p}$) along the vehicle's nominal trajectory.

angle of the beaver tail. The search space D_δ for the control deflection angles δ_i is defined by the bounds $-30 \leq \delta_{1,2} \leq 30$, $-10 \leq \delta_{3,4} \leq 30$, and $-10 \leq \delta_5 \leq 30$. The optimal scheduling of the control surface deflections $\{\delta_i\}$ is then defined as the solution to the single-objective point-wise optimisation problem which aims to provide the desired attitude to the space-access vehicle.

$$\min_{c_\delta \in D_\delta} = \|\hat{M}_{controls} - \hat{M}_{nom}\| \tag{5.4}$$

where M_{nom} is the aerodynamic moment that is required to generate the rotational dynamics of the vehicle that are consistent with its desired nominal trajectory (see again Fig. 5.5) and $M_{controls}$ is the aerodynamic moment that is generated by the vehicle with the control surfaces deflected.

Optimal Flight Controls

The optimal scheduling of the control surface deflections is then determined at each of the collocation points along the trajectory (those are depicted in Fig. 5.5). In the first phase of the trajectory, during which the vehicle operates at approximately constant angle of attack and bank angle, a low density of collocation

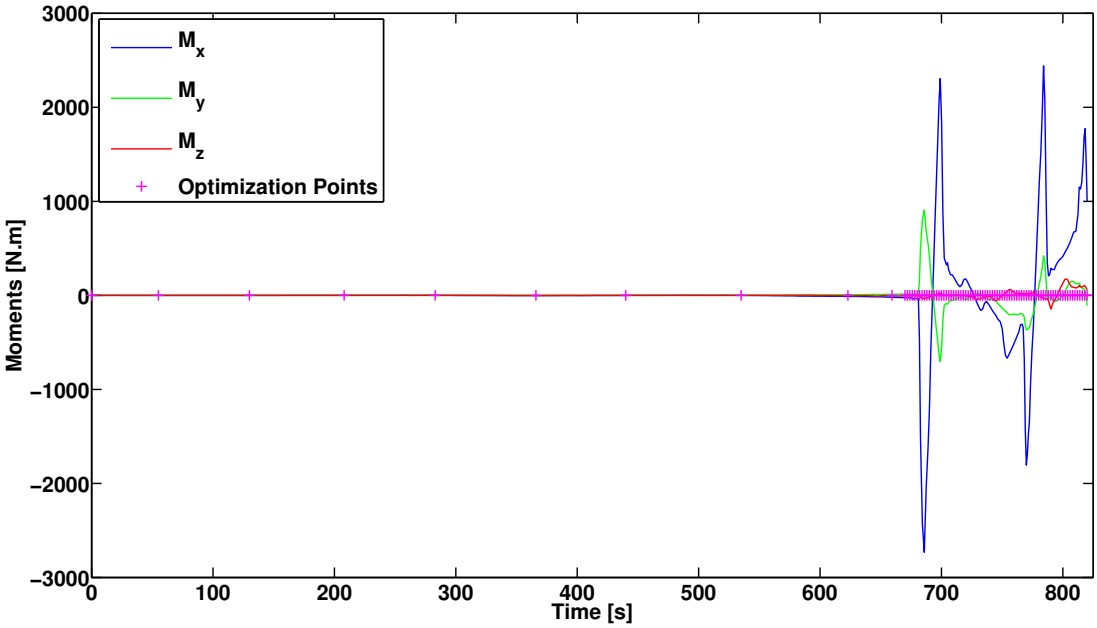

Figure 5.5: Aerodynamic control moments - Aerodynamic moments required to generate the nominal angular accelerations of the vehicle: pitch moment M_x, yaw moment M_y, roll moment M_z. Each of the collocation points used along the trajectory for the optimization of the flight controls are also shown (magenta crosses).

points is adequate to capture accurately the required variations in control surface deflection, whereas from about $t = 665$ s onwards, the attitude of the vehicle changes rapidly enough for a far denser distribution of collocation points to be required (for a total of 86 optimization points). The deflections of the control surfaces along the nominal trajectory of the representative CFASTT-1 vehicle are presented in Fig. 5.6. If the very low-amplitude fluctuation in the control surface deflections is disregarded, all of the control surfaces can be seen to maintain an almost steady deflection during the preliminary phase of the re-entry at very high angle of attack, vindicating the minimal-control aerodynamic design philosophy that was followed to model the shape of the vehicle. As was intended, the beaver tail is the control surface which participates most in the control of the vehicle throughout this preliminary phase of the trajectory by maintaining the pitch attitude of the vehicle. At the onset of the manoeuvre which leads to a rapid decrease in the pitch attitude of the vehicle, the elevons and rear fins begin to take over the attitude control of the vehicle. Indeed, a point is reached, at approximately 780 s into the trajectory, at which the beaver tail is aerodynamically shadowed by the forward fuselage of the vehicle, and is commanded therefore to return to

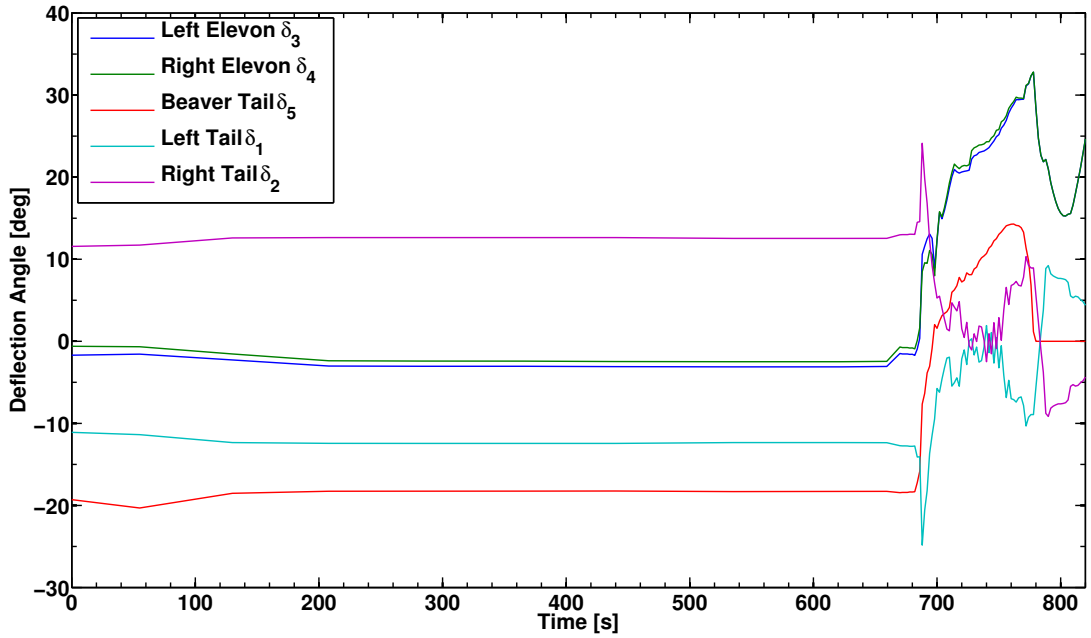

Figure 5.6: Nominal Schedule of Control Deflections - Deflection of the control surfaces along the nominal re-entry trajectory of the CFASTT-1 vehicle.

its neutral attitude (see discussion in Section 4.2.3.1). Finally, the absolute error between the required *control moment* and the moment generated by the vehicle at each optimization point along its nominal trajectory is presented in Fig. 5.7. The relatively small deviations throughout give confidence in the ability of the current control scheme to manage the changes in the vehicle's attitude that are required in order for it to achieve its nominal trajectory.

5.2.3 Thermal Protection System during Re-entry

In the present section, the use of the HyTPS code to model a radiant actively cooled panel, which combines the use of the passive radiative heat shield technology and insulation on the outer surface of a structurally-integrated actively cooled panel, is demonstrated for the thermal protection of the area covered by the forward strakes of the CFASTT-1 vehicle. Such thermal management configurations radiate away (to the atmosphere) a substantial amount of the incident convective heating and therefore reduces appreciably the heat load that must be absorbed and carried away by the flow of a coolant flowing through actively cooled panels (131). It is assumed that the underlying structural skin of future re-usable space-access vehicles will be made of thermally resilient materials. In

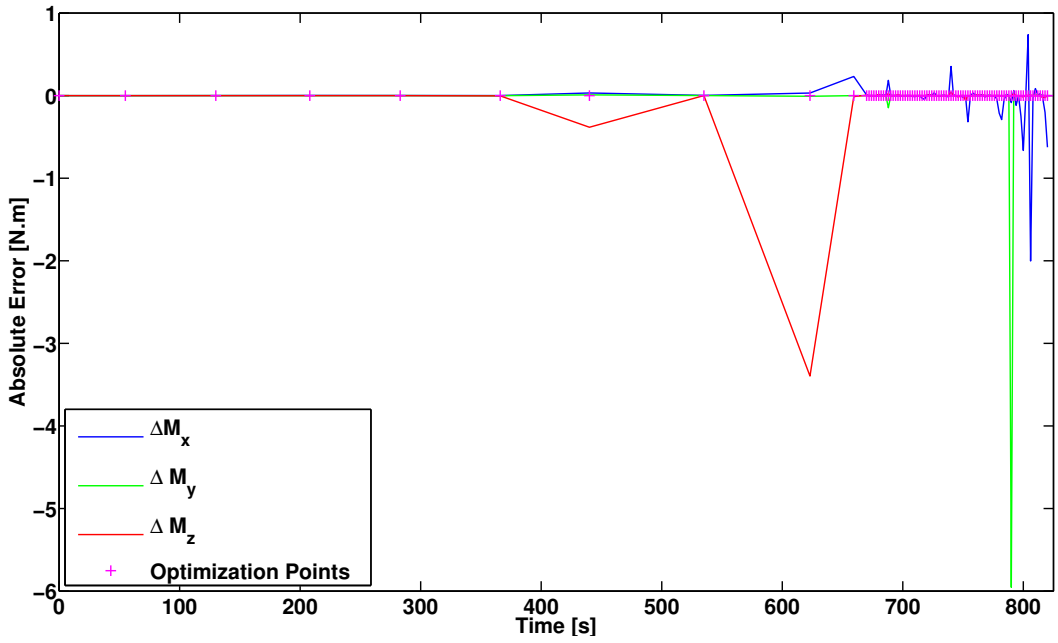

Figure 5.7: Absolute error plot - Absolute error between the required moment and the moment generated by the vehicle along its nominal trajectory: pitch moment ΔM_x, yaw moment ΔM_y, roll moment ΔM_z

fact, this load bearing structure will most likely be made out of titanium alloys or other similar type of advanced materials. Indeed, in the eventuality of an emergency situation – e.g. for example, as a result of some problems related to the active cooling system – the thermal resistivity of advanced titanium alloy structures would be far superior to those made out of aluminum alloys (which is often the material of choice to fabricate the structure of aircraft). In fact, if a cooling system malfunction (e.g. total loss of coolant flow) occurs during the re-entry of the vehicle, the regions of the vehicle's surface that may be affected from a structural point view would greatly be reduced. Consequently, the time period allowed to trigger eventual corrective measures would thus be significantly extended: for instance, if appropriate, the vehicle can be commanded to follow a load-factor reduced trajectory path, a criterion that may become important in securing airworthy operations. Therefore, these ACS panels may have to be designed as fail-safe systems able to absorb the abort heat load in passive mode as presented in the study of Jones *et al.* (108). Finally, these alloys are less subject to other aging degradation phenomena such as corrosion and may therefore reduce the maintenance requirements on the system (reducing, by inference, the operational costs of a mission).

Property	Value	Unit
Density	4550	kg/m^3
Specific Heat	525	J/(kg.K)
Thermal Conductivity	7.06	W/(m.K)

Table 5.2: Material properties of the Timetal 834 titanium alloy - Material properties of the Timetal 834 titanium alloy, at a temperature of 300 K, are presented (properties retrieved from www.matweb.com, last accessed on the 11^{th} of March 2015).

Therefore, for demonstration purposes, a titanium alloy, designated as Timetal 834, has been chosen to compose the structure of the CFASTT-1 vehicle configuration (an alloy used to fabricate blades for aero-engines). The main advantage of using such an alloy is its maximum operational temperature, fixed to $T_{max} = 870$ K, compared with that of other titanium alloys: Ti-6242S (790 K), Ti-6242 (720 K), Ti-811 (670 K) and Ti-6-4 (570 K) – Ref. (132) cited Ref. (133).

Radiative Actively Cooled Panel Modelling

For present purposes, the use of a combination of actively cooled *sandwiched* panels in conjunction with a passive radiative TPS (set up in a Direct Cooling System (DCS) architecture – see Section 4.3.1.2) has been investigated for the re-entry phase of the mission of our representative RLV. The analysis presented below uses the thermal modelling approach introduced in Section 4.3 of Chapter 4 to demonstrate the advantages over the use of a passive thermal protection system of adopting an active thermal management system in which the re-circulation of a cryogen, e.g. liquid hydrogen fuel, is used to enhance the efficiency of the TPS in those areas of the vehicle which are most exposed to a severe heating environment (such as at the leading edge of the wings, or at the nose stagnation region), or even to actively cool certain elements of the propulsion system (mainly the combustor). In this section, the structural skin of the vehicle is assumed to be made out of a 2-mm-thick Timetal 834 titanium alloy material layer (represented by a single diffusive node with finite capacitance in the current thermal network scheme) which is directly attached to the TPS arrangement (see material properties in Table 5.2). Furthermore, an additional safety margin was first assumed in order to account for the reliability of the system and the maximum allowable temperature was therefore held fixed at $T_{max} = 500$ K (since the thermal loads will be repeated

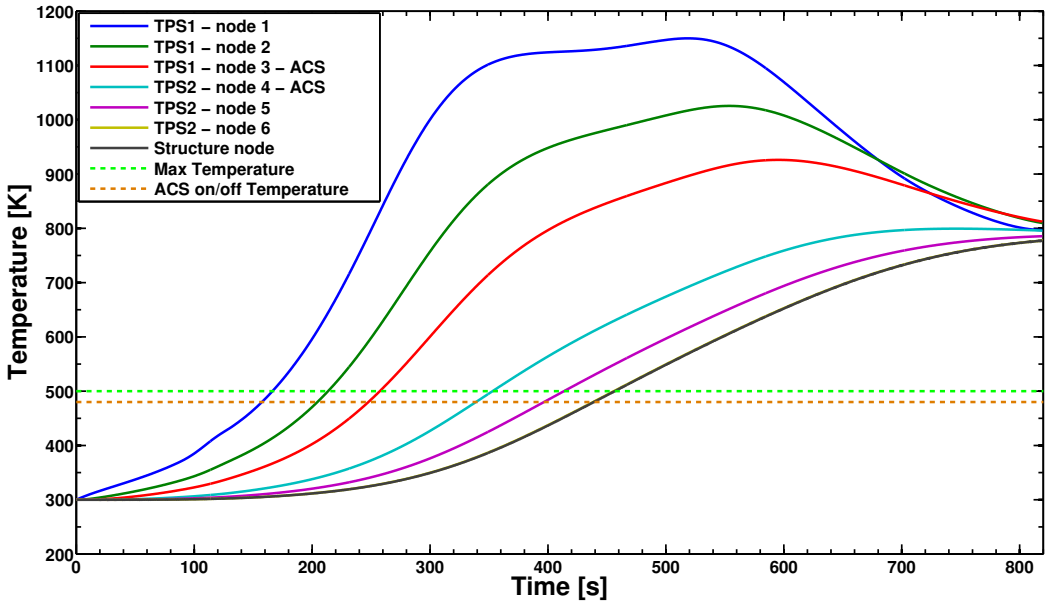

Figure 5.8: Thermal Response Passive TPS - Thermal performance of a passive TPS with a reduced thickness of about 6 cm.

mission after mission) whose foreseen consequence is to increase the required thickness of insulation layers to provide conservatism (reliability) in the present analyses. Then, the variation in structural skin nodal temperature (i.e. thermal amplitude ΔT) was limited by maintaining the temperature of the structure in a small region below the 500 K temperature threshold (i.e. limiting thermal cycling). Finally, in the present thermal network, each layer of insulation material consists of a set of three diffusive nodes. The present thermal network model is the same as that pictured in Fig. 4.13.

For present purposes, a simple "on/off" controller has been modelled (as defined in Section 4.3.1.5), allowing the ACS to be switched on or off when the temperature of the underlying structural skin of the vehicle attains a prescribed threshold value. In the results presented here, the threshold was set to include a 10% margin below the material's critical temperature (here assumed to be 500 K) to account for thermal inertia within the structure (i.e. in the present configuration, the structural skin is not directly adjacent to the cooling passages). The mass flow rate of coolant $\dot{m}_{cool}$ was held constant at 5 kg/s when the ACS system was switched on, and the hydraulic diameter of the ACS feeder pipes was set to 5 cm. It shall however be remarked that a more comprehensive analysis than that presented here would be required in order to evaluate the optimal combination

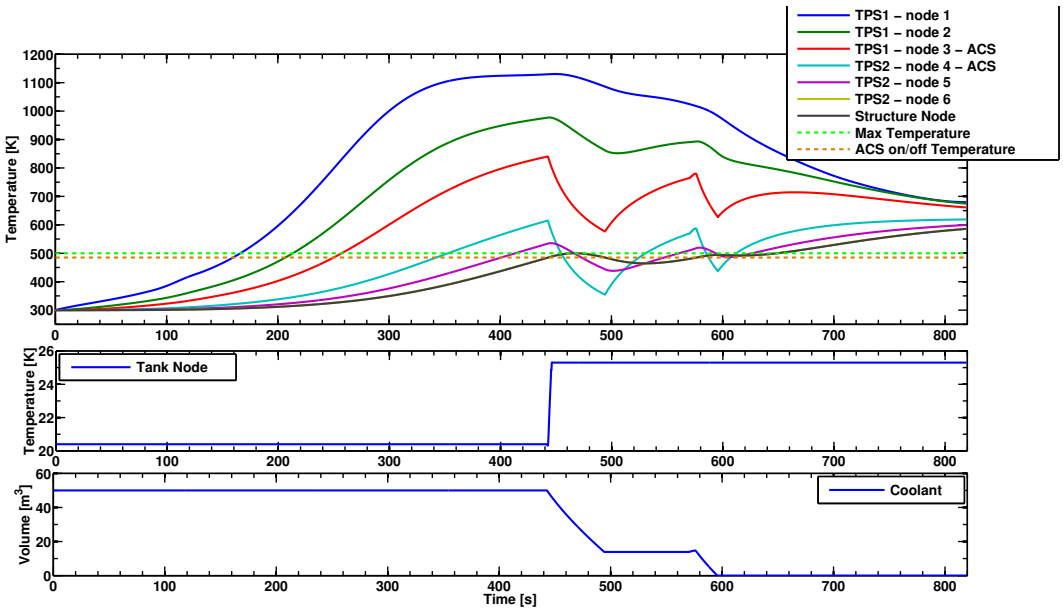

Figure 5.9: Active cooling system with 50 m^3 of coolant - Thermal performance of an Active Cooling System with a coolant reserve of 50 m^3.

of design parameters that result in the most efficient and lightweight thermal protection system for the vehicle (see the end of the present section). Similarly, a more sophisticated control system for the flow rate through the system could be adopted (this particular problem will be discussed at a later stage). In designing a simple ACS for the forward leading edges of the wings which allows straightforward comparison with the performance of an equivalent passive TPS, the thickness of an RCC panel was modified by reducing the overall thickness of the RCC layer from its nominal optimal thickness of 96.8 mm (necessary to maintain the structure below 500 K and obtained via a simple iterative Newton-Raphson procedure) to a value of 60 mm, creating two layers of 3 cm-thick RCC, denoted TPS1 and TPS2, one on either side of the ACS feeder lines (see Fig. 4.12): in the present example, node 1 is a balance node at the surface of the vehicle, node 2 is within TPS1, node 3 and node 4 are in thermal contact with the coolant pipe lines, node 5 is within TPS2, and node 6 is at the interface between TPS2 and the vehicle structure. As a point of comparison, the performance of the system with the ACS switched off entirely during the descent is depicted in Fig. 5.8. As can be seen in the figure, the temperature within the structure rises to about 800 K by the end of the descent, and thus the thermal management system, at least when operated in this passive mode, clearly does not meet the design requirement that the temperature of the structure be maintained below

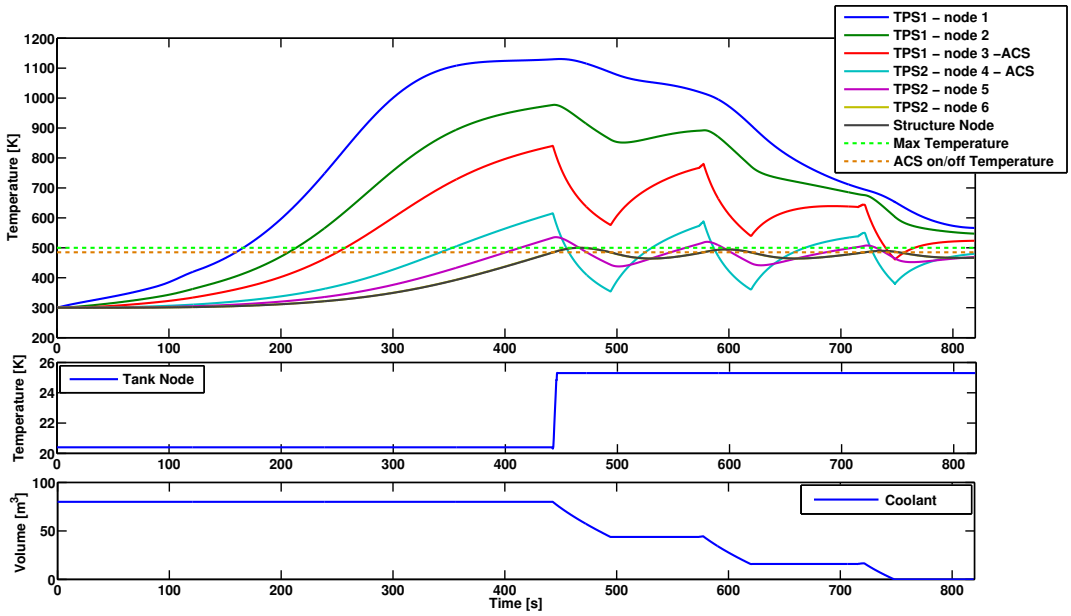

Figure 5.10: Active cooling system with 80 m^3 of coolant - Thermal performance of an Active Cooling System with a coolant reserve of 80 m^3.

500 K for the duration of the mission. In order to ameliorate the heat load on the underlying structure, the thermal management system is thus run in active mode for which auxiliary hydrogen is carried for cooling during that specific entry flight phase. The variation of temperature within the TPS when the ACS is allocated a total cryogen volume of 50 m^3 is shown in Fig. 5.9. At the end of a short initial phase during which the system works as a passive TPS (up to $t = 445$ s), the temperature of the structure becomes high enough to activate the cryogen flow within the ACS. The system responds by maintaining the temperature of the structure below its critical temperature until a point at about $t = 650$ s into the descent where, due to boil-off, all the cryogen within the tank has been consumed. Thereafter, the TPS continues to act as a passive thermal shield for the remainder of the trajectory (limiting the eventual structural damage). This cooling strategy results in the structural temperature reaching 580 K by the end of the re-entry path. Despite a significant reduction in the temperature of the structure as compared to a fully passive TPS of the same thickness (which reduced the final temperature by about a third), this system also does not meet the design requirements. Figure 5.10 shows the behaviour of the same system as before, but when instead 80 m^3 of cryogen is made available to the ACS. In this case, the ACS manages to keep the temperature of the structural skin within the desired limits throughout the duration of the re-entry, even though all the

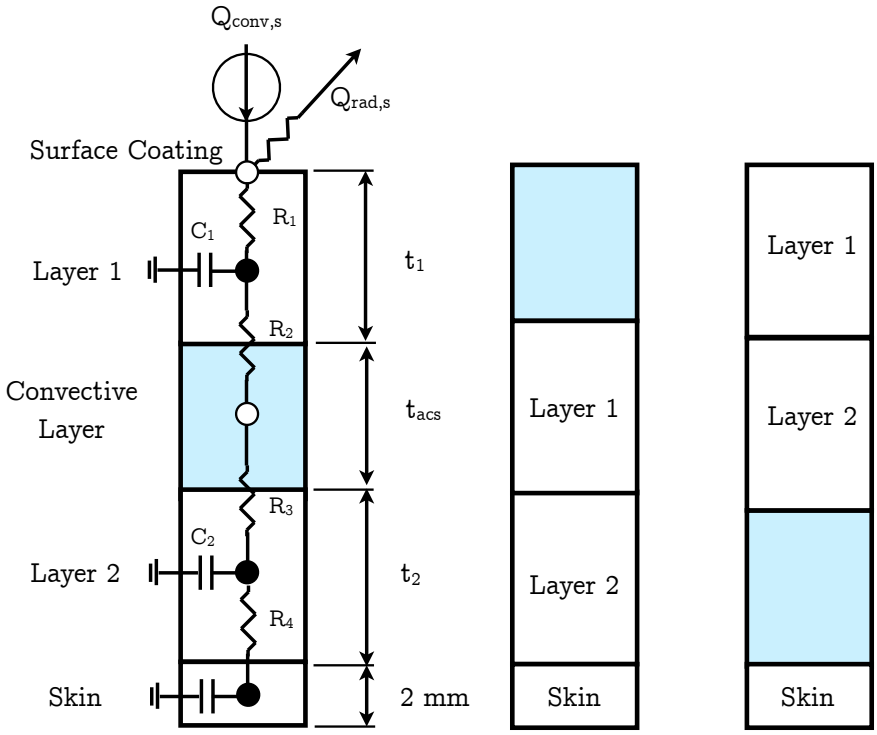

Figure 5.11: ACS optimization problem - The topological optimization problem for the actively cooled panels is illustrated. Considering only three layers (two re-usable insulation layers and the cooling passage layer) and since the selection of the materials used to fabricate the two insulation layers represents an additional variable to the optimization problem, only three distinct topological combinations are possible, namely: *sandwiched* configuration (left), bare configuration (middle) and radiative configuration (right).

cryogen is still consumed shortly before the end-point of the descent is reached. Despite the simplicity of the thermal management system modelled here, these results illustrate the ability of the HyTPS model to enable the type of parametric studies and trade-offs between options that would be necessary for the effective and robust multi-disciplinary design optimisation of any future Re-usable Launch Vehicle (RLV).

Design Optimization of Actively Cooled Panels

The design of an adequate (optimal and robust) thermal shield for a vehicle that must repeatedly operate in the severe heating environment associated with hypersonic flights is a complicated task. An optimal thermal management strategy

Property	Value	Unit
Density	8240	kg/m^3
Specific Heat	541	J/(kg.K)
Thermal Conductivity	18	W/(m.K)
Emissivity	0.85	-

Table 5.3: Properties of the Rene 41 material - Material properties of Rene 41, at a temperature of 300 K, are presented.

is however of the utmost importance for the survival and feasibility of these future re-usable aerospace systems. The objective of the thermal optimization problem described here consists in minimizing the weight of the thermal shield (sum of the ACS mass, denoted $m_{acs} = f(t_{acs}, V_{cool})$, and that of the hot structure and insulation layers noted $m_{tps} = f(t_{ins})$ – see Section 4.5.2 of Chapter 4) while satisfying the thermal limits on material temperature, reliability requirements and other eventual physical constraints (such as, for instance, the maximum allowable fuel flow rate, maximum ACS thickness, coolant pressure drop etc...). The architecture of the actively cooled panel – i.e. either bare ACS panel configuration, *sandwiched* ACS panel configuration or radiative shield ACS panel configuration – may also be made optimal by adopting an optimization strategy that makes use of a genetic algorithm (here, Matlab's *ga* solver has been used). Genetic algorithms represent indeed an efficient class of global optimizers that can combine the use of discrete and continuous optimization variables. This way, the optimal location of the two insulation layers with respect to the convectively cooled passages (represented mathematically as a list of possible permutations without repetitions in the optimization problem) may be determined along with the combination of insulation material required as well as the necessary thicknesses and mass flow rate of coolant. A typical optimization problem, using the present thermal model, is illustrated in Fig. 5.11. In the present design study, the structural skin is still considered to be made out of a 2 mm-thick titanium alloy layer (whose material properties are shown in Table 5.2) directly attached to the TPS arrangement. The numerical optimization requires thus a repeated assessment of the objective and constraints of the thermal problem: these function evaluations are performed based on a trajectory-based heat transfer analysis using the time history of the convective heat transfer rates obtained via the coupling of both the flight simulation model and the HyFlow code. An attempt at designing an ACS

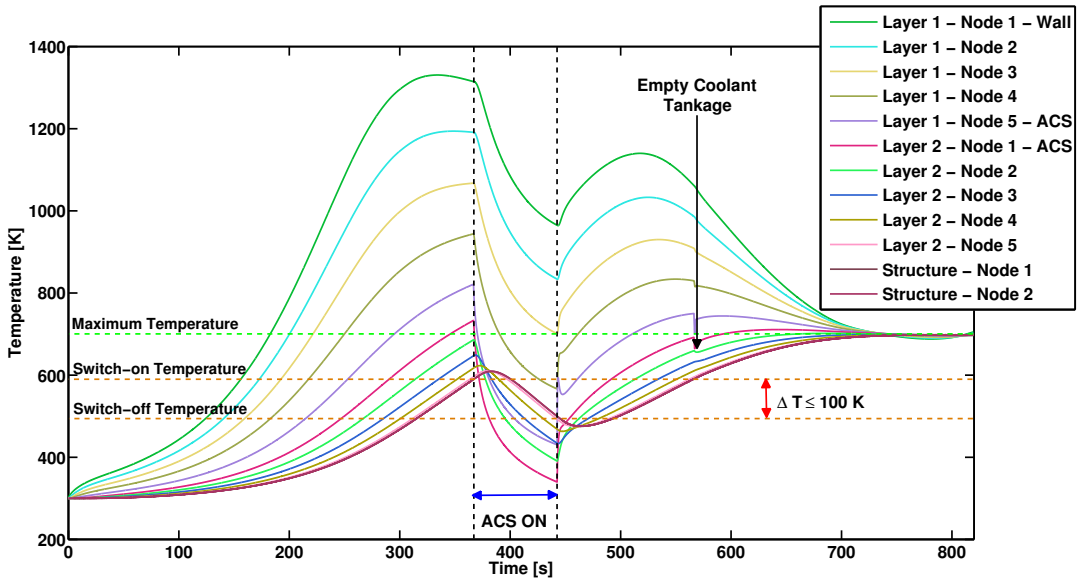

Figure 5.12: ACS optimal design - A first optimal actively cooled panel design, designated "*Single-Impulse ACS*", is depicted.

for the leading edge of the wings of the CFASTT-1 re-usable launcher (exposed to a peak heat flux of 450 kW/m^2) is presented below.

First, non-linear inequality constraints and design bounds have to be carefully added to the optimization problem. Above all, it must be ascertained that the temperature limits of each material layer of the TPS stack is not surpassed (mainly that of the surface layer and that of the underlying titanium structure, here $T_{max} \leq 700$ K). Furthermore, the equivalent hydraulic diameter of the combined cooling pipelines (i.e. ACS thickness) must be, for obvious reasons, smaller than the radius of curvature of the wing leading edges to have enough room for their accommodation (i.e. considering the CFASTT-1 vehicle, $D_h < 10$ cm). In this first optimization case, the flow of coolant is activated when the structural node temperature reaches a value of 600 K and is then switched off as soon as the temperature reduces down to 500 K, thus limiting the maximum ΔT and avoiding too sudden a change in the thermal conditions (rapid switch between hot and cold conditions provokes thermal fatigue) induced in the structure and coolant passages. For demonstration purposes, the optimizer was given the choice of two possible passive materials: RCC (see material properties in Table 4.1) and Rene 41 materials (whose properties are summarized in Table 5.3). The result of this optimization problem is shown in Fig. 5.12: the optimal TPS architecture (given the bounds and constraints of the present optimization problem) is an almost

single-impulse ACS system composed of cooling lines (whose equivalent diameter is equal to 5 cm) sandwiched between two layers of RCC material: the layer exposed to the external flow is 1.04 cm-thick while that adjacent to the structure is 2.14 cm-thick. As observed in the figure in question, the temperature of the titanium structure is maintained well below its maximum allowable temperature and the surface RCC layer is also far below its 1650 K re-usability limit (134). In the present scheme, the TPS acts again as a passive thermal barrier first until the structure reaches a temperature of 700 K (380 seconds after entry) which triggers the flow of coolant (i.e. $\dot{m}_{cool} = 4.9967$ kg/s) through the ACS panels during a total period of 50 seconds and is then switched-off (a total volume of less than 10 m^3 of propellant is consumed) after which the TPS acts again as a passive system. The ACS is very briefly switched on and then off a second time at t = 585 seconds (boiling off the rest of the coolant reserve); the concomitant effect is to slightly inflect the temperature profile of the structure node, just enough for the coolant-less TPS to carry on in its passive mode while ensuring a structural temperature below 700 K until the end of the re-entry simulation. The total mass of the ACS arrangement for the leading edges was found equal to 4.3 tons. In this study, important engineering details may have been overlooked such as system redundancy (for safety and reliability), constraint on minimum volume in order to fill the pipes or even pipelines distribution. Furthermore, a limit on the maximum allowable Mach number of the coolant flow, in order to avoid for instance compressibility effects (i.e. $M_{cool} < 0.25$) as suggested in the study of Shore (135), could also be added. Nonetheless, the comments above reflect on the continuing nature of the development of the HyTPS model and the purpose of the parametric study presented here is to demonstrate that such simple (but detailed) parametric actively cooled panel models can provide an excellent platform for trade-off analyses in preliminary design studies. In future investigations, it may be interesting to consider the on/off conditions as part of the parameters varied by the optimizer in order to determine whether a permanently cooled structure, instead of a single-impulse type of control as obtained previously, induces a lower mass penalty or not.

Discussion

When making use of such active cooling methods, although supplementary TPS items – i.e. such as extra structures (e.g. dedicated coolant tank, pumps) and

hydrogen tankage for cooling – may have to be considered, one of the many findings provided by the comprehensive study of Helenbrook *et al.* (99) for a Mach 6 hypersonic cruiser, performed in 1971, has shown that the more attractive actively cooled airframe concepts indicated potential payload increases ranging from 40% to over 100% as compared to the results of previous studies of a similar vehicle configuration composed instead of a passive thermal protection system. The previous comment (when combined with the various analyses performed in the previous section) emphasizes even further the interesting potential of convectively cooled airframe structures to provide technical feasibility to the concept of re-usability.

Nonetheless, a few additional comments are necessary to temper the previously reported non-optimal and optimal hybrid TPS analyses: first, the external skin of the vehicle (i.e. structurally integrated TPS) will, in all likelihood, be attached to (or blended into) a stiffer load-bearing structure that constrains it from being free to deform. Therefore, the outer skin of the vehicle will only be able to expand/contract as much as the underlying airframe structure to which it will be attached. It is thus crucial to remark that the local thermal stresses (e.g. eventually leading to material fatigue), that are induced by the intermittent use of the ACS (even more so when a bang-bang controller is used), must be accommodated before a particular design of convectively cooled panels can be considered successful. Indeed, the resulting thermal stress, here simply denoted σ, can be approximated by

$$\sigma = \frac{\alpha_T E}{1-\nu}\,(T_{wall} - T_{struct}) = \frac{\alpha_T E}{1-\nu}\,\Delta T \tag{5.5}$$

where E and α_T are, respectively, the Young's modulus and coefficient of thermal expansion of the structural skin's material and ν is the material's Poisson's ratio. If it is assumed that the structural skin can be maintained at a relatively low temperature thanks to convectively cooled passages, it can be seen from Eq. 5.5 that the resulting thermal stress may become much greater than the level of stress the TPS arrangement may possibly be able to accommodate ($\sigma > \sigma_{max}$), and would therefore expose the structurally-integrated actively cooled panels to the possibility of thermal fatigue failure. A first solution may be to use a structural material with lower stiffness (low Young's modulus), however this choice might go against other aerodynamic design principles. Therefore, an other approach consists in adopting a material with high conductivity (and low thermal diffusivity), since

by application of Fourier's law, Eq. 5.5 can be approximated as

$$\sigma \propto \frac{\alpha_T E}{(1-\nu)k} \tag{5.6}$$

Therefore, although this phenomenon is beyond the scope of the present dissertation, its tight relation to the re-usability of future space-access vehicles is key, and thus its effects should necessarily be addressed in future studies. For present purposes however, a careful selection of the insulation materials that compose the hybrid TPS panels and a constraint on the maximum allowable thermal fluctuation (i.e. ΔT) were considered as sufficient measures to mitigate this particular problem (and to palliate the lack of in-depth structural analysis capabilities). Similarly, a more sophisticated control system for the flow rate through the cooling system could be adopted in order to reduce the cyclic thermal loads that the current control strategy induces in the internal structure. For instance, a central control algorithm could be used to coordinate the local *zone controllers* to efficiently distribute the coolant flow where it is required: this would reduced sensitivity to off-nominal heat loads and make an efficient use of available cooling resources. This complex strategy was proposed by Krause and Ianculescu for the NASP programme (136). These extensions to the thermal models described here, in particular the use of a more sophisticated control strategy for the coolant flow rate, would be relatively straightforward to implement, and the various models presented here serve thus simply to demonstrate their capabilities in the context of both rapid preliminary design and concept exploration studies.

5.3 Ascent-to-Orbit Phase

One of the numerous complex problems associated with the ascent-to-orbit phase of the mission concerns the design of hybrid engines that can both sustain air-breathing hypersonic propulsion over a useful portion of the vehicle's ascent and function over a wide range of densities across the various layers of the terrestrial atmosphere. The various modes of the engine will have to be sequentially switched on and off following a dedicated schedule of operations – i.e. the design of the optimal sequence requires a great deal of care in order to exploit efficiently the various advantages provided by the several operational modes of the powerplant. The propulsive device of the CFASTT-1 vehicle that is the subject of

this particular work is assumed to be a Rocket-Based Combined Cycle (RBCC) engine system, derived from the propulsion system that was first proposed for Hyperion, a launch vehicle conceived by the Aerospace Systems Design Laboratory at Georgia Institute of Technology in Atlanta (110). It shall be remarked that this particular HyPro model of Hyperion's RBCC has been validated against the results of SCCREAM (76). Furthermore, that particular engine configuration has been selected since it can, at least in theory, operate over a wide range of flight conditions by changing its internal configuration to allow operation in the several different modes listed below:

- First, the *ejector mode* which involves the use of an air-augmented rocket with post-combustor. The engine, when in this mode, is able to provide thrust from the subsonic regime up to low supersonic flight conditions with higher specific impulse than a conventional rocket.
- Then, the *pure ramjet mode*: once sufficient speed has been attained, the rocket engine is turned off to take advantage of the higher specific impulse of the full ramjet mode.
- Finally, the *pure rocket mode* is eventually employed to provide the final boost required for orbital insertion, and is adopted when either the thermal limits of the ramjet are reached or the atmosphere becomes too rarefied to sustain air-breathing propulsion.

5.3.1 Propulsion System Modelling

A schematic of the HyPro model for the Hyperion propulsion system (110) is depicted in Figs. 5.13 (a), (b) and (c). In Table 5.4, the various sectional areas of the engines at the junctions between the various engine parts are listed. Both the intake and the nozzle have variable geometry in order to allow the engine to adapt to the wide operational range described in the previous introductory paragraph: the table lists the maximum and minimum areas of the various engine modules. It should also be borne in mind that the HyPro model allows for full control over the switching between the three propulsion modes of the engine. Indeed, in the version of the model used in the study of Wuilbercq, Pescetelli, Mogavero, Minisci and Brown (14), the switching between modes was simply governed by the free-stream conditions, in particular the Mach number, M_∞, and the total pressure

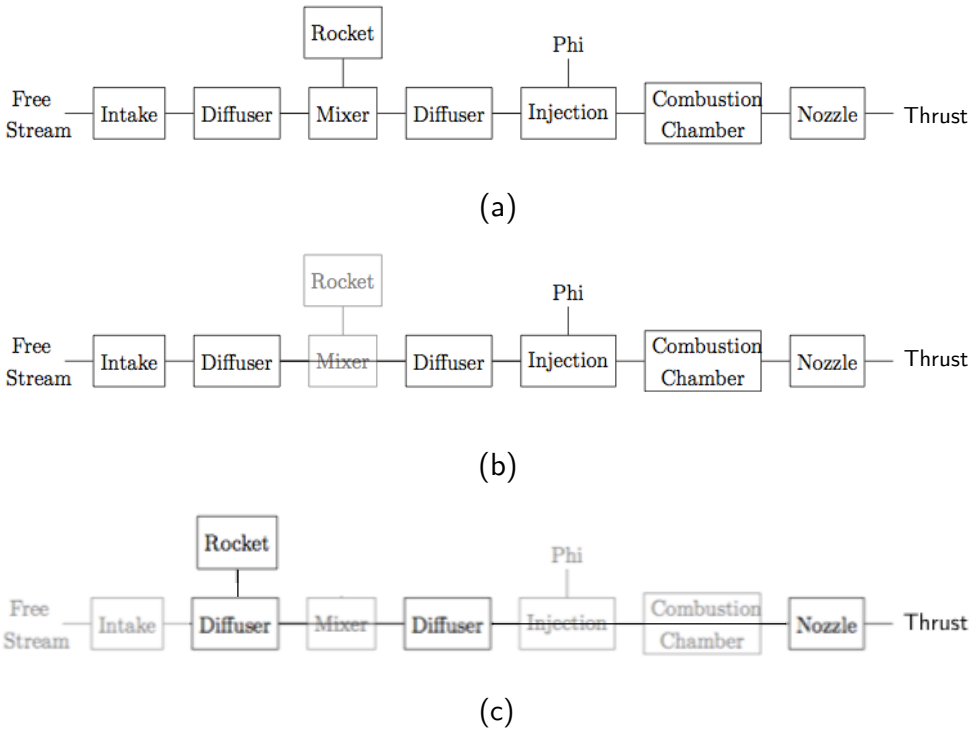

Figure 5.13: HyPro model of the Hyperion engine - The modelling in HyPro of the three different modes of operation of the Hyperion propulsion system are shown (14): (a) ejector mode, (b) pure ramjet model and (c) pure rocket mode.

P_0, as delimited by the operational range for the engine in each of its modes as listed in Table 5.5. As can be seen in the table in question, the operational ranges of the various propulsive modes overlap to some extent: when a situation arises in which two different modes can be selected, the switching strategy embedded in HyPro will first give priority to the mode that is already in operation. In doing so, any un-realistic cycling between the various propulsion modes, particularly near the operational boundary of a particular mode, is avoided.

5.3.2 Ascent Trajectory Planning

The vehicle can be dynamically controlled using either the propulsive or the aerodynamic forces. The magnitude of the propulsive force can be modulated by throttling the engines. For the planning of the ascent trajectory, the control law should thus account for the thrust F_T in addition to the aerodynamic control via the bank angle, μ, and angle of attack α. The nature of the optimal ascent control problem is presented in the next paragraphs.

	Area [m^2]	
Node name	Min	Max
Pre-Intake	0	∞
Intake	0	2.5084
Throat	0	0.6271
Pinch Point	0.7655	0.7655
Primary	1.0452	1.0452
Mixer End	1.0452	1.0452
Rocket Outlet	0.2796	0.2796
End Diffuser	2.0903	2.0903
Injection	2.0903	2.0903
End Chamber	2.0903	2.0903
Nozzle	0	8.8258

Table 5.4: Nodal areas within the HyPro model of the Hyperion engine (110).

	Mach Number		$p_0[Pa]$	
Mode	Min	Max	Min	Max
Ejector Mode	0	3.0	$1 \cdot 10^4$	∞
Pure Ramjet Mode	2.5	8.0	$5 \cdot 10^5$	∞
Pure Rocket Mode	0	∞	0	∞

Table 5.5: HyPro model of the Hyperion engine: operating ranges for each propulsion mode (110).

Optimal Control Problem

To obtain the ascent trajectory for the re-usable launcher, the control vector c is given by the variation of the angle of attack α, the bank angle μ and the throttle control δ_T (and hence the engine thrust F_T) along the trajectory. The optimal control problem aims to maximize the payload mass on board of the vehicle, i.e. to find

$$\max_{\mathbf{c}\in D} \; m_{pay} \tag{5.7}$$

subject to the dynamics described in Section 4.2 and initial conditions (i.e. at $t = 0$) $h_0 = 8.2$ km, $v_0 = 0.470$ km/s, $\gamma_0 = 8$ deg, $\chi_0 = 0$ deg, $\lambda_0 = 0$ deg, $\theta_{L0} = 0$ deg set to start after the transition into the supersonic regime. The terminal

conditions (i.e. at $t = t_f$) are $h_f = 80$ km, $v_f = 8.2$ km/s, and $\gamma_f = 0.2$ deg are those required to enter into a circular orbit at 80 km altitude. Path constraints are imposed on both the peak heat flux at the nose stagnation point, $\dot{q}$ and the dynamic pressure q_∞, as well as on the normal and axial accelerations, a_y and a_z experienced by the vehicle.

Ascent Aero-thermodynamics

A mix of methods has been adopted here: the Tangent-Cone method has been used first at the beginning of the ascent trajectory and then, once the vehicle reached a higher speed, the classic Newtonian Theory was then employed.

Nominal Ascent Trajectory

The resultant nominal ascent trajectory of the vehicle is shown in Fig. 5.14. Moreover, the original schedule of angle of attack from the work of Pescetelli *et al.* (120) has been increased as it was found that the downward attitude of the engine pods located at the tip of the wings lead to some lift-generation problems at the very beginning of the simulation. As a result, the terminal conditions may not necessarily correspond to those described in the previous optimal control problem. The non-optimality of the control law used here can also be noticed in the rightmost figure of Fig. 5.14 where the flight path angle, γ, appears to be negative for a short period of about 30 s (inducing a small descent rate). As can be seen, the time taken to ascend to orbit is slightly less than 200 s. In the bottom-middle graph in Fig. 5.14, it can clearly be seen that the discontinuities observed in the thrust profile correspond to a change in propulsion mode, e.g. at about 80 s from the start of the ascent trajectory, the engine switches between its ejector and ramjet modes. The high specific impulse of the combined-cycle configuration of the powerplant is taken advantage of until the vehicle reaches an altitude of 38 km. At this altitude, the engine employs its pure rocket mode to ascend up to the orbital boosting conditions at 80 km altitude.

5.3.3 Variability in Engine Parameters

Variability in the performance of the engines, and indeed the consequences of the selection of certain key design variables, has a critical impact on the feasibility of

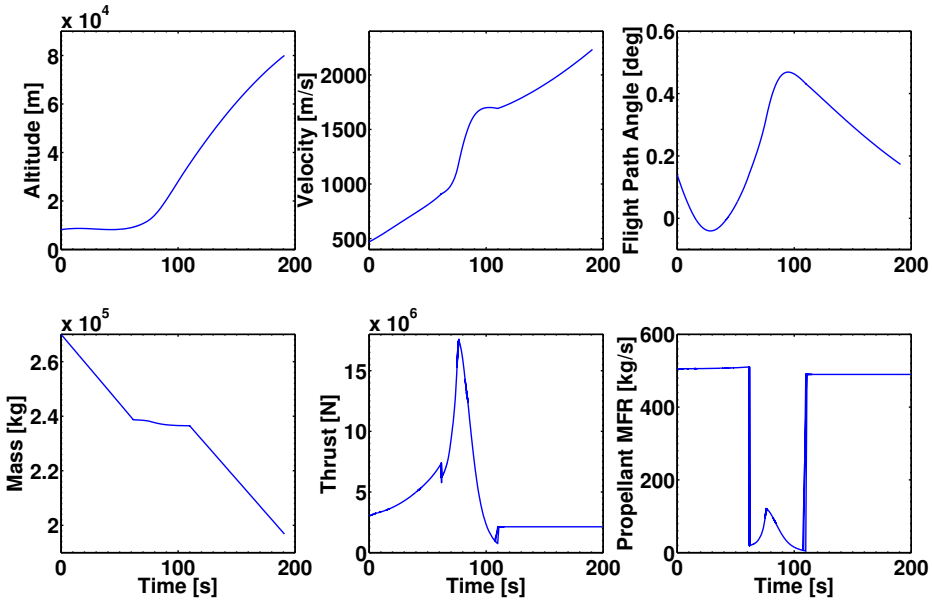

Figure 5.14: Nominal ascent trajectory - Baseline ascent trajectory for the CFASTT-1 vehicle.

the vehicle's ascent trajectory. The effect on the feasibility of the nominal ascent trajectory, presented in Section 5.3.2, of varying the mixer efficiency of the engine when in ejector mode, the Mach number at which the system switches from ejector to ramjet mode, and the relative size of the rocket and ramjet components of the propulsion system of the vehicle, are presented in the next few paragraphs.

5.3.3.1 Size of the Rocket and Ramjet Components

Figure 5.15 illustrates the sensitivity of the ascent trajectory to the relative size of the rocket and ramjet components of the propulsion system. The aim of the analysis is to assess the performance of the system under the trade-off where the propulsion system, at the extremes of the analysis, is either predominantly air-breathing or predominantly rocket-like in its behaviour. The overall size of the engine was thus increased (or decreased) by 30% while the rocket size, and consequently the mass flow rate of its propellant, was correspondingly decreased (or increased) by the same percentage. As can be seen, the adoption of an over-sized ramjet results in a slight gain in final payload mass over the nominal case (see fuel mass flow rate graph – bottom-right in Fig. 5.15), but at the expense of extremely poor performance early on in the vehicle's trajectory. In the opposing situation

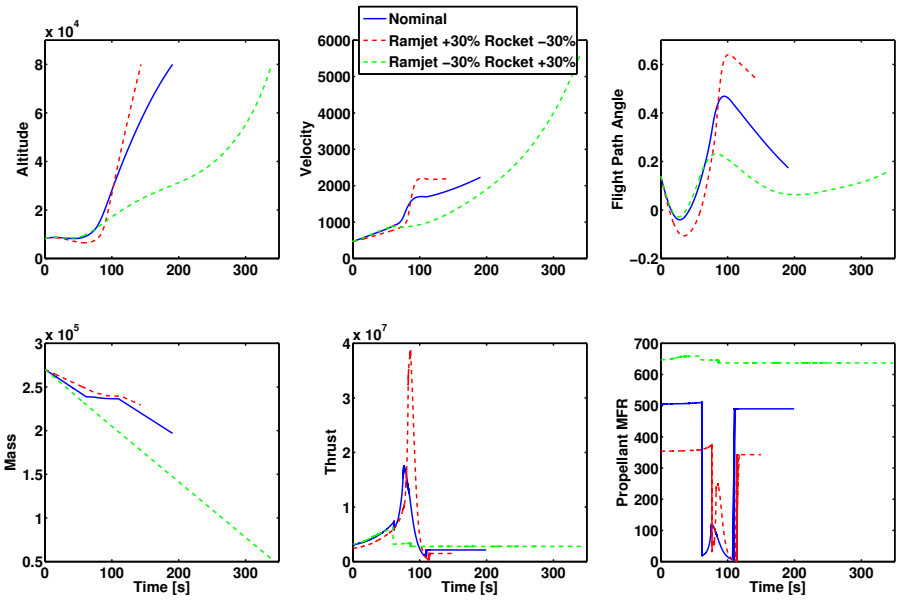

Figure 5.15: Sensitivity of the performance during ascent 1 - Sensitivity of the ascent trajectory to the relative size of the rocket and ramjet components of the propulsion system.

where the rocket is enlarged, the time taken to ascend to orbit is significantly extended (about 340 s), and, as a result of the low effective specific impulse of the propulsion system in this configuration, there is a significant loss in payload performance. Put simply, the undersized ramjet is, as expected, close to being just a simple rocket, and allows very little advantage to be gained at all from the combined-cycle configuration of the powerplant. In comparison, the over-sized ramjet design might, at least at first glance, seem very attractive even in comparison to the baseline configuration. The effect of increasing the size of the engine on the remainder of the vehicle design needs to be borne in mind very clearly, however, particularly given the multi-disciplinary focus of the present study.

5.3.3.2 Mixing Efficiency

Figure 5.16 shows the sensitivity of the vehicle's performance to the efficiency of the mixing between the primary air-flow through the engine and the secondary flow that is induced by the rocket when the engine is operated in ejector mode. Three off-nominal conditions are considered: two where the mixer efficiency is assumed to be greater than the nominal mixer efficiency of 67% and one condition where the mixer efficiency is taken to be sub-nominal. As is to be expected, the

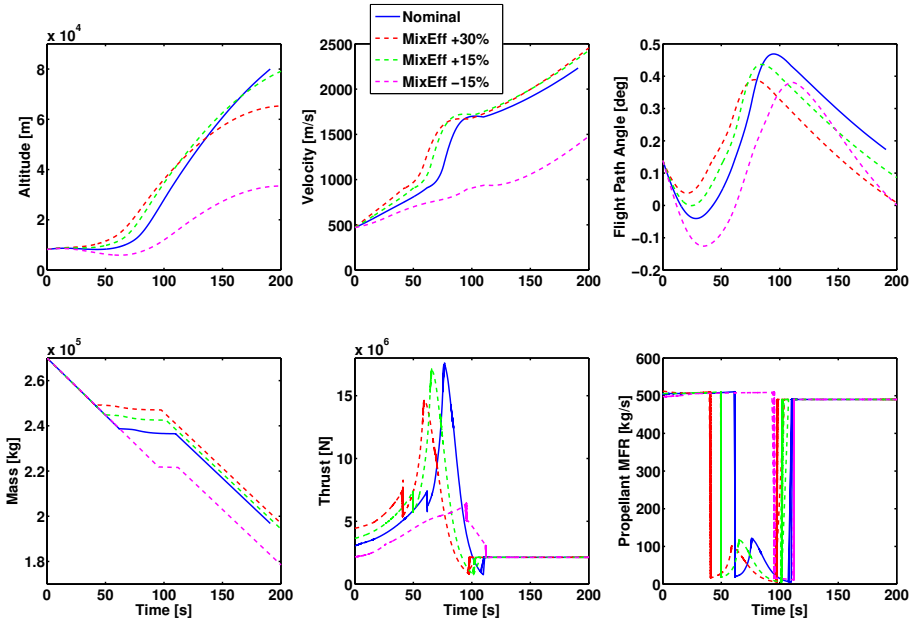

Figure 5.16: Sensitivity of the performance during ascent 2 - Sensitivity of the ascent trajectory to the mixer efficiency of the engine when in ejector mode.

thrust in ejector mode increases as the mixer efficiency is increased, and, as a consequence, the vehicle reaches the Mach number at which the system switches from ejector to ramjet mode earlier in its ascent. It is also clear however that, with the engine in ejector mode, the vehicle climbs faster the higher its mixer efficiency, with the interesting consequence that the engine when in its subsequent ramjet phase produces a lower thrust, resulting overall in a reduction in the performance of the vehicle. Indeed, a vehicle with too high a mixer efficiency appears to be unable to reach its target altitude; in comparison, the vehicle with mixer efficiency just 15% greater than nominal reaches its 80 km with a small time delay and with a lower final mass than the nominal case. It should be borne in mind however when assessing these results that the calculations presented here were all performed using the same control laws, i.e. those that were established for the nominal trajectory of the vehicle, and that re-optimisation of these laws for the vehicle with its off-nominal propulsion system would most likely allow it to better balance the improved ejector performance with the exploitation of the various operational modes of the engine. It is indeed interesting to note the large reduction in fuel consumption during the ejector phase that results from an improvement in the power plant's mixer efficiency. It is possible to speculate that this reduction in fuel consumption could be translated into a large gain in payload mass fraction at the end of the ascent simply by employing a set of control laws

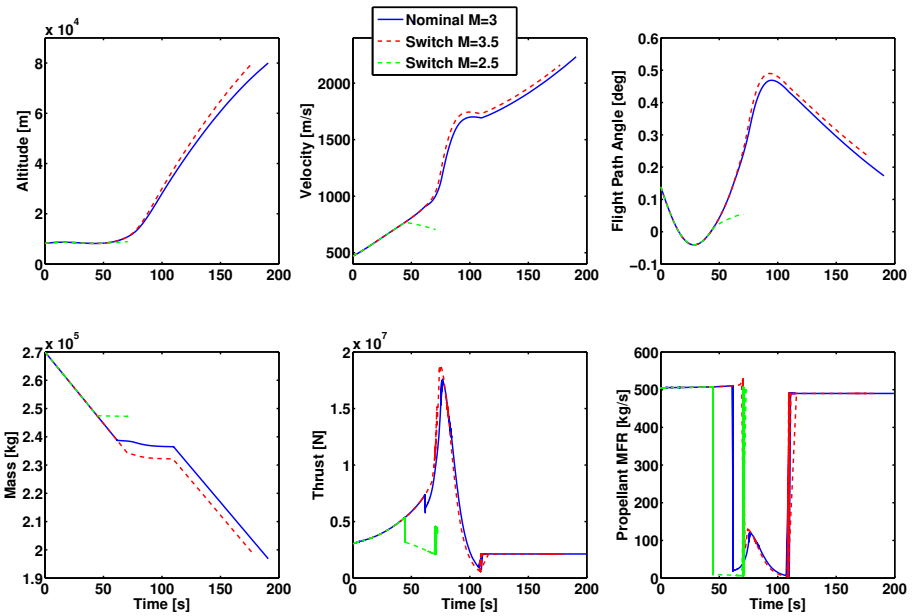

Figure 5.17: Sensitivity of the performance during ascent 3 - Sensitivity of the ascent trajectory to the Mach number at which the system switches from ejector to ramjet mode.

that are better suited to the engine's operational characteristics. By comparison, the inferences from the data when the mixer efficiency is lower than nominal are much more straightforward: it is clear that the ejector performance in this case is so poor that the transition to ramjet mode is delayed too late into the ascent for this part of the propulsion system to be effective in accelerating the vehicle up to its orbital speed and altitude.

5.3.3.3 Mode Switching Condition

Finally, Fig. 5.17 reveals the sensitivity of the system to the Mach number at which the system switches from ejector to ramjet mode (see Section 5.3.1). Early switching between these two engine modes can yield significant savings in fuel consumption thanks to the higher specific impulse of the ramjet mode, but can also result in a significant reduction in the thrust produced by the powerplant, and thus the overall impulse given to the vehicle, during the critical mid-phase of its ascent to orbit. Figure 5.17 shows the clear disadvantage in bringing forward the mode transition to Mach 2.5. In this instance the ramjet is simply not effective enough to continue the vehicle acceleration and thus the speed decreases until the engine switches back to ejector mode. Delaying instead the transition to Mach

3.5 seems to have a beneficial effect on the vehicle's trajectory: the performance of the propulsion system is better matched at the transition between ejector and ramjet modes, as can be inferred from the associated reduction in the size of the discontinuity in the thrust produced by the system at the mode-switch, and the vehicle is able to reach its final target altitude earlier with a slight gain in terms of overall mass to orbit.

5.3.3.4 Discussion

Although the observations and potentialities of the previous sensitivity analyses all need to be seen in the light of more general considerations of the vehicle's performance and operability, the results presented herein again show clearly the benefits of reduced-order modelling in being able to trade and compare various aspects of the performance of the vehicle, and indeed thus to be able to inform early design decisions regarding the key parameters that will govern its eventual configuration. As a result, these analyzes are more than simply used to demonstrate the utility and relevance of the system model for the study of the effects of parametric variations in the properties of the system (here, the engine parameters) on the ascent performance of future re-usable space-access vehicles. In fact, these results shed some light on a set of engine parameters that may have a significant impact on the performance of the propulsive device and, by consequence, on the feasibility of the ascent trajectory. In future investigations, the engine performance with fuels other than hydrogen could represent an interesting addition to the present sensitivity analysis in order to emphasize even further both the flexibility of the overall vehicle engineering model and its practical use to perform trade-off studies.

5.4 Ground-hold Phase

As discussed in Section 4.3.2, the thermal shield of the vehicle must be designed not only to protect the vehicle from the thermal loads experienced in flight, but also during those times when the vehicle is being held on the ground prior to a mission and its tanks are full of cryogenic fuel. Indeed, the risk is that cooling of the structure might result in the build-up of a layer of ice on the outer surface of the vehicle. To demonstrate the use of the HyTPS code to model this particular phenomenon, a 20 metre-long integral tank, containing a volume of 420 m^3 of fuel

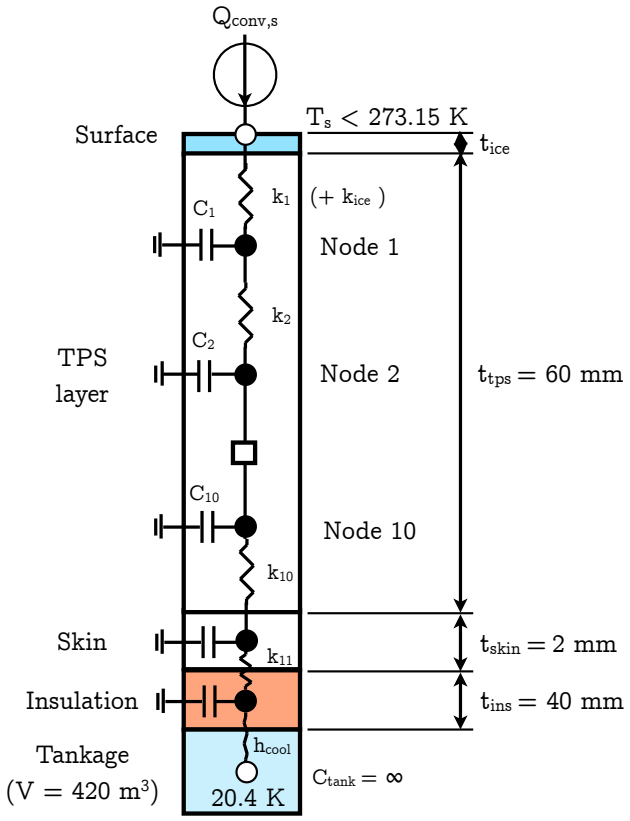

Figure 5.18: Thermal network model of the ground-hold phase - In the ground-hold thermal network model, the ice layer is represented by a dynamically varying layer. Indeed, this layer grows or regresses as a result of the thermal conditions observed at the surface of the TPS arrangement.

and located within the forward fuselage of the CFASTT-1 vehicle, was assumed to be insulated using a foam material with a 4 cm thickness. The tank was considered to be directly attached to the load-bearing structural skin of the vehicle, which in turn was assumed to be covered by the same TPS as that described in the previous Section 5.2.3 (although, for obvious reasons, the active element of the system was switched off for the entire analysis). The behaviour of the ice layer on the surface of the vehicle during a 2-hour long ground-hold phase in sea-level ambient conditions was therefore modelled using the approach described in Section 4.3.2 (during these two hours, the cryogenic tank is considered fully loaded). For present purposes, the tank has been modelled as a boundary node of constant temperature equal to the storage temperature of liquid hydrogen fuel. The thermal network used to assess the ground-hold phase of the mission is depicted in Fig. 5.18.

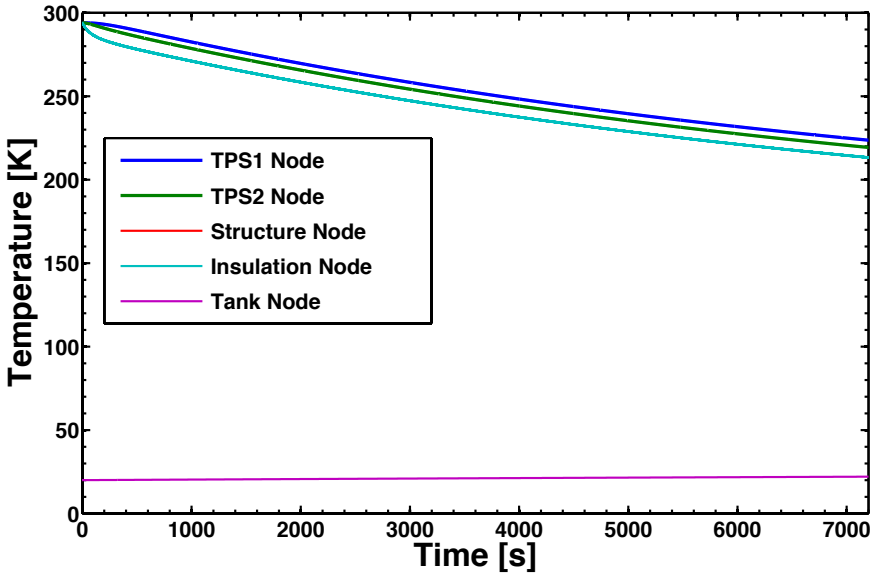

Figure 5.19: Temperature history of the ACS system during ground-hold for case 1 - Evolution of the nodal temperatures during ground-hold operations when the hybrid TPS solution is considered.

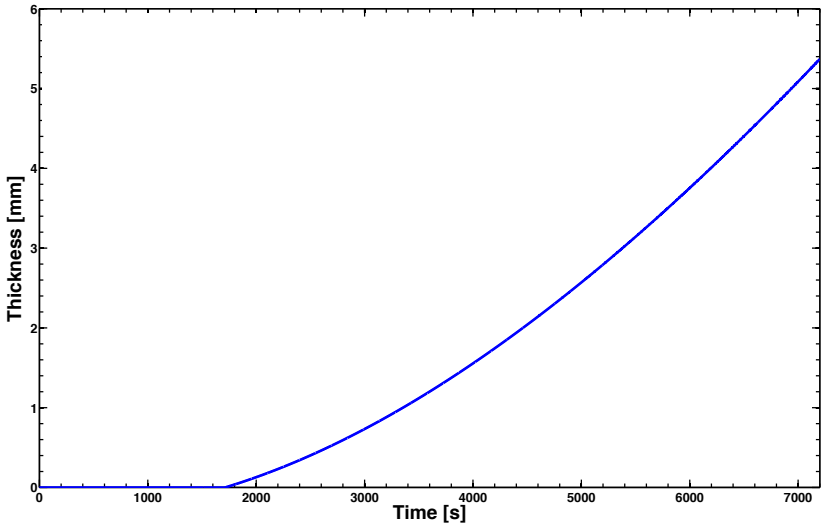

Figure 5.20: Growth of the ice layer for case 1 - Growth of the ice layer during ground-hold operations when the hybrid TPS solution is considered.

5.4.1 Ice Layer Growth

The evolution of the temperature within the tank, its insulation, and the TPS during the ground-hold operation is shown in Fig. 5.19. The temperature in the tank (assumed to contain liquid hydrogen at 20.4 K) is responsible for drawing

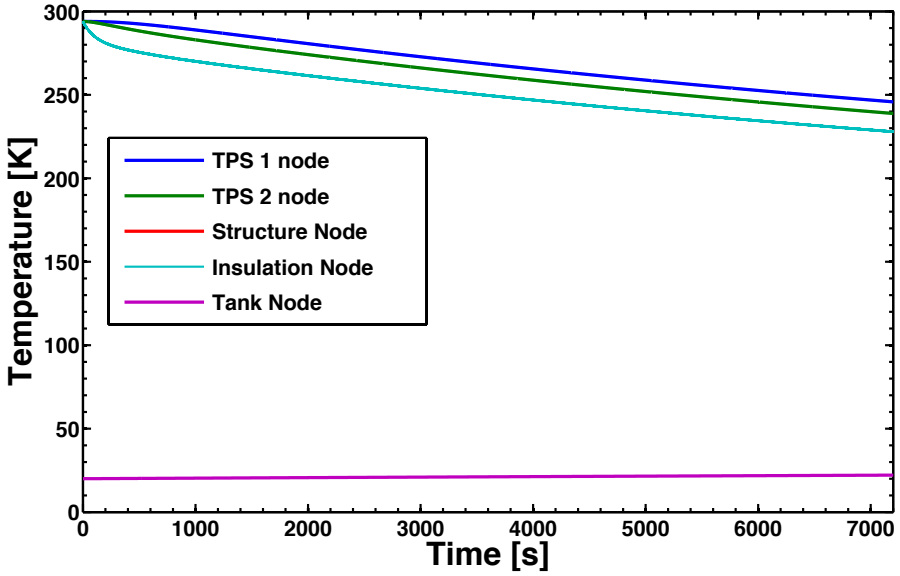

Figure 5.21: Temperature history of the ACS system during ground-hold for case 2 - Evolution of the nodal temperatures during ground-hold operations.

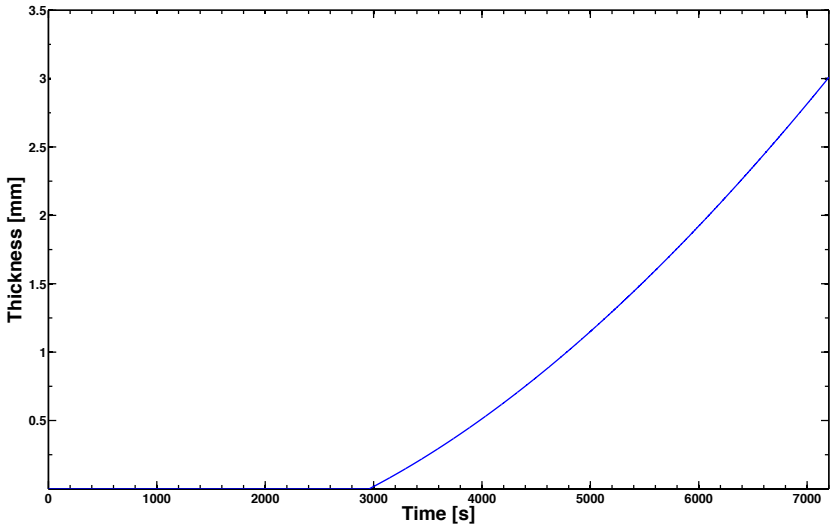

Figure 5.22: Growth of the ice layer for case 2 - Growth of the ice layer during ground-hold operations when the fully passive TPS solution is considered.

down the temperature within the remainder of the system, to the extent that, at the end of the ground hold, the temperature at the surface of the vehicle reduces from 288 K to 225 K. The associated growth of the layer of ice on the surface vehicle over the duration of the ground hold is shown in Fig. 5.20. As can be seen, the layer of ice appears first at about 28 minutes after the tank has been filled up. The total thickness of the layer of ice reaches about 5.5 mm after two hours,

amounting to a mass of water attached to the vehicle of approximately 55 kg per square metre of surface area covered (this amount of ice could potentially increase the Gross Take-Off Mass (GTOM) of the CFASTT-1 vehicle by about 414 kg even if only the forward-fuselage strakes were to be coated). If, instead, the fully passive TPS considered in Section 5.2.3 were to cover the vehicle (in other words a system consisting of a 10 cm-thick layer of RCC instead of a 6 cm layer) then, as shown in Figs. 5.21 and 5.22, the ice first begins to appear about 50 minutes after the ground-hold phase has started, and the layer reaches a thickness of only 3 mm (i.e. about 225 kg added to the GTOM of the CFASTT-1 vehicle) after two hours.

5.4.2 Discussion

This comparison reveals a rather interesting mechanism whereby a lightweight, advanced cooling system, designed for maximum in-flight performance, may in fact become somewhat of a liability when the formation of ice during the ground-hold element of the mission is considered. The resolution of this conundrum is not entirely apparent as yet - certainly the obvious route of increasing the thickness of the insulating layer between the tank and the structural skin would appear to be at least partially self-defeating. Nonetheless, as suggested by the study of Stone (137), some sort of ground support provisions may thus have to be used in order to prevent frost build-up during the ground-hold phase of the mission, even more so when adverse weather conditions are to be encountered (e.g. winter temperatures, rain...). In the reference study of Stone, it has been proposed to heat up the coolant and to circulate it through the actively cooled panels during groundhold.

From a modelling point of view, it could also be interesting to model the tank node as a diffusive node (instead of a boundary node) to see whether the temperature of the tank would rise to a point where boiling of the fuel may occur. Furthermore, an *all-at-once* type of optimization procedure in order to determine the optimal structure that combines both relatively high heat flux capability during ascent and entry as well as resistance to ice build-up and fuel boil-off (i.e. coupled optimization of the TPS arrangement and tankage insulation layer) could also be performed in later studies, albeit that these studies will be computationally very intensive.

5.5 Chapter Summary

In this chapter, various inter-related aspects of the multi-disciplinary design of a re-usable aerospace plane have been explored over three representative phases of its mission: atmospheric entry, ascent and ground-hold. First, the properties of the thermal protection system that will be required not only to shield the vehicle from the high thermal-flux that it will experience both during its ascent into orbit and its subsequent re-entry through the terrestrial atmosphere, but also from the effects of ice formation during ground-hold operations have been evaluated. The advantages of employing an active cooling system rather than a thicker and possibly much heavier passive system are evaluated in terms of the system architecture, the scheduling of the flow of coolant through the system, and the amount of fuel that needs to remain in the vehicle's tanks in order to be exploited as an effective coolant during re-entry. Additionally, a parametric model of an actively cooled panel created using HyTPS has also been used in the derivation of an optimal active cooling system.

Then, the sensitivity of the performance during the ascent phase of the mission to various engine design parameters has been discussed. Indeed, certain key design variables within the hybrid air-breathing propulsion system of the vehicle, particularly the relative sizing of the rocket and ramjet elements of its hybrid configuration, but also the Mach number at which transition between modes is scheduled to take place and the efficiency with which its rocket plume can be mixed with the primary air-flow through the engine, are shown to have critical influence on the success of its mission, and the allowable bounds on these parameters are discussed in the context of the engineering framework described throughout this dissertation.

The robustness of the various solutions provided by the reduced-order models throughout this chapter may still be questionable and requires a more in-depth assessment of the reliability of the models. In fact, uncertainty in the inherent characteristics of the reduced-order models have to be accounted for in order to provide a certain degree of confidence in the design solutions that are generated using this approach: this particular topic will therefore be the focus of the next chapter.

Nomenclature

List of Symbols

A	Panel area
a_y	Normal acceleration
C	Aerodynamic coefficient
c	Control law
D	Drag force
D_{pipe}	Hydraulic diameter
E	Young's modulus
F_T	Thrust
h	Altitude
Kn	Knudsen number
L	Body length
M	Mach number or Moment
m	Mass
$\dot{m}$	Mass flow rate
$\dot{p}$, $\dot{q}$, $\dot{r}$	Angular rates
$\dot{q}$	Heat transfer rate
S	Surface area
t	Time or Layer thickness
v	Velocity
α	Angle of attack
α_T	Coefficient of thermal expansion
γ	Flight path angle
δ	Deflection angle of the control surfaces
θ_L	longitude
λ	Latitude
μ	Bank angle
ν	Poisson's ratio
ρ	Density
σ	Stress
χ	Heading angle

Subscripts

0	Initial Condition
acs	Active cooling system
$cool$	Coolant
f	Final condition
ins	Insulation
L	Lift force

max	Maximum
nom	Nominal condition
pay	Payload
ref	Reference parameter
$stag$	Stagnation condition
tps	Thermal protection system
∞	Freestream condition

Chapter 6

Uncertainty Modelling in Preliminary Design Studies

"All models are wrong, but some models are useful."
– Robustness in the strategy of scientific model building, George E.P. Box (1979).

In this chapter, the importance and benefits of accounting for design uncertainties as early on in the preliminary design process as is possible are demonstrated in Section 6.1. In Section 6.2, the effect of uncertainty in the predicted characteristics of the atmosphere through which the vehicle descends during its re-entry trajectory is first discussed, while the uncertainty in the processes and parameters that may govern the nature of the transition of the flow over the vehicle from a laminar state to turbulence is then explained in Section 6.3. Thereafter, the uncertainty in the material properties of the Thermal Protection System (TPS) or that embodied in an Active Cooling System (ACS) type of thermal shield are discussed in Section 6.4. Finally, some concluding remarks will be given in Section 6.5.

6.1 Introduction

The design of future re-usable space plane-like vehicles intrinsically encompasses numerous "*known unknowns*" and possibly "*unknown unknowns*" (quoted from the briefing of the Secretary of Defense Donald H. Rumsfeld on February 12,

2002) that can potentially induce a large amount of uncertainty in the preliminary design process. In fact, the flight experience from the American Space Shuttle programme has revealed several elements of operational impact that should have been accounted for earlier in its design as well as that of future re-usable launch vehicles: namely the variability in the atmospheric properties as a result of climatological and weather-related phenomena, the uncertainty in the nature of the boundary layer transition, that in the level of aerodynamic heating resulting from shock-shock interaction phenomena and, finally, the uncertainties in the thermo-optical properties of the materials employed to shield the vehicle from the severe aerodynamic heating environment that always accompanies hypersonic flights. Nonetheless, it shall be remarked that although the problem related to shock-shock interactions is herein mentioned (and was earlier discussed in Section 2.8), its solution is beyond the scope of the present work and therefore only the remainder of the aforementioned design uncertainties will be further explored in the present chapter.

As mentioned earlier in Section 4.6 of Chapter 4, due to the strong coupling that exists between its various system components (e.g. between the propulsion system and the aerodynamics for instance), the task of designing a Re-usable Launch Vehicle (RLV) is inherently multi-disciplinary: in fact, many of the design parameters have a considerable mutual influence, and design objectives and constraints embody the risk of being mutually conflicting to an extent which is amplified by the extremely tight tolerances on vehicle performance that need to be achieved. It becomes therefore essential to be able to quantify, as early on in the design process as is possible, the effects of uncertainty in some of the key design parameters in order to provide reliable and realistic estimates of the margins on the likely performance of the vehicle. The main advantage of reduced-order (but comprehensive) models for preliminary design, such as those presented in the present work, is indeed the ease with which parametric variations in the properties of the system may rapidly be explored. This particular aspect indeed greatly simplifies the process of varying certain key design parameters in the system components as a means to assess their effects on the overall performance of the vehicle.

In the design of re-usable launchers, two fundamentally different types of uncertainty are inherent to the system. The first type is the *stochastic* uncertainty (also called random uncertainty) that is associated with inherent variations in the physical system or its environment. An example would be the natural variability in the properties of the material used to construct the layers of TPS on the

vehicle, or the natural fluctuations in atmospheric temperature at a particular altitude because of turbulence and winds. A second, perhaps even more important type of uncertainty in the context of design is however the *epistemic* uncertainty that results from the use of inadequate, incomplete or even erroneous physical models to encapsulate the behaviour of the system, especially when the design process relies exclusively on reduced-order models. In this vein, a statistical characterization of the performance of future re-usable space transportation systems in the presence of uncertainties in some of its key design characteristics may be conducted in order to demonstrate how variability or uncertainty within these characteristics, whether as a result of true physical randomness or deficiencies that are inherent in the modelling approach, can have a very strong impact on the robustness of the final design. As a result of such variability, the risks that accompany the development costs of fully re-usable space-access vehicles are significant (12). In fact, the conceptual design activities that are always carried out at the beginning of a new vehicle development are, in general, characterized by a large amount of uncertainty and various unknowns that need to be dealt with early during concept exploration activities. Indeed, such design variability carries the potential to quite dramatically impinge on the performance of a preliminary design concept and induce additional development costs if not accounted for early enough (it could even represent a threat to the overall vehicle development programme). It is therefore easy to recognize how a robust design methodology, that accounts for items of uncertainty throughout the preliminary design phase, can represent a valuable design strategy in order to efficiently and robustly conceive and optimise these future trans-atmospheric vehicles at a system level.

Nonetheless, an adequate strategy must be devised: in the design of complex aerospace technologies such as re-usable space transportation systems, it is common practice to add design margins to both the inputs and outputs of the design process in order to account for the uncertainties in the describing data. However, the larger the uncertainty in the design parameters is (which depends on the design phase), the larger are the design margins that must consequently be employed. This approach embodies the risk of adopting an excessive design margin, to the detriment of the performance of the space transportation system being designed: in fact, the risk could be to integrate significant margins whose collateral effect on the vehicle would be to reduce the amount of payload the system can carry into orbit. For example, if the design margins added to the properties of the TPS material are exaggerated to the point where indications are that a full switch

from a passive system to an active TPS is required, a costly, potentially massive and very complex system may then be introduced un-necessarily. For example, the Space Shuttle had to carry a large amount of extra propellant dedicated to its Reaction Control System (RCS) during re-entry in order to accommodate any weather-related uncertainty, which, in turn, increased the mass of the vehicle (and, by inference, mission costs) and also reduced its orbital manoeuvring capabilities (138). Therefore, when assessing the amount of uncertainty in the design process, it should clearly be accurately estimated in order to reduce design development risks, costs and time. To summarize, it is thus fundamental that the multi-disciplinary design approach, introduced in Chapter 4 for the evaluation of the performance of the vehicle, be augmented in order to be capable of functioning reliably in an integrated *robust* design environment. Therefore, the effect of uncertainty in the various components that constitute the overall vehicle system model has to be established. Section 6.2 introduces first a method to account for uncertainties in the characteristics of the atmospheric model.

6.2 Atmospheric Uncertainty

As discussed in the study of Findlay (139), several shuttle-derived atmospheric data sets have exposed the existence of regions where atmospheric density can vary by as much as 60% as a consequence of miscellaneous meteorological factors. The existence of highly variable density shear regions in the atmosphere add a significant amount of uncertainty to the environment in which future air-breathing spaceplanes will be conceived to operate. Such variability in the atmospheric conditions might overly constrain the design of future re-usable space transportation systems unless design margins are accurately estimated from either a series of prescribed flight data or using higher order atmospheric models. The approach based on the processing of flight data may, in fact, become extremely helpful in improving the atmospheric models presently used to estimate the performance of air-breathing vehicles at a conceptual design stage.

Indeed, designers often employ relatively simplified or averaged standard atmospheric models during conceptual design (e.g. the US Standard Atmosphere 1976 discussed in Section 4.2.1). However, these models do not account for the density shear regions, nor they account for phenomenon such as gravitational waves and

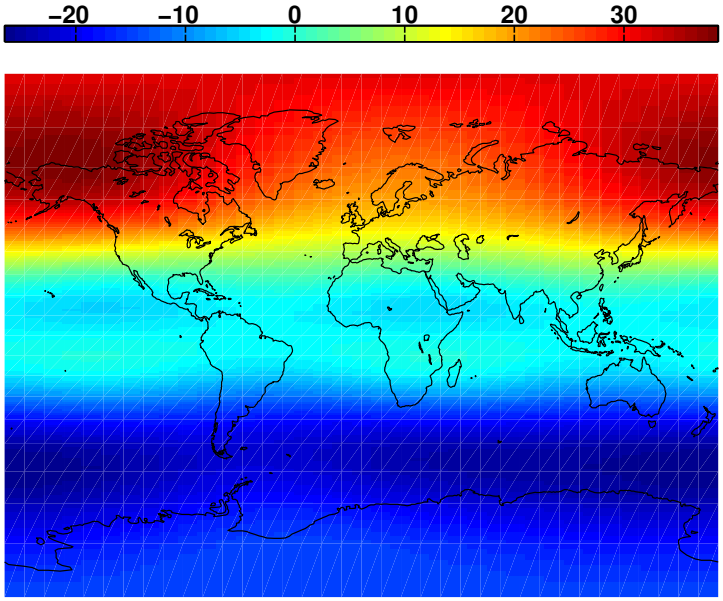

Figure 6.1: Atmospheric temperature variability - Temperature difference for an altitude of $h = 50$ km between the 1^{st} of January 2013 and the 1^{st} of July 2013 using the MSIS-E-1990 Atmosphere Model. The figure exemplifies the intrinsic variability in atmospheric temperature T_∞ based on both the location (latitude and longitude) and the seasons (Winter and Summer).

the effect of seasons, latitude and longitude which, in general, force the atmosphere to depart from these standards as demonstrated in Fig. 6.1. In the figure in question, the MSIS-E-1990 atmosphere model, suggested by Hedin for studies "*that reach across several atmospheric boundaries*" (140), was used to compare temperatures between a summer and a winter day at an altitude of 50 km. The main advantage of employing a model such as the MSIS-E-1990 representation of the Earth's atmosphere (compared to standard atmosphere representations) for the study of re-usable space planes is that it incorporates data directly derived from several Space Shuttle flights, satellites, rocket flights and newer incoherent scatter results for altitude above 72.5 km (140). Furthermore, a comparison of the predictions from the MSIS-E-90 model with rocket and miscellaneous other data highlighted the capability of this atmospheric model to represent relatively well the current knowledge of the climatological average, although some discrepancies were still observed near the mesopause (i.e. around 80 km) (140). The importance of improving these standard representations of the Earth's atmosphere (through uncertainty quantification) for the design and trajectory planning of future re-

usable space planes, in order to account for variability in the properties of the terrestrial atmosphere, can thus easily be recognized. For instance, as stated by Garner (138) and confirmed by Hale *et al.* (51), the amount of drag experienced by the Space Shuttle vehicle (closely related to the value of free-stream density) has varied by nearly 20% in a matter of a few seconds on some of its flights at hypersonic speeds. These abnormal density fluctuations may thus also have a direct impact on several other critical subsystems such as the air-breathing propulsion system (for which a trajectory at constant dynamic pressure is often sought for), propellant consumption and flight controls of future space planes. For example, in Eq. 4.88, it can readily be seen that atmospheric variability could impinge on the maximum thrust the engine is able to produce. Additionally, recalling the simplistic approximation for the heat transfer rates acting on space-access vehicles given in Eq. 4.50, it can clearly be seen that changes in atmospheric density may also have direct consequences on the level of heat flux experienced by this class of vehicles.

Consequently, an uncertain atmospheric model must be derived in order to provide designers with valuable insights into the effects of non-nominal atmospheric properties on the likely performance of the future generation of ramjet or scramjet-powered hypersonic vehicles. A procedure that is capable of perturbing the results from standard atmosphere models to represent an accurate measure of the variability in thermodynamic properties will therefore be presented in Section 6.2.1. Then, an approach to derive more accurate design margins will be explained in Section 6.2.2. Finally, a Monte Carlo analysis of the re-entry trajectory of a representative space-access vehicle, performed with a a set of perturbed atmospheric profiles derived using the method presently discussed, will be introduced in Section 6.2.3.

6.2.1 Perturbed Atmosphere Model

The uncertainty in the properties of the atmosphere can be represented by treating the atmospheric temperature profile, denoted $T_\infty(h)$, where h denotes altitude above mean sea-level, as a random variable. More specifically, if the nominal temperature profile within the atmosphere is denoted as $T_\infty^{nom}(h)$, then a representation of the temperature profile in the presence of uncertainty can be constructed as

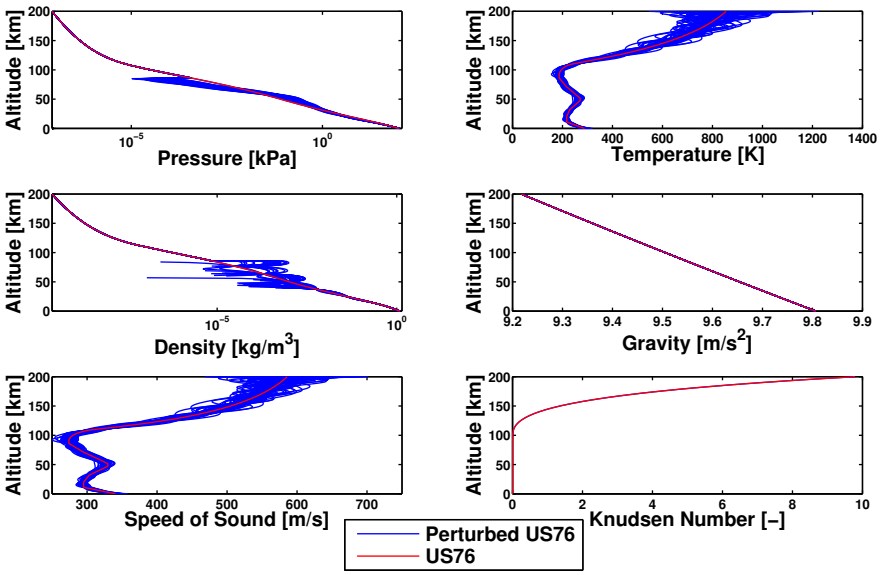

Figure 6.2: Perturbed atmosphere model - 1976 US Standard Atmosphere subject to uncertainty in the temperature variation with altitude (nominal atmospheric conditions in red). The uncertainty in the atmospheric temperature is taken to vary from 10% of the nominal value (at sea level) to 30% at 200 km altitude.

$$T_\infty(h) = T_\infty^{nom}(h) + \varepsilon(h)S(h) \tag{6.1}$$

In this expression, ε is an error bound function which captures the statistical variation of the temperature with altitude. This function can, at least in principle, be determined from measurement. However, it is for now assumed that, in the absence of better information, ε can be modelled very simply by linear interpolation between assumed bounds ε_L and ε_U on the uncertainty at the lower ($h = 0$) and upper ($h = h_U$) edges of the atmosphere (120), respectively, so that

$$\varepsilon(h) = (1 - h/h_U)\,\varepsilon_L + (h/h_U)\,\varepsilon_U \tag{6.2}$$

The function $S(h)$ captures the detailed statistical form of the distribution of the temperature perturbations about the nominal variation with altitude. For present purposes it is assumed simply that $S(h)$ is a uniform distribution on the interval $[-1, 1]$. As will be shown later, this assumption, although appearing at first sight to be physically rather simplistic, is of great utility when testing the robustness of a design as opposed to when performing a direct simulation of its likely performance. Finally, the variability that is introduced into the free-stream temperature using this approach is propagated into the remainder of the

atmospheric model by imposing the hydrostatic equilibrium in order to perturb the pressure profile (only valid for $h \leq 86$ km) as

$$P_{\infty}(h) = P_{ref} \exp\left(-\frac{h - h_{ref}}{H_{\infty}(h)}\right) \tag{6.3}$$

where P_{ref} is the pressure at the reference level (i.e. h_{ref}) and $H_{\infty}(h)$ is the geopotential scale height (which has been assumed constant over each of the thin layers that compose the planetary atmosphere) defined by

$$H_{\infty}(h) = \frac{R_{gas} T_{\infty}(h)}{M_{air} g(h)} \tag{6.4}$$

where M_{air} is the mean molecular mass of air (= 28.97 kg/kmol), and R_{gas} is the universal gas constant (= 8.3144621 J.mol^{-1}.K^{-1}). Then, the density profile $\rho_{\infty}(h)$, related to the pressure profile by application of the ideal gas law, is also computed as a result of these departures from the nominal temperature profile. For the regions of the upper atmosphere ($h > 86$ km), the free-stream temperature profile obtained in Eq. 6.1 is employed in the calculation of the number densities that are thereafter used to derive the remainder of the atmospheric properties (see discussion in Section 4.2.1).

A typical set of realisations of the variation of the atmospheric properties with altitude generated using this approach (from Eq. 6.1 to 6.4) is shown in Fig. 6.2 where the uncertainty in the atmospheric temperature profile is taken to vary arbitrarily from 10% of the nominal value at sea-level to 30% at 200 km altitude. In Section 6.2.2, a simple process to better define the statistical variation of the free-stream temperature and density with altitude using a higher-order analytical representation of the atmosphere will be demonstrated.

6.2.2 Realistic Design Margins

In the present section, the aim is to conceive a set of realistic design margins that can be used to perturb the reference US76 atmosphere model described in Section 4.2.1 (in place of $\varepsilon(h)$ in Eq. 6.2) that incorporates both geographical variability (i.e. latitude and longitude) as well as seasonal and monthly variability of thermodynamic properties (along with other meteorological phenomena based, for instance, on Shuttle-derived atmospheric data). In doing so, the MSIS-E-90 atmosphere model was used to create a series of atmospheric profiles for a

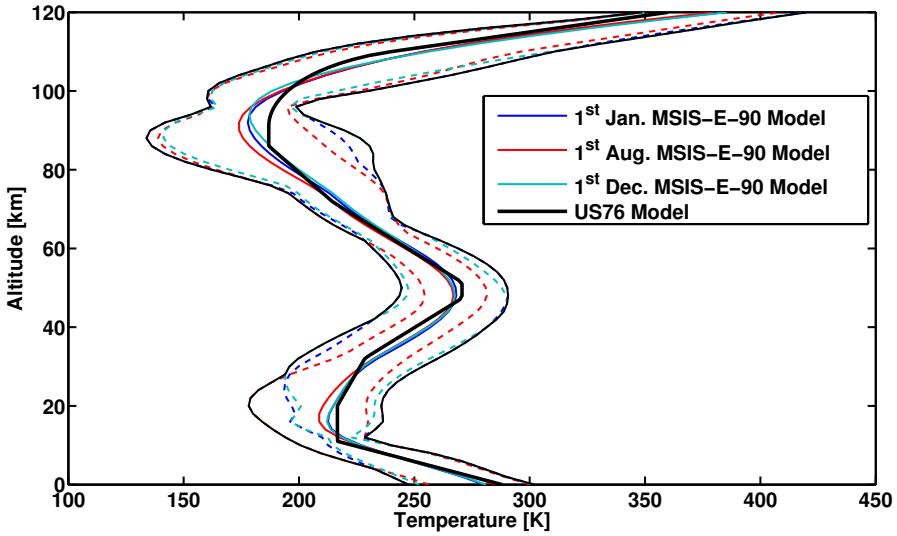

Figure 6.3: Illustration of the process of generating the margins for the atmosphere model - A series of averaged temperature profiles, derived using the analytic MSIS-E-90 atmospheric model for a number of winter and summer days, are compared to the nominal profile obtained via the 1976 US Standard Atmosphere Model from an altitude of 160 km down to sea level (black line). The upper and lower bounds of the MSIS-90 profiles are hereafter used to derive a set of design margins in order to quantify uncertainty in the US76 model.

number of days throughout the year (including summer and winter days – one day per month of the year 2013) and for the whole span of latitude (from -90 deg to 90 deg) and longitude (from -180 deg to 180 deg) in order to obtain full geographical coverage as well.

In Fig. 6.3, an example of such process is shown: after a series of profiles have been derived from the reference MSIS-E-90 model, their mean thermodynamic properties (here, atmospheric temperature is presented) is plotted against the nominal profile returned by the US76 standard atmosphere model along with their lower and upper bounds (dotted lines) in order to account for geographical variability (see Fig. 6.3). As can be seen from the figure in question, while the mean MSIS-E-90 profiles follow quite closely the values of temperature returned by the US76 standard model, the upper and lower bounds demonstrate a large amount of variability in the predicted values. Thereafter, the upper and lower bounds of the US76 were simply assumed to be the maximum and minimum of these MSIS-E-90 derived upper and lower bounds respectively, in order to finally account for both seasonal and monthly variability in the atmospheric proper-

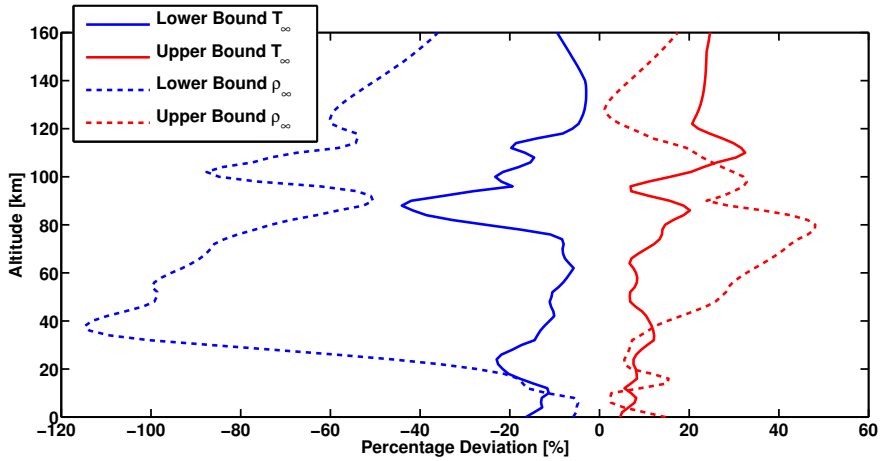

Figure 6.4: Density and temperature design margins - The resulting lower and upper percentage deviations, around the nominal value of both temperature and density returned by the US Standard Atmosphere 1976 as function of altitude, are presented.

ties. This relatively straightforward process allows for more precise margins to be obtained, as shown in Fig. 6.3, that average the climatological factors embedded within the higher-order MSIS-E-90 atmosphere model while accounting for geographical and seasonal variability.

The resulting margins (percentage deviations from the nominal US76 values) for both the temperature and density profiles are shown in Fig. 6.4. As can be seen from the figure in question, the density seems to be quite significantly affected by the meteorological, geographical and seasonal variability embedded within the MSIS-E-90 model. Nonetheless, it can be remarked that the largest margins are to be found around the mesopause (and at about 40 km for the atmospheric density) which was reported by Hedin (140) as the only region of the atmosphere where the validity of the model was in fact difficult to prove (see Section 6.2). Finally, these design margins can then be used to perform a Monte Carlo analysis in order to investigate the perturbation to the nominal trajectory that results from uncertainty in the atmospheric conditions pertaining along the flight path.

6.2.3 Stochastic Simulations

The sensitivity of a nominal control law to uncertainties within the atmospheric model, as investigated using the Monte Carlo method, is described. It is here assumed that a representative space-access vehicle will follow, during its re-entry,

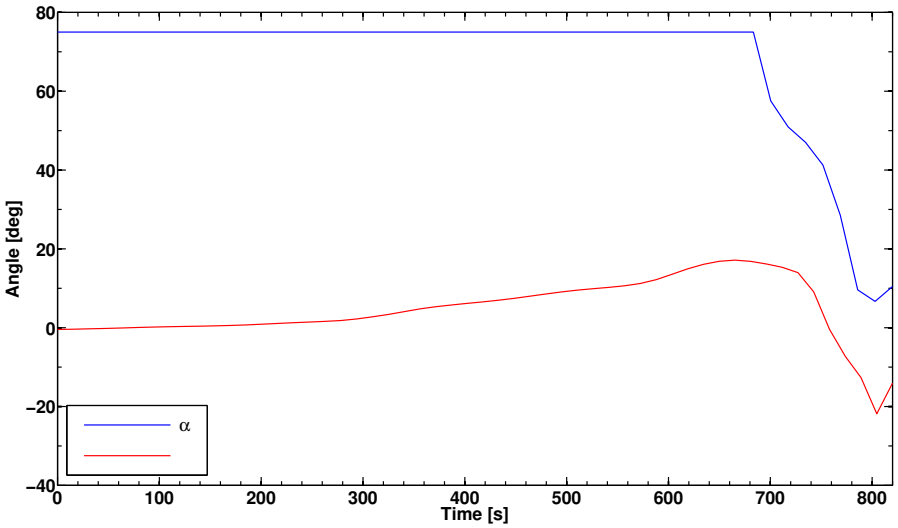

Figure 6.5: Nominal control law - Nominal schedule of bank angle and angle of attack.

the schedule of bank angle and angle of attack shown in Fig. 6.5 where the vehicle maintains a high incidence during a significant portion of its entry trajectory (thus increasing its deceleration in regions where the atmospheric density is quite low). This particular control law is adapted from the one that was optimally derived (121) to bring the vehicle from its re-entry point down to the Terminal Area Energy Management (TAEM) interface – i.e. the point along the trajectory which corresponds to the transition from the high angle of attack re-entry to aerodynamically controlled supersonic flight – while the total integrated heat load along the trajectory was minimized. A set of a thousand randomised atmospheric profiles, obtained by combining Eqs. 6.1-6.4 and the design margins derived in Section 6.2.2, has been used in order to perform a thousand integrations of the re-entry path of the representative CFASTT-1 vehicle (see description in previous chapter) using the aforementioned baseline control law. In an attempt to isolate the effect of variability in the atmospheric properties, it should finally be noted that these integrations have been performed by only accounting for inviscid pressure forces (i.e. neglecting viscous effects such as boundary layer transition).

The resulting perturbed trajectory profiles (blue lines) along with the nominal re-entry path followed by the vehicle (red line) are shown in Fig. 6.6. The distributions of the final states of the vehicle in the presence of variability in the temperature profile within the atmosphere are then depicted in Fig. 6.7 (altitude and velocity are presented). As sought, none of the re-entry paths meets the

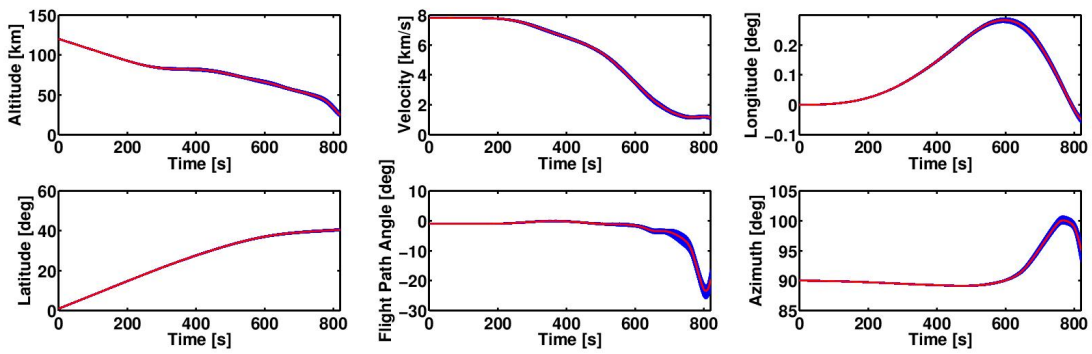

Figure 6.6: Perturbed trajectory profiles - Evolution of the states, where the bold red line refer to the nominal trajectory, and the blue lines refer to the trajectories which have been integrated in the presence of atmospheric perturbations.

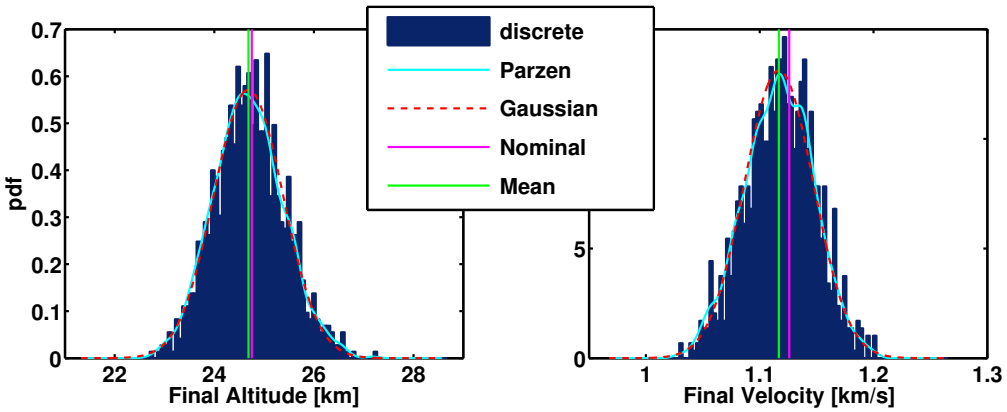

Figure 6.7: Altitude and velocity final states - Probability Density Function (PDF) of the final states when the nominal schedules of bank angle μ and angle of attack α are integrated using a perturbed atmospheric model.

nominal conditions (magenta line) when variability in the atmospheric properties is accounted for. Instead, the final states of the system are dispersed about the nominal, desired, target conditions following a quasi-Gaussian distribution (confirmed by the Parzen probability density function represented by the cyan blue line in Fig. 6.7) where in general the average values of the final states are lower than the nominal values, but the variance is widely different depending on the variable being considered.

For instance, the assumed variability in the atmospheric temperature profile results in a variance of approximately 3 km in the final altitude and 200 m/s in the final speed of the vehicle, a fact which may be of significant concern to the space transportation system's designers for example, if the vehicle is expected to

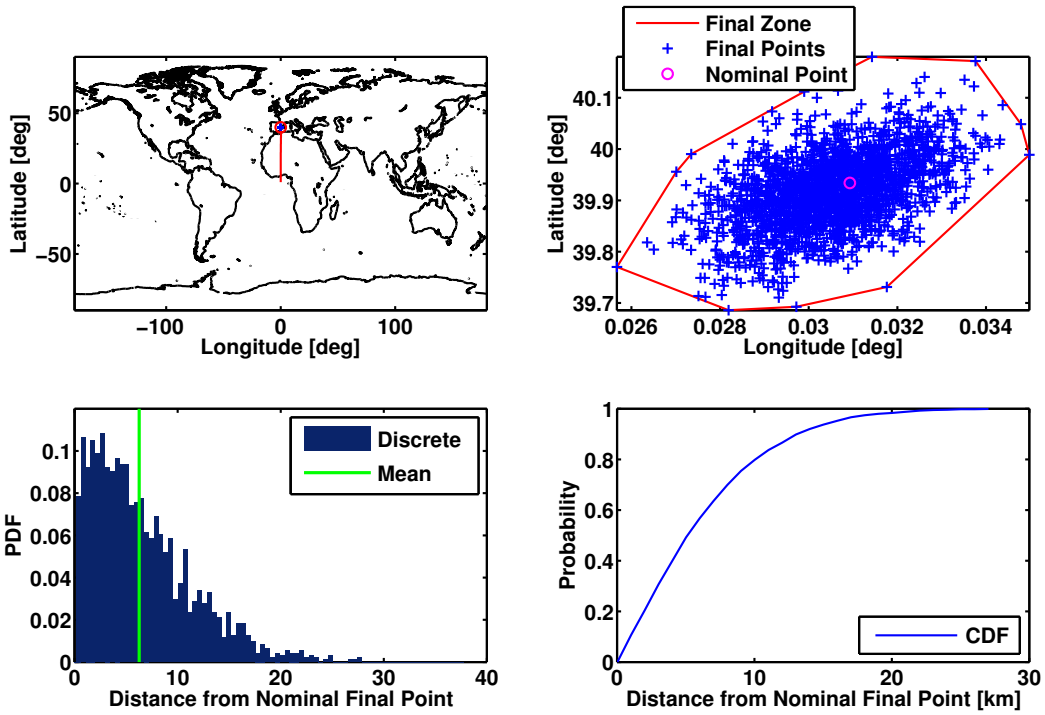

Figure 6.8: Latitude and longitude final states - Probability Density Function (PDF) of the final states when the nominal schedules of bank angle and angle-of-attack are integrated in the presence of perturbed atmospheric profiles (bottom-left). The top-right graph shows a "splash down" view of the geographical dispersion of final points as a result of those off-nominal atmospheric properties. The bottom-right graph represents the Cumulative Density Function (CDF) of the geodetic distance between the final TAEM points and the nominal desired final point.

interface precisely with air traffic management restrictions at the end of its flight. Similarly, the implications of the observed dispersion in longitude and latitude of the final point of the trajectory in Fig. 6.8 can only be assessed once the vehicle is placed into its broader operational context, but at least, by adopting the approach that is demonstrated here, the relevant data is available to the designer for further analyses.

For the example shown in Fig. 6.8, it can be seen that the geodetic distance d_f from the desired/targeted final point can vary by up to 30 km, as estimated by application of the Haversine formula (for a spherical Earth) given by

$$d_f = 2r \arcsin\left(\sqrt{\sin^2\left(\frac{\lambda_2 - \lambda_1}{2}\right) + \cos(\lambda_1)\cos(\lambda_2)\sin^2\left(\frac{\theta_2 - \theta_1}{2}\right)}\right) \tag{6.5}$$

where λ_i and θ_i are, respectively, the latitude and longitude of the nominal and perturbed final points, or up to 32 km when Vicenty's algorithm (141) is used instead to derive the geodetic distance over the surface of the Earth, represented as a WGS84 ellipsoid. Statistical analysis (i.e. Cumulative Density Function (CDF) plot in Fig. 6.8 – see bottom-right) then suggests that if the assumed variability in atmospheric properties is accurate, then designing the system to operate with the previously prescribed (nominal) control law would result in the vehicle having a 50% likelihood of being at least 8 km away from its predicted final point, which as discussed previously could potentially lead to air-traffic management issues.

Nonetheless, the study performed by Pescetelli *et al.* (121) has confirmed that the re-optimisation of the nominal control law in the presence of perturbed atmospheric quantities (i.e. using the randomised atmospheric profiles) might be sufficient to guarantee convergence towards the originally targeted final states.

6.3 Boundary Layer Transition

It is well known that the aerodynamic heating experienced by an RLV during re-entry can increase by a factor of two to eight when the boundary layer on the vehicle's surface undergoes a transition from laminar to turbulent flow (142). The physical models used to characterize the parameters that influence transition (see Eq. 2.42) are subject to errors and uncertainties too. These uncertainties are usually a consequence of miscellaneous combined factors that include inherent assumptions, lack of knowledge, lack of corroborative experimental and flight data, application of models beyond their validated range, and other sources of errors that have been accepted, perhaps if only in the interest of developing a convenient and rapid design methodology such as that described throughout Chapter 2. The physical models that are used are thus often subject to a large inherent uncertainty which may lead in practice to large discrepancies between predicted and in-flight values of important parameters such as instantaneous heat flux, integrated heat load, or viscous drag.

Therefore, the prediction of boundary layer transition becomes a complicated task (for the aerodynamicist) at hypersonic speeds since this phenomenon is affected by a very large number of parameters which are difficult to either determine or evaluate. Indeed, under re-entry conditions, although the flow over the windward

surface of a space-access vehicle should ostensibly be laminar, the particular form of TPS used, and indeed its manufacturing process, can affect the roughness and temperature at the surface of the vehicle. In theory, premature transition of the boundary layer from laminar to turbulent flow is triggered by the resultant local increase in the effective Reynolds number of the flow near the surface of the vehicle. In practice however, the degree to which the surface is roughened, or how the roughness of the surface influences the properties of the flow is, *a priori*, not always easy to determine (e.g. because of randomly scattered defects on the heat shield as a result of micro-meteoroid impact, manufacturing defects and tolerances, etc...). The Shuttle Transportation System (STS) was particularly susceptible to this syndrome. For instance, on Shuttle flight STS-50, a measurable amount of extra propellant had to be used to correct the yawing moment that resulted from an asymmetrical boundary layer transition on the leeward surface of the vehicle. During mission STS-114, an unprecedented space-walking repair even had to be carried out in order to remove the threat posed by two forward-located, dislodged, gap fillers (i.e. pieces of ceramics located between TPS tiles) which could have potentially affected the integrity of the TPS in the case of an early onset of transition during re-entry (143).

Because of these issues, the planning of the re-entry path followed by an RLV as well as its performance from its high-angle-of-attack re-entry down to its landing site are highly dependent on accurate prediction of the transition from laminar to turbulent flow. The validity and robustness of the results of the optimisation are thus intrinsically linked to the accurate prediction of laminar-turbulent transition. In fact, in the National Aerospace Plane Review published by the Defense Science Board in 1992 (144), it was stated that estimates of the transition location could range from 20% to 80% along the body length and could thus affect the designed vehicle Gross Take-Off Weight (GTOW) by a factor of two or more. Indeed, since fully turbulent analysis does not permit accurate predictions of thermal gradient and results in excessive TPS weight penalties, and since fully laminar analysis can lead to under-design of the TPS with resultant impact on vehicle survivability in the hypersonic flight environment, it is of paramount importance that numerical optimisation tools represent the phenomenon of boundary layer transition properly in order to provide confidence in the robustness of the design of future RLVs from the earliest stages of their conceptual evolution.

In the following Section 6.3.1, the nature of the uncertainty that may trigger an early onset of boundary-layer transition will first be described. Thereafter, in

Section 6.3.2, the effect of atmospheric variability on the smooth-surface transition correlation, presented in Chapter 2, will be discussed through an additional Monte-Carlo analysis. Finally, the effects and risks implied by the roughness-induced transition phenomenon on the likely performance of future space-access vehicles will be demonstrated in Section 6.3.3.

6.3.1 Definition of Transition Uncertainty

Laminar-turbulent transition intrinsically encompasses the two types of uncertainty described in Section 6.1. The first one is the *stochastic* uncertainty: the windward surface of future re-usable space-access vehicles will, in all likelihood, be comprised of overlapping, sharp-cornered panels made out of very-high-temperature resistant materials (indeed, thermal expansion considerations will, most probably, limit panel size). Under repeated use, these panels might eventually yield a pattern of asperities with edges that protrude into the local flow (56). These protective panels might also bow under the aero-thermal loads of re-entry. This could potentially result in premature transition from a laminar state to turbulence and could, in turn, lead to downstream surfaces being subjected to a more severe heating environment (and skin friction) than might otherwise be the case. Another major source of uncertainty for hypersonic vehicles is often the extent to which the condition of the TPS surface has deteriorated in flight prior to transition, or indeed prior to or during launch as a result of manufacturing and maintenance errors. Finally, boundary-layer transition comprises the *epistemic* type of uncertainty which is the result of the lack of knowledge that arises from the use of possibly inadequate physical models in the representation of the boundary layer transition phenomenon. Indeed, as discussed in Section 2.5, there is no universal value for the transitional Reynolds number Re_t, and the inherent uncertainty in predictions that results from the evaluation of this parameter, for instance through correlations such as Eq. 2.43, needs to be be quantified in order to obtain a measure of the robustness of the current design process.

6.3.2 Smooth-Surface Transition

Natural variations in the atmospheric pressure P_∞ and temperature T_∞ (previously discussed in Section 6.2), through their effect on the flow conditions at

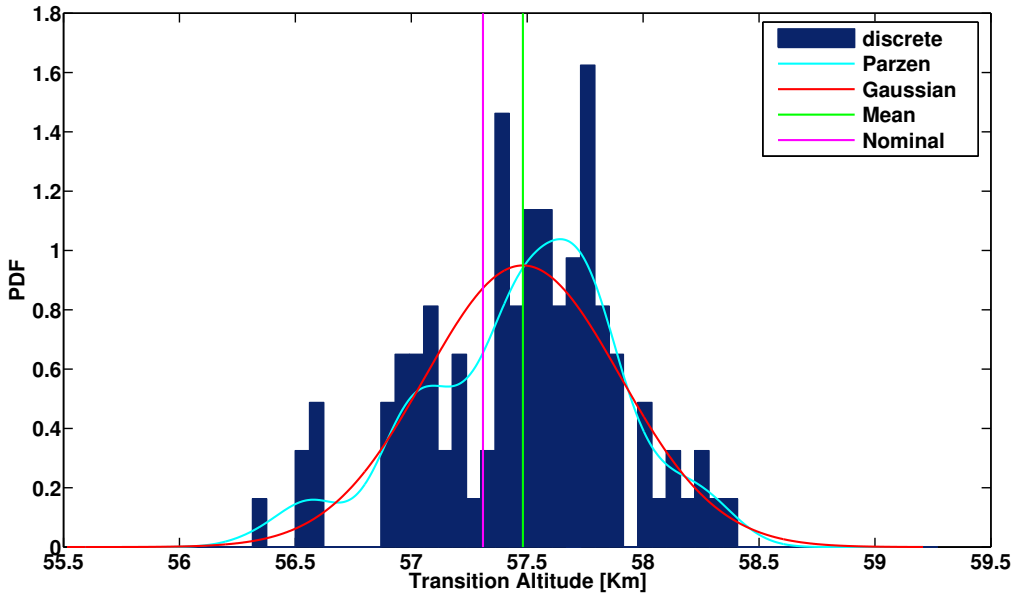

Figure 6.9: Smooth-surface transition altitude - Result of a Monte-Carlo simulation with 1,000 sample re-entry trajectories to estimate the effect of variability within the atmospheric temperature profile on the altitude at which smooth-surface transition of the boundary layer on the surface of the CFASTT-1 vehicle is triggered.

the edge of the boundary layer, are major sources of uncertainty when predicting the onset of laminar-turbulent transition (see Section 2.4.2). Uncertainty in these parameters of course has an impact on the inherent uncertainty in many other parameters within the atmospheric model, for instance the speed of sound a_∞ and the density ρ_∞ through the gas equation of state. By perturbing the outputs of the atmospheric model, uncertainty is therefore generated within the aerodynamic model through its inputs, such as the Mach number M_∞ and dynamic pressure Q_∞. By this means, the atmospheric uncertainty is propagated into the various models for boundary layer transition that are embedded within the HyFlow reduced-order model, and most notably into the conditions at the edge of the boundary layer, such as M_{edge}, whose derivations are presented in Section 2.4.2.

Stochastic Simulations

A Monte-Carlo simulation consisting of 1,000 different re-integrations of the re-entry trajectory with the nominal control law and randomizing the atmospheric

temperature profile (see Section 6.2.3) was performed to examine the effect of uncertainty in the atmospheric conditions pertaining during re-entry on the altitude at which the first onset of smooth-surface laminar-turbulent transition takes place on the surface of the vehicle, thus on its aerodynamic performance and subsequently on its ability to satisfy its mission objectives. Bearing in mind the various assumptions within the models, the effect of uncertainty in the atmospheric temperature, shown in Fig. 6.9, appears to create a quasi-Gaussian distribution of transition altitudes about the nominal height for transition (predicted here to be about 57.3 km) with a slight bias towards transition taking place at a higher than nominal altitude (the distribution mean is predicted to be about 57.5 km and the most likely value about 57.7 km (see Parzen PDF in the figure in question), bearing in mind the limitations of the relatively small sample size in identifying these values accurately). Since smooth-surface boundary layer transition occurs at such low altitudes on a vehicle with this configuration, its effect (in isolation) on the heating rates experienced by the vehicle are minimal. The resultant effect on the maximum heat flux experienced by the vehicle during its re-entry is shown in Fig. 6.10, where the stagnation instantaneous heat flux resulting from the presence of variability in the atmospheric thermodynamic properties is plotted. This figure suggests however a non-negligible effect of atmospheric variability (and, to a lesser extent, smooth-surface transition) on the level of aerodynamic heating experienced at transition. Indeed, values may range from 410 kW/m^2 to 470 kW/m^2 as shown in the figure in question.

6.3.3 Roughness-Induced Transition

Additional variability is introduced into the transition model if, in addition to smooth-surface transition, transition from laminar to turbulent flow can also take place through the formation of turbulent wedges on the surface of the vehicle as described in section 2.5.2. This may occur as the result of the presence of localized elements of roughness on the surface of the vehicle. The creation of these turbulent wedges can be triggered, during trajectory integration for instance, when the local roughness Reynolds number written in the form of a criterion suggested by Reda (56) is defined as

$$Re_{k_r} = \left(\frac{\rho_{k_r} \, U_{k_r} \, h_{wedge}}{\mu_{k_r}} \right) \tag{6.6}$$

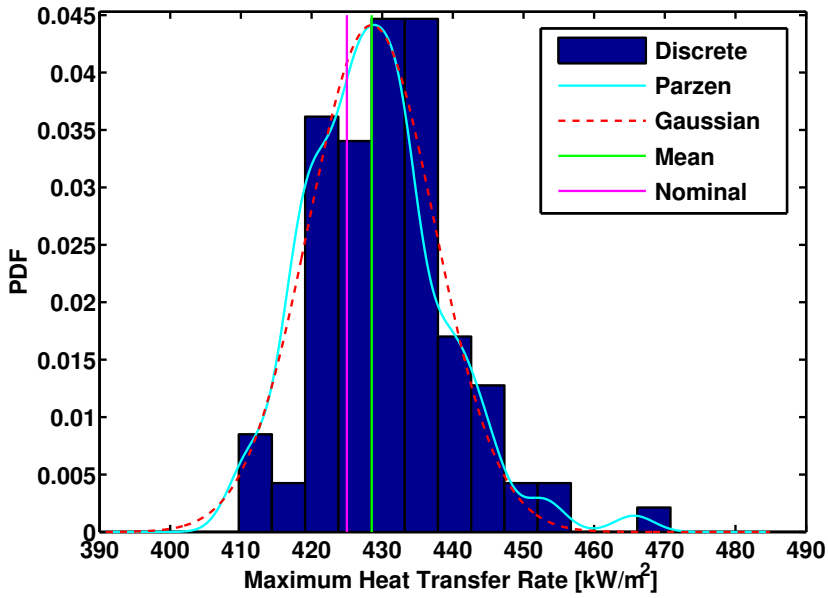

Figure 6.10: Peak heat transfer rate - Result of a Monte-Carlo simulation with 1,000 sample re-entry trajectories to estimate the effect of variability within the atmospheric temperature profile on the maximum heat flux experienced by the CFASTT-1 vehicle.

satisfies the criterion $Re_{k_r} \geq 300$, where h_{wedge} is the height of the surface roughness element that was responsible for causing the turbulent wedge in the first place. Furthermore, as suggested by Passaro and Baccarella (145), a complete transition, where the turbulent flow remains attached to the roughness element, is found only when, in addition to the previous criterion, the two conditions $M_{edge,kr} \geq 1$ and $h_{wedge}/\delta_L > 0.45$ are also satisfied, where δ_L represents the height of the laminar boundary layer that can be predicted using an empirical flat plate formula such as that suggested by Bowcutt (63)

$$\delta_L = 4.64 \frac{x_L}{\sqrt{Re^*}} \sqrt{\frac{\mu^* \ T^*}{\mu_{edge} \ T_{edge}}} \tag{6.7}$$

Finally, it shall be remarked that the development of the turbulent wedge region is considered instantaneous in the present work and occurs as soon as the previously defined conditions are met (i.e. the rate of growth of the turbulent wedge has indeed been neglected after conceding that its influence on the results would be small). Therefore, the characterization of the sensitivity of the design of a representative re-usable space transportation system (the CFASTT-1 vehicle

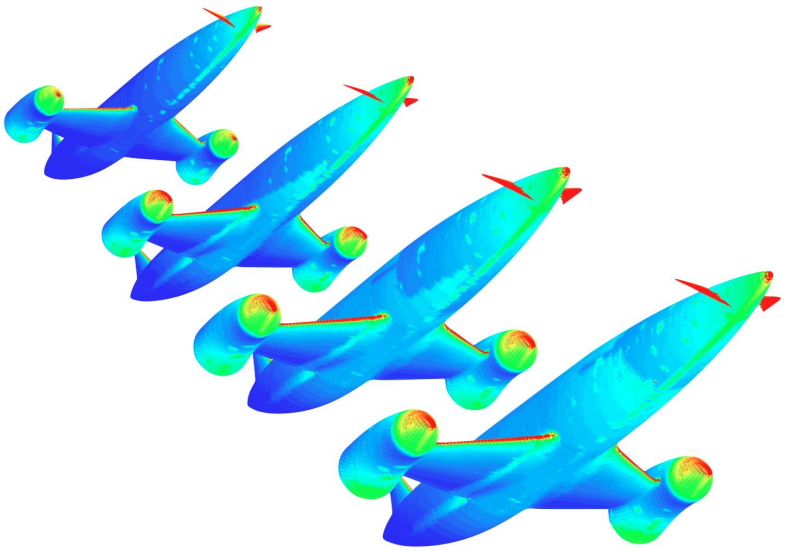

Figure 6.11: Turbulent-wedge formation along the re-entry trajectory - An illustration of the effect of the turbulent wedge model on the HyFlow-predicted surface heat transfer rates of the Skylon SSTO vehicle at various points along its re-entry trajectory. The calculation starts from a fully laminar flow (top left), before a turbulent wedge appears (middle). The wedge develops, subsequently to merge into the "smooth-surface" turbulent flow that envelops most of the surface of the vehicle towards the end of its trajectory (bottom right).

is again used in this section) to the effects of roughness-induced transition – as possibly exacerbated by uncertainty in the atmospheric conditions – can be phrased as an optimal control problem and divided into three distinct steps:

1. First, an optimal design of a nominal trajectory for the representative RLV, where the effect of roughness-induced boundary layer transition is neglected, is determined.

2. Then, the perturbation to the nominal trajectory, that results from the presence of roughness-induced transition, is computed.

3. Finally, the optimal scheduling of control surface deflections, that enables the vehicle to fly the desired nominal trajectory even in the presence of roughness-induced transition, is derived.

For present purposes, the optimal control law introduced in Fig. 6.5 is again used, and the resulting nominal trajectory (with viscous effects) shown in Fig. 6.12.

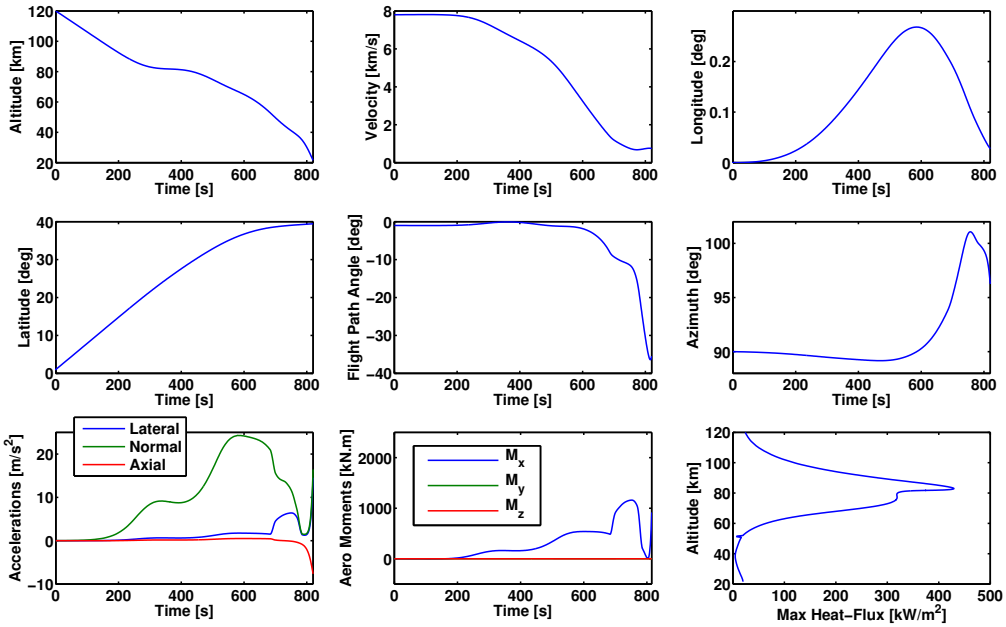

Figure 6.12: Nominal re-entry trajectory - Nominal re-entry trajectory of the CFASTT-1 vehicle governed by the optimal control law in Fig. 6.5 – i.e. non-trimmed trajectory, see moments (middle-bottom plot).

Then, a statistical picture of the robustness of the design can be built up by performing a Monte-Carlo analysis in which elements (2) and (3) above are repeated a large number of times, each time sampling the parameters governing the position and character of the onset of roughness-induced transition from their appropriate statistical distributions. The number of turbulent wedge regions, as well as the geometrical extent of each such region on the vehicle surface, is then updated at each time-step throughout the re-entry simulation. The effect of each wedge on the local aerodynamic loads and heat flux is accounted for until the smooth-surface turbulent region merges with and subsumes the roughness-induced turbulence (see Fig. 6.11). The effect of asymmetric transition through the mechanism of turbulent wedge formation is to temporarily unbalance the aerodynamic forces on the vehicle. The resultant aerodynamic moments must then be counteracted by appropriate deflection of the control surfaces. The trimming of the aerodynamic moments in this way might increase the overall drag on the vehicle with concomitant effects on its re-entry trajectory. In addition, the local increases in aerodynamic heating that result from the presence of surface roughness may have to be accommodated into the constraints that are applied within the trajectory planning procedure (see Chapter 5).

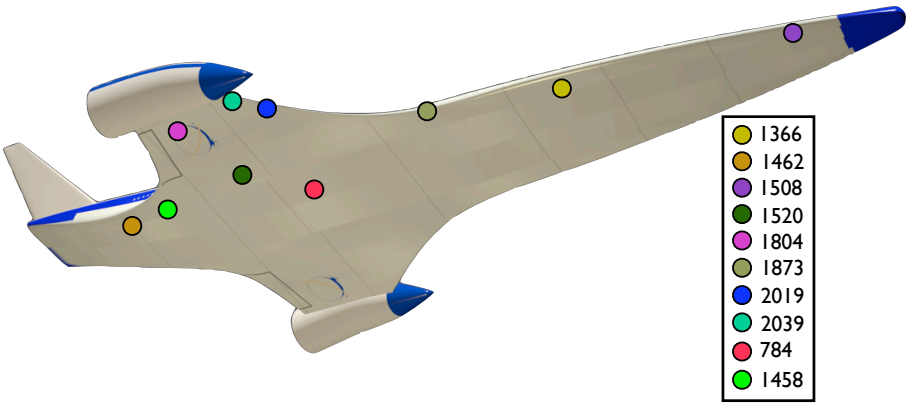

Figure 6.13: Windward locations of the elements of surface roughness - The locations of the various simulated surface asperities used to trigger the onset of roughness-induced laminar-turbulent transition.

Stochastic Simulations

To provide a proof of concept, a relatively small set of 20 distinct trajectories were generated with an element of surface roughness located at various locations on the right side of the under-surface of the vehicle as depicted in Fig. 6.13. Calculations were repeated for elements with height $h_1 = 4$ cm and $h_2 = 6$ cm in order to examine the sensitivity of predictions to the size of the surface asperities that might be responsible for transition. The effect of the resultant turbulent wedge regions on the controllability of the vehicle was evaluated in terms of the perturbations from nominal, denoted ΔM, that the presence of the turbulent wedge induced in the aerodynamic moments acting on the vehicle. The resultant evolution along the trajectory of the perturbations about the pitch, yaw and roll axes, for the various roughness locations that were considered, is presented in Fig. 6.14. As can be seen, the direct effect of the presence of roughness-induced transition is to introduce an additional contribution to the shear force on the surface of the vehicle, which, if asymmetrically located with respect to the centre of mass, temporarily unbalances the aerodynamic forces acting on the vehicle and must be counteracted by an additional deflection of the control surfaces away from their nominal positions. The influence of the height of the roughness element, h_{wedge}, is to modify the time at which the onset of transition of the boundary layer takes place. Indeed, for a roughness element with height $h_1 = 4$ cm, the earliest time of occurrence of transition is predicted to be about 635 s (i.e. with the vehicle at an altitude of about 60 km compared to the 57 km or so at which

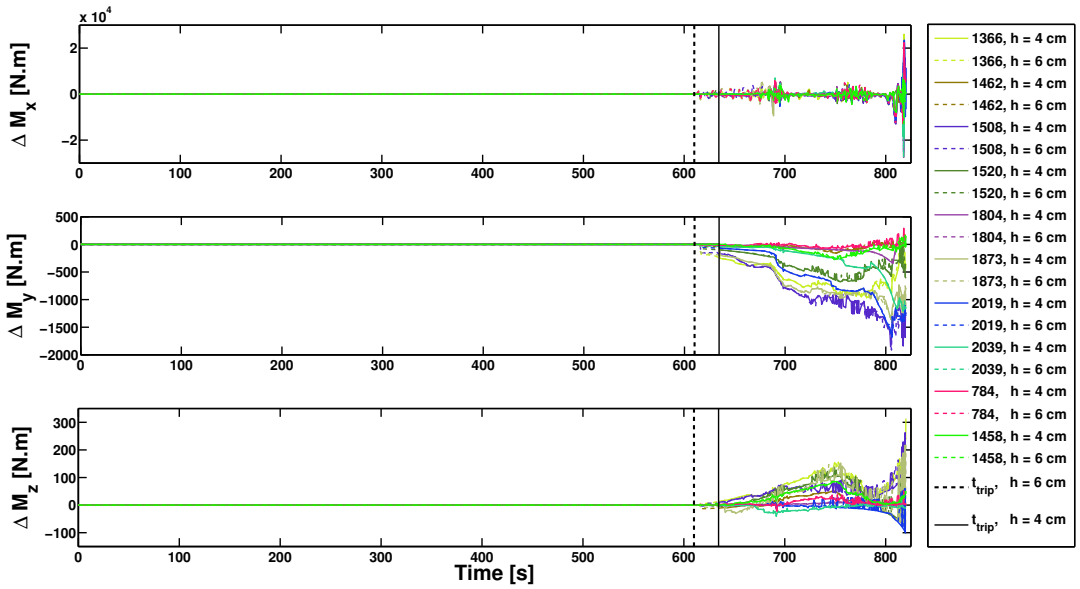

Figure 6.14: Perturbed aerodynamic moments - Perturbations to the nominal aerodynamic moments in the presence of roughness-induced boundary layer transition on the surface of the vehicle: pitch moment ΔM_x, yaw moment ΔM_y, roll moment ΔM_z.

smooth-surface transition takes place as seen in the previous Section 6.3.2), while if the characteristic height of the local surface asperity is increased to 6 cm, the formation of turbulent wedges can occur somewhat earlier (at about 610 s into the descent, with the vehicle at an altitude of about 65 km). This behaviour is fully consistent with experience on vehicles such as the American Space Shuttle. As expected, the presence of a roughness element located close to the centreline, e.g. element 784 in Fig. 6.14, has very little influence on the overall aerodynamic characteristics of the vehicle, while, as can be seen in the same figure, if the roughness is located slightly further off the centreline, e.g. elements 2019 and 1508 in Fig. 6.13, the region of turbulent flow within the resultant turbulent wedge can be responsible for a significant increase in moment about the centre of mass of the vehicle. As the vehicle descends, the wedge continues to develop, its apex angle changing with Mach number according to Eq. 2.44. The resultant steady increase in the effects of the turbulent wedge, as the vehicle decelerates, is clearly visible in the trend of the data, as is the point at which the the smooth-surface turbulent region starts to subsume the turbulence in the wedge and hence the loads on the vehicle start to fall back towards their nominal values. The growth of the smooth-surface turbulent region is not fast enough in all cases, however, to fully subsume the effects of the turbulent wedges by the time the vehicle reaches

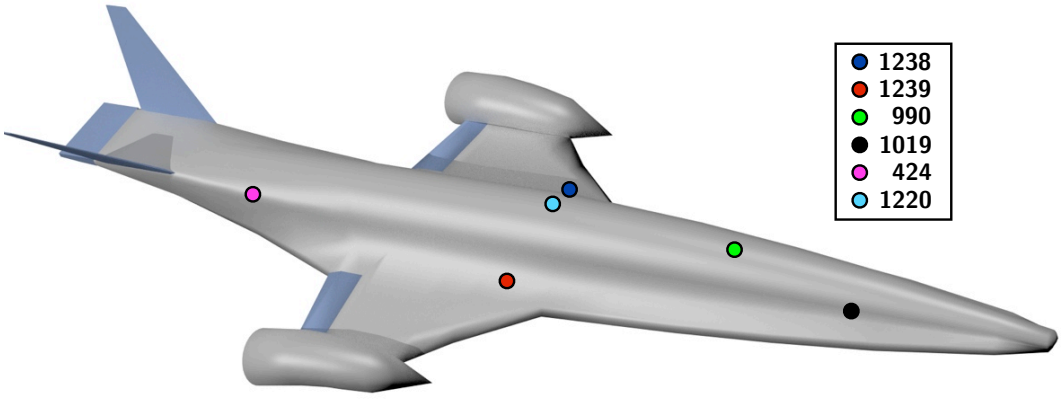

Figure 6.15: Leeward locations of the elements of surface roughness - The CFASTT-1 space-access vehicle with its control surfaces (in blue). Furthermore, the various elements of surface roughness located on the leeward side of the vehicle that have been used in the present uncertainty analysis are also depicted.

the terminal point of its trajectory. Indeed, at the TAEM interface only about 75% of the flow over the surface of the vehicle is predicted by the HyFlow model to be fully turbulent, implying that the effects of roughness-induced transition could potentially persist on into the terminal and possibly the landing phases of the mission. Nonetheless, a much larger sample size of perturbed trajectories profiles would have to be investigated before these remarks may be confirmed.

Roughness-Induced Transition on the Leeward Side

As discussed in the introduction of the present section, on the STS-50 mission, an asymmetrical boundary layer transition was triggered over the leeward side of the vehicle; the concomitant effect was an additional yawing moment acting on the vehicle. Therefore, for the sake of completeness, an additional set of trajectory integrations has been performed in the present section to determine the effect of roughness-induced transition when the element of surface roughness (the height of which was here assumed equal to 6 cm to maximize the resulting effects) is located on the leeward surface of the vehicle (see Fig. 6.15). The resultant evolution along the trajectory of the perturbations about the pitch, yaw and roll axes, for these various roughness elements located in the shadow region is presented in Fig. 6.16. As can be seen from the figure in question, the perturbations in aerodynamic moments are, as is to be expected, quite small in comparison to those when the roughness element is instead placed on the windward surface of the vehicle. It can

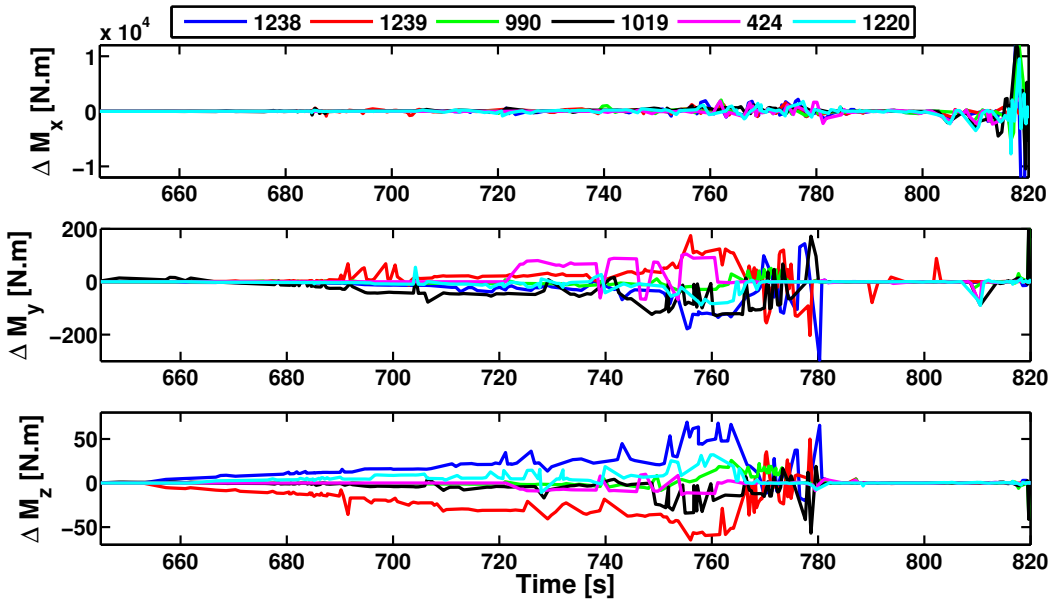

Figure 6.16: Perturbed aerodynamic moments as a result of the presence of a roughness element on the leeward side of the vehicle - Perturbations to the nominal aerodynamic moments in the presence of roughness-induced boundary layer transition on the leeward surface of the vehicle: pitch moment ΔM_x, yaw moment ΔM_y, roll moment ΔM_z. It shall be noted that the horizontal axis starts from the turbulent wedge formation time at $t = 645$ s.

also readily be seen from the same figure that the roughness-induced transition occurs slightly later on that side of the vehicle, i.e. at about $t = 645$ s. As opposed to the previous windward case, the effect of the disturbances in yawing and rolling moments seem to be fully annihilated – at about $t = 785$ s – by the smooth-surface transition (as it fully subsumed the region delimited by the turbulent wedge) while those in pitching moment persist, most likely as a result of a slight change in the vehicle's entry trajectory.

Controls Scheduling in the Presence of Roughness-Induced Transition

The controls of the CFASTT-1 SSTO vehicle (see Fig. 6.15) are comprised of two fins arranged in a butterfly configuration at the rear of the fuselage, which are used both for yaw and roll control, as well as for pitch control in low-speed flight. The rear fuselage, flattened into a pen-nib shape, accommodates a rear beaver-tail control surface *à la* Space Shuttle for pitch attitude control during re-entry. Finally, two elevons are attached to the trailing edge of the wings for

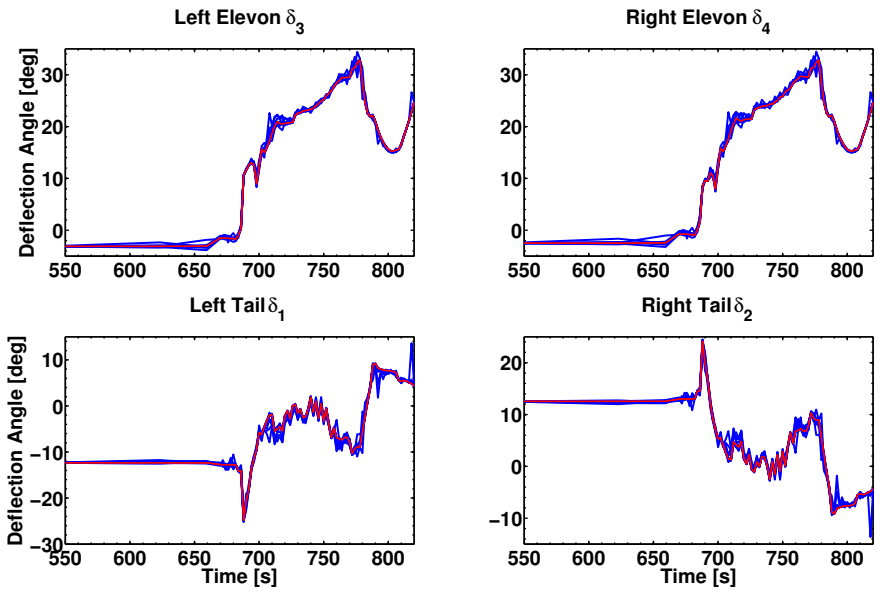

Figure 6.17: Perturbed controls - Scheduled deflections of the elevons and rear fins in the presence of roughness-induced boundary layer transition on the windward side of the vehicle (Blue). Nominal control surface deflections shown in Red.

additional pitch and roll control.

As a means of quantifying the aerodynamic and performance penalties on the vehicle that accrue from the formation of turbulent wedges on its surface, the scheduling of the control surface deflections required to fly the nominal trajectory when accounting for the presence of roughness-induced transition was calculated using the approach outlined below: the control vector, denoted c_δ, is first defined as

$$c_\delta = \{\delta_i\} \tag{6.8}$$

where δ_i controls the rotation angles of the flight controls. The optimal scheduling of the control surface deflections $\{\delta_i\}$ is then defined as the solution to the multi-objective point-wise optimisation problem which aims to minimize the aerodynamic penalties induced by control deflection while providing the desired attitude to the space-access vehicle.

$$\min_{c_\delta \in D} = \|\hat{M}_{controls} - \hat{M}_{nom}\| \tag{6.9}$$

$$\min_{c_\delta \in D} = \|P_{nom} - P\| \tag{6.10}$$

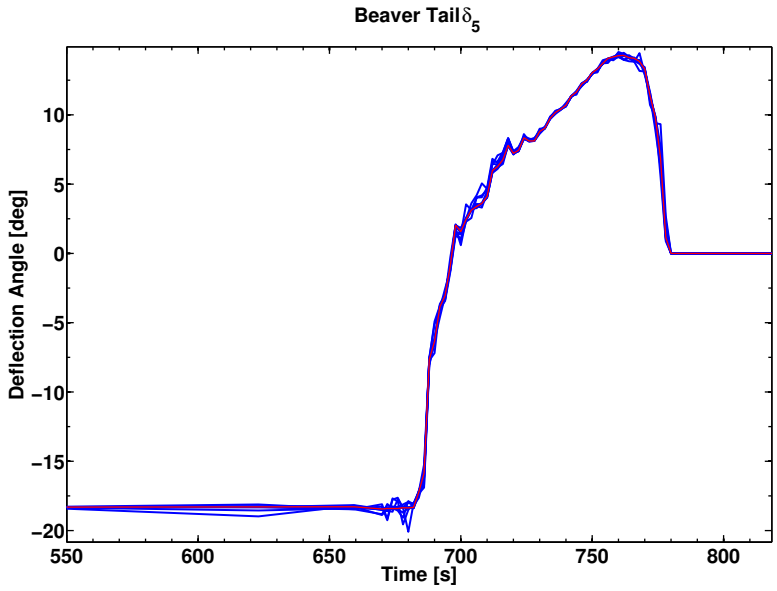

Figure 6.18: Perturbed beaver control - Scheduled deflections of the beaver tail in the presence of roughness-induced boundary layer transition on the windward side of the vehicle (Blue). Nominal control surface deflections shown in Red.

where M_{nom} is the aerodynamic moment that is required to generate the rotational dynamics of the vehicle that are consistent with its desired nominal trajectory (see desired aerodynamic moments in Fig. 6.12 – bottom-middle plot – obtained using the method described in Section 4.2.3) and $M_{controls}$ is the aerodynamic moment that is generated by the vehicle with the control surfaces deflected (as computed by the HyFlow model). Similarly $P_{nom} = (L/D)_{nom}$ and $P = (L/D)$ are, respectively, representative measures of the aerodynamic performance of the vehicle under nominal conditions, and where deviations from nominal conditions along the trajectory (for example, due to perturbations in the atmospheric conditions or variability in the aerodynamic loads as a result of uncertainties in the position and time of boundary layer transition) might possibly require the controls to be deflected by an additional amount. This second, disturbance rejection, element to the optimisation in effect biases the scheduling of the control surfaces towards a solution that, even in the presence of aerodynamic perturbations, keeps the trajectory of the vehicle as close as possible to its nominal optimal trajectory.

The results of this analysis are shown in Fig. 6.17 and Fig. 6.18 (considering the windward cases only as those displayed the most important disturbances),

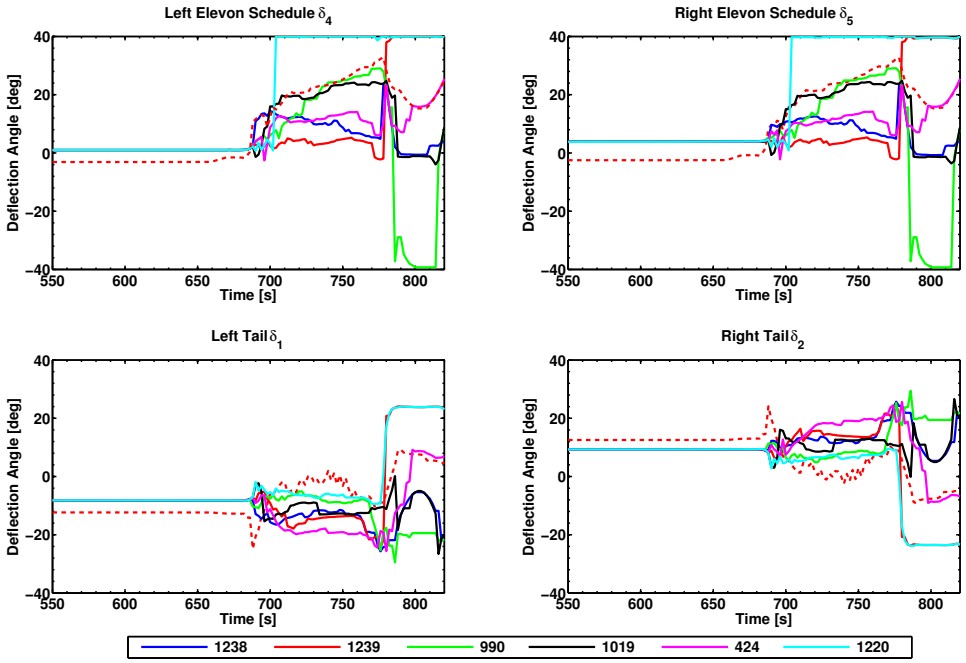

Figure 6.19: Perturbed controls as a result of the presence of a roughness element on the leeward side of the vehicle - Scheduled deflections of the elevons and rear fins in the presence of roughness-induced boundary layer transition on the leeward side of the vehicle (Blue). Nominal control surface deflections shown in Red.

which focus on that part of the trajectory post-transition i.e. from $t = 550$ s to $t = 820$ s (since before that, the attitude of the controls remains of course un-changed). As depicted, the nominal control schedules (in red) are perturbed to some extent in counteracting the additional aerodynamic loads that are induced by the increased viscous stresses acting on the vehicle within the turbulent wedges. Although the resultant perturbations to the nominal deflections seem rather small in most cases, there are some short-lasting events during which the control deflections required to overcome transient moments induced on the vehicle by the turbulence are indeed quite large compared to their nominal values (the tail deflections close to the very end of the trajectory are a case in point), and on the basis of this information a prudent engineer would most likely order a more in-depth characterization of the unsteady aerodynamic loads on the vehicle before prescribing design limits on the deflections of the control surfaces. Indeed, as suggested by Bowcutt, it must be checked that trim (to counteract any in-flight disturbance) does not employ more than half of the total available control deflection in order to ensure adequate control power for hypersonic vehicles (146).

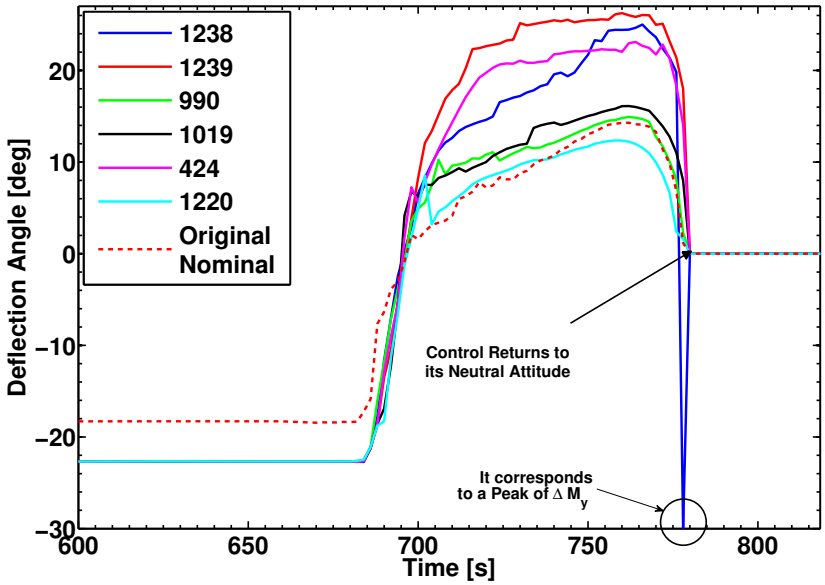

Figure 6.20: Perturbed beaver control as a result of the presence of a roughness element on the leeward side of the vehicle - Scheduled deflections of the beaver tail in the presence of roughness-induced boundary layer transition on the leeward side of the vehicle (Blue). Nominal control surface deflections shown in Red.

Controls Scheduling in the Presence of Roughness-Induced Transition on the Leeward Side

The influence of the boundary layer transition induced by a element of surface roughness on the leeward side of the vehicle has been investigated. The previous optimal control scheduling problem has thus been solved again but this time with the fully developed turbulent criterion (see Section 6.3.3) the effect of which is to slightly delay the development of the turbulent wedges as compared to the previous windward analysis. It is here shown that roughness-induced transition on the leeward side of the vehicle may have a non-negligible effect on the scheduling of control surfaces, as depicted in Figs. 6.19 and 6.20. Indeed, in Fig. 6.20 the trend followed by the perturbed beaver tail control deflection angles shows an increase in the amount of deflection required by up to 10 degrees (approaching the pre-defined upper bound of the control surface). The schedule of deflection angles followed by the beaver tail as a result of an element of surface roughness at the location labelled 1238 (i.e. at about $t = 775$ seconds where $\delta_3 = -30$ deg) is seen to correspond to a peak perturbation in yawing moment and is

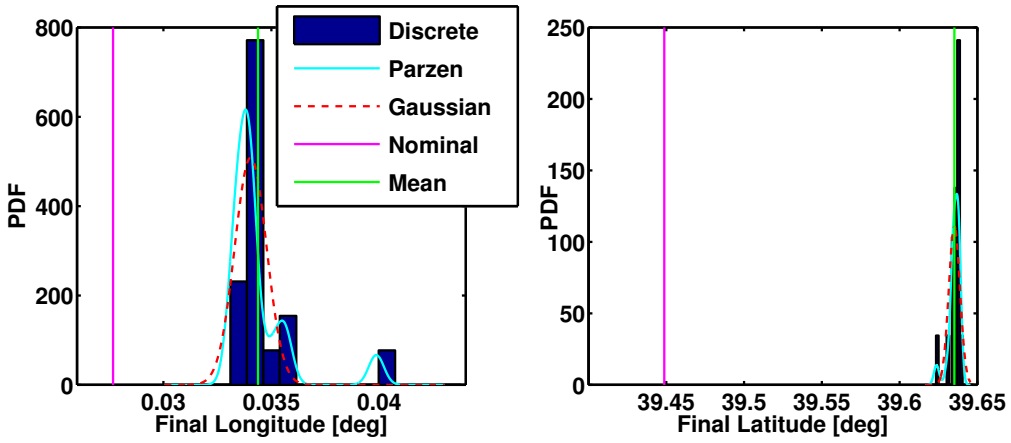

Figure 6.21: Latitude and longitude final states with roughness-induced transition - Results of the integration of twenty-six sample re-entry trajectories to estimate the effect of surface roughness-induced transition of the boundary layer on the aerodynamic performance of the CFASTT-1 vehicle, showing the resultant spread of final longitudes and latitudes about the nominal.

therefore believed to be the result of a numerical error as the beaver tail is only responsible for the control of the pitch attitude of the vehicle (see Fig. 6.16). In Fig. 6.19, the original nominal trend (dotted red line) is properly followed by the perturbed control profiles apart from at a small number of points along the re-entry trajectory. In fact, the roughness elements 1220, 1239 and 990 induce some "*interesting*" behaviours at a number of points along the entry path. For instance, in the 990 case, both elevons reach their full deflection state (i.e. $\delta_{1,2} \approx -40$ degrees) when the beaver tail starts to become aerodynamically shadowed and is thus commanded to return to its neutral condition.

Resulting Trajectories

To gain an appreciation of the effects of roughness on the performance of the system that result through the direct imposition of the additional viscous loads on the vehicle as well as through the secondary mechanism of the additional aerodynamic force (principally drag) that results from the deflection of the control surfaces, the dispersion of final latitude and longitude that result from calculating the re-entry trajectories with roughness-induced transition accounted for is plotted in Fig. 6.21. Although the statistics for the performance of the vehicle in the presence of roughness-induced transition are extremely sparse as yet, given the computational effort required to generate them even with a reduced-order model,

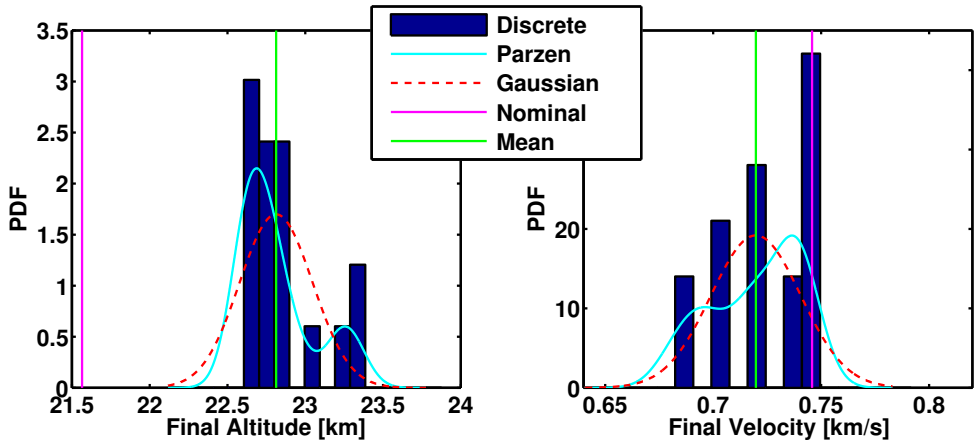

Figure 6.22: Altitude and velocity final states with roughness-induced transition - Results of the integration of twenty-six sample re-entry trajectories to estimate the effect of surface roughness-induced transition of the boundary layer on the aerodynamic performance of the CFASTT-1 vehicle, showing the resultant spread of final longitudes and latitudes about the nominal.

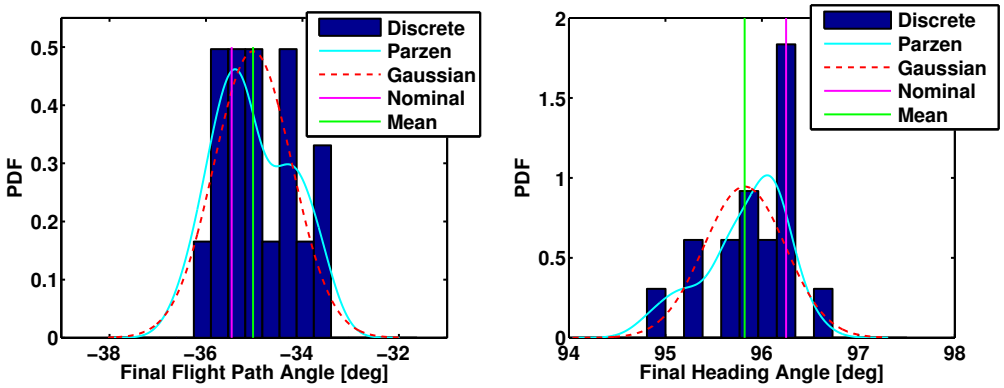

Figure 6.23: Flight path angle and heading angle final states with roughness-induced transition - Results of the integration of twenty-six sample re-entry trajectories to estimate the effect of surface roughness-induced transition of the boundary layer on the aerodynamic performance of the CFASTT-1 vehicle, showing the resultant spread of final longitudes and latitudes about the nominal.

a comparison with the results shown in Fig. 6.8 (top-right figure), where only smooth-surface transition was accounted for, is rather illuminating. Although the scatter of the predictions in the two cases is comparable, the data, as sparse as it is, seems to reveal a small but consistent bias towards an increase in the final longitude and latitude attained by the vehicle when the presence of roughness-induced transition is accounted for. Furthermore, the variation of final altitude and velocity as well as that of final flight path angle and heading angle that re-

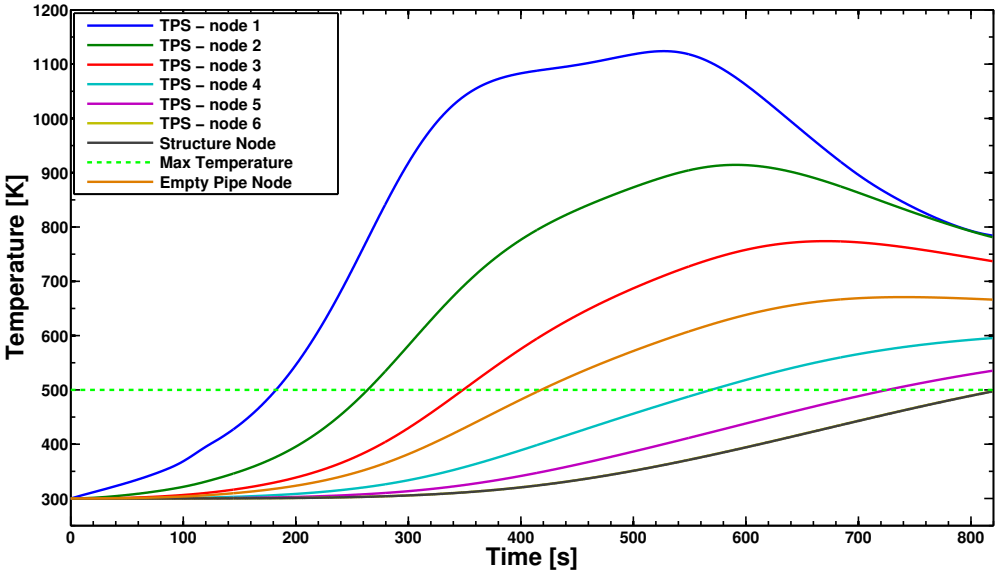

Figure 6.24: Nominal thermal performance - Thermal performance of a passive TPS with a nominal optimal thickness of about 9.7 cm as predicted by the hybrid TPS model described in Section 4.3.1. An empty pipe node (i.e. ghost node) is used in order to apply the hybrid TPS panel model designed in Section 5.2.3 in its passive mode.

sult from calculating the re-entry trajectories with roughness-induced transition accounted for are respectively plotted in Figs. 6.22 and Figs. 6.23. As can be seen in Fig. 6.22, the small increase in drag that is caused by the extra deflection of the controls results in an additional reduction of the final speed of the vehicle.

6.4 Thermal Analysis

The effects of uncertainty in both the properties of the material used to fabricate the passive insulation layers and in the intrinsic parameters of an Active Thermal Management Unit (ATMU) are discussed in Section 6.4.1 and in Section 6.4.2 respectively.

6.4.1 Material Thermo-Optical Properties

Variability in the thermal properties of the materials used to construct the TPS of the vehicle can have a significant impact on the temperature that its surface attains during operation (86). Indeed, in order to avoid any unexpected behaviour

of the materials being used for the thermal shield of the Space Transportation System (STS), the thermal properties of the protective tiles were measured in a number of laboratories – i.e. commercial laboratories, aerospace companies, and government facilities – using various techniques in order to minimise experimental uncertainty (i.e. it emphasizes even further the critical and utmost importance of the TPS design in hypersonic vehicle development programmes). All these experimental data were then compiled to define a set of average properties that could be used for design purposes. However, because of (1) extended thermo-optical properties are not available in the open literature for materials that may equip future trans-atmospheric vehicles, either for materials with relatively Low Technology Readiness (TRL) level or for well-proven materials that have been engineered through many years of research (NASA's TPSX database being off-fline and unavailable at the moment of writing the present dissertation), and (2) the lack of access to dedicated experimental facilities, therefore the combined influence of uncertainties in the material's emissivity ϵ_{tps} (i.e. on the amount of radiative cooling that takes place), specific heat, c_{tps}, and conductivity, denoted here k_{tps}, on the thermal response predicted by the hybrid TPS model (presented in Section 4.3.1) can instead be investigated using a Monte Carlo simulation as introduced in the upcoming paragraphs.

Stochastic Simulations

For demonstration purposes, a Monte-Carlo analysis with $1,000$ optimization runs was set up to design a passive thermal insulator for the leading edge of the wings of a representative RLV (i.e. CFASTT-1 vehicle). The TPS was assumed to be composed from a layer of Reinforced Carbon-Carbon (RCC) insulation material (directly attached to the structural skin to form a fully integrated TPS configuration) in order to retain the temperature of the underlying structure below 500 K for the whole duration of the re-entry. It should be noted that because of the simplistic nature of the problem (i.e. single variable optimization), a rapid Newton-Raphson iterative method was used to optimise the thickness of the insulation layer. When the nominal RCC properties defined in Table 4.1 are considered, the optimal thickness returned by the optimizer was found to be equal to 9.7 cm (as already discussed in Section 5.2.3 of Chapter 5). The thermal performance of the resulting passive TPS with the nominal optimal thickness is

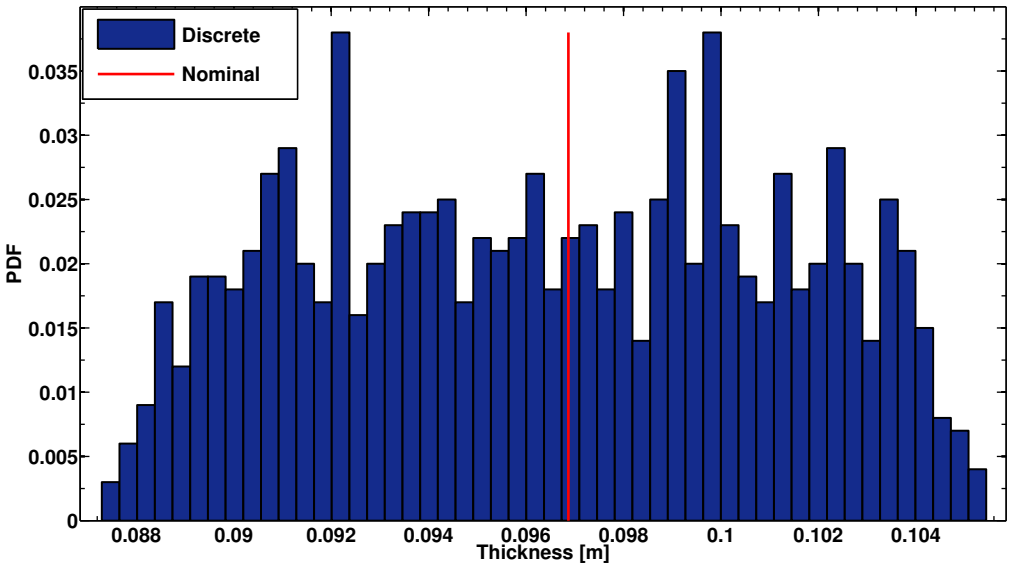

Figure 6.25: Stochastic thermal analysis - Results of a 1000-sample Monte-Carlo simulation of the performance of the leading edge TPS along the nominal re-entry trajectory described throughout the present chapter. The TPS is assumed to be made out of Reinforced Carbon-Carbon (RCC) material with stochastic emissivity $\epsilon_{tps} = 0.79 \pm 20$ %, specific heat $c_{tps} = 0.770$ kJ/(kg.K)$\pm$20 %, and conductivity $k_{tps} = 4.3$ W/(m.K)$\pm$20 %.

depicted in Fig. 6.24 (as required, the structural skin temperature is maintained below the temperature limit).

Thereafter, a uniform distribution of material properties with a $\pm$20% deviation around their nominal values was adopted in order to characterise the inherent variability in the fabrication of the TPS together with the possibility of thermal degradation and mechanical damage during the previous flight history of the craft.

The results of this Monte Carlo analysis, presented in Fig. 6.25, shows that this assumption results in a distribution of predicted TPS optimal thickness about the nominal value of 97 mm (see Fig. 6.25). Statistical analysis (see CDF curve in Fig. 6.26) then suggests that if the assumed variability in material properties is accurate, then designing the system to the predicted nominal TPS thickness would result in higher than nominal heating of the structure of the vehicle on 55 % of missions, but that, if a design margin of, say, 110 % of nominal was adopted, then the likelihood of the system not meeting its specified performance would be very small indeed. The great advantage of the statistical process is that

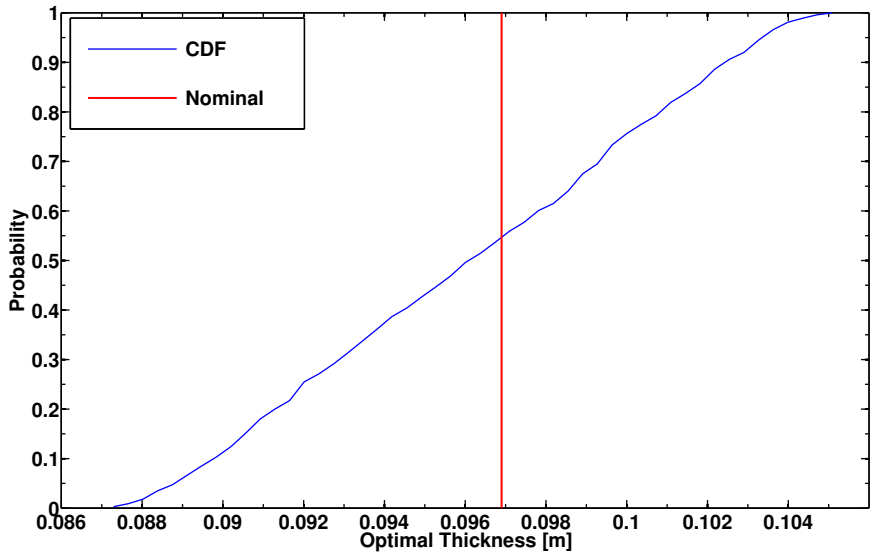

Figure 6.26: Statistical analysis of a passive TPS - Cumulative Density Function (CDF) curve for the optimal TPS thickness. The nominal optimal thickness is represented by the vertical red line.

it allows the safety margins and required design tolerances on the system to be revealed in this way, allowing adequate margins to be incorporated into the TPS design or, alternatively, focusing attention on those elements of the system that need to be better quantified before the design can proceed to fruition.

6.4.2 Active Cooling System

In this section, the reliability of the pseudo-optimal Active Cooling System (ACS) derived in Section 5.2.3 of Chapter 5 to protect the leading edge of the wings from the severe aero-thermal environment at re-entry is evaluated. The analysis attempts to assess the reliability of an ACS under off-nominal heat conditions during re-entry.

ACS Reliability Analysis

The heat profile experienced by spaceplanes during their hypersonic flights could vary considerably with regards to the pre-flight estimates, i.e. as was confirmed by the Space Shuttle programme. Therefore, it may appear that an active thermal control of some of the critical zones of the airframe structure has a clear

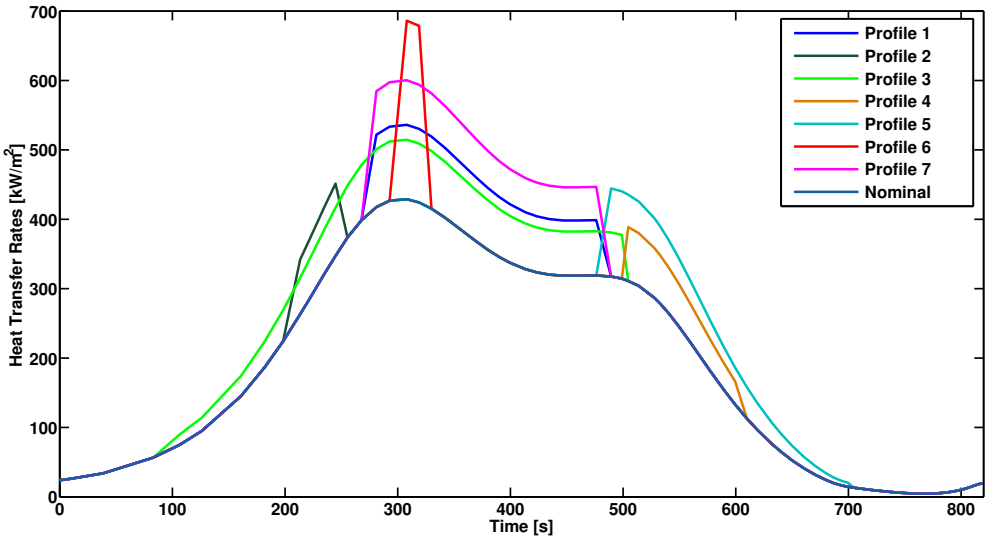

Figure 6.27: Perturbed heating profile during re-entry - The figure shows a series of perturbed re-entry heat-flux profiles as a result of flight disturbances or manoeuvres.

advantage over the use of a passive thermal shield as the former can be controlled to be responsive to eventual disturbances in the profile of heat to which the vehicle is subjected under flight conditions, i.e. as a result of perhaps an early onset of boundary layer transition (i.e. roughness-induced transition), an off-nominal manoeuvre, some unpredicted climatological phenomenon or simply a shock impingement over the leading edge of the wings (hot spots). Here, this first analysis is thus related to the following interrogation: "*Can the optimal ACS be used to maximize survivability of the vehicle in case of a sudden increase in heat load?*" If the answer is *yes*, then it would prove that switching to an active type of thermal control (with a dedicated and responsive centralized controller to optimally distribute the coolant where most needed) over critical regions of the flow field is not an option but a key enabling technology to secure airworthy operations. Mathematically, the optimal set of design parameters has been maintained (see Section 5.2.3 in Chapter 5) and the resulting ACS is here defined as the nominal design. Therefore, the strategy consists in optimizing the control temperature bounds, i.e. the temperatures at which the ACS is set on or off. The optimal strategy thus becomes the variation of control temperatures that minimize the maximum temperature experienced by the structural skin of the vehicle (i.e. maximizing the vehicle's survivability). The seven heat flux profiles considered in this work are depicted in Fig. 6.27.

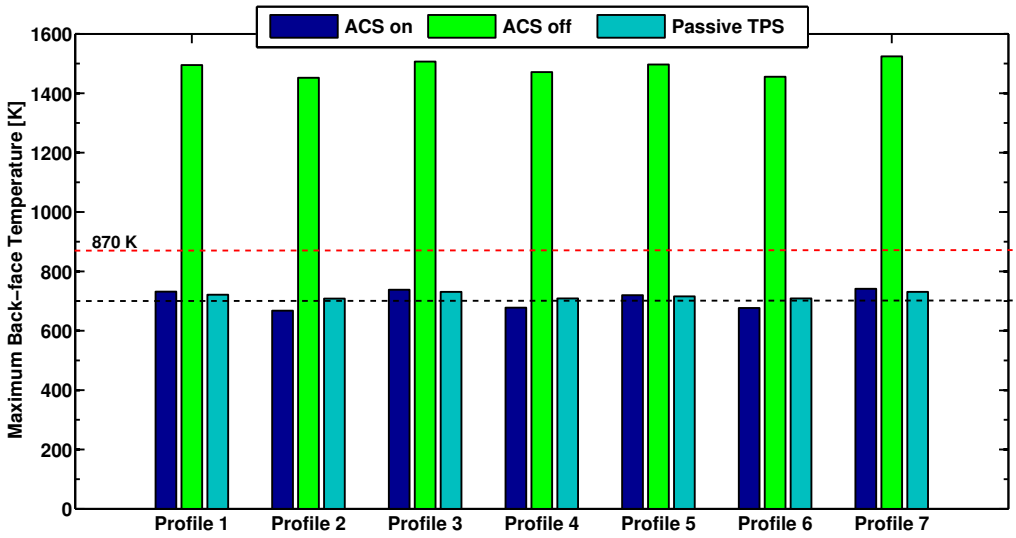

Figure 6.28: Maximum temperature of the structural skin as a result of unforeseen changes in nominal heat flux profile - The figure shows a the maximum temperature reached by the structural skin when the vehicle is subjected to perturbed heat flux profiles. The results are shown for the ACS on with optimal temperature control (blue), ACS off (green) and the passive RCC tile TPS (cyan).

Results

The maximum temperature attained by the structural skin when the vehicle (equipped with an ACS or a passive TPS) is subjected to these perturbed heat profiles is depicted in Fig. 6.28. As shown, both the passive TPS and optimal ACS are capable of maintaining the structural temperature around the desired temperature limit of 700 K (and far below the critical temperature of the consituting Timetal 834 titanium alloy). However, when the vehicle operates with its ACS switched off during re-entry (as a result of a failure), the thermal shield does not provide the required level of performance. Figure 6.29 depicts the maximum temperature attained by the surface of the RCC tile when the vehicle experiences the considered off-nominal heating conditions. It becomes apparent from the figure in question that although the passive TPS might provide the survivability of the vehicle in most cases, it may however experience a temperature which is beyond the reusability temperature of the RCC tile and could thus add serious complications in terms of the maintainability of the vehicle's thermal protection (i.e. four failures out of seven cases). On the contrary, the optimally-controlled ACS induces only one failure out of the seven simulation cases that have been considered in this work (i.e. it failed for profile 6). It shall be noted that this

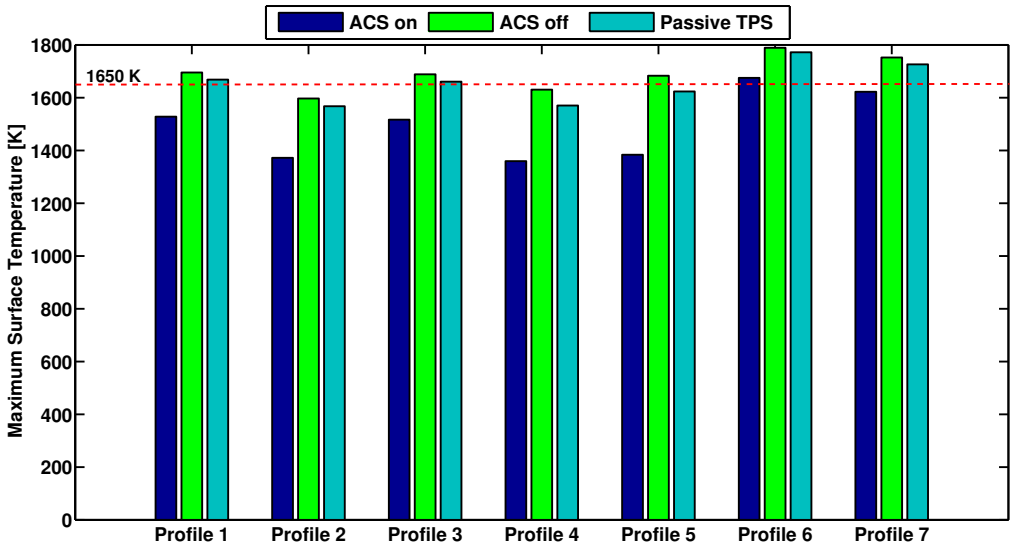

Figure 6.29: Maximum temperature of the RCC tile as a result of unforeseen changes in heat flux profile - The figure shows a the maximum temperature reached by the RCC layer when the vehicle is subjected to perturbed heat flux profiles. The results are shown for the ACS on with optimal temperature control (blue), ACS off (green) and the passive RCC tile TPS (cyan).

level of performance was attained even without considering an additional small reserve of cryogenic fuel. Furthermore, it is believed that a more sophisticated control of the coolant mass flow rate would be sufficient to solve that particular case. This analysis emphasizes the flexibility of the ACS strategy to off-nominal heating conditions when it is compared to the use of a passive TPS.

Finally, a future analysis could be performed to express the benefit and potential of adding an extra thin layer of insulation (i.e. low conductivity material) between the first RCC layer and the coolant passage. This extra layer of insulation could be used (1) to decrease the heat load that goes into the coolant when the ACS is switched on, and (2) to ensure that the temperature of the structure does not reach its upper limit (i.e. $T_{fail} = 870$ K) if the active thermal control system fails (perhaps as a result of a pump failure or a leakage in the feeding line due to pipe cracking).

6.5 Chapter Summary

In the present chapter, various methods of predicting the inherent uncertainty within the system components that compose future re-usable space-access vehicles

have been introduced.

First, the sensitivity of the re-entry trajectory to natural variations in the temperature within the atmosphere have been explored. It has been shown that the statistical scatter of results obtained via a Monte-Carlo simulation of the entry trajectory in the presence of atmospheric variability allows the design to be evaluated in terms of the permissible margins on its performance, for instance if the vehicle were to be integrated into a tightly-controlled air traffic management system.

Then, the effect of two distinct mechanisms for the boundary layer transition from a laminar state to turbulence on the nominal trajectory of a representative re-usable space-access vehicle has been investigated. It has been shown that the disturbances to the nominal aerodynamic moments as a result of the formation of so-called turbulent wedges, while often quite small, may however have a finite influence on the design of the nominal flight controls introduced in Chapter 5.

Finally, the combined effects of uncertainties in the properties of the materials (such as emissivity, specific heat and thermal conductivity), used in the present study to provide thermal insulation for a representative re-usable launcher, and in the Active Cooling System (ACS) used to cool the most exposed parts of the vehicle, have also been investigated in this chapter.

The advantage of a statistical approach such as that illustrated here is that it depicts the performance characteristics of the vehicle in the form of a likely spread of outcomes, and thus allows an estimate of the variability in the inherent assumptions within the design process, faults in the characterization of the system, and, indeed, uncertainty in the conditions that may pertain during the operation of the vehicle itself, to be integrated, at preliminary design stage, into a measure of the robustness of the vehicle configuration. The final aim of such studies is therefore to allow appropriate and realistic margins to be built into the design very early on in its evolution towards a workable prototype.

Nomenclature

List of Symbols

c	Control law or Thermal capacitance
D	Drag force
g	Gravity acceleration
H	Scale Height
h	Altitude
h_{wedge}	Height of an element of surface roughness
k	Thermal conductivity
Kn	Knudsen number
M	Mach number or Moment
P	Pressure
Q	Dynamic pressure
$\dot{q}$	Heat transfer rate
R_{gas}	Universal gas constant
S	Uniform distribution between 0 and 1
T	Temperature
α	Angle of attack
γ	Flight path angle
δ	Deflection angle
δ_L	Laminar boundary layer thickness
ϵ	Error bound function or Emissivity of the material
θ_L	longitude
λ	Latitude
μ	Bank angle or Viscosity
ρ	Density
χ	Heading angle

Subscripts & Superscripts

$edge$	Boundary layer edge condition
$fail$	Temperature limit of the material
kr	Condition at the element of surface roughness
l	Lower bound
max	Maximum
nom	Nominal condition
sea	Sea-level condition
t	Transition
tps	Thermal protection system
u	Upper bound
∞	Freestream condition

Chapter 7

Conclusions and Suggestions for Further Work

"Perfection is achieved, not when there is nothing more to add, but when there is nothing left to take away."

– Antoine de Saint-Exupéry, Airman's Odyssey.

In this final chapter, the research objectives of the thesis are first re-visited in their broader context and overall conclusions are given where the general contributions and limitations of the current research are acknowledged. Finally, the present chapter outlines recommendations for future research directions.

7.1 Research Summary

The present thesis takes the reader on a *journey* through the numerous challenges related to the rapid modelling of Single-Stage-To-Orbit (SSTO) vehicles and addresses a number of those via the reduced-order modelling of some of the critical disciplines involved in their design. SSTO vehicles are promising long-term launch systems capable of taking off from a conventional airport runway, delivering a payload into Low Earth Orbit (LEO) and then gliding back to their spaceport before getting ready for re-launch. SSTOs are thus foreseen to reduce drastically the cost of access-to-space through the adoption of a quick turnaround time similar to that of conventional airliners. A number of programmes to develop SSTO vehicles are indeed active worldwide, e.g. the development of the Skylon

SSTO vehicle by Reaction Engines Ltd in the United Kingdom (8). Nonetheless, the emphasis on their full re-usability combined with both the severe environment in which these vehicles will be operating and the use of air-breathing engines leads to a multitude of engineering complexities that must be overcome through innovative design solutions. The preliminary design phase of these complex aerospace systems is thus often considered critical as a tight integration between the miscellaneous system components of the vehicle is necessary to achieve the desired high level of performance. Indeed, although SSTOs borrow numerous design elements from traditional aircraft, these are however far beyond the complexity of conventional airplanes, i.e. as it is impossible to treat the various disciplines involved in isolation. In fact, in the design of aerospace planes, the performance coupling between system components challenges conventional design processes (118). The use of an adequate approach for the modelling of the next generation of winged launcher, particularly crafted for conceptual design, embody therefore the potential to become an important support in moving the promising SSTO concept from its current paper state to a workable prototype. For example, the assistance provided by reduced-order models in the development of the American Space-Shuttle programme was key to its success (e.g. the SHAPB model of Gentry *et al.* (20)). Similarly, the use of reduced-order models is likely to play an essential role in the successful design of long-term re-usable space-access technology.

The primary objective of the thesis was therefore the development of a set of *robust*, *integrated*, *sufficiently detailed* and *modular* reduced-order models that can assist in the preliminary modelling of the next generation of heavy-lift re-usable airplane-like SSTO launchers destined for serving reliably space transportation needs to Low Earth Orbits (LEO) at a fraction of the current costs of access-to-space. To accurately evaluate the performance of a re-usable space-access vehicle, a series of critical system components must therefore be modelled such as aerodynamics, aeroheating, flight simulation, thermal protection system, propulsion and mass. Nonetheless, the conceptual design of future SSTO vehicles requires those preliminary design tools to be augmented and integrated within a multi-disciplinary environment. The result of such an approach takes the form of unconventional design processes covering a large number of technical cross-disciplines. The resulting interwoven set of engineering models, developed in the context of the Object-Oriented Programming (OOP) formalism, describes the vehicle as an assembly of parametric system components/disciplines and thus enables the type

of parametric and trade-off studies often necessary in the early design stage of air-breathing-powered Space Transportation Systems (STS), i.e. varying and testing a multitude of design options. Indeed, despite recent advances in computational power, these reduced-order codes embed the capacity to conceive, perhaps with more flexibility, relatively detailed design analyses that embed engineering and expert knowledge potentially overlooked or too costly to be inserted into higher fidelity models. Additionally, since Multi-disciplinary Design Analysis and Optimisation (MDAO) often requires a large number of function evaluations, the practicality of higher fidelity models in the context of concept exploration, beyond their key role in validation studies, is still questionable.

In the present work, the various engineering tools have been implemented in a modular fashion. Indeed, each system component is conceptually represented as a *black box*: this feature allows the development, improvement and update of a given disciplinary tool without altering the remainder of the system component models. Furthermore, this type of software architecture facilitates the communication between the various design disciplines. In the thesis, it has been shown that if applied within the limits of their applicability, this set of engineering tools can be used to provide insights into complex design problems and to define innovative solutions. Those reduced-order models can be tailor-made to account for the various couplings between system components and identify key design variables in order to provide guidelines during the detailed design phase of the development program. It is also important to emphasize the important role of validation in the process of establishing this reduced-order methodology as a suitable design tool in the preliminary evaluation of the performance of a vehicle concept. Indeed, these must be sufficiently accurate to direct the search for an optimal solution towards a realistic concept, or at least towards a solution that more sophisticated techniques would have led to in the first place. To summarize, the near-term goals of a multi-disciplinary design environment such as that presented here are:

- to provide a rapid but sufficiently accurate evaluation of the aerothermodynamic environment around arbitrary hypersonic vehicle configurations, i.e. validated with the help of more sophisticated numerical methods and experiments.

- to prove the technical feasibility of the re-usability concept through a holistic and in-depth preliminary design study of each major constituting components in the context of system design, i.e define design interactions.

- to avoid any confusion, disbeliefs and uncertainties with regard to the existence of *design barriers* by quantifying stochastically the effects of eventual uncertainties (i.e. "*known unknowns*") on the mission of future STS.
- to reduce the design margins to a more realistic level so that the SSTO concept can challenge economically current Expendable Launch Vehicles (ELVs) in their mission to deliver payload into Low Earth Orbits (LEOs).
- to provide a parametric and modular modelling platform that designers can use to strive for innovative design solutions.

In the next section, a series of conclusions are given highlighting the major contributions and current limitations of the models described in this dissertation.

7.2 Conclusions

To quantify the aero-thermodynamic environment of complex hypersonic vehicle configurations (with fins, protrusions, wings...) over their full range of operating regimes, a computer program dubbed HyFlow has been created. A self-contained and comprehensive engineering methodology was derived and introduced in this work. The method employs a number of well-proven Local Surface Inclination (LSI) methods to provide estimates for the inviscid pressure from free-molecular flow conditions when the vehicle operates at the edge of the terrestrial atmosphere to the continuum regime in the lower atmosphere. To provide flexibility to the computer program, the input mesh can be partitioned into a number of surface regions and each of the selected regions can be analyzed using a user-specified method. To switch between rarefied and continuum approaches, the HyFlow model makes use of the Knudsen number (either that of the free-stream flow or that measuring the local importance of the particulate nature of the gas) – this capability may lead the way towards the development of a hybrid engineering solver capable of detecting local non-continuum effects. Furthermore, the HyFlow model embeds rapid and efficient algorithms to account for the effect of partial or complete shadowing of parts of the vehicle's surface – these simple and unconventional algorithms are comprehensively described in the thesis. An efficient computation of the surface streamlines as well as simplifying assumptions with regards to the local flow properties allow the viscous loads to be evaluated over the entire surface of the vehicle. The reduced-order model is also capable

of running in transitional mode to account for the onset of boundary layer transition from a laminar state to turbulence. Finally, a mixed-approach has been implemented to evaluate both the acreage and stagnation region heating. The aero-thermodynamic model has been created in the context of MDO and therefore the emphasis is on its rapidity of execution as well as the accuracy of its predictions. In its current implementation, the computational time for a single case varies from less than a second when the streamlines are pre-computed to a few minutes at most when those need to be calculated – it is highly dependent on the complexity of the input mesh, however. Nonetheless, it is believed that the re-implementation of the *bottleneck* streamline algorithm (i.e. slowest part of the computation) in a compiled programming language (such as the C++ language) will provide the required computational speed-up necessary to analyze a geometry on-the-fly, i.e. particularly relevant in the case of shape optimization.

To prove that the algorithms within HyFlow have been correctly implemented and that the simulated output yields a good approximation to the predictions of high-fidelity methods, the various assumptions embedded within the reduced-order aero-thermodynamic model have been re-visited. Indeed, HyFlow has been validated for a number of representative test cases with reasonably good fidelity. The configurations used for this validation work were representative of the whole span of hypersonic geometries, i.e. from a simple nearly-sharp blunt-nosed cone, through a ballistic fusiform shape to a historical re-usable space-access vehicle. The validation compared the HyFlow output (in terms of pressure, force and moment coefficients, boundary layer edge conditions and heat flux) with a mix of experimental and numerical data, which lead to the conclusion that HyFlow can be used for the analysis of complex hypersonic configurations in the context of concept exploration. An additional zonal analysis has been carried out whereby an optimization process has been used to identify the best combination of LSI methods that minimize the total error in aerodynamic coefficients. It was shown that a counter-intuitive choice of methods can sometimes provide better results than what intuition dictates. This approach (when supported by either experimental or numerical results) may be used to derive a unified method for the preliminary planning of trajectories.

The system design environment introduced in the present work, while still in its infancy, represents however a first step towards the development of a large number of tools and a rapid design procedure to aid in the Multi-disciplinary Design and Optimisation (MDO) of the next generation of hypersonic vehicles.

A number of system components have been created and integrated into a design framework: flight simulation model, hybrid thermal protection system and mass model. In this work, this new integrated design environment has been used in the evaluation of the performance of a representative space-access vehicle over several phases of a typical mission, namely ascent, subsequent re-entry and ground-hold. To provide the capability for modelling the ascent-to-orbit phase of the mission, a validated *in-house* hybrid propulsion model, dubbed HyPro, has been coupled to the rest of the system disciplines. A sensitivity analysis on a number of engine parameters performed using HyPro and the design environment confirmed that variability in the performance of the engines, and indeed the consequences of the selection of certain key design variables, can have a critical impact on the feasibility of the vehicle ascent trajectory.

To compute the trajectory and corresponding performance of space-planes in sufficient detail, a flight simulation model has been implemented. The model can be used to perform simulations using the equations of translational motion (i.e. three degrees of freedom), thereby treating the vehicle as a point with varying mass. The model has been augmented to account for rigid body characteristics. Indeed, a method to reverse engineer the control deflections necessary to rotate the vehicle into its desired nominal attitude has been developed. The aerodynamic effect of control surfaces has been accounted for by rotating the mesh of the controls and then using the HyFlow code to compute the resulting increment in aerodynamic force and moment. A method to account for the effect of shadowing on the controls has also been created, which involves the computation of an efficiency parameter representing a measure of the surface area impacted by the oncoming hypersonic flow. The flight simulation model embeds a method to perform statistical analysis such as Monte-Carlo simulations.

In the present work, a method has been generated to incorporate uncertainties within the US76 standard atmosphere model as a result of climatological phenomena, e.g. the combined effects of seasons and geographical location. Additionally, more realistic design margins have been derived using the higher order MSISE-90 atmosphere model. This method allows the computational efficiency of the US76 atmosphere model and its practicality to be conserved (as it does not require date, time, location etc...) while accounting for variability in the properties of the terrestrial atmosphere. To illustrate the effect that uncertainties in the atmosphere has on the re-entry mission of an SSTO, a series of Monte-Carlo simulations have

been performed where the nominal entry trajectory of a representative SSTO vehicle has been re-integrated a large number of times using a nominal control law but with variability added to the properties of the atmosphere through which the vehicle descends. It has been shown that the effect of uncertainties in the atmospheric properties on the final states of the trajectory can be significant, that on the altitude at which boundary-layer transition occurs is non-negligible, and the resulting increase in heat flux level can potentially be important, i.e. inducing potential problems for both the interface with air-traffic management and the survivability of the vehicle. The advantage of a statistical approach such as that illustrated in this work is that it depicts the performance characteristics of the vehicle in the form of a likely spread of outcomes and thus provides a measure of the system robustness to eventual design uncertainties.

To provide the capability to conceive hybrid (active and passive) Thermal Protection Systems (TPS) at a preliminary design level, the HyTPS model has been developed. The model makes use of the thermal network analogy to model the type of thermal control systems foreseen to enable the re-usability of future RLVs. The current model is restricted to only one-dimensional thermal analysis (i.e. where the TPS is modelled as a thermal network) but can be augmented by coupling a series of networks together. The computer program has been validated for its use in passive mode (i.e. single-layer and stack of materials TPS) but may still require additional validation for its active cooling mode. The HyTPS computer program can create a large number of thermal management systems through three basic types of thermal network, i.e. an insulator, a duct and a heat exchanger. The former can be used to create a stack of insulation materials, the second can be used to create convective cooling channels of any shape and finally the latter can be used to model a heat exchange process between two thermal models. These models can be duplicated and automatically combined to form any type of TPS arrangement. In the present dissertation, a parametric model of an actively cooled panel has been created. A preliminary optimization study using a generic genetic algorithm has been performed to conceive a radiative actively cooled panel that combines the use of a hot structure (i.e. Carbon-Carbon) with the cooling capabilities of liquid hydrogen. A parametric TPS model such as HyTPS permits the definition of a large number of hybrid TPS solutions. The model is capable of accounting for the boiling of the liquid hydrogen as it flows across actively cooled panels. Currently, two different cooling system architectures have been modelled: a *direct cooling* configuration where the heated cryogen is directly re-circulated

through the cryogenic tank and a *regenerative cooling* system involving the heat exchange between a coolant and the fuel as it is fed into the engines during the ascent-to-orbit phase of the mission. Nonetheless, only the former has been applied in the present work as the latter does require additional development. The benefits of a versatile tool such as the HyTPS model is taken advantage of by modelling the state of the TPS during the ground-hold phase of the mission when the vehicle is being serviced between successive missions. Indeed, the use of HyTPS to monitor the formation of frost (i.e. ice was modelled as a dynamic resistance whose layer builds up and regresses with time) over surfaces that are in close thermal contact with fully loaded integrated cryogenic tanks has been demonstrated. The simulation considered a two-hour long ground-hold operation (i.e. time between fuel tanks filling and take-off). It has been shown that the surface regions that are protected in-flight by an ACS are of course more exposed to the hazardous formation of ice as a result of their thinner structures; a more comprehensive design study of the fully integrated tank structure may reduce this particular problem. The optimization of a passive TPS with stochastic material properties has also been carried out and emphasized the importance of properties such as emissivity, specific heat and thermal conductivity in the capability of hot structures to perform their task of thermally insulating the vehicle.

A novel engineering method used to model the effect of asymmetric transition (i.e. turbulent wedge) as a result of an element of surface roughness over the surface of a hypersonic vehicle configuration has been created, e.g. roughness might appear as a result of micro-meteoroid impact during orbital operations. The wedge angle is governed by an empirical relationship based on the local velocity. When a pre-defined criterion is met, asymmetric transition conditions can be triggered during trajectory integration in order to study the effect of a turbulent wedge on the resulting heat flux and viscous loads acting on the vehicle. In its current implementation, the roughness-induced transition model does not account for the shape of the roughness element. Future development of the model may account for the wedge-like or cone-like shape of the roughness element and determine the flow field behind it by solving for the oblique shock relations or Taylor-Maccoll equations (32), as appropriate. When triggered, the development of the turbulent wedge is here considered to be instantaneous. The effects of asymmetric boundary layer transition on the nominal schedule of control surface deflection angles has been evaluated. It has been shown that the additional rotation of the controls required to correct the moments induced by the formation

of a turbulent wedge resulted in a bias in the final states of the trajectory such as final latitude and longitude, i.e. which may be of significant concern again for air-traffic management interface. Additionally, in some cases, the extra deflection angle challenged the pre-defined limits on the control surface deflections. However, it should be borne in mind that these inferences, no matter how suggestive or interesting, are of course the results of reduced-order models and may require conformation via additional validation studies with more sophisticated numerical methods. Nonetheless, the analysis presented here has confirmed the importance of accounting for such phenomena early on in the design of an RLV.

7.3 Suggestions for Further Work

Although the current version of the reduced-order models can already be used to provide a number of insights into the preliminary design of the ascent and subsequent re-entry missions of future Re-usable Launch Vehicles (RLVs), those various system components could be extended with more complex and detailed models that, in turn, may provide a better representation of the actual system. A number of these possible extensions have been identified and are thus presented here as suggestions for future research directions. Additionally, the integrated use of these reduced-order models to provide a full mission optimization (ascent and subsequent entry) appears as an important step even before any extensions are made to the models.

The Aero-thermodynamic Model

A long series of extensions to the HyFlow model could well contribute to the improvement of the accuracy and capabilities of the code. For example, a panel method could be added to quantify the aerodynamics of the vehicle at subsonic speed and therefore provide the capacity to study the mission from take-off to landing. However, here, only some of the major possible sources of improvement related to the current work are enumerated:

- A critical limitation of the current version of the HyFlow model concerns its lack of information about the flow field surrounding a geometry. A methodology for rapid *shock reconstruction* that could work for complex

configurations without relying on inviscid Euler solvers should be of high priority on the to-do list (see discussion in Section 2.8 of Chapter 2). This feature could indeed represent one of the most valuable contributions to the HyFlow code as the shock structure could then be used to evaluate the properties behind the bow shock and improve current estimates of the conditions at the outer edge of the boundary layer. Indeed, recalling the HB-2 test case presented in Section 3.2.1 of Chapter 3, the awareness of the change of entropy across the curved bow shock upstream of the vehicle (which has been considered normal) and that across the subsequent secondary (weaker) shock upstream of the flare region should ameliorate the pressure and heat transfer estimates over the length of the vehicle. An engineering method to model the effect of a *variable-entropy flow* would represent an interesting addition to the HyFlow code as it has been shown that the resulting phenomenon of entropy layer swallowing can have a significant effect on the conditions at the outer edge of the boundary layer and hence on heat transfer estimates. Additionally, a shock reconstruction method could also be used to study complex flow phenomena such as *shock-shock interactions*. As discussed in Section 2.8, the characterization of shock impingement is indeed highly relevant to the design of the TPS as it may induce local hot spots over critical regions of the vehicle's surface (e.g. leading edges of the wings) – these effects should be taken into account in the preliminary process of sizing the thermal shield of the vehicle.

- A better description of the flow over the *leeward side of the vehicle* could also represent an interesting addition since that particular region of the flow field is currently poorly treated in HyFlow. This was confirmed by the various validation cases presented in Chapter 3.

- The inclusion of *real-gas effects* is most likely to be the next extension to the HyFlow solver as those are important for the characterization of high-temperature flows. A method to account for these real-gas effects has been described in Section 2.8 of Chapter 2. Indeed, the influence of real-gas effects in the results of the Re-entry F flight experiment in Section 3.3 of Chapter 3 (high enthalpy case) is likely to explain the discrepancies observed between the results of HyFlow (where a calorically and thermally perfect gas is assumed) and those of the experiment. Additionally, it has been shown in Ref. (58) that accounting for gas chemistry (i.e. chemically reacting gas)

could lead to a reduction of the thermal loads acting on the vehicle by as much as 20%. Real-gas effects are thus important considerations in the design of complex hypersonic systems due to their tight design margins.

- Albeit challenging, a *validation of the turbulent wedge model* could also be performed using some of the experimental data from the Space Shuttle programme; e.g. from Ref. (50). Such a validation effort could then be used to calibrate the current version of the model. Moreover, as the presence of an element of surface roughness generates a shock wave as well as other flow phenomena such as a shear layer and vortex structures (53), the *shape of the roughness* may have to be accounted for to update the local properties of the panels located within the turbulent wedge with a better knowledge of its shock structure (i.e. conical shock or simple oblique shock theory could be used).

- A *surface mesh optimization* technique that locally refines regions of the geometry with high surface curvature along with surfaces in the vicinity of stagnation features could possibly enhance the predictions of the computer code as thoroughly described by Wuilbercq *et al* (7).

Trajectory Planning

The flight dynamics part of the present work could be improved in many ways. First, an optimization of the control law (i.e. schedule of bank angle and angle of attack) for both the ascent-to-orbit phase of the mission and the subsequent entry trajectory should now be performed combining some of the optimization techniques developed by fellow PhD students in Refs (120) and (121) with the integrated design environment discussed in this work, i.e. this will indeed be the subject of a paper. Additionally, such optimization work could provide, in turn, various insights into a number of questions related to hypersonic flights (e.g. system reliability).

- A series of *abort mission scenarios* could be derived to prove the reliability of the system in the case of adverse conditions, a fact that may be of great importance to secure airworthy operations. For instance, mission abort scenarios such as an engine failure during ascent or payload non-delivery will have to be considered to test the robustness of the concept.

- It will also be interesting to optimize the trajectory with more refined constraints and objective functions to take advantage of the capabilities of HyFlow and HyPro, e.g. a trajectory could be optimized *to postpone the occurrence of the first onset of boundary layer transition* during the descent of the vehicle. Nonetheless, the modelling of boundary layer transition will have to be improved.

- Additionally, the flight simulation model and the mass model should be coupled to provide an *active centre of mass management capability* during the ascent-to-orbit phase as suggested in Section 4.6 of Chapter 4 to make use of the propellant consumption as an additional means of controlling the longitudinal stability of the vehicle.

- Finally, integrating the *orbital phase* of the mission into the computation may also represent an interesting addition. Indeed, the effect of the initial conditions at entry on the trajectory of the vehicle could be investigated to study the resulting effect on the nominal re-entry path of an SSTO vehicle. Furthermore, the velocity impulse required to circularize the orbit at orbital insertion and that required to de-orbit the vehicle after payload delivery will have to be incorporated in the total fuel budget of the vehicle.

Thermal Protection System Model

In the present work, the emphasis was on the direct convective cooling type of active TPS configuration. In future studies, the emphasis should be on the regenerative cooling systems to demonstrate the use of the heat exchanger model described here. A future study could introduce the coupling between the HyTPS and HyPro models, whereby an active cooling system could be used to improve the combustion efficiency by slightly raising the temperature of the fuel through a heat exchange process before it is fed into the combustor. The versatility of the thermal network modelling approach offers indeed the capacity to model a very large number of design solutions. This instance indeed provided the main reason for choosing that particular type of thermal analysis in the first place. Since the development of the HyTPS code will be continued, below is a list of possible improvements. Some of these are planned to be included within an upcoming study.

- An *all-at-once optimization* of the structurally integrated TPS could be performed where the structural stack of materials should include the thermal insulator and its embedded cooling passages as well as the structural skin of the vehicle and the structure of the tank with its insulation layer (using a thermal network similar to that shown in Fig. 5.18). This constrained optimization process should be performed over a simulation period that corresponds to the three phases of the mission discussed in the present thesis, i.e. each phase having a set of design constraints (e.g. maximum backface temperature of the TPS during ascent and entry, and ice formation during the ground-hold phase of the mission).

- The optimization of the Active Cooling System (ACS) should include *structural constraints* (e.g. maximum thermal stress) since the optimal thermal control solution should limit the thermal fatigue induced within the structure as a result of thermal cycling, i.e. to avoid the formation of cracks after repeated use.

- A future study should include the optimization of a distributed network of actively cooled regions. Instead of a simple bang-bang controller, this future work should make use of a more sophisticated *centralized control of the thermal zones* perhaps conceived to be responsive to eventual off-nominal heating conditions.

- Finally, the HyTPS code could be extended to provide the capacity to perform two-dimensional thermal analyses (or even three-dimensional thermal analyses using, for instance, the tessellated mesh of the geometry to define a mesh suitable for thermal analysis). At least, the effect of two dimensionality (to provide more realistic margins) may have to be accounted for through correlations obtained by a careful validation of the model against the predictions of higher fidelity methods, e.g. possibly using a Finite Element Analysis (FEA) software. Indeed, the current one-dimensional analysis provides conservative estimates. Therefore, if the heat transfer through additional dimensions is incorporated within HyTPS, the estimates of the model would provide a more realistic representation of the thermal diffusion through the TPS structure.

Design Integration and Couplings

Finally, despite the effort and time devoted to provide the present design environment with the capability to model couplings and to integrate the various reduced-order models into a coherent whole, a large amount of work remains and could possibly represent a dedicated area of scholarship on its own. The hypersonics community fully agrees that understanding the couplings between the various multi-disciplinary activities that constitute the preliminary design phase of a new development is the key to unlocking the potential of hypersonic vehicles, and SSTOs to an even greater extent. One of the major areas pointed out by the community as critical and which is unfortunately lacking in the present work concerns the airframe/engine coupling (the design platform has been derived concurrently with the HyPro model, and therefore extended studies were not possible at the time of writing this dissertation). Indeed, because of the long ramps that are required to compress the freestream air to the desired conditions at the inlet of an air-breathing engine, the inlet of the engine will most likely be integrated into the forebody of the vehicle, and thus both the airframe and the inlet (i.e. similarly, the nozzle and rear part of the vehicle) should be concurrently conceived. Nonetheless, a few additional models require further development before this crucial feature can be implemented:

- A modular and flexible *parametric geometry generator* should be developed. This capability should provide the opportunity to explore a very large number of design solutions by modelling a vehicle with a propulsion system directly integrated into its airframe, i.e. a geometry generator would help to streamline the time-consuming process of mesh creation.
- It needs also to be ascertained that the physical representation of the engine matches its mathematical representation, e.g. that the size and parameters of the engine as produced by the HyPro model (e.g. the section areas of the modules) should translate directly into a three-dimensional external mesh with reliability and precision.

7.4 Lessons Learnt and Concluding Remarks

One of the many lessons learnt during the course of this Ph.D. is that the process of developing collaborative reduced-order models for the preliminary design

of hypersonic vehicles is far from being straightforward. Considering the multi-disciplinary nature of integrated systems such as an aerospace plane, it is complicated for an engineer to be an expert in all the relevant disciplines involved in their design. It shall be recognized that the set of reduced-order models embedded within the integrated multi-disciplinary design environment introduced in this dissertation are inherently simpler than more detailed disciplinary analysis tools. Nonetheless, these reduced-order models have been concurrently developed to be part of an engineering framework conceived to be intuitive and to convey a realistic representation of the physical behaviour of the overall real system for which it is intended to become a surrogate. In fact, the overarching aim of the conceptual design platform is to provide a virtual representation of the whole integrated space-access system, not necessarily to model each and every single constituting component in fine detail. Furthermore, the present design platform has been implemented to facilitate future developments so that more detailed models can be added if appropriate.

Additionally, the necessary requirement to reproduce, to the last word in fidelity, the results from more sophisticated methods with a sufficient level of accuracy using simple yet often empirical models has proved to be a difficult endeavour. Developing tools that are sufficiently versatile to function over a wide range of design applications and for parametric studies rather than conceiving tools for a specific application is time-consuming but is rewarding. The most difficult part of the work described in this dissertation was to design an engineering tool, the embedded assumptions within which would hold over a wide range of applications: a mixed approach was often necessary. It is also worth mentioning that a major drawback in the hypersonic literature is the frequent lack of experimental or numerical analyses with exploitable data (i.e. with all the necessary setup variables). In fact, this instance does not help in the necessary validation process of reduced-order models. Furthermore, while the emphasis was here on the reduced-order modelling of space-access vehicles, a synergy between the use of reduced-order models and experimental/numerical analyses early on in the design process is paramount to help in the development of future SSTO vehicles.

Finally, considering the large amount of comments and the emphasis on user-friendliness during the development of this modelling platform for SSTO vehicles, it is hoped that the embedded tools will have their development continued, their capabilities improved and, above-all will be useful to the preliminary design of future space-access vehicles.

References

[1] Butrica, A. J., *Reusable Launch Vehicles or Expandable Launch Vehicles? A Perennial Debate*. In: Dick, S. J., Launius, R. D., *Critical Issues in the History of Spaceflight*, pp. 301-341, 2006. 2

[2] Launius, R. D., "Is there an Intrinsic Superiority of Reusable Space Launch Vehicles over Those That are Expendable?," Accessed March 18, 2015, launiusr.wordpress.com, 2012. 2

[3] Bentley, M. A., *Spaceplanes: From Airport to Spaceport*, Springer Science and Business Media, 2009. 2

[4] Sanger, E., and Sanger-Bredt, I., "A Rocket Drive For Long Range Bombers," translation CGD-32, Tech. Information Branch, Bur. Aero, Navy Dpt., August 1944. 3

[5] Heppenheimer, T. A., *Facing the Heat Barrier: A History of Hypersonics*, NASA SP-2007-4232, The NASA History Series, 2007. 4, 8

[6] Varvill, R., and Bond, A., "A Comparison of Propulsion Concepts for SSTO Reusable Launchers," *Journal of the British Interplanetary Society*, Vol. 56, pp. 108-117, 2003. 6

[7] Wuilbercq, R., Ahmad, A. O., Scanlon, T., and Brown, R. E., "Towards Robust Aero-Thermodynamic Predictions for Re-usable Single-Stage-To-Orbit Vehicles," *18th AIAA/3AF International Space Planes and Hypersonic Systems and Technologies Conference*, Tours, France, 2012. 6, 8, 15, 19, 22, 23, 25, 70, 292

[8] Hempsell, M., and Longstaff, R., *The Skylon Users' Manual*, Reaction Engines Limited, 2010. 7, 283

[9] Kuczera, H., Sacher, P.W., *Reusable Space Transportation Systems*, Springer Praxis Books, Astronautical Engineering, 2011. 9

[10] Robinson, J. S., and Martin, J. G., "An Overview of NASA's Integrated Design And Engineering Analysis (IDEA) Environment," *6th Modeling and Simulation / 4th Liquid Propulsion / 3rd Spacecraft Propulsion Joint Subcommittee Meeting*, Orlando, Florida, 2008. 10, 129

[11] Rowell, L. F., and Korte, J. J., "Launch Vehicle Design and Optimization Methods and Priority for the Advanced Engineering Environment," NASA TM-2003-212654, 2003. 11

[12] Hirschel, E. H., and Weiland, C., *Selected Aerothermodynamic Design Problems of Hypersonic Flight Vehicles*, Springer, 2009. 11, 19, 55, 127, 150, 244

[13] Wuilbercq, R., Pescetelli, F., Minisci, E., and Brown, R., "Influence of boundary layer transition on the trajectory optimisation of a reusable launch vehicle," *19TH AIAA International Space Planes and Hypersonic Systems and Technologies Conference*, Atlanta, Georgia, United States, 2014. 14, 71, 195

[14] Wuilbercq, R., Pescetelli, F., Mogavero, A., Minisci, E., and Brown, R. E., "Robust multi-disciplinary design and optimisation of a reusable launch vehicle," *19TH AIAA International Space Planes and Hypersonic Systems and Technologies Conference*, Atlanta, Georgia, United States, 2014. 15, 131, 226, 227

[15] Wuilbercq, R., Brown, R. E., "Rapid Aero-Thermodynamic Analysis for Hypersonic Air Vehicles," *8th European Symposium on Aero-thermodynamics for Space Vehicles*, Lisbon, Portugal, March 2015. 15

[16] Anderson, J. D. Jr., *Hypersonic and High Temperature Gas Dynamics*, McGraw-Hill Book Company Series in Aeronautical and Aerospace Engineering, 1988. 17, 18, 25, 27, 29, 35, 39, 50, 64

[17] Bertin, J. J., *Hypersonic Aerothermodynamics*, AIAA Education Series, 1994. 17, 29, 39, 44, 80

[18] Blake, W. B., "Missile Datcom: Users Manual - 1997 Fortran 90 Revision," Tech. Rep. AFRL-VA-WP-TR-1988-3009, U.S. Air Force Research Laboratory, Wright-Patterson AFB, Ohio, 1998. 18

[19] Hoerschgen, M., "Sounding Rocket Aerodynamics - Analysis, Evaluation and Adaption of the Missile DATCOM Program Solution for the Flight Dynamics Prediction," Diploma Thesis, DLR-MORABA, 2002. 18

[20] Gentry, A. E., Smyth, D. N., Oliver, W. R., "The Mark V Supersonic-Hypersonic Arbitrary-Body Program. Volume II. Program Formulation," Douglas Aircraft Corporation, Long Beach, California, 1973. 18, 283

[21] Kinney, D. J., "Aero-Thermodynamics for Conceptual Design," *42nd AIAA Aerospace Sciences Meeting and Exhibit*, Reno, Nevada, January 2004. 18, 60, 147

[22] Kinney, D. J., "Aerothermal Anchoring of CBAERO Using High Fidelity CFD," *45th AIAA Aerospace Sciences Meeting*, Reno, Nevada, January 2007. 18, 40, 60, 122

[23] Dirkx, D., and Mooij, E., "Continuous Aerodynamic Modelling of Entry Shapes," *AIAA Atmospheric Flight Mechanics Conference*, Portland, Oregon, 08-11 August 2011. 18, 30, 35, 37, 106, 108, 111

[24] Villa, F., "Algebraic Model for Aerodynamic Coefficients Calculation During The Atmospheric Entry," Master's Thesis, Politecnico di Milano, 2001. 19, 36

[25] Jazra, T., and Smart, M., "Development of an Aerodynamics Code for the Optimisation of Hypersonic Vehicles," *47th AIAA Aerospace Sciences Meeting Including The New Horizons Forum and Aerospace Exposition*, Orlando, Florida, 5 - 8 January 2009. 19

[26] Sherman, M. M., "Entry Gasdynamic Heating," NASA SP- 8062, 1971. 21

[27] Scanlon, T.J., and Roohi, E., and White, C., and Darbandi, M., and Reese, J.M., "An open source, parallel DSMC code for rarefied gas flows in arbitrary geometries," *Computers and Fluids*, 2010. 22

[28] Hayes, W. D., Probstein, R. F., *Hypersonic Flow Theory*, New York: Academic Press, 1959. 23, 30, 47, 62

[29] Lockerby, D.A. and Reese, J.M. and Struchtrup, H., "Switching Criteria for Hybrid Rarefied Gas Flow Solvers," *Proceedings A: Mathematical, Physical and Engineering Sciences*, 465 (2105). pp. 1581-1598, 2009. 24

[30] Wilmoth, R.G., Blanchard, R.C., and Moss, J.N., "Rarefied Transitional Bridging of Blunt Body Aerodynamics," *21st International Symposium on Rarefied Gas Dynamics*, Marseille, France, 1998. 25, 32, 33

[31] Lees, L., "Hypersonic Flow," *5th International Aeronautical Conference*, Los Angeles, CA, 1955. 26

[32] Taylor, G. I., and Maccoll, J. W., "The air pressure over a cone moving at high speeds," *Proceedings from Royal Society*, Ser. A, Vol 139, no. 838, pp. 278-311, Feb. 1993. 28, 289

[33] Pittman, J. L., (appendix by C. L. W. Edwards), "Application of Supersonic Linear Theory and Hypersonic Impact Methods to Three Non Slender Hypersonic Airplane Concepts at Mach Numbers From 1.10 to 2.86," NASA TP- 1539, 1979. 28

[34] Garcia, M. A., Basanez, L., "Fast Extraction of Surface Primitives from Range Images," *13th IAPR International Conference on Pattern Recognition*, Vol. III, Applications and Robotic Systems, Vienna, Austria, pp. 568-572, 1996. 30

[35] Hankey, W. L., *Re-entry aerodynamics*, Washington, DC: American Institute of Aeronautics and Astronautics, 1988. 32, 56, 62, 131, 149, 204

[36] Bornemann, W. E., *Aerodynamic Design Data Book. Volume 1 - Orbiter Vehicle STS-1*, Rockwell International, 1980. 32, 106

[37] Bonner E., Clever W., and Dunn K., "Aerodynamic preliminary analysis system: Part 1 Theory," NASA CR-165628, 1981. 36

[38] Havel, J., and Herout, A., "Yet Faster Ray-Triangle Intersection (Using SSE4)," *IEEE Transactions on Visualization and Computer Graphics*, Vol. 16, No. 3, pp. 434-438, 2010. 37

[39] Sibson, R., "A brief description of natural neighbor interpolation (Chapter 2)," In V. Barnett. Interpreting Multivariate Data. Chichester: John Wiley. pp. 21-36, 1981. 42

[40] Oppenheimer, M. W., Doman, D. B., McNamara, J. J., Culler, A. J., "Viscous Effects for a Hypersonic Vehicle Model," *AIAA Atmospheric Flight Mechanics Conference and Exhibit*, Honolulu, Hawaii, 2008. 39

[41] DeJarnette, F., "Calculation of Inviscid Surface Streamlines and Heat-Transfer on Shuttle Type Configurations, Part 1 - Description of Basic Method," NASA CR-111921, 1971. 39, 43, 64

[42] Tricoche, X., Garth, C., and Scheuermann, G., "A Fast and Robust Method for Visualizing Separation Line Features," *Mathematics and Visualization*, pp 249-263, 2006. 41

[43] Suli, E., and Mayers, D., *An Introduction to Numerical Analysis*, Cambridge University Press, 2003. 41

[44] Kinney, D., "Approximate Entropy Layer Swallowing Model for the Engineering Level Aerothermodynamics Code CBAERO," *49th AIAA Aerospace Sciences Meeting including the New Horizons Forum and Aerospace Exposition*, Orlando, Florida, 4-7 January 2011. 44

[45] Crabtree, L. F., Dommett, R. L., and Wooldley J. G., "Estimation of Heat Transfer to Flat Plates, Cones and Blunt Bodies," *Aeronautical Research Council Reports and Memoranda*, No. 3637, London, July 1965. 46, 47, 56

[46] Meador W. E. and Smart, M., "Reference Enthalpy Method Developed from Solutions of the Boundary-Layer Equations," *AIAA Journal*, Vol. 43, No. 1, pp. 135-139, 2005. 46, 47

[47] Schlichting, H., *Boundary Layer Theory*, 7th Edition, McGraw-Hill, New York, p. 664, 1979. 47

[48] Stetson, K. F., "Comments on Hypersonic Boundary-Layer Transition," TR-90-3057, Wright Research and Development Center, Wright Patterson AFB, Dayton OH, September 1990. 48

[49] Chen, F., and Malik, M. R., "Comparison of Boundary Layer Transition on a Cone and Flat Plate at Mach 3.5," *26th AIAA Aerospace Sciences Meeting*, Reno, Nevada, 11-14 January 1988. 49

[50] Horvath, T. J., Zalameda, J. N., Wood, W. A., Berry, S. A., Schwartz, R. J., Dantowitz, R. F., Spisz, T. S., and Taylor, J. C., "Global Infrared Observations of Roughness Induced Transition on the Space Shuttle Orbiter," NATO, RTO-MP-AVT-200. 50, 292

[51] Hale, N. W. Jr., Lamotte, N. O., and Garner, T. W., "Operational Experience with Hypersonic Flight of the Space Shuttle," *11th AIAA/AAAF International Space Planes and Hypersonic Systems and Technology Conference*, Orleans, France, 29 September - 4 October 2002. 49, 247

[52] Bowcutt, K. G., Anderson, D. J., and Capriotti, D., "Viscous Optimized Hypersonic Waveriders," *25th AIAA Aerospace Sciences Meeting*, Reno, Nevada, 12-15 January 1987. 50

[53] Kelly, A. S., "Development of a Hybrid DSMC/CFD Method for Hypersonic Boundary Layer Flow over Discrete Surface Roughness," PhD Dissertation, University of Texas, Austin, US, 2012. 51, 292

[54] Ryan K. M., Lewis M. J., and Yu K. H., "Comparison of Robust Optimization Methods Applied to Hypersonic Vehicle Design," *AIAA Modeling and Simulation Technologies Conference*, Boston, Massachusetts, 19-22 August, 2013. 51

[55] Doorly, D. J., and Smith, F. T., "Initial-Value Problems for Spot Disturbances in Incompressible or Compressible Boundary Layers," *Journal of Engineering Mathematics*, Vol. 26, pp. 87-106, 1992. 51

[56] Reda, D. C., "Review and Synthesis of Roughness-Dominated Transition Correlations for Re-entry Applications," *Journal of Spacecraft and Rockets*, Vol. 39, No. 2, pp. 161-167, 2002. 52, 195, 257, 259

[57] Mebius, J. E., "Derivation of the Euler-Rodrigues formula for three-dimensional rotations from the general formula for four-dimensional rotations," *arXiv General Mathematics*, 2007. 52, 147

[58] Scanlon, T. J., White, C., Borg, M. K., Palharini, R. C., Farbar, E., Boyd, I. D., Reese, J. M., and Brown, R. E., "Open-Source Direct Simulation Monte Carlo Chemistry Modeling for Hypersonic Flows," *AIAA Journal*, Vol. 53, No. 6, pp. 1670-1680, 2015. 56, 291

[59] White, F. M., *Viscous Fluid Flow*, McGraw-Hill, 3rd Edition, 2006. 56

[60] Hansen, C. F., "Approximations for the Thermodynamic and Transport properties of High-Temperature Air," NACA TN 4150, 1958. 56

[61] Hamilton, H. H., "Approximate Method of Calculating Heating Rates at Three Dimensional Stagnation Points during Atmospheric Entry," NASA Technical Memorandum 84580, November 1982. 57, 58

[62] Fay, J. A., and Riddell, F. R., "Theory of Stagnation Point Heat Transfer in Dissociated Air," *Journal of the Aeronautical Sciences*, Vol. 25, No. 2, pp. 73-85, 1958. 58

[63] Bowcutt, K., "Hypersonic Vehicle Systems Integration: Vehicle Aerothermodynamic Analysis and Thermal Management Design," PowerPoint Presentation, Boeing Phantom Works, 12 September 2007. 59, 260

[64] Cohen-Steiner, D., and Morvan, J. M., "Restricted Delaunay Triangulations and Normal Cycle," *19th ACM Symposium on Computational Geometry*, San Diego, California, 8-10 June 2003. 58, 59

[65] Wang, Z. H., *Theoretical Modelling of Aeroheating on Sharpened Noses Under Rarefied Gas Effects and Nonequilibrium Real Gas Effects*, Springer Theses, 2015. 61

[66] Eggers, T., Dittrich, R., and Varvill, R., "Numerical Analysis of the SKYLON Spaceplane in Hypersonic Flow," *17th AIAA International Space Planes and Hypersonic Systems and Technologies Conference*, San Francisco, California, 11-14 April 2011. 63

[67] Iliff, K. W., and Shafer, M. F., "A Comparison of Hypersonic Vehicle Flight and Prediction Results," NASA Technical Memorandum 104313, 1995. 63

[68] McBride, B. J., and Gordon, S., "Computer Program for Calculation of Complex Chemical Equilibrium Compositions and Applications II. Users Manual and Program Description," NASA Reference Publication 1311, 1996. 64

[69] Srinivasan, S., and Tannehill, J. C., "Simplified Curve Fits for the Transport Properties of Equilibrium Air," NASA Contractor Report 178411, 1987. 64

[70] Gilchrist, A. R., and Williams, M. J., "Pressure Distributions and Forces on AGARD Models HB-1 and HB-2 at M = 7.5," Aeronautical Research Labs., Australian Defence Scientific Service, Aerodynamics Note 346, February 1974. 70

[71] Jones, J. H., "Pressure Tests on the Standard Hypervelocity Ballistic Model HB-2 at Mach 1.5 to 5," Von Karman Gas Dynamics Facility, TR AEDC-TDR-64-246, Arnold AFB, TN, 1964. 70

[72] Gray, J. D., "Summary Report on Aerodynamic Characteristics of Standard Models HB-1 and HB-2," Von Karman Gas Dynamics Facility, TR AEDC-TDR-64-137, Arnold AFB, TN, 1964. 70, 89

[73] Savino, R., and Paterna, D., "Blunted Cone-Flare in Hypersonic Flow," *Computers & Fluids*, Vol. 34, pp. 859875, 2005. 71

[74] Tissera S., Drikakis D., and Birch T., "Computational Fluid Dynamics Methods for Hypersonic Flow Around Blunted-Cone Cylinder Flare," *Journal of Spacecraft and Rockets*, Vol. 47, No. 4, pp. 563-570, 2010. 72, 74, 89, 91, 94

[75] Kuchi-ishi, S., Watanbe, S., Nagai, S., Tsuda, S., Koyama, T., Hirabayashi, N., Sekine, H., and Hozumi, K., "Comparative Force/Heat Flux Measurement Between JAXA Hypersonic Test Facilities Using Standard Model HB-2 (Part 1: 1.27 m Hypersonic Wind Tunnel Results)," JAXA Research and Development, Rept. JAXA-RR-04- 035E, March 2005. 72, 84, 85, 94

[76] Mogavero, A., Taylor, I., and Brown, R. E., "Hybrid Propulsion Parametric and Modular Model: a Novel Engine Analysis Tool Conceived for Design Optimization," *19th AIAA International Space Planes and Hypersonic Systems and Technologies Conference*, Atlanta, Georgia, 16-20 June 2014. 73, 130, 177, 186, 197, 226

[77] Greenshields, C., Weller, H., Gasparini, L., and Reese, J., "Implementation of Semi-Discrete, Non-Staggered Central Schemes in a Colocated, Polyhedral, Finite Volume Framework, for High-Speed Viscous Flows," *International Journal for Numerical Methods in Fluids*, Vol. 63, No. 1, pp. 121, 2010. 73

[78] Popinski, Z., "Compressible Laminar Boundary Layers on Sharp Cone at Incidence with Entropy Swallowing," *AIAA Journal*, Vol. 13, No. 9, pp. 1135-1136, September 1975. 83

[79] Rumsey, C. B., Carter, H. S., Hastings, E. C., Raper, J. L., and Zoby, E. V., "Initial Results from Flight Measurements of Turbulent Heat Transfer and Boundary-Layer Transition at Local Mach Numbers near 15 (Reentry F)," NASATM X-1856, 1969. 99

[80] Barnhardt, M., and Candler, G. V., "Detached-Eddy Simulation of the Reentry-F Flight Experiment," *Journal of Spacecraft and Rockets*, Vol. 49, No. 4, pp. 691-699, 2012. 99, 102, 103

[81] Schneider, S. P., "Flight Data for Boundary-Layer Transition at Hypersonic and Supersonic Speeds," *Journal of Spacecraft and Rockets*, Vol. 36, No. 1, pp. 8-20, 1999. 100, 101, 102, 105

[82] Kleb, W. L., and Weilmuenster K. J., "Characteristics of the Shuttle Orbiter Leeside Flow During A Reentry Condition," Technical Report, NASA Langley Technical Report Server, 1992. 111

[83] Hamilton II, H. H., Greene, F. A., and DeJarnette, R. R., "Approximate Method for Calculating Heating Rates on Three-Dimensional Vehicles," *Journal of Spacecraft and Rockets*, Vol. 31, No. 3, pp. 345-354, 1994. 112, 118

[84] Zoby, E. V., "Analysis of STS-2 Experimental Heating Rates and Transition Data," *Journal of Spacecraft and Rockets*, Vol. 20, No. 3, pp. 237-237, 1983. 112, 114, 116, 117, 121

[85] Zoby, E. V., Thompson, R. A., and Wurster, K. E., "Aeroheating Design Issues for Reusable Launch Vehicles – A Perspective," *34th AIAA Fluid Dynamics Conference*, Portland, Oregon, United States, 28 June - 1 July 2004. 122

[86] Glass, D.E., "Ceramic Matrix Composite (CMC) Thermal Protection Systems (TPS) and Hot Structures for Hypersonic Vehicles," *15th AIAA Space Planes and Hypersonic Systems and Technologies Conference*, Dayton, Ohio, 28 April - 1 May 2008. 125, 273

[87] Rhodes, R. E., and Walker, S. W., "Evaluation of Ice and Frost Accumulation on the Space Shuttle External Tank," *13th Space Congress*, 7 - 9 April, 1976. 127

[88] Tetlow, M. R., and Doolan, C. J., "Comparison of Hydrogen and Hydrocarbon-Fueled Scramjet Engines for Orbital Insertion," *Journal of Spacecraft and Rockets*, Vol. 44, No. 2, MarchApril 2007. 128

[89] Peckham, D. H., and Crabtree, L. F., "The Range Performance of Hypersonic Aircraft," Aeronautical Research Council Papers, C.P. No. 932, 1967. 128

[90] Starkey, R. P., Liu, D. D., Chen, P. C., Sengupta, A., Chang, K. T., and Rankins, F., "Integrated Aero-Servo-Thermo-Propulso-Elasticity (ASTPE) Methodology for Hypersonic Scramjet Vehicle Design/Analysis," *48th AIAA*

Aerospace Sciences Meeting Including the New Horizons Forum and Aerospace Exposition, Orlando, Florida, 4 - 7 January 2010. 129

[91] Tewari, A., *Atmospheric and Space Flight Dynamics – Modeling and Simulation with MATLAB and Simulink*, Birkhauser Boston, 2007. 132

[92] Civil Aviation Authority, "UK Government Review of Commercial Spaceplane Certification and Operations," Technical Report, UK, July 2014. 132

[93] United States Committee on Extension to the Standard Atmosphere, "U.S. Standard Atmosphere 1976," National Oceanic and Atmospheric Administration, National Aeronautics and Space Administration, United States Air Force, Washington D.C., 1976. 133

[94] Pietrobon, S. S., USSA1976 Program, www.sworld.com.au, Small World, Australia, Accessed March 18, 2015. 134

[95] Vinh, N. X., Busemann, A., and Culp, R. D., *Hypersonic and Planetary Entry Flight Mechanics*, University of Michigan Press, Ann Arbor, MI, 1980. 135, 136

[96] Mooij, E., "The Motion of a Vehicle in a Planetary Atmosphere," Delft University of Technology, Faculty of Aerospace Engineering, Report LR-768, 1994. 136, 139, 142

[97] Diston, D. J., *Computational Modelling of Aircraft and the Environment: Platform Kinematics and Synthetic Environment Volume 1*, John Wiley & Sons, p. 35, 2009. 137, 146

[98] Shore, C.P., "Review of Convectively Cooled Structures for Hypersonic Flight," NASA Technical Memorandum 87740, 1986. 150

[99] Helenbrook, R. G., and Anthony, F. M., "Design of a Convective Cooling System for a Mach 6 Hypersonic Transport Airframe," NASA CR-1918, December 1971. 150, 224

[100] Helenbrook, R. G., and Anthony, F. M., "Evaluation of Active Cooling Systems for a Mach 6 Hypersonic Transport Airframe," NASA CR-1917, December 1971. 150

[101] Anthony, F. M., Dukes, U. H., and Helenbrook, R. G., "Internal Convective Cooling Systems for Hypersonic Aircraft," NASA CR-2480, February 1975. 150, 157

[102] Troltzsch A., Siggel, M., Kopp A., and Schwanekamp, T., "Multidisciplinary Analysis of the DLR Spaceliner Concept by Different Optimization Techniques," *11th World Congress on Computational Mechanics, 5th European Conference on Computational Mechanics, 6th European Conference on Computational Fluid Dynamics*, 2014. 151

[103] Valdevit, L., Vermaak, N., Zok, F. W., and Evans, A. G., "Optimal design of actively cooled panels for scramjets," *AIAA Journal*, Submitted in 2007. 151

[104] K&K Associates, "Thermal Network Modeling Handbook, National Aeronautics and Space Administration," Manned Spacecraft Center, Contract NASA 9-10435, 2000. 152, 157

[105] Incropera, F. P., and DeWitt, D. P., *Fundamentals of Heat and Mass Transfer*, 6th edition, Hoboken: Wiley,. pp. 490, 515, 2007. 158

[106] Izon, S. J., "Improvements in Thermal Protection Systems Sizing Capabilities for TCAT," AE 8900 Special Project, Georgia Institute of Technology, 2001. 166

[107] Cowart, K. K., Olds, J. R., "Integrating Aeroheating and TPS Into Conceptual RLV Design," *9th International Space Planes and Hypersonic Systems and Technologies Conference and 3rd Weakly Ionized Gases Workshop*, Norfolk, VA, 1-5 November 1999. 169, 171

[108] Jones, R. A., Braswell, D. O., and Richie, C. B., "Fail-Safe System for Actively Cooled Supersonic and Hypersonic Aircraft," NASA TM X-3125, 1975. 169, 173, 215

[109] Garbers, N., "Overall Preliminary Design of the Thermal Protection System for a Long Range Hypersonic Rocket-powered Passenger Vehicle (Spaceliner)," *7th European Workshop on Thermal Protection Systems and Hot Structures*, ESA, ESTEC, Noordwijk, TheNetherlands, 8 April, 2013. 169

[110] Olds, J., and Bradford, J., "SCCREAM (Simulated Combined-Cycle Rocket Engine Analysis Module): A Conceptual RBCC Engine Design Tool," *33rd AIAA/ASME/SAE/ASEE Joint Propulsion Conference & Exhibit*, Seattle WA, 6-9 July 1997. xvii, 178, 185, 226, 228

[111] Carlomagno, G. M., *Elementi di Gasdinamica*, Liguori, 2009. 182

[112] Tran, K., "One Dimensional Analysis Program for Scramjet and Ramjet Flowpaths," Masters thesis, Virginia Polytechnic Institute and State University, Blacksburg, VA, 2010. 182

[113] Bradford, J. and Olds, J., "Improvements and Enhancements to SCCREAM, a Conceptual RBCC Engine Analysis Tool," *34th AIAA/ASME/SAE/ASEE Joint Propulsion Conference & Exhibit*, Cleveland, OH, 13-15 July, 1998. 182

[114] Segal, C., "Propulsion Systems for Hypersonic Flight," RTO AVT Lecture Series on "Critical Technologies for Hypersonic Vehicle Development," held at the von Karman Institute, Rhode-St-Gense, Belgium, 10-14 May, 2004, and published in RTO-EN-AVT-116. 185

[115] Harloff, G.J., and Berkowitz, B. M., "HASA-Hypersonic Aerospace Sizing Analysis for the Preliminary Design of Aerospace Vehicles," NASA CR-182226, November 1988. 189, 190

[116] Yokoyama, N., Suzuki, S., and Tsuchiya, T., "Multidisciplinary Design Optimization of Space Plane Considering Rigid Body Characteristics," *Journal of Spacecraft & Rockets*, Vol. 44, No. 1, pp. 121-131, January-February 2007. 189, 195

[117] Dirkx, D., and Mooij, E., "Optimization of entry-vehicle shapes during conceptual design," *Acta Astronautica*, Vol. 94, pp. 198-214, 2013. 189

[118] Bowcutt, K., "A Perspective on the Future of Aerospace Vehicle Design," *12th AIAA International Space Planes and Hypersonic Systems and Technologies*, Norfolk, Virginia, 15-19 December, 2003. 193, 283

[119] Chavez, F. R., and Schmidt, D. K., "Analytical Aeropropulsive/Aeroelastic Hypersonic-Vehicle Model with Dynamic Analysis," *Journal of Guidance, Control and Dynamics*, pp. 1308-1319, 1994. 193

[120] Pescetelli F., Minisci E., Maddock C., Taylor I., and Brown R.E., "Ascent Trajectory Optimisation for a Single-Stage-ToOrbit Vehicle with Hybrid Propulsion," *18th AIAA/3AF International Space Planes and Hypersonic Systems and Technologies Conference*, Tours, France, 24-28 September 2012. 205, 229, 248, 292

[121] Pescetelli, F., Minisci, E., and Brown, R. E., "Re-entry Trajectory Optimization for a SSTO vehicle in the Presence of Atmospheric Uncertainties," *5th European Conference for Aeronautics and Space Science (EUCASS)*, Munich, Germany, 1-4 July, 2013. 205, 208, 252, 255, 292

[122] Allen, H. J., and Eggers, A. J., "A Study of the Motion and Aerodynamic Heating of Ballistic Missiles Entering the Earths Atmosphere at High Supersonic Speeds," NACA-TR-1381, 1958. 205, 207

[123] Arrington, J., and Jones, J., "Shuttle Performance: Lessons Learned," In: NASA Conference Publication 2283, 1983. 205

[124] Henry, J. R., and McLellan, C. H., "The Air-Breathing Launch Vehicle for Earth-Orbit Shuttle - New Technology and Development Approach," *AIAA Advanced Space Transportation Meeting*, Cocoa Beach, Florida, 4-6 February, 1970. 205

[125] Kasen, S. D., "Thermal Management at Hypersonic Leading Edges," PhD Dissertation, University of Virginia, May 2013. 205

[126] Chapman, D. R., "An Approximate Analytical Method for Studying Entry Into Planetary Atmospheres," NASA TR R-11, 1959. 206

[127] Vasile, M., "Finite Elements in Time: a Direct Transcription Method for Optimal Control Problems," *AIAA/AAS Astrodynamics Specialist Conference*, Toronto, Canada, 2-5 August, 2010. 208

[128] Betts, J. T., *Practical Methods for Optimal Control and Estimation Using Nonlinear Programming*, Second Edition, SIAM, 2010. 208

[129] Costa, M., and Minisci, E., "MOPED: a Multi-Objective Parzen-based Estimation of Distribution algorithm," *2nd international conference on Evolutionary Multi-criterion Optimization*, Turin, Italy, 8-11 April, 2003. 208

[130] Vasile, M., Minisci, E., and Locatelli, M., "An Inflationary Differential Evolution Algorithm for Space Trajectory Optimization," *IEEE Transactions on Evolutionary Computation*, Vol. 15, No. 2, pp. 267-281, 2011. 208

[131] Ellis, D. A., Pagel, L. L., and Schaeffer, D. M., "Design and Fabrication of a Radiative Actively Cooled Honeycomb Sandwich Structural Panel for a Hypersonic Aircraft," NASA CR-2957, March 1978. 214

[132] Falkiewicz, N. J., and Cesnik, C. E. S., "Proper Orthogonal Decomposition for Reduced-Order Thermal Solution in Hypersonic Aerothermoelastic Simulations," *AIAA Journal*, Vol. 49, No. 5, May 2011. 216

[133] Leyens, C., and Peters, M., *Titanium and Titanium Alloys: Fundamentals and Applications*, Wiley, Hoboken, NJ, p. 343, 2003. 216

[134] Williams, S. D., and Curry, D. M., "Thermal Materials Protection Thermophysical Property Data," NASA Reference Publication 1289, December 1992. 223

[135] Stephen J. Scotti, S. J., Martin, C. J., Lucas, S. H., "Active Cooling Design for Scramjet Engines using Optimization Methods," NASA Technical Memorandum 100581, March 1988. 223

[136] Krause, J. M., Hartmann, G. L., and Ianculescu, G. D., "Active Thermal Control for Hypersonic Vehicle," *29th Conference on Decision and Control*, Honolulu, Hawaii, US, December 1990. 225

[137] Stone, J. E., "A Fuselage/Tank Structure Study for Actively Cooled Hypersonic Cruise Vehicles," Contract No. NAS1-12995, NASA CR-132669, 1975. 238

[138] Garner, T., "International Conference on Space Planes and Hypersonic Systems and Technologies," SR SSD 2002-31, Technical Attachment, 2002. 245, 247

[139] Findlay, J. T., Kelly, G. M., Troutman, P. A., "FINAL REPORT - Shuttle Derived Atmospheric Density Model, Part 2: STS Atmospheric Implications for AOTV Trajectory Analysis - a Proposed GRAM Perturbation Density Model," NASA Contractor Report 171824, December 1984. 245

[140] A. E. Hedin, "Extension of the MSIS Thermospheric Model into the Middle and Lower Atmosphere," *J. Geophys.*, Res. 96, 1159, 1991. 246, 251

[141] Vincenty, T., "Direct and Inverse Solutions of Geodesics on the Ellipsoid with Application on Nested Equations," Survey Review, XXII. 176, April 1975. 255

[142] Schneider, S. P., "Hypersonic Boundary Layer Transition on Reusable Launch Vehicles," *RLV/SOV Airframe Technology Review*, Meeting was ITAR restricted, NASA Langley,19-22 November 2002. 255

[143] Berry, S. A., and Horvath, T. J., "Discrete Roughness Transition for Hypersonic Flight Vehicles," *45th AIAA Aerospace Sciences Meeting and Exhibit*, Reno NV, 8-11 January 2007. 256

[144] Defense Science Board Task Force, "National Aero-Space Plane (NASP) Program", November 1992. 256

[145] Passaro, A., and Baccarella, D., "Roughness Induced Transition in Hypersonic Regime Over a Flat Plate," *17th AIAA International Space Planes and Hypersonic Systems and Technologies Conference*, San Francisco, California, 11 - 14 April 2011. 260

[146] Bowcutt, K., "Hypersonic Vehicle Systems Integration: Vehicle Stability and Control," PowerPoint Presentation, Boeing Phantom Works, 12 September 2007. 269